Searches for supersymmetric partners of third generation quarks and measurement of the $t\bar{t} + Z$ process using the ATLAS detector at the CERN Large Hadron Collider

Josh McFayden

Supervisor: Prof. Dan Tovey

A Thesis Submitted for the Degree of Doctor Of Philosophy in Physics

Department of Physics and Astronomy
University of Sheffield, August 2013

Abstract

This thesis presents results using data collected by the ATLAS experiment during 2011 and 2012 at $\sqrt{s} = 7$ TeV and 8 TeV respectively. The focus of the work presented in this thesis is separated into two areas, measurement of the $t\bar{t}+Z$ process and searches for the supersymmetric partners to third generation quarks.

Firstly, a search for $t\bar{t}+Z$ production using 4.7 fb^{-1} of $\sqrt{s} = 7$ TeV data is described including the generation of the dedicated simulated signal Monte Carlo samples for the analysis. The result is interpreted in terms of a 95% probability upper limit on the $t\bar{t}+Z$ production cross section of 0.71 pb. This is compatible with NLO Standard Model prediction of 0.14 pb.

Secondly, a number of searches for the supersymmetric partners of bottom (sbottom) and top (stop) quarks are described. The first is a search for sbottom squark pair production in the $\tilde{b}_1 \rightarrow b\tilde{\chi}_1^0$ decay channel using 2.05 fb^{-1} of $\sqrt{s} = 7$ TeV ATLAS data. No significant excess is observed above the Standard Model expectation and exclusion limits at the 95% confidence level are set in the $m_{\tilde{b}_1} - m_{\tilde{\chi}_1^0}$ plane. For a massless neutralino sbottom masses are excluded up to 390 GeV. For neutralino mass of 120 GeV sbottom masses are excluded for $275 < m_{\tilde{b}} < 350$ GeV. Finally two searches for stop squark pair production in the $\tilde{t}_1 \rightarrow t\tilde{\chi}_1^0$ decay channel are described, one using 4.7 fb^{-1} of $\sqrt{s} = 7$ TeV data and the other using 20.5 fb^{-1} of $\sqrt{s} = 8$ TeV data. Again, no significant excess is observed above the Standard Model expectation and exclusion limits at the 95% confidence level are set in the $m_{\tilde{t}_1} - m_{\tilde{\chi}_1^0}$ plane. For a nearly massless neutralino, stop masses between 320 and 660 GeV are excluded. For neutralino mass of 150 GeV, stop masses are excluded between 400 and 620 GeV.

Acknowledgments

I want to thank my mum and dad without whom this thesis would clearly not have been possible. I would especially like to thank my mum for her constant support and inspiration, you are a remarkable person who I have a huge amount of love and respect for.

I would like to say a really big thank you to my supervisor Prof. Dan Tovey for your guidance and support throughout my PhD. Without your remarkable dedication, intellect and imagination for kinematic variables these past four years would probably have been significantly easier but certainly significantly less enjoyable and gratifying.

Thanks to the many clever funny people I've had the pleasure of meeting and working with at the University of Sheffield. In particular Kerim, Davide, Stathes, Ian, Paul(s), Matt, Rich, Mark, Vitaly and Elena. I would also like to thank the not-so-clever, not-so-funny people I've had the dubious pleasure of sharing an office with and being better at football than over the years: Tua, Simon, Steve, Sam, Gary, Brais, Ed and Jon.

A big thank you also to all the people I met whilst out at CERN. Special mentions to Monica D'Onofrio, Anna Sfyrla and Nathan Triplett. A big thank you to the UK-CERN contingent, especially TJ, Chris, Gareth, Will P, Vik, John, Jay, Nick, Kara, Sarah. You guys made St. Genis/Geneva a joy, even though I was mostly too busy working to socialise with you. Clearly the most important mention here goes to *The Core*. In no particular order: Joe, Tom and Adam. Your companionship in all sporting activities has been nothing short of heroic.

I also want to thank all my friends from home, Manchester, Sheffield and elsewhere. Without the welcome distractions you have all so willingly provided over the years, the world of particle physics could have become wild and treacherous place. It is largely down to you all that I'm still here to tell the tale. I would like to give a special mention to my brothers Luke, Max and Alex for the effortless good times you only get from the best of old friends, to Henry for being my partner in crime during undergrad, I'm sure my academic record would have significantly suffered without you, and finally to all of *The Gang*, you know who you are.

Saving the most important until last, I want to thank my beautiful pickle (Suz) for her love and support during the last 8 years. Especially for putting up with the stress, the late nights and me deserting you by running off to Geneva for a year. But mainly for always putting a smile on my face at the end of a tough day.

AUTHOR'S CONTRIBUTIONS

The material presented in this thesis has its foundations in work performed by a large number of people within the ATLAS collaboration. The author's contribution will be stated explicitly at the start of each chapter and is summarised here for completeness.

SCT configuration monitoring

The author was responsible for writing a framework to analyse information about the semiconductor tracker configuration from the configuration database and display it in graphical format on a dedicated website. This work is described in §3.7.2.

$t\bar{t} + \mathrm{V}$ Monte Carlo sample generation

The author was responsible for the generation of $t\bar{t} + V, (V = W, Z)$ simulated samples at both $\sqrt{s} = 7$ and 8 TeV. These samples have been used both as a signal sample and as a background in many ATLAS analyses. The author was also responsible for formulating a procedure for estimating the generator systematic uncertainties associated with these samples.

Topological jet trigger

The author was responsible for the design and implementation of a topological jet trigger for SUSY searches as described in §5.3. This involved writing the trigger algorithm and thorough validation of the algorithm before it was used to collect data. In addition the author provided justification for the allocation of trigger bandwidth for this trigger and others through optimisation of the ATLAS SUSY Working Group trigger strategy, as described in §5.4.

Measurement of $t\bar{t} + Z$

The author was responsible for initiating this analysis and was heavily involved in many aspects of the work described in Chapter 6. This includes an initial sensitivity study to determine the feasibility of such a measurement, generation of the $t\bar{t} + Z$ signal and several background simulated samples and development of a system for estimation of generator systematic uncertainties. This analysis was published in a conference note [1] which the author co-edited.

Search for sbottom pair production

In the analysis outlined in Chapter 8 the author was responsible for the introduction of the contransverse mass variable used for discrimination between signal and background. The author made significant contributions to the signal region optimisation and estimation of the leptonic $t\bar{t}$ and W+jets backgrounds. This analysis was published in a paper [2].

Search for stop pair production

The author was responsible for initiating this analysis, including the introduction of a key new discriminating variable for rejection of the dominant $t\bar{t}$ background. The author was also responsible for signal region optimisation, estimation of the QCD background, generation of the $t\bar{t} + W/Z$ background and estimation of the corresponding generator systematic uncertainties. The analysis using 2011 data was published in a paper [3] and the analysis using 2012 data was published as a conference note [4]. The author co-edited the internal documentation in both cases.

“ *The things that we think we know something about. I’m going to tell you what the theory is, what it looks like, ...just what the thing is.*
- the question is, are you going to understand it?

...When I tell you first, that the first time we really thoroughly explain it to our own physics students is when they’re in the third [graduate] year...
then you think the answer is no,
and that is correct - you will not understand.

But this business about not understanding is a very serious one that we have between the scientists and an audience, and I want to work with you, because I’m going to tell you something:
the students do not understand it either,
and that is because the professor does not understand it!

My task, really, is to convince you not to turn away because it appears incomprehensible. The thing that is exciting about this is that nature is STRANGE...
That the rules ...by which we understand nature are so SCREWY,
you can’t believe them!

There’s saying that you don’t understand it, meaning
‘I don’t believe it, it’s too crazy, ...I’m just not going to accept it.’

Well... I hope you’ll come along with me and you’ll have to accept it, because it’s the way nature works.

If you want to know the way nature works, ...we looked at it carefully - that’s the way it looks!
You don’t like it?
Go somewhere else,
to another universe where the rules are simple,
philosophically more pleasing,
more psychologically easy.
- I can’t help it, OK?! ”

- Richard Feynman.

The Douglas Robb Memorial Lectures 1979 - University of Auckland

Contents

Chapter 1

Introduction

The Large Hadron Collider (LHC) and its experiments are some of the largest and most complex constructions in human history. They were built with the intention of shedding light on fundamental physics and have now been succesfully gathering data for over two years. This thesis will describe a number of analyses that make use of data collected by the ATLAS (**A** **T**oroidal **L**HC **A**pparatu**S**) detector, specifically a measurement of the $t\bar{t}+Z$ process and searches for supersymmetry (SUSY).

Firstly an introduction to the theoretical framework of the Standard Model of particle physics (SM) is given in Chapter 2. This framework represents the best current understanding of funamental particles and their interactions, however it does have some failings. A discussion of these failings, possible theoretical solutions and their experimental signatures is given. One particularly well motivated extension to the SM is SUSY which is introduced in some detail.

In Chapter 3 the LHC and the ATLAS detector are outlined. During 2011 and 2012 the LHC produced proton-proton (p-p) collisions with a centre of mass energy of 7 TeV and 8 TeV respectively. The resulting particle interactions were measured and recorded by ATLAS which is a general purpose detector. Chapter 4 describes many analysis tools that are used in the following Chapters. After a brief introduction to the ATLAS detector in Chapter 3, Chapter 5 provides an overview of the ATLAS trigger system. Particular focus is given to jet triggers and the author's contribution to designing and implementing a topological jet trigger for selecting SUSY events.

The remaining Chapters describe several physics analyses which the author has made significant contributions towards. Firstly, Chapter 6 describes a measurement of production of the $t\bar{t}+Z$ process. This process is predicted by the SM but yet to be experimentally observed. This is the first measurement of this process by ATLAS.

Chapter 7 gives an introduction into searches for SUSY and specifically searches for the supersymmetric partners of third generation quarks. This Chapter gives more detailed theoretical motivation for such searches and describes some of the common aspects of the analyses that are used in the following two Chapters. Chapter 8 describes the first ATLAS search for pair production of the supersymmetric partner to the bottom quark (sbottom). Chapter 9 describes the first ATLAS searches for pair production of the supersymmetric partner to the top quark (stop) using the full 2011 and 2012 datasets. Finally, Chapter 10 summarises the major results and conclusions from the work outlined in this thesis.

Chapter 2

Theory and motivation

2.1 Introduction

In this Chapter a brief overview of the SM will be given, followed by an introduction to one possible extension to the SM - SUSY.

The SM is the theoretical framework which describes the fundamental particles and their interactions which constitute much, but not all, of the known universe. It is the result of many years of collaboration between experiment and theory. The framework of the SM has been used to make predictions which have been confirmed by experiment to very high levels of accuracy. Feynman once remarked of the precision of theoretical calculations and experimental measurement of the anomalous magnetic moment of the electron:

> *" If you were measuring the distance of me to the Moon, the question would come up; 'do you mean from my chin or from the top of my head?'. "*

The current experimental measurement and theoretical calculation of this quantity are in agreement across twelve orders of magnitude [5].

There are, however, some areas in which the SM does not fare quite so well. The SM offers no explanation of one of the four known forces of nature, gravity. There is no prediction of a particle that would constitute a suitable candidate for dark matter (DM). DM is non-luminous matter that constitutes 80% of the gravitating matter in the universe, the existence of which is inferred through measurement of galaxy rotation curves and gravitational lensing [6]. The SM also offers no solution to the *hierarchy problem* (described in detail in §2.2.3). Therefore, some extension to the SM is required to fix these inconsistencies.

	Leptons			Quarks		
	Particle	Mass	Charge	Particle	Mass	Charge
I	electron e	0.511 MeV	-1	up u	2.3 MeV	$+\frac{2}{3}$
	e neutrino ν_e	< 2 eV	0	down d	4.8 MeV	$-\frac{1}{3}$
II	muon μ	105.658 MeV	-1	charm c	1.275 GeV	$+\frac{2}{3}$
	μ neutrino ν_μ	< 2 eV	0	strange s	95 MeV	$-\frac{1}{3}$
III	tau τ	1776.82 MeV	-1	top t	173.07 GeV	$+\frac{2}{3}$
	τ neutrino ν_τ	< 2 eV	0	bottom b	4.18 GeV	$-\frac{1}{3}$

Table 2.1: The SM fermions, spin-1/2 particles, with their corresponding masses taken from [7].

In what follows the basic concepts of the SM will be introduced followed by a brief introduction to SUSY - one plausible extension to the SM which attempts to rectify a number of the failings identified above.

2.2 Standard Model

The SM treats all the fundamental particles as point-like entities with an internal angular momentum quantum number, spin. The spin value of fundamental particles classifies them into one of two categories, *fermions* with half-integer spin and *bosons* with integer spins. Fermions are often referred to as the constituents of matter[1], whilst bosons are the force carriers that mediate interactions between fermions.

The known particle content of the SM is given in Tables 2.1 and 2.2. For each fermion an anti-matter counterpart also exists with the same mass but opposite quantum numbers. Fermions are separated into two categories depending on whether or not they interact via the strong force. Those that do are referred to as *quarks* and those that do not are referred to as *leptons*. Neutrinos are neutral leptons assumed to be massless by the SM that interact only via the weak force. The charged leptons interact via the electromagnetic and weak forces. Quarks interact via all three forces of the SM.

In Table 2.1 the three three quark and lepton generations are denoted by I, II and III. Each generation appears to be identical in every respect other than the particle masses. The reason for there being exactly three generations is not clear.

---

[1] Although only the first generation u-quark, d-quark and electron make up the majority of matter.

Particle		Mass	Charge	Spin
photon	γ	-	0	1
$W^{\pm}$		80.385 GeV	±1	1
Z		91.1876 GeV	0	1
gluon	g	-	0	1
Higgs	h	125.9 GeV	0	0

Table 2.2: The SM bosons, integer-spin particles, with their corresponding masses taken from [7].

The weak interaction does not couple to the "physical" quarks but to weak eigenstates that correspond to a linear combination of the mass eigenstates with some mixing defined by the Cabibbo-Kobayashi-Maskawa (CKM) matrix . The result is the weak interaction violates quark flavour. It is interesting to note for a CP-violating phase to be present in the CKM matrix at least three generations are required. In fact, this was the original motivation for proposing this structure which came even before even the complete second generation was experimentally verified [8,9]. However, no experimental evidence for a fourth generation currently exists and in the neutrino sector experimental evidence suggests that there are only three generations [10].

Not shown in Table 2.1 are the three copies of each quark flavour due to the three quark colour charges, nor the eight gluons in Table 2.2. In total there are 61 distinct particles in the SM: 6 quarks each copied 3 times for each colour, their 18 anti-particles and 8 gluons; 6 leptons, again each with their own corresponding anti-particle, three vector bosons and one photon; and the Higgs boson. All have been experimentally verified with the exception of the Higgs boson. However, both ATLAS and CMS have recently been able to claim observation of a new boson with a mass of ~ 126 GeV [11, 12] whose properties appear consistent with a SM Higgs boson [13, 14].

2.2.1 Quantum field theory

The SM is constructed by a relativistic quantum field theory (QFT) in which particle fields that permeate all space are quantised. Excitations in each respective field correspond to a particle of that field. The Lagrangian formulation is used to derive the dynamics of and interactions between different particle fields. The application of the concept of symmetry to the Lagrangian by imposing local gauge invariance introduces new vector fields. This gives rise to new interaction terms in the Lagrangian which couple the fermion fields to the new vector fields. Unfortunately this new gauge field is required to be massless to preserve local gauge invariance, which is clearly at odds with experimental evidence for the W and Z bosons that are known to be massive [7]. Fortunately however, this issue can be resolved through the introduction of *spontaneous symmetry breaking* and the *Higgs mechanism* which will discussed in more detail in §2.2.2. The SM is mathematically described by the combination of the $SU(3)_C$ symmetry group generated by the *colour* charge and the unified electroweak interaction corresponding to the $SU(2)_L \times U(1)_Y$ group symmetries of left-handed weak isospin and hypercharge, respectively:

$$SU(3)_C \times SU(2)_L \times U(1)_Y. \tag{2.1}$$

QED

Quantum Electrodynamics (QED) is perhaps the simplest formulation of QFT in the SM. This is because the set of gauge transformations of QED commute (the generators are Abelian). In group theory these transformations are said to belong to the $U(1)_Q$ gauge group. Physically this means that the mediating gauge bosons in QED have no self coupling.

This section will describe how imposing local gauge invariance on the Lagrangian of free Dirac fields introduces new vector fields that must be massless[2]. The Lagrangian density for a free Dirac field, ψ, is given by

$$\mathcal{L} = i\bar{\psi}\gamma^{\mu}\partial_{\mu}\psi - m\bar{\psi}\psi. \tag{2.2}$$

It can trivially be shown that this Lagrangian is invariant under the *global transformation*

$$\psi \to e^{i\theta}\psi, \tag{2.3}$$

however it is more interesting to consider the more general case where the gauge transformation is dependent on position

$$\psi \to e^{i\theta(x)}\psi, \tag{2.4}$$

this is a *local gauge transformation.* The x dependance on θ now results in an additional

---

[2] The remainder of this section will closely follow prescriptions taken from [9], [15] and [16].

term in the Lagrangian after transformation from the derivative

$$\mathcal{L} \to \mathcal{L} - (\partial_\mu \theta \bar{\psi} \gamma^\mu \psi). \tag{2.5}$$

However, it is possible to retain invariance under this local gauge transformation by adding an additional term in the Lagrangian, such that the new Lagrangian is given by

$$\mathcal{L} = \bar{\psi} \left(i\gamma^\mu \partial_\mu - m \right) \psi - q\bar{\psi}\gamma^\mu A_\mu \psi. \tag{2.6}$$

A new *gauge* field A_μ has been introduced, which under local gauge transformations transforms as

$$A_\mu \to A_\mu + \partial_\mu \lambda. \tag{2.7}$$

Here $\lambda(x) = -\frac{1}{q}\theta(x)$ and q is the charge of the corresponding particle. This restores the invariance of the Lagrangian under local gauge transformations. However, the Lagrangian is now missing a *free* term for this new vector field. Defining $F^{\mu\nu} \equiv \partial^\mu A^\nu - \partial^\nu A^\mu$ the following free terms are added

$$\mathcal{L} = -\frac{1}{4} F^{\mu\nu} F_{\mu\nu} + \frac{1}{2} m_A^2 A^\nu A_\nu. \tag{2.8}$$

However, this poses a problem, the first term is invariant under (2.7) the second is not. In order for the Lagrangian to be invariant under local gauge transformations $m_A = 0$, i.e. the vector field must be massless. The resulting Lagrangian is

$$\mathcal{L}_{\text{QED}} = \bar{\psi} \left(i\gamma^\mu \partial_\mu - m \right) \psi - \frac{1}{4} F^{\mu\nu} F_{\mu\nu} - q\bar{\psi}\gamma^\mu A_\mu \psi. \tag{2.9}$$

Thus, the QED Lagrangian has been derived by taking the Lagrangian for free Dirac fields and imposing local gauge invariance. This describes all of electrodynamics, free Dirac particles and their interactions. Note that last two terms in (2.9) correspond to the Maxwell Lagrangian with current density $J^\mu = q(\bar{\psi}\gamma^\mu\psi)$.

At this point it is useful to define the *covariant derivative*

$$\mathcal{D}_\mu \equiv \partial_\mu + iqA_\mu. \tag{2.10}$$

This allows the QED Lagrangian to be written, in more compact notation, as follows

$$\mathcal{L}_{\text{QED}} = \bar{\psi} \left(i\gamma^\mu \mathcal{D}_\mu \psi - m \right) \psi - \frac{1}{4} F^{\mu\nu} F_{\mu\nu}. \tag{2.11}$$

QCD

A similar approach can be taken to construct the QCD Lagrangian, however the situation is more complicated. The strong force can be seen as a manifestation of invariance under changes of colour charge. Imposing local gauge invariance under the non-Abelian $SU(3)_C$ transformations of quark states introduces the 8 gauge fields that correspond to the 8 gluons colour states.

The QCD Lagrangian can be written

$$\mathcal{L}_{\mathrm{QCD}} = \bar{\psi}\left(i\gamma^{\mu}\mathcal{D}_{\mu}\psi - m\right)\psi - \frac{1}{4}\mathbf{F}^{\mu\nu}\cdot\mathbf{F}_{\mu\nu}, \tag{2.12}$$

where ψ is defined to be

$$\psi \equiv \begin{pmatrix} \psi_r \\ \psi_g \\ \psi_b \end{pmatrix}, \bar{\psi} \equiv \left(\bar{\psi}_r, \bar{\psi}_g, \bar{\psi}_b\right), \tag{2.13}$$

the covariant derivative is defined to be

$$\mathcal{D}_{\mu} \equiv \partial_{\mu} + iq\boldsymbol{\lambda}\cdot\mathbf{A}_{\mu} \tag{2.14}$$

and $\mathbf{F}^{\mu\nu}$ is defined to be

$$\mathbf{F}^{\mu\nu} \equiv \partial_{\mu}\mathbf{A}^{\nu} - \partial_{\nu}\mathbf{A}^{\mu} - 2q\left(\mathbf{A}^{\mu}\times\mathbf{A}^{\nu}\right). \tag{2.15}$$

In (2.14) λ are the Gell-Mann "λ-matrices" which are the SU(3) equivalent of the Pauli matrices. The $SU(3)$ "cross product" in (2.15) is shorthand for

$$(B\times C)_{\alpha} = \sum_{\beta,\gamma=1}^{8} f_{\alpha\beta\gamma}B_{\beta}C_{\gamma}, \tag{2.16}$$

where the *structure constants*, $f^{\alpha\beta\gamma}$, are defined by the commutators

$$\left[\lambda^{\alpha},\lambda^{\beta}\right] = 2if^{\alpha\beta\gamma}\lambda^{\gamma}. \tag{2.17}$$

Of course (2.12) must be replicated 6 times for each quark flavour. The non-Abelian nature of $SU(3)_C$ results in the addition interaction term in (2.15) which gives rise to the triple and quartic gluon coupling terms. These terms contribute to the weakening of the strong force at higher energies or shorter distance scales, a phenomenon known as *asymptotic freedom*. Another important feature of QCD is *confinement*, the fact that the only free states observed in nature are colour singlets. One important consequence of confinement is that it causes free partons to hadronise, forming colour singlet states of mesons ($r\bar{r}, g\bar{g}, b\bar{b}$) and baryons ($rgb, \bar{r}\bar{g}\bar{b}$). Experimentally this means that high energy quarks and gluons produced in collisions reach the detector as a collimated spray of hadrons, referred to as a particle *jet*.

Electroweak unification

The unification of the electromagnetic and weak forces was first suggested by Glashow in 1961 [17]. The disparity in the coupling strengths of the two forces could be explained if the bosons that mediate weak interactions are very massive. It took the additional insight of Weinberg and Salam to provide a complete solution utilising the Higgs mechanism [18, 19].

The weak current is constructed from the $SU(2)_L$ group of weak isospin which is observed to only couple to left-handed fermions. $U(1)_Y$ is the group of weak hypercharge, Y, which is related to the $U(1)_Q$ symmetry group of QED by $Y/2 = Q - I_3$ where Q is the electric charge and I_3 is the third component of weak isospin.

Once again, the starting point is the Dirac Lagrangian and new vector fields are introduced through imposing local gauge invariance. The electroweak Lagrangian is given by

$$\mathcal{L}_{\text{EW}} = \bar{\psi}\left(i\gamma^\mu \mathcal{D}_\mu \psi - m\right)\psi - \frac{1}{4}\mathbf{W}^{\mu\nu}\cdot\mathbf{W}_{\mu\nu} - \frac{1}{4}B^{\mu\nu}B_{\mu\nu}, \tag{2.18}$$

where ψ are the left-handed doublets and right-handed singlets:

$$\psi_{\text{leptons}} = \begin{pmatrix} \nu_L^e \\ e_L^- \end{pmatrix}, e_R, \begin{pmatrix} \nu_L^\mu \\ \mu_L^- \end{pmatrix}, \mu_R, \begin{pmatrix} \nu_L^\tau \\ \tau_L^- \end{pmatrix}, \tau_R, \tag{2.19}$$

$$\psi_{\text{quarks}} = \begin{pmatrix} u_L \\ d_L \end{pmatrix}, u_R, d_R, \begin{pmatrix} c_L \\ s_L \end{pmatrix}, c_R, s_R, \begin{pmatrix} t_L \\ b_L \end{pmatrix}, t_R, b_R. \tag{2.20}$$

The final two terms in (2.18) correspond to the free terms for the weak vector fields, $\mathbf{W}_\mu$, and the hypercharge vector field, B_μ. The covariant derivative in this case is given by

$$\mathcal{D}_\mu \equiv \partial_\mu + ig_W \boldsymbol{\tau}\cdot\mathbf{W}_\mu + ig_Y \frac{Y}{2} B_\mu, \tag{2.21}$$

where g_W and g_Y are the coupling constants for each respective field and τ represents the generators of the $SU(2)_L$ group. The corresponding electroweak gauge fields $W_\mu^\pm$, Z_μ and A_μ are linear combinations of the weak and hypercharge fields

$$W_\mu^\pm = \frac{1}{\sqrt{2}}(W_\mu^1 \pm iW_\mu^2), \tag{2.22}$$

$$Z_\mu = \cos\theta_W W_\mu^3 - \sin\theta_W B_\mu, \tag{2.23}$$

$$A_\mu = \sin\theta_W W_\mu^3 - \cos\theta_W B_\mu. \tag{2.24}$$

2.2.2 Spontaneous symmetry breaking and the Higgs mechanism

At this stage the gauge fields for the SM bosons of QCD and the electroweak interactions have been generated by imposing local gauge invariance. However, maintaining this invariance requires that the vector fields be massless. This is not a problem for the photon and gluons, but it is known from experiment that the W and Z bosons have mass. Fortunately there is a way to manipulate the theory to incorporate massive gauge fields through *spontaneous symmetry breaking* and the *Higgs mechanism*.

The concept of spontaneous symmetry breaking can be introduced by first considering the simple case of a scalar field φ, for which the Lagrangian is given by

$$\mathcal{L} = \frac{1}{2}(\partial_\mu\varphi)(\partial^\mu\varphi) + \frac{1}{2}\mu^2\varphi^2 - \frac{1}{4}\lambda^2\varphi^4. \tag{2.25}$$

The second term in (2.25) appears to be a mass term but with the wrong sign. Remembering that $\mathcal{L} = \mathcal{T} - \mathcal{U}$, the above Lagrangian has the potential

$$\mathcal{U}(\varphi) = -\frac{1}{2}\mu^2\varphi^2 + \frac{1}{4}\lambda^2\varphi^4, \tag{2.26}$$

where the minimum of $U(\varphi)$ is given by $\varphi = \pm\mu/\lambda$. If a new field variable η is introduced and defined to be

$$\eta \equiv \varphi \pm \frac{\mu}{\lambda}, \tag{2.27}$$

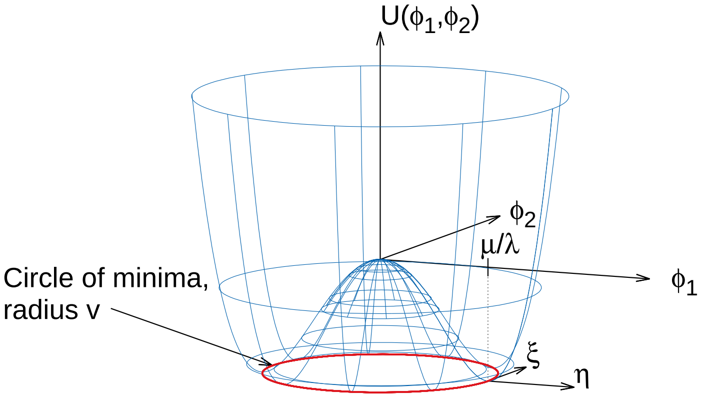

Figure 2.1: The potential for a complex scalar field.

this corresponds to a redefinition of the ground state. The resulting Lagrangian is

$$\mathcal{L} = \frac{1}{2}(\partial_\mu \eta)(\partial^\mu \eta) - \mu^2\eta^2 \pm \mu\lambda\eta^3 - \frac{1}{4}\lambda^2\eta^4 + \frac{1}{4}(\mu^2/\lambda)^2. \tag{2.28}$$

The second term in (2.28) now gives mass term with the correct sign, corresponding to a field with mass

$$m = \sqrt{2}\mu, \tag{2.29}$$

and the third and fourth terms correspond to triple and quartic scalar couplings.

Whereas the original Lagrangian (2.25) is even, i.e. symmetric, under the exchange $\varphi \to -\varphi$, the new Lagrangian (2.28) is not even in η; the symmetry has been *broken*. This is due to the fact that one of the “vacuum” states must arbitrarily be chosen to work with, thus *spontaneously* breaking the symmetry. The intrinsic symmetry of the Lagrangian is hidden by the arbitrary choice of an asymmetric ground state.

This can now be extended to the $SU(2)$ symmetry group, considering a complex scalar field, φ, with Lagrangian

$$\mathcal{L} = \frac{1}{2}(\partial_\mu \varphi)^*(\partial^\mu \varphi) + \frac{1}{2}\mu^2(\varphi^*\varphi) - \frac{1}{2}\lambda^2(\varphi^*\varphi)^2. \tag{2.30}$$

With a potential shown in Figure 2.1. Once more, the requirement that the Lagrangian is invariant under local gauge transformations

$$\varphi \to e^{i\theta(x)}\varphi, \tag{2.31}$$

can be imposed. Of course this means introducing the massless vector field A_μ and the Lagrangian becomes

$$\mathcal{L} = \left[\left(\partial_\mu - iqA_\mu\right)\varphi^*\right]\left[\left(\partial^\mu + iqA^\mu\right)\varphi\right] + \mu^2\varphi^*\varphi - \lambda^2(\varphi^*\varphi)^2 - \frac{1}{4}F^{\mu\nu}F_{\mu\nu}. \tag{2.32}$$

Similarly to (2.27) two new fields can be defined

$$\eta \equiv \varphi_1 - \frac{\mu}{\lambda} \quad , \quad \xi \equiv \varphi_2 \tag{2.33}$$

where ξ corresponds to a massless Goldstone boson. By choosing a specific gauge[3] the resulting Lagrangian is

$$\mathcal{L} = \left[\frac{1}{2}\left(\partial_\mu\eta\right)\left(\partial^\mu\eta\right) - \mu^2\eta^2\right] + \left[-\frac{1}{4}F^{\mu\nu}F_{\mu\nu} + \frac{1}{2}\left(q\frac{\mu}{\lambda}\right)^2 A_\mu A^\mu\right] + \mathcal{L}_{\text{int}} \tag{2.34}$$

Thus, a massive scalar field η has been introduced which corresponds to the famous Higgs boson and the vector field A_μ has been given mass. This combination of gauge invariance and spontaneous symmetry breaking is the *Higgs mechanism*.

In the SM this corresponds to the W and Z bosons acquiring mass whilst the photon remains massless. The masses are related by

$$m_{W^\pm} = \frac{1}{2}v g_Y \tag{2.35}$$

$$m_Z = \frac{v}{2}\sqrt{g_Y^2 + g_W^2} \tag{2.36}$$

$$\cos\theta_W = \frac{m_W}{m_Z} \tag{2.37}$$

where θ_W is the Weinberg angle and g_Y and g_W are the hypercharge and weak current coupling strengths.

---

[3] This choice is made to eliminate the unwanted Goldstone boson and the troublesome interaction terms it introduces. The specific gauge choice is $\theta = -\tan\varphi_1/\varphi_2$, which in the transformation $\varphi \to \varphi'$ results in φ' being real ($\varphi_2' = 0$).

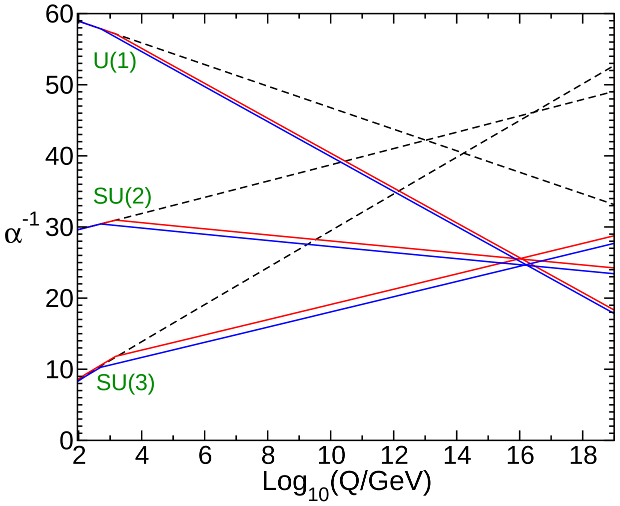

Figure 2.2: The evolution of the gauge coupling in the SM (dashed lines) and the MSSM (solid lines). Figure from [20].

The Higgs mechanism also gives mass to the fermions. The terms in the Lagrangian corresponding to the the Higgs' couplings to the first generation fermions take the form

$$\mathcal{L} = -\lambda_e \bar{l}^i_L \varphi_i e_R - \lambda_d \bar{q}^i_L \varphi_i d_R - \lambda_u \epsilon_{ij} \bar{q}^i_L \varphi^*_j u_R \quad + \quad \text{hermitian conjugate} \tag{2.38}$$

$$\tag{2.39}$$

where l_L and q_L are the left-handed lepton and quark doublets and e_R, d_R and u_R are the electron, d- and u-quark right-handed singlets. λ_e, λ_d and λ_u correspond to the electron, d- and u-quark Yukawa couplings, where the Yukawa couplings are related to the fermion masses by $m_f = \lambda_f v/\sqrt{2}$. The Yukawa couplings are not predicted by the SM, hence neither are the fermion masses which must be experimentally measured.

2.2.3 Failings of the Standard Model

Although the SM is theoretically and experimentally one of the great triumphs of physics in the 20th century, it is not without fault. The SM contains several free parameters; it is not known why there are three generations of fermions or why the masses of the quarks differ by orders of magnitude. The extent of CP violation and electroweak mixing are further examples of parameters which must be determined by experiment.

Experimental evidence of neutrino oscillations [21] imply that neutrinos must have

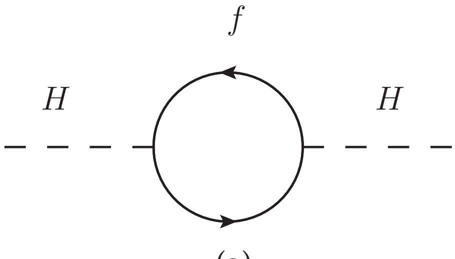

(a)

Figure 2.3: Feynman diagrams showing contributions to the Higgs boson mass from fermion loops.

mass. However, in the SM the weak interaction only couples to left-handed neutrinos which are predicted to be massless indicating the SM is incomplete in this regard.

In other areas the SM model provides no explanation at all. Gravity is not incorporated in the SM and despite indirect experimental evidence for DM the SM does not postulate any candidates for DM. Unification of the fundamental forces is certainly a desirable quality in a "theory of everything". Although, as can be seen in Figure 2.2, there is some convergence of the strength of the force couplings at very high energies they do not converge exactly. Another serious concern for the SM is what is known as the *hierarchy problem*.

The hierarchy problem

The *hierarchy problem* [22–25] refers to the fact that the Higgs boson mass, m_H^2, receives divergent quantum corrections from virtual effects of all particles that couple to the Higgs boson field. The relevant Lagrangian contains the term $-\lambda_f H\bar{f}f$ and the corresponding correction to m_H^2 due to fermion loops, such as the diagram shown in Figure 2.3, is given by

$$\Delta m_H^2 = -\frac{\lambda_f^2}{8\pi^2}\left[\Lambda_{\mathrm{UV}}^2 - 6m_f^2 \ln\left(\Lambda_{\mathrm{UV}}/m_f\right) + ...\right] \tag{2.40}$$

where λ_f is the fermion Yukawa coupling and Λ_{UV} is the ultraviolet momentum cut-off which corresponds to the lower limit at which new physics can enter which alters the high-energy behaviour of the theory. The largest contributions come from the top quark as $\lambda_f \simeq 1$. It is known that the SM is only an effective field theory, since gravity is not included. As such, it can only be valid up to some cut-off scale, the Planck scale, $M_P \sim 10^{19}$, where the effects of gravity become comparable to the other forces. If it is assumed that

$\Lambda_{\rm UV} \simeq M_P$ the resulting corrections to the m_H^2 are of order 10^{34} GeV. However, from electroweak precision measurements, such as electroweak couplings and the W and top masses, the Higgs boson mass is expected to be $\mathcal{O}(100\ \text{GeV})$ [26]. Not only that, but in order to preserve unitarity in vector boson scattering the Higgs boson mass is required to be below ~ 1 TeV [27, 28]. Therefore, in order to achieve a Higgs boson mass at the scale expected from precision measurements and unitarity arguments cancellations in the various contributions to m_H^2 must be precise to 17 orders of magnitude. The requirement for this seemingly very unnatural level of cancellation is referred to as the *hierarchy problem*.

2.3 Supersymmetry

Several theories exist that provide extensions to the SM in order to rectify some of the issues described in the previous section. Examples of such theories are Large Extra Dimensions [29] and Kaluza-Klein [30] models. However, the theory that the rest of this section is dedicated to describing is the theory of *supersymmetry* (SUSY)[4] [31–39]. The simple concept of SUSY is to introduce a symmetry between bosons and fermions resulting in the prediction of many new *superpartner* particles that accompany the existing SM particles.

A natural introduction to this idea comes in the context of the hierarchy problem, previously discussed in §2.2.3. In (2.40) the contributions to m_H^2 from fermion loops are given. It possible to imagine similar contributions from a massive complex scalar of the form

$$\Delta m_H^2 = \frac{\lambda_S}{8\pi^2}\left[\Lambda_{\rm UV}^2 - 2m_S^2 \ln\left(\Lambda_{\rm UV}/m_S\right) + ...\right] \tag{2.41}$$

where λ_S is the Yukawa coupling of the scalar.
The corresponding Feynman diagrams for these fermion and scalar contributions are shown in Figure 2.3 and Figure 2.4, respectively. Comparing the form of (2.40) and (2.41) a clear similarity in structure is present which implies a deeper underlying fermion-boson symmetry could exist. Note the difference in sign of these contributions. In fact the contributions from Figure 2.3 and Figure 2.4 give the following total radiative correction to the Higgs boson mass:

$$\Delta\, m_H^2\Big|_{\rm total} = \frac{\lambda_f^2}{4\pi^2}\left[\left(m_f^2 - m_S^2\right)\ln\left(\Lambda_{\rm UV}/m_S\right) + 3m_f^2 \ln\left(m_S/m_f\right)\right], \tag{2.42}$$

---

[4] The description given in this section closely follows that of [20].

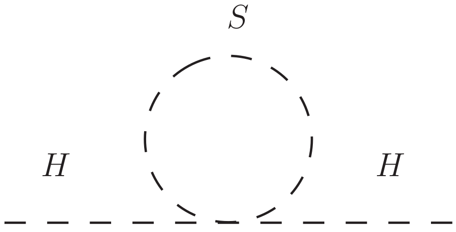

(a)

Figure 2.4: Feynman diagram showing contributions to the Higgs boson mass from scalar loops.

and will cancel exactly if each SM fermion has partnering complex scalars with $\lambda_f^2 = -\lambda_S$ and $m_f = m_S$. This boson-fermion symmetry is SUSY.

2.3.1 Foundations of SUSY

The supersymmetric transformation operator, Q, is defined such that it transforms a bosonic state into a fermionic state and a fermionic state into a bosonic state

$$Q\,|\text{Boson}\rangle = |\text{Fermion}\rangle\,, \tag{2.43}$$

$$Q\,|\text{Fermion}\rangle = |\text{Boson}\rangle\,. \tag{2.44}$$

A single particle state has corresponding fermion and boson states that are organised into a *supermultiplet*. Each state in the supermultiplet must have equal mass and must reside in the same representation of the gauge group because the SUSY generators commute with the gauge transformation generators. Therefore, all states in a supermultiplet share the same quantum numbers of electric charge, weak isospin, and colour. Each supermultiplet has the same number of fermionic and bosonic degrees of freedom.

The result is that SM particles must reside in either chiral or gauge supermultiplets with a superpartner that differs by half a unit of spin. The SM quarks and leptons form one component of a chiral supermultiplet alongside spin-0 scalar superpartners. These scalar particles are denoted with a tilde and their names are prepended with an "s" for scalar. For example, the superpartner of the quark is referred to as a *squark* and is denoted $\tilde{q}$. As the left-handed quarks and leptons have different gauge transformation properties, so do their superparters. The left-handed quark q_L has the superpartner $\tilde{q}_L$, but in this case the label refers only to the handedness of the squark's superpartner and not the helicity

Name	spin-0	spin-1/2	$SU(3)_C$,$SU(2)_L$,$U(1)_Y$
quarks, squarks (× 3 families)	$(\tilde{u}_L\tilde{d}_L)$	$(u_L d_L)$	$(3, 2, \frac{1}{6})$
	$\tilde{u}^*_R$	$u^\dagger_R$	$(\bar{3}, 1, -\frac{2}{3})$
	$\tilde{d}^*_R$	$d^\dagger_R$	$(\bar{3}, 1, \frac{1}{3})$
leptons, sleptons (× 3 families)	$(\tilde{\nu}\tilde{e}_L)$	(νe_L)	$(1, 2, \frac{1}{3})$
	$\tilde{e}^*_R$	$e^\dagger_R$	$(1, 1, 1)$
Higgs, higgsinos	$(H^+_u H^0_u)$	$(\tilde{H}^+_u \tilde{H}^0_u)$	$(1, 2, \frac{1}{2})$
	$(H^0_d H^-_d)$	$(\tilde{H}^0_d \tilde{H}^-_d)$	$(1, 2, -\frac{1}{2})$

Table 2.3: Chiral supermultiplets.

Name	spin-1/2	spin-1	$SU(3)_C$,$SU(2)_L$,$U(1)_Y$
gluon, gluino	$\tilde{g}$	g	$(8, 1, 0)$
W bosons, Winos	$\tilde{W}^\pm, \tilde{W}^0$	$W^\pm, W^0$	$(1, 3, 0)$
B boson, Binos	$\tilde{B}^0$	W^0	$(1, 1, 0)$

Table 2.4: Gauge supermultiplets.

of the sparticle. However, as the superpartners share the same gauge group it is only the left-handed squarks and sleptons that couple to the W boson.

Similarly, the gauge bosons combine with their spin-1/2 superpartners to form a gauge supermultiplet. The superpartners of the gauge bosons are referred to as *gauginos* and also denoted with a tilde. The gaugino fermions are required to have the same transformation properties for left- and right-handed components. The superpartner to the W boson is called the *Wino*, the superpartner of the B-boson is the *Bino* and the superpartner to the gluon is called the *gluino*.

Having spin-0 it appears that the Higgs boson should belong to a chiral supermultiplet. In the *minimal supersymmetric standard model* (MSSM) there are two Higgs supermultiplets, one which gives masses to the up-type quarks, H_u, and the other to the down-type quarks, H_d. Keeping the notation of suffixing the spin-1/2 superpartners with "-ino" the superpartners of the Higgs boson are called *higgsinos*.

The chiral supermultiplets and gauge supermultiplets which constitute the MSSM [40–44] are shown in Table 2.3 and Table 2.4.

With the formulation of SUSY described so far in this section the superpartners are still expected to have the same mass as their SM counterparts. Such particles would have been straightforward to discover and the lack of experimental evidence for them implies that SUSY is a *broken* symmetry. Furthermore, the symmetry should be broken in such a way as to preserve the cancellations in contributions to m_H^2 that are such an attractive aspect of SUSY. This kind symmetry breaking is referred to a *soft* symmetry breaking. If the mass scale associated with terms in the supersymmetric Lagrangian corresponding to this soft symmetry breaking is given by m_{soft}, the corresponding corrections to m_H^2 are given by

$$\Delta m_H^2 = m_{\text{soft}}^2 \left[\frac{\lambda}{16\pi^2} \ln \left(\Lambda_{\text{UV}} / m_{\text{soft}} \right) + ... \right], \tag{2.45}$$

where λ is the relevant coupling. From (2.45) it is clear that m_{soft} cannot be too large otherwise the m_{soft}^2 corrections to m_H^2 would be unnaturally large and the solution to the hierarchy problem is lost.

The superpartners described so far, and listed in Table 2.3 and Table 2.4, are not necessarily the mass eigenstates of the theory after symmetry breaking. There can be mixing between the electroweak gauginos and the higgsinos, and within the various sets of squarks and sleptons and Higgs scalars. The neutral fermionic MSSM content, consisting of the neutral bino, wino and Higgsino $(\tilde{H}_u^0, \tilde{H}_d^0)$, mix to form four neutral particles called neutralinos and denoted $\tilde{\chi}_{1,2,3,4}^0$. Two chargino states, $\tilde{\chi}_{1,2}^{\pm}$, arise from a mix of the charged winos $\tilde{W}^{\pm}$ and Higgsinos $(\tilde{H}_u^+, \tilde{H}_d^-)$. In the squark sector the amount of mixing is proportional to the corresponding standard model partner mass and is hence only non-negligible in the third generation. The stop $\tilde{t}_L$ and $\tilde{t}_R$ mix to form the $\tilde{t}_1$ and $\tilde{t}_2$. Similarly the superpartners of the right and left handed sbottom mix to form the $\tilde{b}_1$ and $\tilde{b}_2$, this is described in more detail in §7.2.1. The same applies to sleptons and only staus are considered to mix significantly, forming the $\tilde{\tau}_1$ and $\tilde{\tau}_2$ from the $\tilde{\tau}_L$ and $\tilde{\tau}_R$. The mixing is summarised in Table 2.5.

2.3.2 Unification

The electromagnetic and weak forces are now known to be two components of the *unified* electro-weak force. This implies that there could be some *grand unification theory* (GUT) which unifies all of the fundamental forces [45]. Therefore, the forces are manifest as distinct entities simply because this unification occurs at a very high energy scale. Such a unification is a certainly an attractive property for any new theory of beyond the SM (BSM) physics.

Original states	Mass eigenstates	Names
$\tilde{B}^0$,$\tilde{W}^0$,$\tilde{H}_u^0$,$\tilde{H}_d^0$	$\tilde{\chi}_1^0$,$\tilde{\chi}_2^0$,$\tilde{\chi}_3^0$,$\tilde{\chi}_4^0$	neutralinos
$\tilde{W}^{\pm}$,$\tilde{H}_u^+$,$\tilde{H}_d^-$	$\tilde{\chi}_1^{\pm}$,$\tilde{\chi}_2^{\pm}$	charginos
$(\tilde{t}_L,\tilde{t}_R)$,$(\tilde{b}_L,\tilde{b}_R)$	$(\tilde{t}_1,\tilde{t}_2)$,$(\tilde{b}_1,\tilde{b}_2)$	stops and sbottoms
$(\tilde{\tau}_L,\tilde{\tau}_R)$	$(\tilde{\tau}_1,\tilde{\tau}_2)$	staus

Table 2.5: The mass eigenstates that result from mixing in the MSSM.

The evolution of each of the couplings in the SM is shown by the dashed lines in Figure 2.2. The SM particle content is not sufficient to ensure that the electromagnetic, weak and strong couplings all converge at some high unification scale. However, the new particles predicted by SUSY cause the evolution of the running couplings to change. Figure 2.2 (solid lines) shows that the additional particle content of the MSSM has just the right effect on the evolution of the couplings that close to perfect unification occurs at $\sim 10^{16}$ GeV. This result is one of the many attractive aspects of SUSY.

2.3.3 R-parity

There are processes in the MSSM which allow for proton decay. An example of such a process is shown in Figure 2.5. Experimental evidence provides a lower limit on the proton lifetime, for example the Super-Kamiokande collaboration sets a limit on the $p \to K^+\bar{\nu}$ decay channel of $> 2.3 \times 10^{33}$ years [46]. This implies that if such a process did exist it must be inconceivably rare. One way such processes can be avoided is by imposing the requirement that *R-parity*, R_P, is conserved. The result of this ad-hoc requirement is that all lepton number violating terms in the supersymmetric Lagrangian are disallowed. R_P is defined as follows

$$R_P = (-1)^{2S+3B+L} \tag{2.46}$$

where S, B and L refer to spin, baryon number and lepton number respectively. The requirement that this multiplicative quantum number is conserved in all interactions has several important consequences for SUSY phenomenology. From the definition of (2.46) it is clear that SM particles have $R_P = +1$ and SUSY particles $R_P = -1$. As the LHC is a p−p collider, the initial state has $R_P = +1$, therefore all SUSY interactions must contain two SUSY particles. This means that SUSY particles must be produced in even numbers and

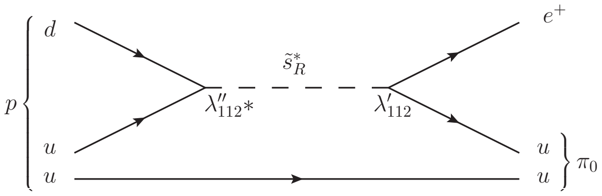

Figure 2.5: An example process that could lead to proton decay if R-parity were violated. Figure from [20].

they must decay to an odd number of SUSY particles. Importantly it also means that the lightest supersymmetric particle (LSP) must be stable. The fact that no such stable SUSY particle has been observed implies that it must be neutral and weakly interacting. Thus, R-parity conserving SUSY predicts a stable massive neutral weakly-interaction particle - these are the required properties for a DM candidate. This seemingly innocuous requirement to preserve the proton lifetime appears to resolve yet another shortcoming of the SM. It should be stated that not all SUSY models provide just the right kind of LSP to give the observed DM density as will be discussed in the following section.

2.3.4 Implications of cosmological and precision measurements

The LHC and its detectors are not the first experiments to search for supersymmetric particles. Constraints exist from previous generations of collider experiments, most significantly the *Large Electron-Positron* (LEP) collider at CERN and the Tevatron proton-antiproton collider at Fermilab. In addition, there are constraints from cosmological measurements, such as the observed DM relic density, and from direct DM detection experiments. Finally, there are also constraints from indirect measurements of low-energy observables.

Each will now be discussed in more detail. For convenience, and because until recently it has been the focus of a large proportion of SUSY searches, the following shall be considered specifically in the context of the Constrained MSSM (CMSSM) [47–52]. The CMSSM is defined by only five parameters; the scalar superpartners along with the gauginos have a common masses at the SUSY-breaking scale, denoted m_0 and $m_{1/2}$ respectively; the universal trilinear scalar coupling, A_0, the ratio of the vacuum expectation values of the two Higgs boson fields, $\tan\beta$, and the sign of the higgsino mass parameter, μ.

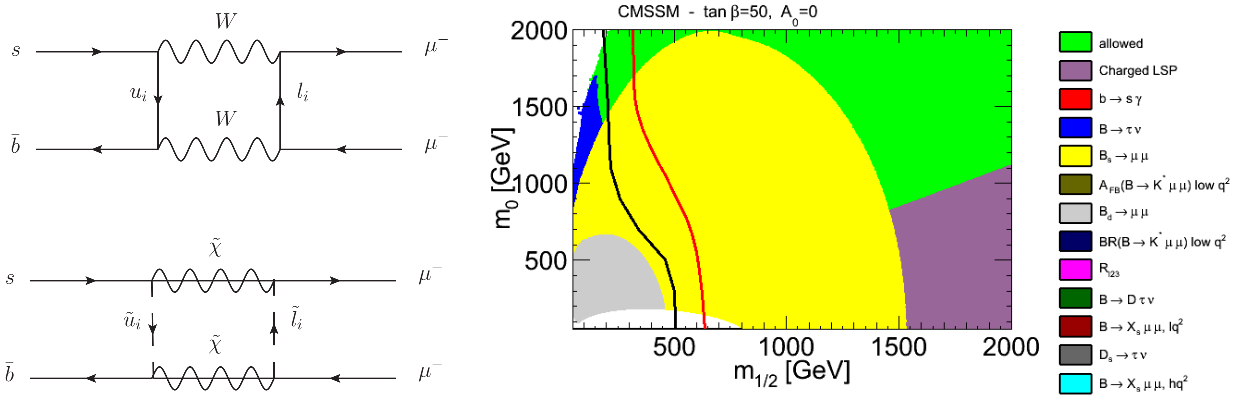

(a) **(b)**

Figure 2.6: (a) Feynman diagrams that contribute to $B_S \to \mu\mu$ from the SM (top) and a possible SUSY scenario (bottom). (b) Constraints on the CMSSM from flavour physics measurements. The colours indicate which regions of the $m_{1/2} - m_0$ plane are excluded by the corresponding measurement given in the legend. Figure (b) from [54].

Indirect constraints

Flavour physics measurements place tight constraints on SUSY parameter space and on models for BSM physics in general. The precise measurement of branching fractions of rare B-meson decays is interesting as such decays can be rare because they involve loop diagrams mediated by heavy particles. Measurements can, therefore, exclude the possibility of contributions from new heavy particles. For example the $B_S \to \mu\mu$ branching ratio is sensitive to additional interactions that contribute via loop diagrams, such as the one shown on the bottom of Figure 2.6(a), which are sensitive to some SUSY scenarios. Several such measurements and their impact on the CMSSM $m_0 - m_{1/2}$ plane are discussed in [53] and shown in Figure 2.6(b).

Another low-energy measurement that indirectly constrains SUSY parameter space is the anomalous magnetic moment of the muon, or $g-2$. Again, heavier particles can contribute in the loop corrections. The latest results are described in [55] and their implications for SUSY discussed in [56, 57].

Astrophysical constraints

Astrophysical observations also serve to constrain SUSY parameter space. Most notably, the compatibility of SUSY models with the observed DM relic density. After the universe

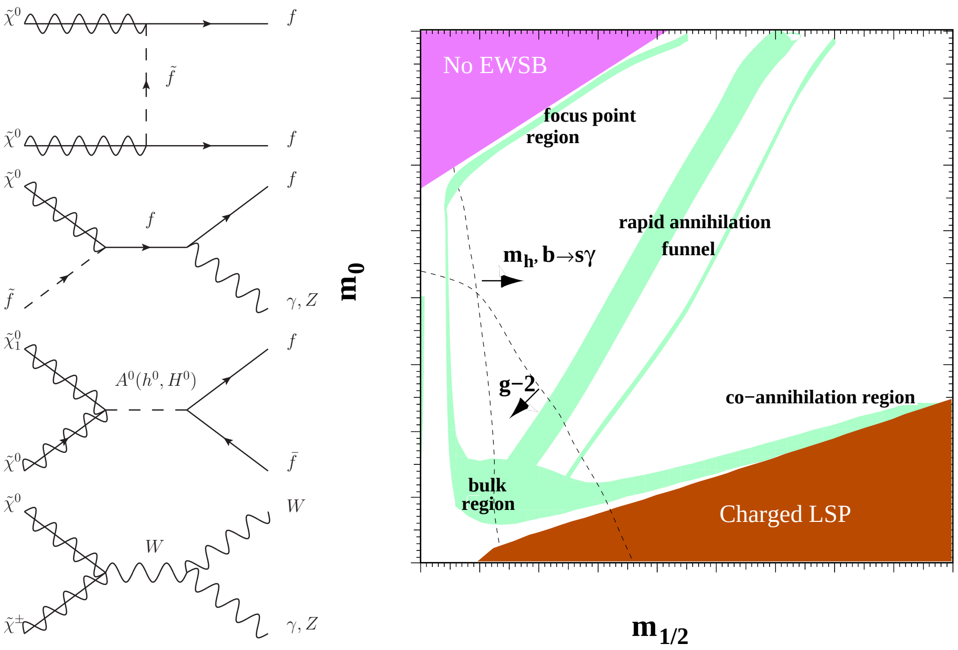

(a) (b)

Figure 2.7: (a) Feynman diagrams of possible mechanisms for reduction of the DM relic density. These diagrams (from top to bottom) correspond to the following regions on the CMSSM $m_{1/2} - m_0$ plane: the bulk region, the co-annihilation region, the funnel region and the focus point. (b) A schematic diagram of the CMSSM $m_{1/2} - m_0$ plane showing the above mentioned regions and the (green shaded) areas on the plane where the predicted DM relic density coincides with the observed value. The magenta shaded area shows the region where electroweak symmetry no longer occurs and the brown shaded region shows the area where the stau is the LSP and is therefore excluded by constraints against charged dark matter. Figure (b) from [58].

has expanded sufficiently, the DM particle density is becomes so low that the probability of one DM particle finding another to annihilate is very small. At this point the amount of DM is said to have *frozen out* and the density of remaining DM is the relic density. The most recent DM relic density measurement from WMAP is $\Omega_{\mathrm{DM}} \simeq 0.227 \pm 0.014$ [59].

R-parity conserving SUSY models predict a LSP which would be consistent with a weakly-interacting massive particle (WIMP), one possible manifestation of DM. But the nature of the predicted LSP vary for different models and are by no means guaranteed to provide an LSP and resulting DM density prediction that is compatible with the observed value. While SUSY models are not required to provide all of the DM in the universe, many SUSY models predict too high a relic density. The DM annihilation cross section increases with increased LSP coupling and decreases with increasing LSP mass. Therefore, SUSY models with LSPs that have too small couplings, or are too heavy, or both, result in too low a rate of annihilation and too high a relic density when the freeze out occurs. Fortunately, there are mechanisms that reduce the relic density as will now be described.

Figure 2.7(b) shows the CMSSM $m_{1/2} - m_0$ plane, the green shaded area corresponds to the region in which the calculated relic density is found to be consistent with a relic density of $0.1 < \Omega_\chi h^2 < 0.3$. The green band has several distinct regions which correspond to different mechanisms for reducing the relic density.

For all values of $\tan\beta$ there is a *bulk* region at low $m_{1/2}$ and m_0 where annihilation via sfermion exchange is dominant. At large $m_{1/2}$, stau and stop *co-annihilation* contributes as the sfermion becomes nearly degenerate with the neutralino. For larger values of $\tan\beta$ with increasing $m_{1/2}$, the pseudo-scalar mass, m_A begins to drop so that $2m_\chi \simeq m_A$ and s-channel annihilation via an A-boson contribute. This gives rise to the *funnel* region. At very large m_0 the value of μ falls and the LSP becomes more Higgsino-like and annihilation proceeds through scattering into WW, ZZ, hh and Zh channels. This is referred to as the *focus point*. Feynman diagrams that contribute to the above four regions, respectively in the order discussed, are shown in Figure 2.7(a) from top to bottom.

Collider constraints

Previous colliders such as LEP and the Tevatron have searched for supersymmetric particles in a number of scenarios. Some of the limits on searches for supersymmetric partners to third generation squarks are described in more detail in Chapter 7.

The Tevatron experiments set limits with analyses focussing on final states with jets and missing transverse momentum, vetoing events with leptons. At the Tevatron

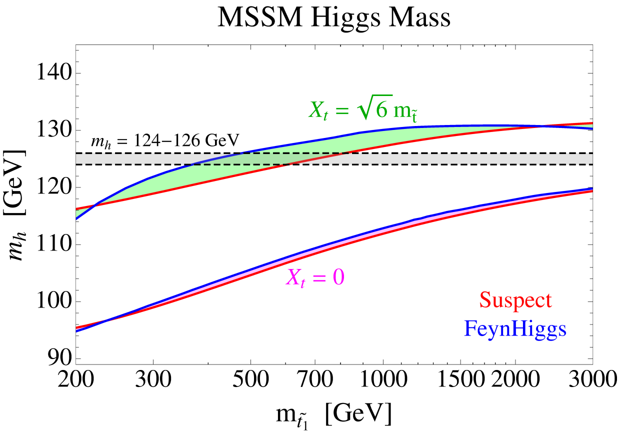

Figure 2.8: The Higgs boson mass in the MSSM as a function of the lightest top squark mass, $m_{\tilde{t}_1}$, with red/blue solid lines computed using Suspect [67]/FeynHiggs [68–71]. The two upper lines are for maximal top squark mixing assuming degenerate stop soft masses, while the two lower lines are for zero top squark mixing. Figure from [65].

(and the LHC) the QCD production cross sections of squarks and gluinos production are dominant. Exclusion limits on squark and gluino masses were set by CDF [60] and D0 [61] of ~ 400 GeV in the CMSSM framework. At LEP the DELPHI experiment performed a search for gauginos and sleptons in a CMSSM model [62] and set lower limits on the masses of the lightest neutralino and chargino of 45.5 GeV and 94 GeV respectively. In addition, limits on slepton masses were set by DELPHI [62] and ALEPH [63] of between 80 and 100 GeV.

More recently, the discovery of a particle compatible with the SM Higgs boson has significant implications for SUSY. In the MSSM after symmetry breaking the two Higgs boson doublet fields, H_u and H_d, result in five physical Higgs bosons; two neutral CP-even scalars, h and H, a neutral CP-odd pseudoscalar A and a pair of charged scalars $H^{\pm}$. Over most of the MSSM parameter space, the lightest Higgs boson, h, is SM-like so that SM Higgs boson search results can also be re-interpreted in terms of h [64]. In the MSSM, given constraints from LEP, m_h is expected to be lighter than ~ 135 GeV [65], so the measured value of ~ 126 GeV appears to be in the required region. However, at tree-level m_h is approximately equal to m_Z. Raising m_h up towards the measured value can be achieved via radiative corrections, but with the consequence that relatively high sparticle masses or maximal mixing stop mixing is required [66] as shown in Figure 2.8. This also has important implications for naturalness and fine-tuning which will be discussed in more detail in §7.2.1.

LHC general SUSY searches

The LHC has been collecting data for over two years and, in the absence of any observed deviation from the SM, has set exclusion limits over a significant range of SUSY parameter space. Some of these limits are derived in the context of searches for stop and sbottom squarks, these are not discussed here as they are subject of Chapters 7, 8 and 9.

Some of the most inclusive SUSY searches looks for events containing jets and missing transverse energy and vetoing those with leptons. In ATLAS these are referred to as *0-lepton* analyses. Such analyses target squark and gluino production in hadronic final states. The analysis model is to veto events with leptons then suppress the QCD multijet background with some kinematic requirements based on the configuration of the jets and missing transverse energy. The sensitivity to squark and gluino production is then enhanced with several other kinematic quantities such as m_{eff} [72], *Razor* variables [73], α_{T} [74] and MT2 [75].

No significant excess is observed in either the $\sqrt{s}$ = 7 TeV or $\sqrt{s}$ = 8 TeV datasets. The $\sqrt{s}$ = 7 TeV results are interpreted in the CMSSM $m_0 - m_{1/2}$ plane as shown in Figure 2.9(a) and (b) for ATLAS and CMS respectively. Figure 2.9(c) and (d) show the ATLAS exclusion $\sqrt{s}$ = 8 TeV exclusion limits for the CMSSM $m_0 - m_{1/2}$ and $m_{\tilde{q}}-,_{\tilde{g}}$ planes respectively.

A large range of the CMSSM plane is now excluded and, more significantly with respect to third generation squark production, first and second generation squarks and gluinos are excluded for masses up to ~ 1 TeV. This imposes strong constraints for natural SUSY models and firmly directs the emphasis on a natural solution to the hierarchy problem towards the third generation squarks. This is discussed in more detail in §7.2.1.

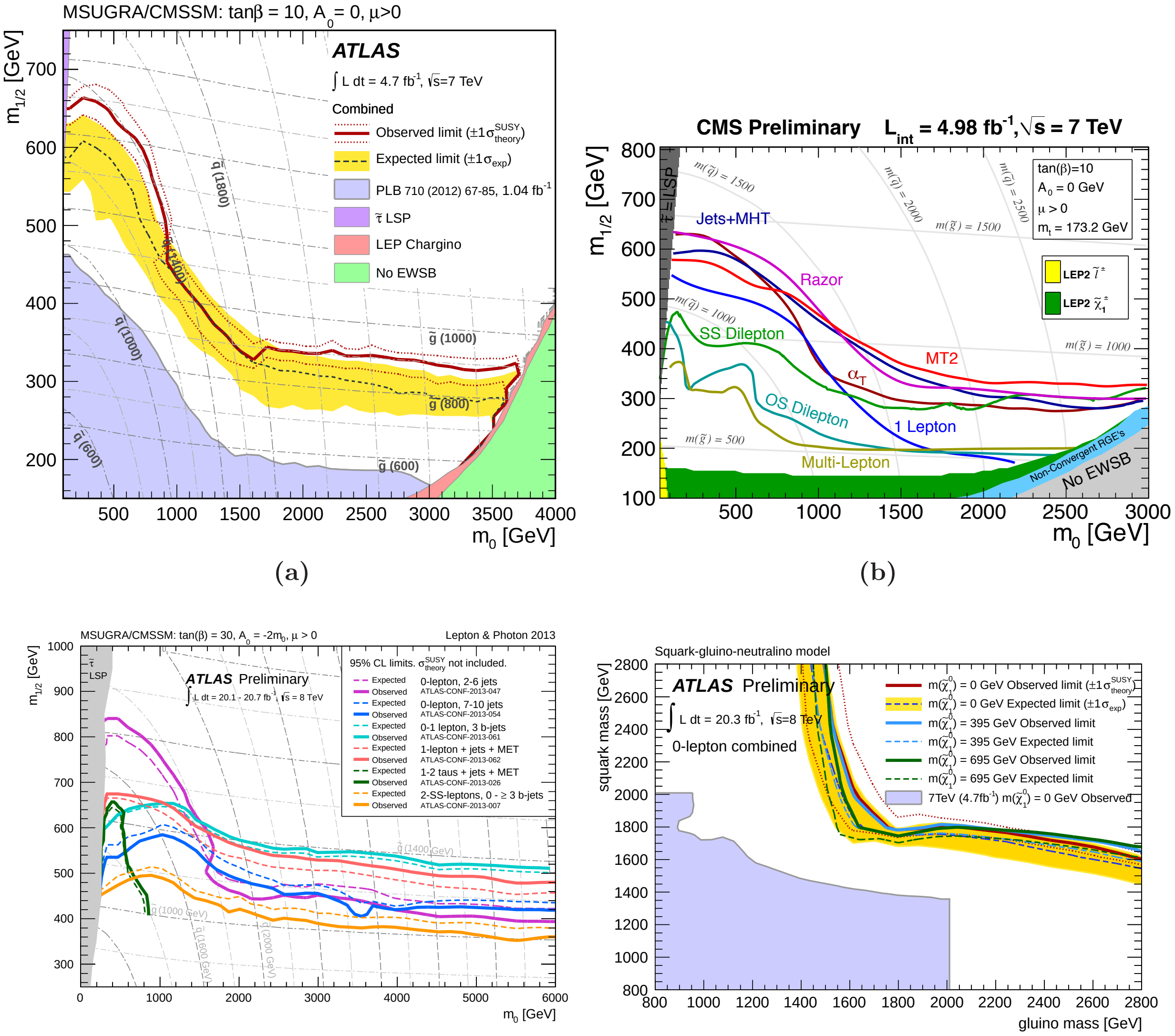

(a) **(b)**

(c) **(d)**

Figure 2.9: Exclusion limits in the CMSSM $m_0 - m_{1/2}$ plane with 2011 $\sqrt{s} = 7$ TeV data from ATLAS (a) and CMS (b). Figures from [72] and [76]. Exclusion limits from ATLAS in the CMSSM $m_0 - m_{1/2}$ (c) and $m_{\tilde{g}} - m_{\tilde{q}}$ (d) planes using 2012 $\sqrt{s} = 8$ TeV. Figures from [77] and [78].

Chapter 3

The LHC and ATLAS detector

3.1 Introduction

To probe physics at the TeV scale high energy particle collisions are required. Accelerating particles to these very high energies necessitates large scale projects such as the LHC. The LHC and its four main detectors, ATLAS, CMS, LHCb and ALICE are based at CERN (the European Organisation for Nuclear Research), located on the Franco-Swiss border outside Geneva, see Figure 3.5(b). This Chapter will give a short introduction to hadron colliders, a brief description of the LHC and the CERN accelerator complex and an overview of the ATLAS detector.

The author's contribution in this Chapter is described in §3.7.2; the implementation of a framework to read information about the ATLAS semiconductor tracker configuration and display it in graphical format on a dedicated webpage.

3.2 Hadron colliders

Since the late 1960s the experimental setup of particle colliders has remained essentially unchanged [79]. Two beams of particles (or antiparticles) accelerated and directed by electric and magnetic fields are brought together for head-on collisions at the *interaction points* inside the detectors. The collision centre-of-mass (CoM) frame approximately coincides with the laboratory frame.

The benefit of colliding beams over the preceding fixed target approach is that all the energy of the beams can be converted into mass for new particles. In fixed target experiments conservation of momentum requires that some of the collision energy must go

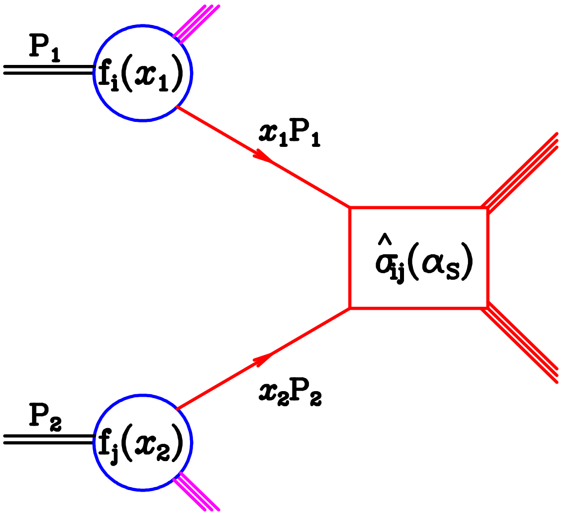

Figure 3.1: Schematic diagram of the parton model of a hard scattering process. Figure from [80].

into giving kinetic energy to the particles produced in the collision. This energy is then not available to contribute to production of heavier particles.

Although the LHC is capable of colliding ions, such as lead, the data used in this thesis are only those collected during pp collisions.

3.2.1 The parton model

At the high energies and correspondingly small distance scales probed at the LHC the incoming protons cannot be thought of as point particles, instead collisions are the result of interactions between quarks and gluons. The formulation for describing these interactions is known as *the parton model* [81] and is described schematically in Figure 3.1.

In the case of an e^+e^- collider the CoM frame is the laboratory frame, however this is not the case for a pp collider. The proton constituents, u-quarks, d-quarks and gluons as well as *sea* quarks and anti-quarks that arise due to quantum fluctuations can all take part in the interaction, albeit the latter with a significantly lower probability. These partons carry some fraction, x, of the proton energy. *Deep Inelastic Scattering* (DIS) experimental measurements have shown that quarks carry only approximately 50% of the proton energy at Q^2 100 GeV^2, the rest is carried by the gluons [82]. *Parton Distribution Functions* (PDFs) which describe the probability of a given parton having a particular x value are shown in Figure 3.2.

As the partons involved in the hard interaction can carry different fractions of the

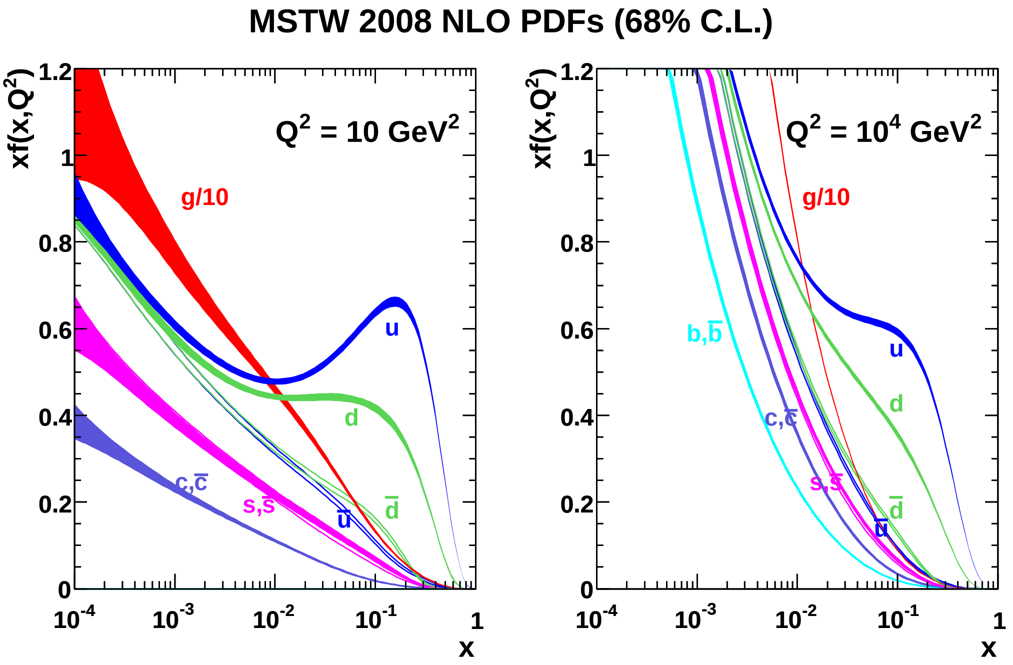

Figure 3.2: MSTW 2008 NLO parton distribution functions at 10 GeV^2 (Left) and 10^4 GeV^2 (Right). Figures from [83].

proton momenta it is possible for there to be an asymmetry in the collision and hence the CoM frame undergoes a Lorentz boost in the z-direction. This has an important effect on event kinematics and reconstruction, introducing an additional unknown into calculations, as is discussed further in Chapter 4.

3.2.2 Luminosity

An important consideration for any collider experiment is the number of events that will be produced for a given process. This number is given by the process production cross section multiplied by the integrated luminosity, L,

$$N_{\text{event}} = \sigma_{\text{event}} L = \sigma_{\text{event}} \int \mathcal{L}\, dt. \tag{3.1}$$

The cross sections for a number of SM processes are shown in Figure 3.3. The instantaneous luminosity, $\mathcal{L}$, of a pp collider is given by

$$\mathcal{L} = \frac{N_b^2 n_b f_{\text{rev}} \gamma_r}{4\pi \epsilon_n \beta^*} F, \tag{3.2}$$

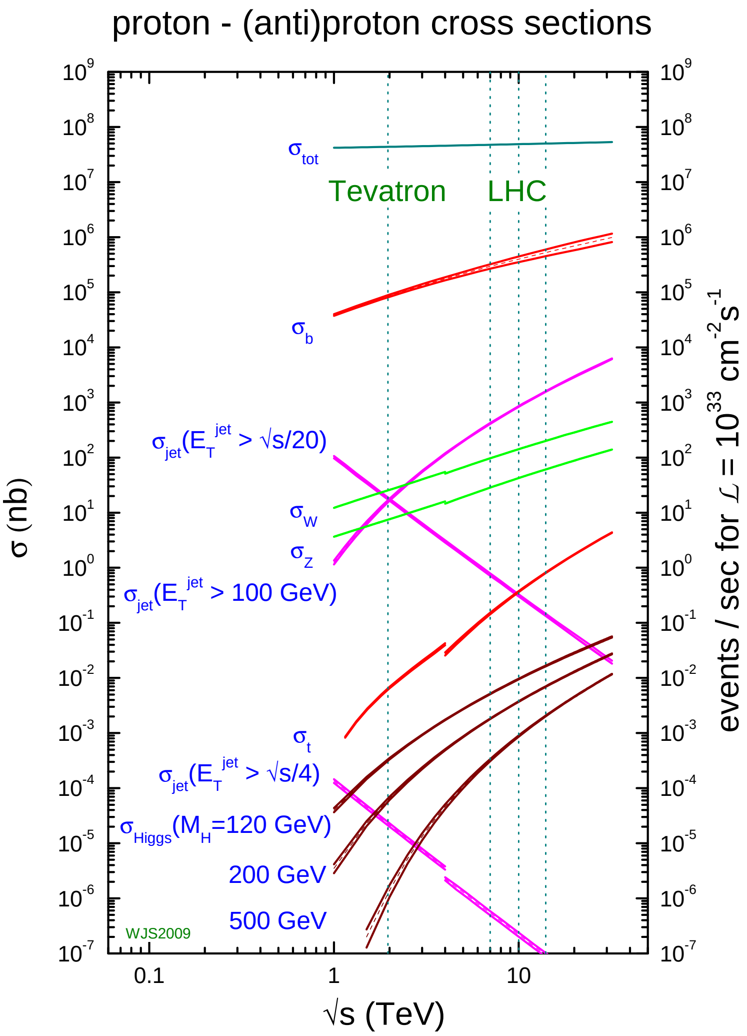

Figure 3.3: MSTW 2008 NLO Standard Model process cross sections as a function of collider energy. Figure from [83].

where N_b is the number of particles per bunch, n_b is the number of bunches per beam, f_{rev} is the revolution frequency, γ_r is the relativistic gamma factor, ϵ_n is the normalised transverse beam emittance, β^* is the beta function at the collision point and F is the geometric luminosity reduction factor due to the crossing angle at the interaction point [84]. The product of ϵ_n and β^* essentially gives the area of the beam spot at the interation point.

To maximise the number of events produced for a given process in a given time, it is clearly important to have the largest possible instantaneous luminosity. From (3.2) it can be seen that there are a number of ways to increase this value. For example, increasing the number of particles in the bunches or the number bunches per beam, or both.

3.2.3 Structure of an event

Collision conditions are sensitive to the beam parameters. With an increase in the number of particles per bunch the probability of a hard collision increases, but also the number of soft interactions per bunch crossing. A single bunch crossing containing several *pp* interactions is referred to as *in-time pileup*. This can lead to a large background of predominately soft hadronic activity in collisions, which has several effects on event reconstruction, as will be described in §3.5.

Increasing the number of bunches per beam can lead to more *out-of-time pileup*. This is where the detector hardware, that has an operation cycle of similar or longer timescale to the time between bunch crossings, can be affected by the bunch crossings before or after the one under consideration. However, In 2011 and 2012 data-taking it has proved to be considerably less significant than in-time pileup. In the rest of this thesis, unless explicitly stated, the term pileup will relate to in-time pileup.

Another background in *pp* collisions comes from interactions between the remnant partons of the colliding protons not involved in the hard processes. This is referred to as the *underlying event* (UE). It is also possible to have collisions where multiple partons from the same proton are involved in hard interactions. This is referred to as *multi-parton interactions* (MPI).

Accelerated charges (colour or electromagnetic) will emit radiation. This gives rise to two other important phenomena at colliders: *initial state radiation* (ISR) and *final state radiation* (FSR). ISR corresponds to emissions associated with the incoming partons and FSR corresponds to emissions associated with the outgoing partons and decay products of particles produced in the interaction.

It is clear that the environment of a *pp* collision can be very messy indeed. Figure 3.4

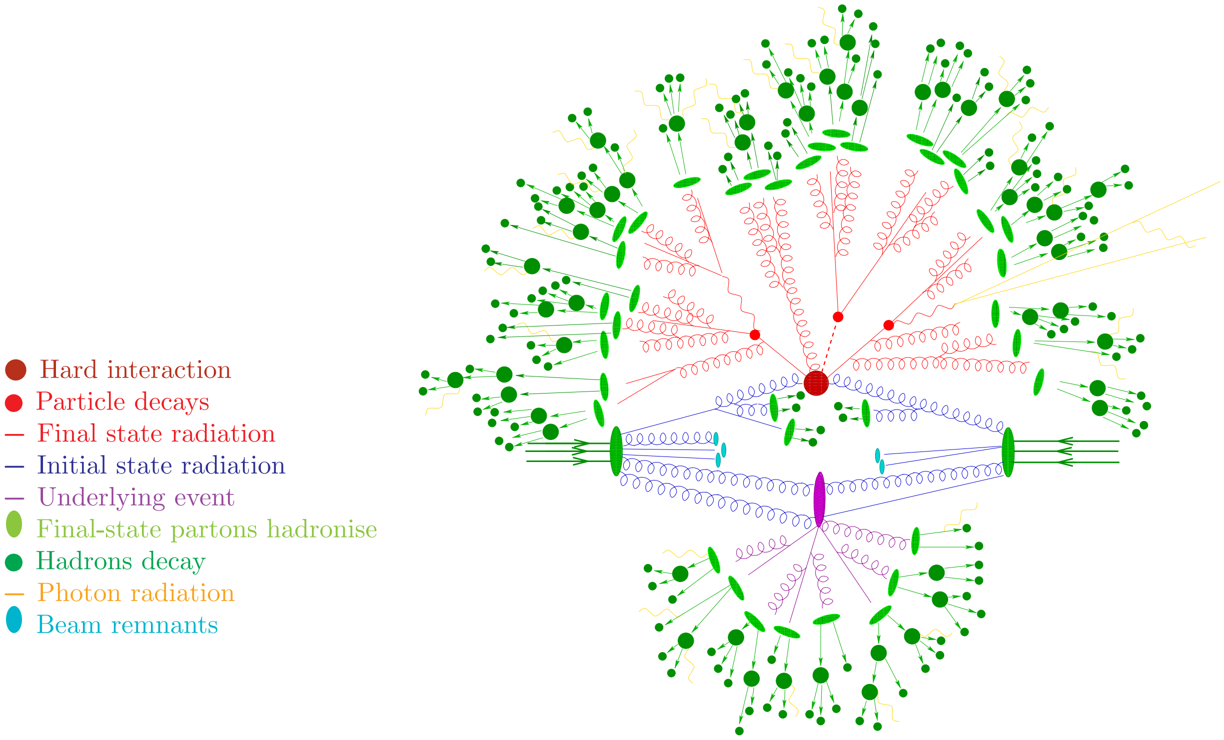

Figure 3.4: Pictorial representation of a $t\bar{t}h$ event as produced by an event generator. Figure from [85].

provides a schematic diagram of the many contributions that constitute an event. A more detailed discussion of the simulation of these contributions is given in §4.5.

3.3 The Large Hadron Collider

The LHC is a particle accelerator, 27 km in circumference, capable of accelerating protons and lead ions to higher energies than any other existing experiment. Particles are accelerated around the LHC ring directed by its 1232 dipole and 506 quadrupole superconducting magnets which operate with a peak magnetic field of 8 T.

The LHC is the final step in a chain of accelerators at CERN, see Figure 3.5(a). A humble gas bottle supplies hydrogen atoms from which the electrons are stripped using an electric field. The remaining protons are accelerated to an energy of 50 MeV by Linac 2, before being accelerated further to 1.4 GeV by the Proton Synchrotron Booster (PSB). The proton beam then enters the Proton Synchrotron (PS) and the beam energy is increased to 25 GeV. Finally, the beam is accelerated up to an energy of 450 GeV by the Super Proton Synchrotron (SPS). From here the beam is split in two and each part is accelerated around

Parameter	Nominal	2011	2012	Units
Proton energy	7000	3500	4000	GeV
Number of particles per bunch	1.15×10^{11}	1.45×10^{11}	1.5×10^{11}	
Number of bunches	2808	1380	1380	
Peak luminosity in IP1 and IP5	1.0×10^{34}	3.8×10^{33}	7.7×10^{33}	$\text{cm}^{-2}\ \text{s}^{-1}$
Time between collisions	49.90	49.90	24.05	ns
Delivered integrated luminosity	-	5.5	23.3	fb^{-1}

Table 3.1: LHC operating parameters, nominal values from LHC Design Report [84], 2011 values from 3rd Evian Workshop on LHC beam operation [88] and 2012 values from 4th Evian Workshop on LHC beam operation.

the LHC in different directions.

The two beams are forced to collide at four interaction points around the LHC. These correspond to the four main experiments ALICE, ATLAS, CMS and LHCb. The nominal design values of selected LHC operating parameters are shown in Table 3.1, along with the actual values reached during 2011 and 2012 data taking.

3.4 The ATLAS detector

ATLAS [89] is one of four main detectors situated along the LHC ring. It is a multipurpose detector designed with the aim of operating a wide physics program, from high precision measurements to searches for new physics.

ATLAS has a mass of ~ 7000 tonnes and its design is largely dominated by the choice of magnet system: a thin central superconducting solenoid and three large outer superconducting toroids. The detector consists of several different sub-detectors arranged in concentric forward-backward symmetric cylindrical layers, giving near-hermetic coverage. The inner detector, located within the solenoid and immersed in a 2 T magnetic field, is dedicated to measuring particle tracks. Starting from the detector closest to the beam pipe it is subdivided into a silicon pixel detector, a silicon strip detector, known as the semiconductor tracker (SCT), and a straw-tube tracking detector, known as the transition radiation tracker (TRT). Outside of the solenoid, the calorimetery is located. The inner electromagnetic calorimeter makes use of a liquid argon scintillator (LAr) and the outer hadronic calorimeter is constructed of iron/scintillator tiles. A toroidal magnet system is located outside of the calorimeters and is surrounded by an array of muon detectors.

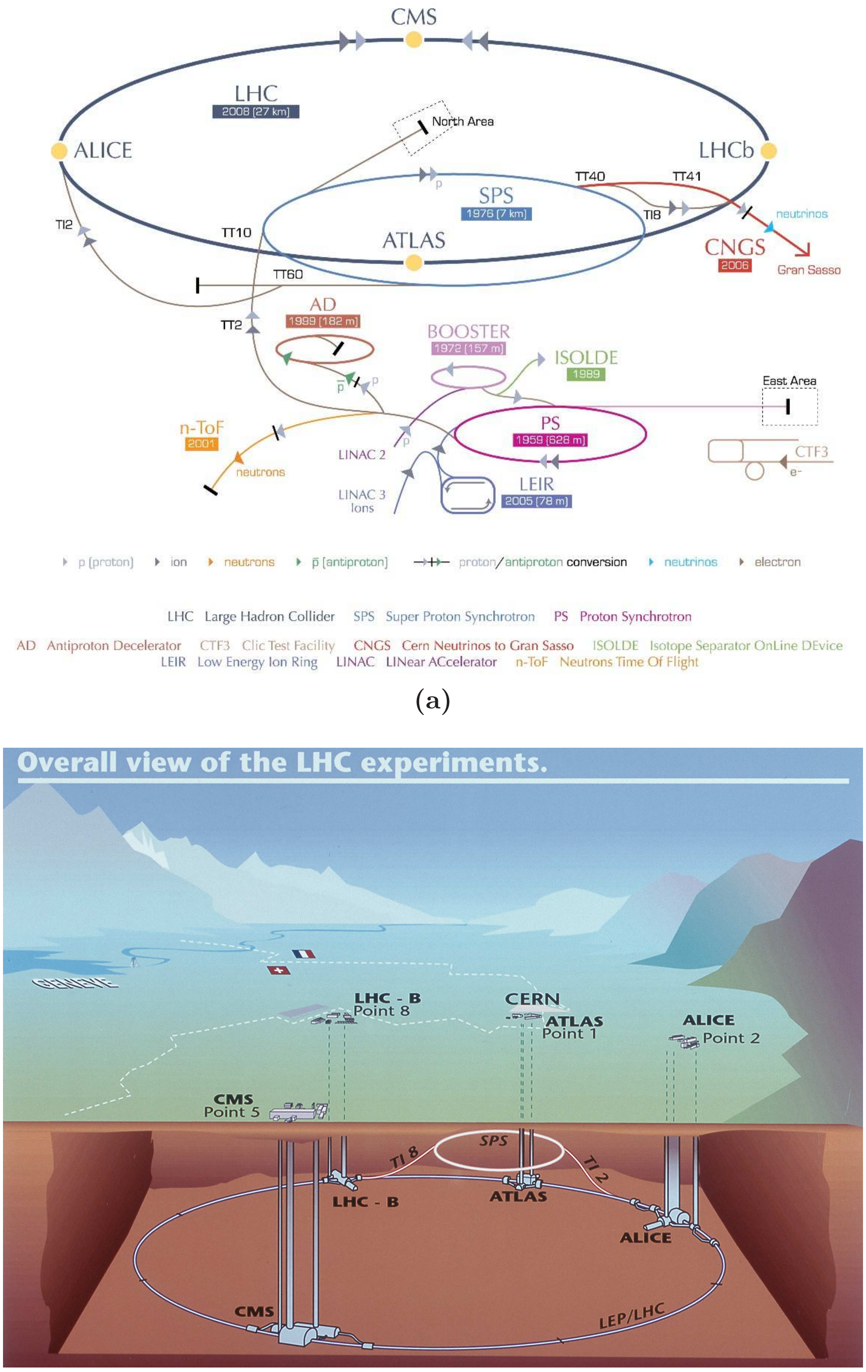

(a)

(b)

Figure 3.5: The CERN accelerator complex (a) and schematic diagram of the position of the LHC and experiments underground (b). Figures from [86] and [87].

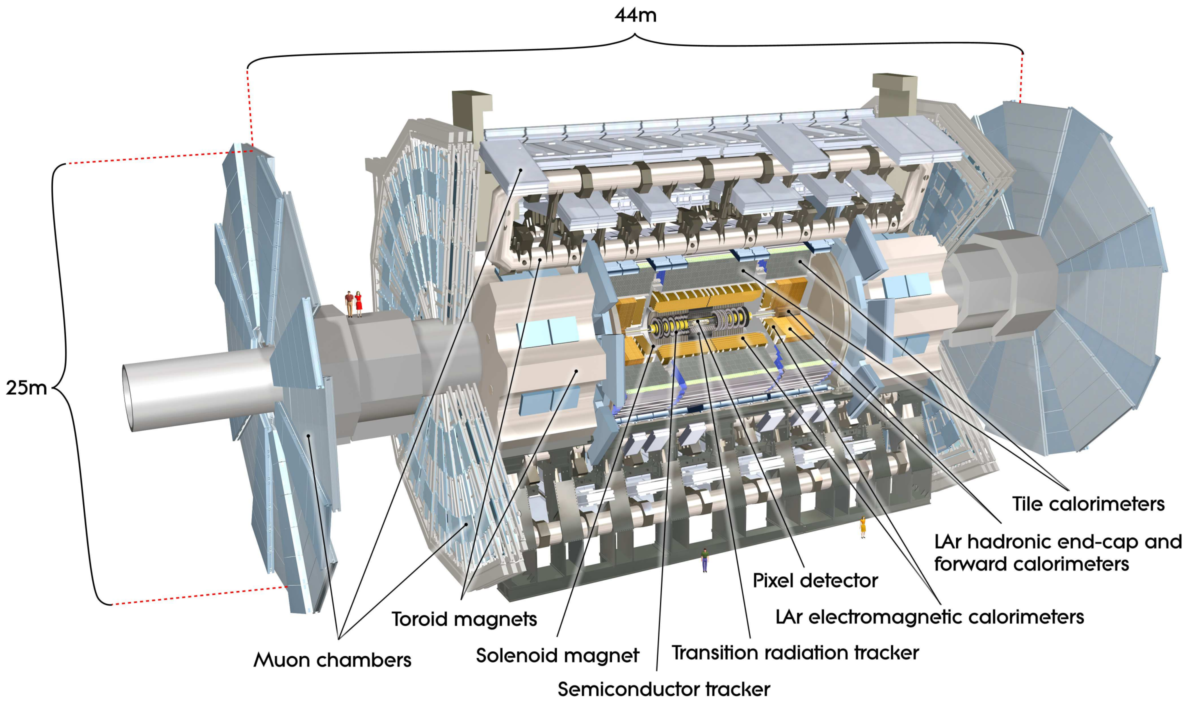

Figure 3.6: Schematic diagram of the ATLAS detector. Figure from [89].

3.5 Co-ordinate system

In ATLAS a combination of both cartesian and spherical co-ordinate systems are used. In both cases the origin is defined to be the nominal interaction point. In the right-handed cartesian co-ordinate system the z-axis is defined to be the direction of the beam, the positive x-axis points from the interaction point to the centre of the LHC ring and the positive y-axis points upwards. The azimuthal angle φ is measured around the beam axis, and the polar angle θ is the angle from the beam axis.

It is often useful to define variables transverse to the direction of the beam. The partons involved in hard interactions have an unknown fraction of the momentum of the incoming protons. Therefore, collisions will not be at rest in the z-direction in laboratory frame. However, in the transverse plane there is negligible net momentum, so conservation of momentum can be applied. Transverse quantities refer to projections in the x-y plane, for example transverse momentum, p_{T}, and transverse energy E_{T}. It is also useful to define the quantity pseudorapidity, $\eta = -\ln[\tan(\theta/2)]$, which is an approximation to rapidity, $y = 1/2\ln[\frac{E+p_z}{E-p_z}]$, for massless objects. This is often used in place of θ as differences in y are invariant under longitudinal Lorentz boosts. Another useful parameter to define is the distance between objects in the η-φ plane defined as follows,

$$\Delta R = \sqrt{\Delta\varphi^2 + \Delta\eta^2}. \tag{3.3}$$

Note that this quantity is also invariant under longitudinal Lorentz boosts.

3.6 Magnet system

Precise measurement of charged particle momenta requires a strong magnetic field. ATLAS utilises a hybrid system of a central superconducting solenoid and three outer superconducting toroids. In totality the magnet system is 22 m in diameter and 26 m in length, providing a magnetic field over a volume of 12,000 m^3, with a stored energy of 1.6 GJ [89].

The solenoid provides the inner detector with a 2 T axial magnetic field. Crucially, this high field strength is obtained whilst keeping the solenoid thin in order to reduce the material in front of the electromagnetic calorimeter. The solenoid is aligned to the beam axis, it is 5.8 m in length and has an outer diameter of 2.56 m.

The toroid system is divided into three regions, the barrel and two endcaps. The barrel region is constructed from eight coils and produces a toroidal magnetic field of ap-

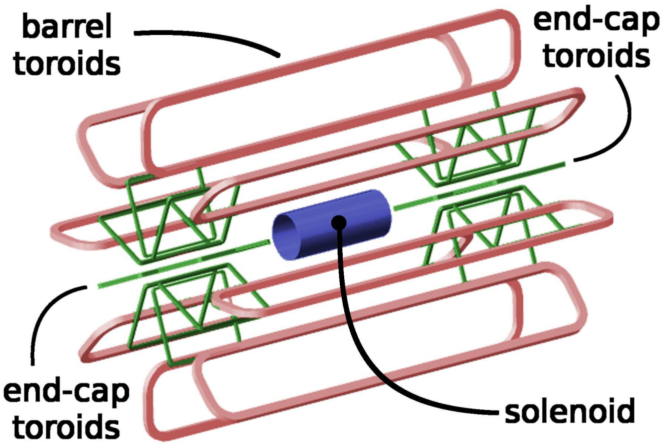

Figure 3.7: Schematic diagram of the ATLAS magnet system. Figure from [90].

proximately 0.5 T for the central muon detectors. The endcap toroids are also constructed from 8 coils each and produce a magnetic field of approximately 1 T for the muon detectors in the end-cap regions.

3.7 Inner detector

The inner detector, shown in full in Figure 3.8(a), and with a cross section of the barrel in Figure 3.8(b), is the closest detector to the beam pipe. It is responsible for measuring the position and momentum of charged particle tracks to very high precision. This is especially important for measurement of primary and secondary vertices and electron identification. With the luminosity produced by the LHC the track density in ATLAS is expected to be extremely high. In order to obtain the precise vertex and momentum resolution fine-granularity detectors are essential. The various components of the inner detector are designed to have the best possible resolution whilst minimising the amount of material placed in front of the calorimeters. The inner detector is composed of three subdetectors which are described in more detail in the following sections. Table 3.2 gives an overview of the intrinsic measurement accuracies of the inner detector subdetectors which are driven by the performance requirements of ATLAS [89].

3.7.1 Pixel detector

The pixel detector is the closest detector the to beam line and has the finest granularity of detecting material and hence the best resolution. The pixel detector is composed of 1744

Detector component		Intrinsic accuracy μm
Pixel		
	barrel	$10(R-\varphi)\ 115(z)$
	endcap	$10(R-\varphi)\ 115(R)$
SCT		
	barrel	$17(R-\varphi)\ 580(z)$
	endcap	$17(R-\varphi)\ 580(R)$
TRT		130

Table 3.2: Inner detector intrinsic measurement accuracies [89].

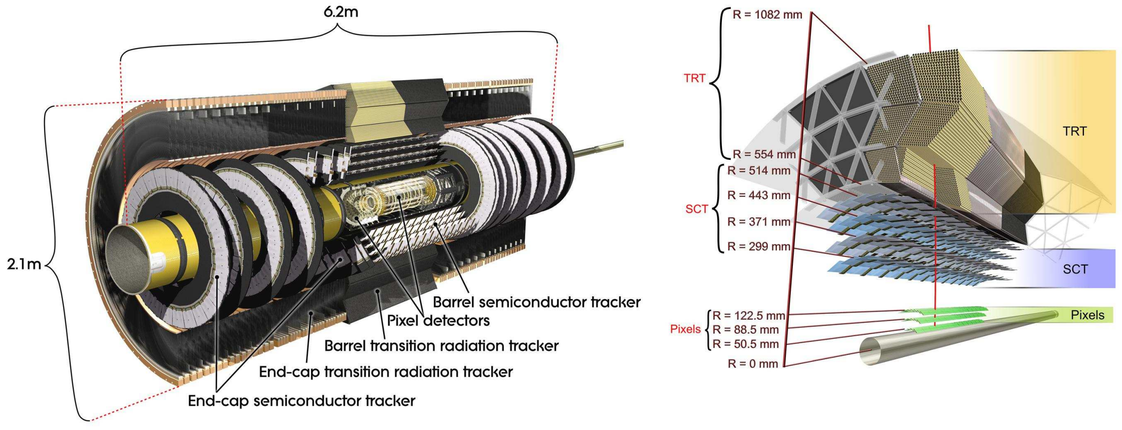

(a) (b)

Figure 3.8: Schematic diagram of the ATLAS inner detector (a) and of a particle traversing the different sub-detectors in the inner detector barrel region. Figures from [89].

modules each with ~50,000 $50 \times 400 \mu\text{m}^2$ pixels. These are arranged into 3 barrel layers and 6 endcap disks (3 on each end). In total there are ~140 million silicon pixels. The pixel detector has an intrinsic accuracy of 10 μm in the $R - \varphi$ direction and 115 μm in the z direction [89], hence its high resolution and vertexing capability.

3.7.2 Semiconductor tracker

The semiconductor tracker (SCT) is situated outside the pixel detector and like the pixel detector is of modular silicon design. The SCT however makes use of silicon strips rather than pixels. The construction of the SCT is heavily influenced by the requirement to reduce the amount of material in front of the calorimetry which is especially important due to the relatively high density of the pixel detector.

The SCT is composed of 4088 modules and is characterised by two regions, the barrel and endcaps. Two types of SCT module exist, one for each region. The barrel modules are arranged into 4 concentric layers (2112 modules) and the endcaps into 18 disks, 9 on each side, (1976 modules) [89] as shown in Figure 3.8(a). The two types of SCT modules are shown in Figure 3.9.

Although differing in shape between barrel and endcap the general structure of all modules is the same. Each module consists of two back-to-back wafers covered with 768 silicon strips (1536 per module). The two wafers are offset by a stereo angle of 40 mrads. This allows for 2D track hit reconstruction and reduces noise. In the barrel the SCT has a hit precision of 17 μm in the $r - \varphi$ coordinate and 580 μm in the z coordinate. The forward region has a precision of 17 μm in the $z - \varphi$ coordinate and 580 μm in the r coordinate. [91].

SCT readout system

The SCT modules communicate with the off-detector electronics through optical connections, as shown in the schematic diagram in Figure 3.10(a). The off-detector hardware is composed of the Data Acquisition system (DAQ) and the Detector Control Systems (DCS). The DAQ is composed of Readout Driver (ROD) crates, each containing up to 16 ROD and Back of Crate (BOC) card pairs which work together and are each responsible for 48 modules.

DCS manages the monitoring of all the detector subsystem's common infrastructure and communication with the CERN services such as cooling, power supplies, ventilation and

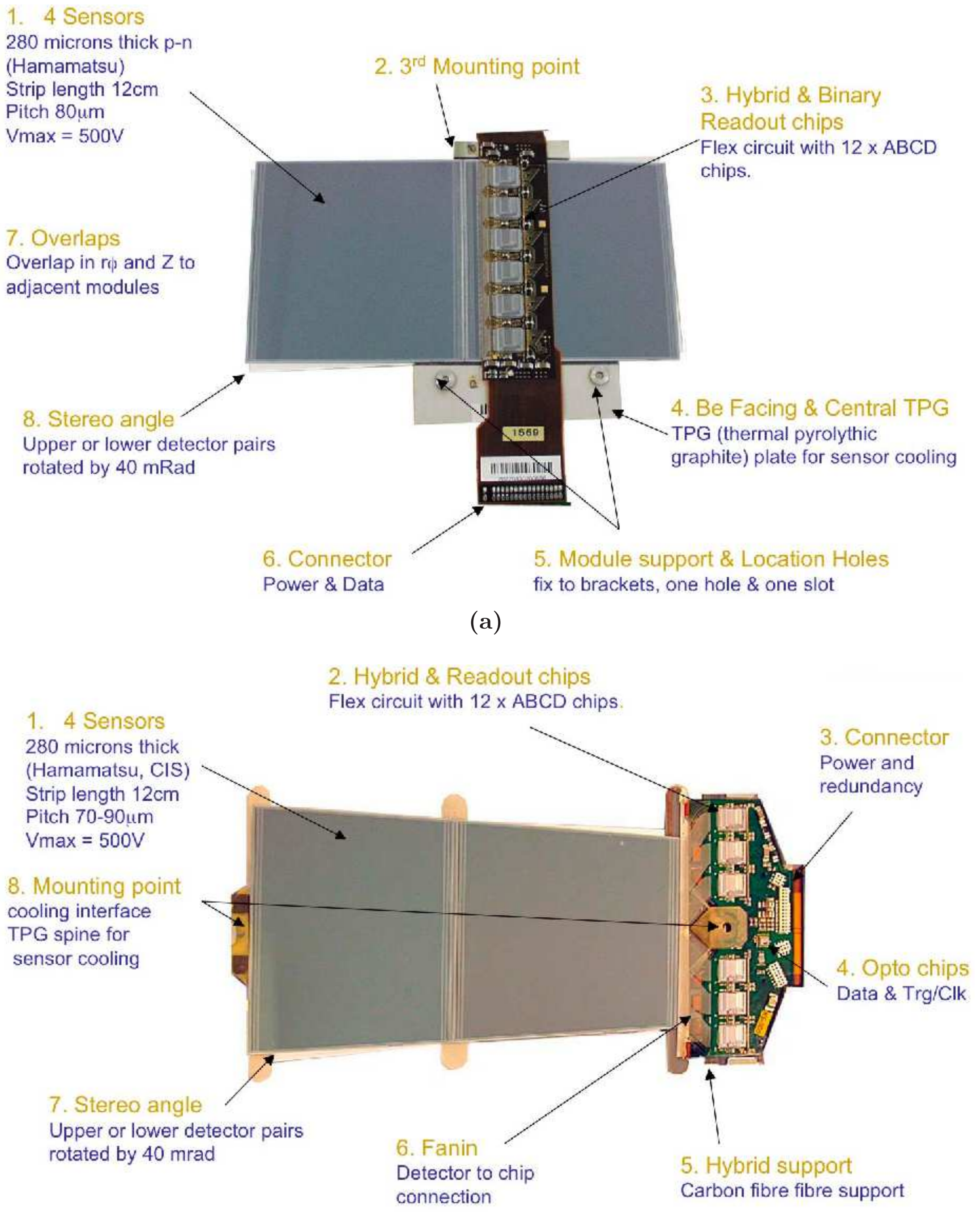

(a)

(b)

Figure 3.9: SCT barrel module (a) and endcap module (b).

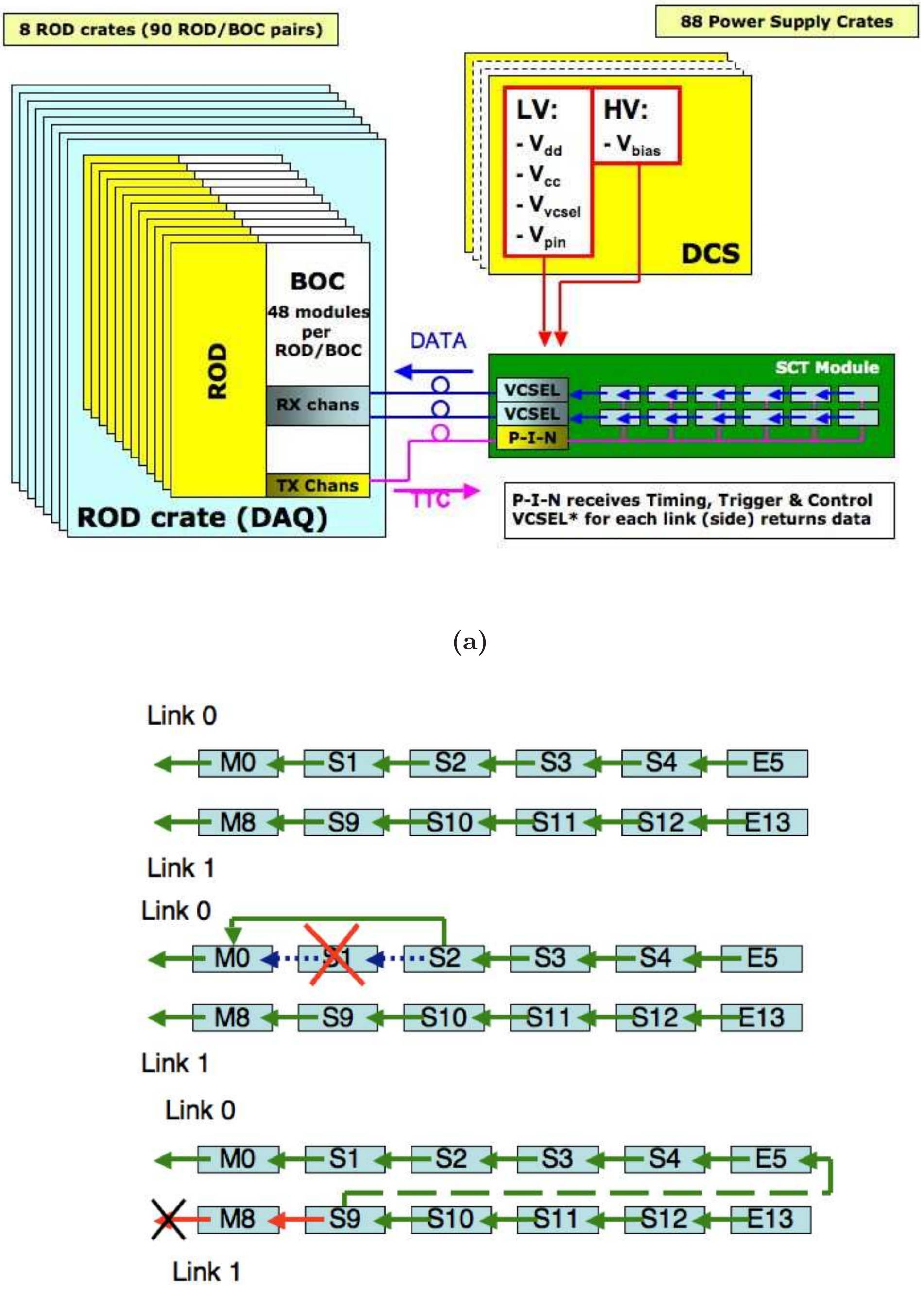

(a)

(b)

Figure 3.10: (a) SCT DAQ system schematic. (b) Standard module readout configuration (Top), module configuration for bypassing a failed chip (Middle) and module configuration for broken optical Rx link or master chip (Bottom). Figures from [92] and [93].

safety. The RODs are responsible for forwarding the data on to ATLAS's Readout Buffer (ROB) which compiles all the data for event building. They also control the generation of the command signals to be sent to the BOC as well as interpreting the returning signals received by the BOC from the modules. The BOC card manages optical signals transmitted to the modules through the transmit (Tx) channels and those returning from the modules through the receive (Rx) channels. Each module has an optical package which contains one PIN[1] diode and two VCSELs[2]. The PIN diode receives the clock and command signals sent from the Tx fibres and the two VCSELs send the optical signals converted from the readout generated by the two master chips along the Rx fibres.

The module readout is initiated by a L1 accepted trigger (the ATLAS trigger system is described in Chapter 5) signal which is sent along the Tx channel. The master chip (as shown in Figure 3.10(b)) then begins readout with a L1 trigger and bunch crossing indicator and then reads the hit information from the chip itself before passing a token to the following chip in the chain. In the normal configuration this chain of chip data readout and token passing goes through all the chips until the end chips have read out out their hit data, see Figure 3.10(b - top). However, there are built in redundancies; if the chips or optical links fail the chain can still follow through to all other chips, examples are shown in Figure 3.10(b - middle and bottom).

SCT configuration monitoring

As described above the SCT is constructed from a huge number of component parts, in total the SCT has over 6.2 million readout channels [91]. Monitoring of these parts is essential to maintain the design performance of the detector. The SCT configuration is a snapshot of the SCT settings as applied in the ATLAS control room at Point 1. Information is stored regarding each SCT strip, chip, module, ROD, BOC etc. in the configuration database.

The parameters that are monitored can be separated into two categories, those relating to SCT modules and those relating to SCT chips. For each the relevant parameters with a description of their relevance are given in Table 3.3. A selection of three of the most interesting monitored parameters plotted as function of time are shown in Figure 3.11. The capability to display these paramters as a function of time is a unique addition to the SCT monitoring package and this is the first instance of such variables being presented in this format. The figure showing the number of modules in "select 1" mode as a function of

---

[1] $p-i-n$ junction, i stand for intrinsic silicon

[2] Vertical Cavity Surface Emitting Laser

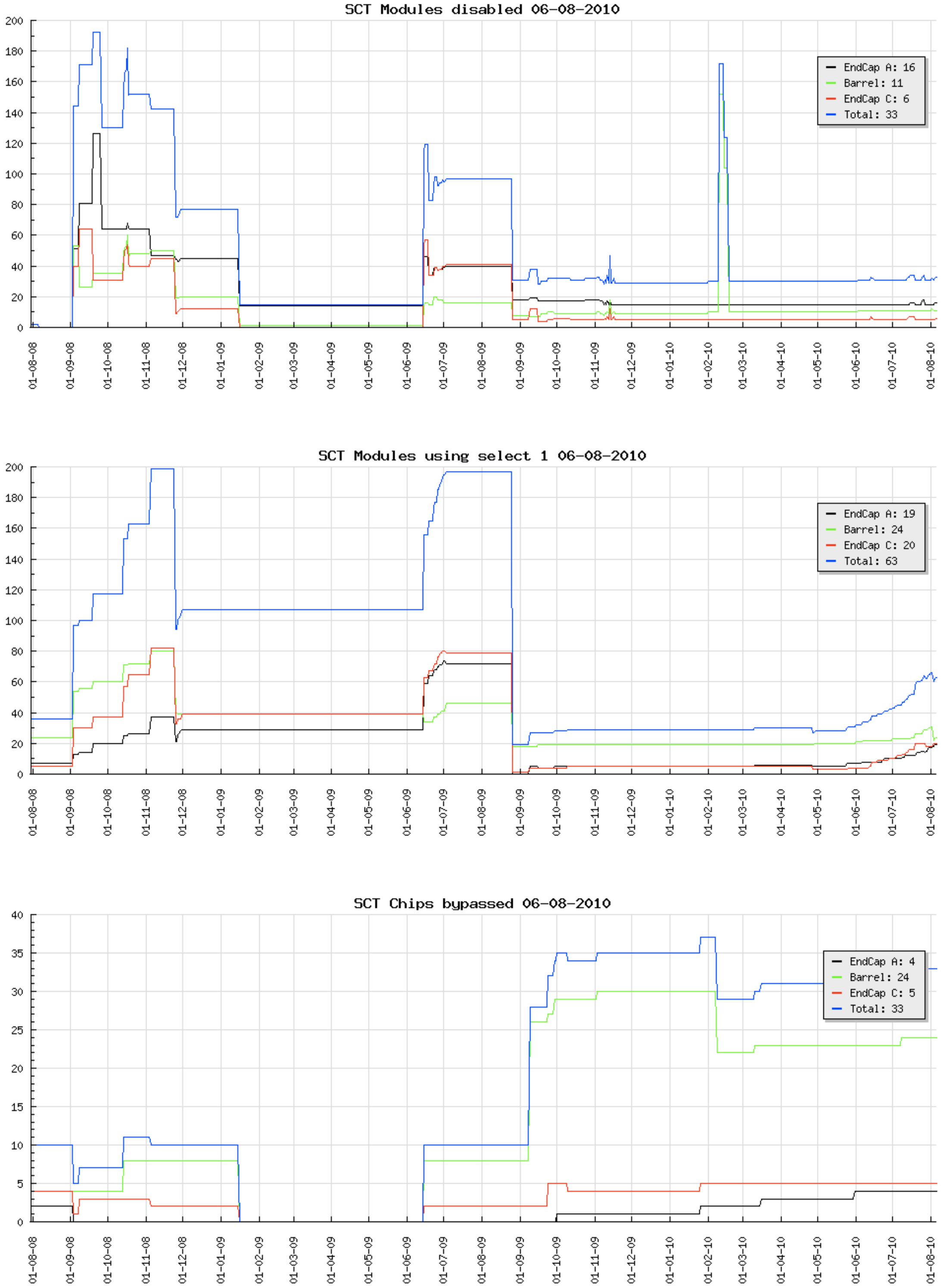

Figure 3.11: A selection of the most interesting monitored parameters displayed as a function of time. Top: Disabled SCT modules. Middle: Modules using Tx redundancy. Bottom: Total number of bypassed chips.

Module parameter	Description
Disabled modules	Removed from data taking due to various faults.
Modules in select=0 mode	Primary (default) Tx channel is being used.
Modules in select=1 mode	Tx redundancy is being used due to issue with primary.
Modules in link=0(1) mode	Only link 0(1) Rx channel is used to read out, problem with the link 1(0) master chip or optical link.
Chip parameter	**Description**
Masked chips	For master chips in the barrel that cannot be bypassed.
Masked strips	Individual strips can be masked by the chip if they are too noisy or do not return data.
Bypassed chips	Bypassed if faulty or connections between chips fail.
Chip trim range settings	Chip-wide trim correction for variations in response from the front-end amplifiers for each strip.
Chip thresholds	Threshold that charge deposit must exceed to record a hit.

Table 3.3: Module and chip parameters in configuration being monitored.

time is of particular interest. An issue regarding the lifetime of the VCSEL packages on the BOCs was observed and confirmed by this monitoring package from the upward trend starting in May 2010. This is due to the module PINs receiving very low currents along the Tx optical fibres. Without replacements this would certainly result in large portions of the SCT being excluded from data taking. Knowing the rate of these failures and the number of replacements required is exactly the kind of information that a monitoring tool is designed to provide and neatly demonstrates the justification for such an infrastructure.

3.7.3 TRT detector

The TRT is the outermost layer of the inner detector. It is very different in design to the two previously described sub-detectors and enables stand-alone electron identification. It is composed of 73 barrel layers and 224 endcap layers (112 in each) and in total contains $\sim 372,000$ straws [94]. The straws are orientated axially in the barrel and radially in the endcaps. Therefore the TRT gives better z resolution but worse $R-\varphi$ resolution compared to the pixel detector and SCT.

The TRT uses gas straw tubes where a charged particle passing through leaves a trail of ionisation electrons but also transition radiation photons produced when charged ultra-relativistic particles pass through boundaries between different media. The energy deposit due to transition radiation photon absorption provides a characteristic from which it is possible to differentiate between electrons and pions. The time taken for the electrons to drift to the centre wire gives the distance from the wire and hence the position and orientation of the track.

3.8 Calorimeters

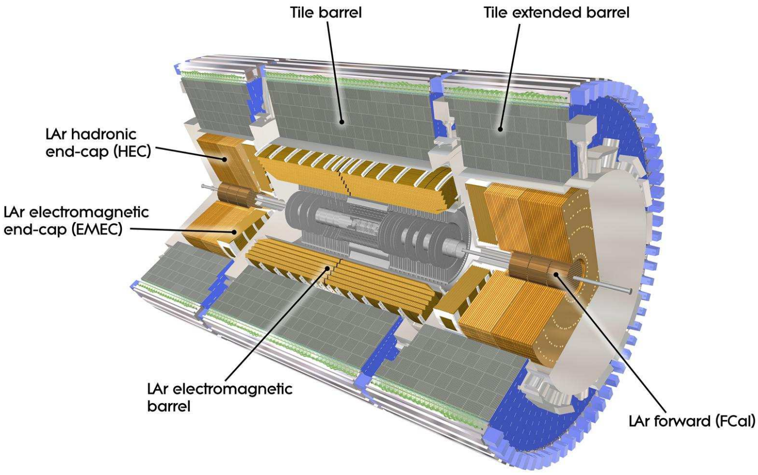

Figure 3.12: Schematic diagram of the ATLAS calorimeter system. Figure from [89].

The ATLAS calorimetry, located outside the inner detector, is composed of electromagnetic (EM) and hadronic sampling calorimeter systems. Two different active media are employed; liquid argon scintillator (LAr) and plastic scintillator tiles. The EM barrel and all endcap calorimeters (EM, hadronic and forward) make use of the liquid argon scintillator whilst the hadronic barrel calorimeter uses a tile scintillator. These two technologies are described in more detail in the following sections, §3.8.1 and §3.8.2.

The geometry of the different subcomponents of the calorimeter system can been seen in Figure 3.12. The EM barrel covers the range $|\eta| < 1.52$, the central barrel and extended barrel tile calorimeters have coverage $|\eta| < 1.7$. The endcap region consists of three subcomponents; the EM endcap which has coverage $1.375 < |\eta| < 3.2$, the LAr hadronic endcap (HEC) with coverage $1.5 < |\eta| < 3.2$ and the LAr forward calorimeter (FCal) which covers the range $3.1 < |\eta| < 4.9$. This gives near-hermetic hadronic calorimetry coverage which is essential for accurate reconstruction of forward jets and for calculation of missing transverse momentum which is important for many of the analyses described later in this thesis. The granularity of each of the subdetectors are given in Table 3.4.

Detector component	Granularity $\Delta\eta \times \Delta\varphi$
EM calorimeter	
barrel	$0.025/8 - 0.075 \times 0.025$
endcap	$0.025/8 - 0.1 \times 0.025 - 0.1$
LAr hadronic endcap	$0.1 - 0.2 \times 0.1 - 0.2$
LAr hadronic endcap	$0.1 - 0.2 \times 0.1 - 0.2$
FCal	$3.0 - 5.4 \times 2.6 - 4.7$
Scintillator tile	
barrel	$0.1 - 0.2 \times 0.1$
endcap	$0.1 - 0.2 \times 0.1$

Table 3.4: Granularity of the calorimeter subdetectors [89].

3.8.1 Liquid Argon calorimeter

Liquid-argon is used as the active detector medium in the EM barrel calorimeter and all three subdetectors in the endcaps. This allows the endcap modules to share the same cryostat.

The barrel and endcap EM calorimeters are constructed with an accordion geometry as shown for a barrel module in Figure 3.13. In the barrel the accordion waves are axial and run in φ, in the end-caps the waves are radial and run axially. This allows readout of the signal from either end of the module and avoids cracks in the direction of the waves. The absorbing material in this case is lead. The hadronic endcap calorimeters are constructed with a flat-plate design and use copper plates as the absorbing material. The forward calorimeter is split into three segments; an inner EM module (FCal1) where copper is used as the absorbing material and two outer hadronic modules (FCal2 and FCal3) where tungsten is the absorbing material.

Figures 3.14(a) and (b) show the amount of material in front of and including the EM calorimeters. Significant material before the accordion modules can lead to energy losses to incident particles, therefore pre-samplers are placed before these modules in order to correct for such losses. The EM barrel provides at least 22 radiation lengths of material which ensures that all the EM shower will be contained within the calorimetry.

3.8.2 Tile calorimeter

The tile calorimeter is segmented into three sections, the central barrel ($|\eta| < 1.0$) and two extended barrels ($0.8 < |\eta| < 1.7$). The active medium is scintillating plates and the

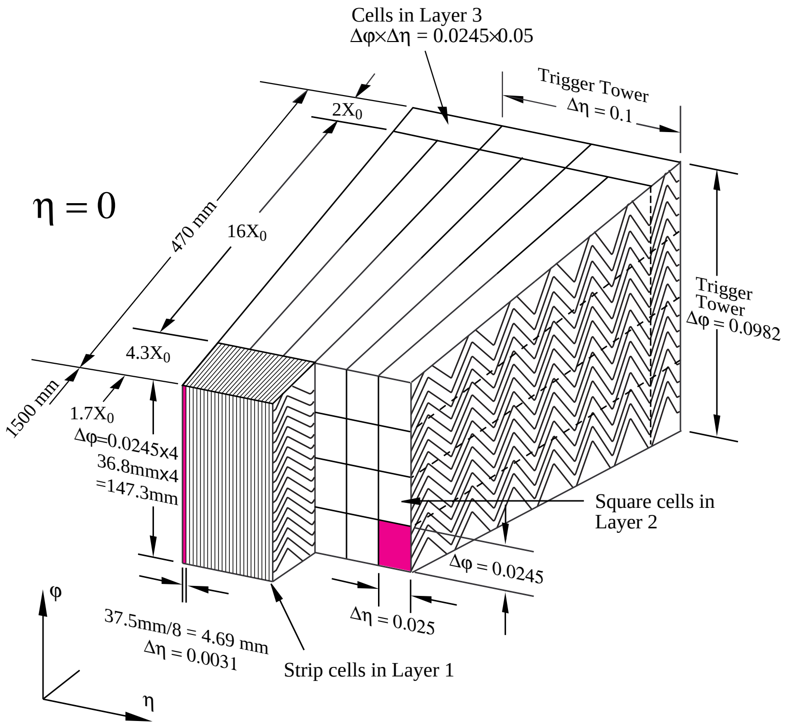

Figure 3.13: Schematic diagram of the EM barrel calorimeter module construction. Figure from [89].

absorber is steel. The main purpose of the tile calorimeter is the energy reconstruction of jets and, combined with the endcap and forward calorimeters, measurement of the missing transverse momentum.

The design of a tile calorimeter module is shown in Figure 3.15(a). The steel absorbing material and scintillator active material are arranged in a periodic structure in planes perpendicular to the beam allowing for excellent coverage in φ.

Figure 3.15(b) shows the amount of material that each part of the ATLAS calorimetry contributes. Across the whole range of η the calorimetry provides at least 10 interaction lengths of material which ensures that the full hadronic shower will be contained within the calorimeter even up to very high energies.

3.8.3 Energy resolution

For several key analyses at ATLAS excellent energy resolution is required. For example in $H \to \gamma\gamma$ searches where good mass resolution, and hence EM energy resolutions, is key to identifying a narrow resonance above the large irreducible $\gamma\gamma$ background. Also jet energy

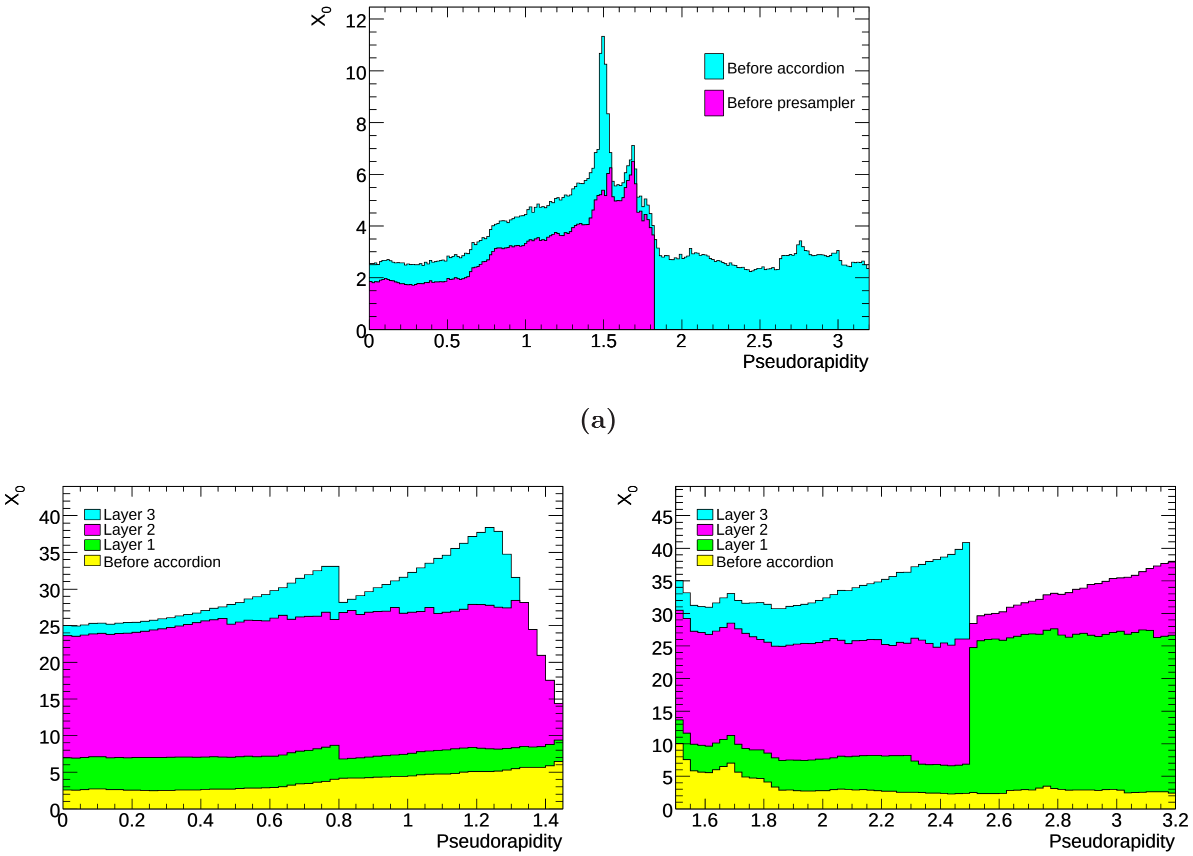

(a)

(b)

Figure 3.14: Cumulative amount of material in front of (a) and including (b) the EM calorimeters as a function of $|\eta|$ in units of radiation length X_0. Figures from [89].

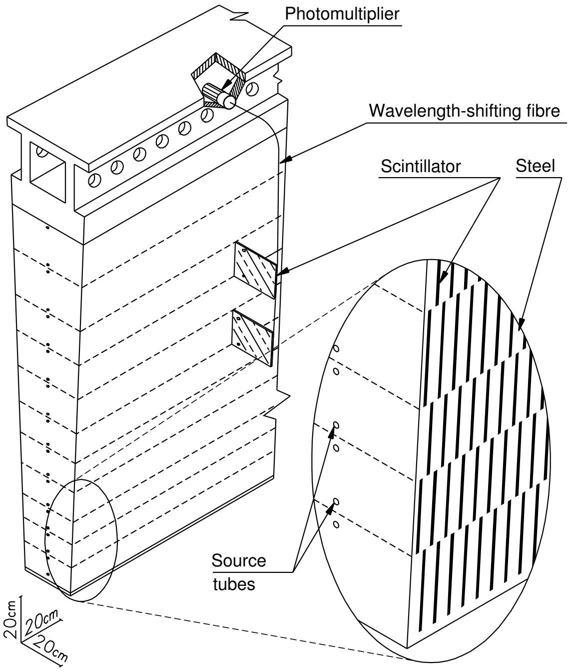

(a)

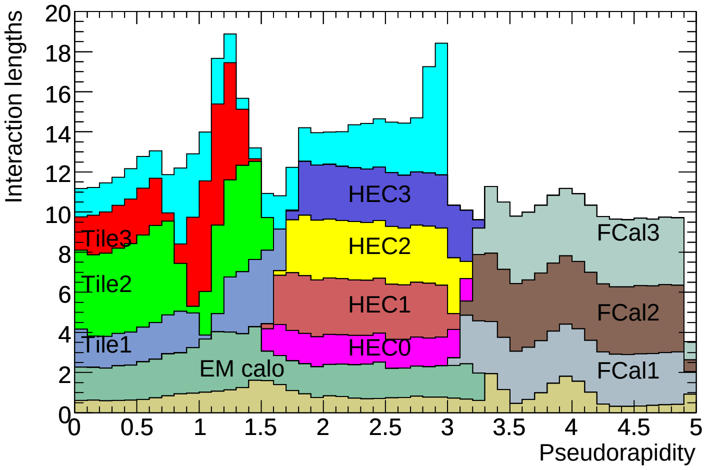

(b)

Figure 3.15: (a) Schematic diagram of a tile calorimeter module. (b) Cumulative amount of material in front of and including the calorimeter systems as a function of $|\eta|$ in units of interaction length I_0. Figures from [89].

Detector component	Required resolution
EM calorimetry	$\sigma/E = 10\%/\sqrt{E} \oplus 0.7\%$
Hadronic calorimetry	
barrel	$\sigma/E = 50\%/\sqrt{E} \oplus 3\%$
endcap	$\sigma/E = 100\%/\sqrt{E} \oplus 10\%$

Table 3.5: Calorimeter energy resolution performance goals.

resolution is vital for many analyses, for example the measurement of the top quark mass and SUSY searches in hadronic final states.

The energy resolution can be described with the following expression [95],

$$\frac{\sigma}{E} = \frac{a}{\sqrt{E}} \oplus \frac{b}{E} \oplus c \tag{3.4}$$

where a is the *s*tochastic term due to the intrinsic fluctuation in the shower evolution, b is the *noise term* due to electronic noise in the readout chain and c is the *constant term* due to instrumental effects. The LHC performance goals for energy resolution are summarised in Table 3.5.

3.9 Muon spectrometer

The muon spectrometer is designed to measure the momentum of charged particles exiting the calorimetry system in the region $|\eta| < 2.7$ and trigger on those charged particles for $|\eta| < 2.4$. The detector is required to give standalone high precision transverse momentum resolution (10% for 1 TeV tracks) [89]. The tracking chambers are oriented in 3 concentric cylindrical layers in the barrel and in large wheels perpendicular to the beam axis in the endcaps, see Figure 3.16.

The precision tracking chambers in the barrel use Monitored Drift Tubes (MDTs) over most of the η range. In the forward region of the inner most layer $2 < |\eta| < 2.7$ Cathode Strip Chambers (CSCs) are used. In the trigger system Resistive Plate Chambers (RPCs) are used in the barrel whilst Thin Gap Chambers (TGCs) are used in the endcaps.

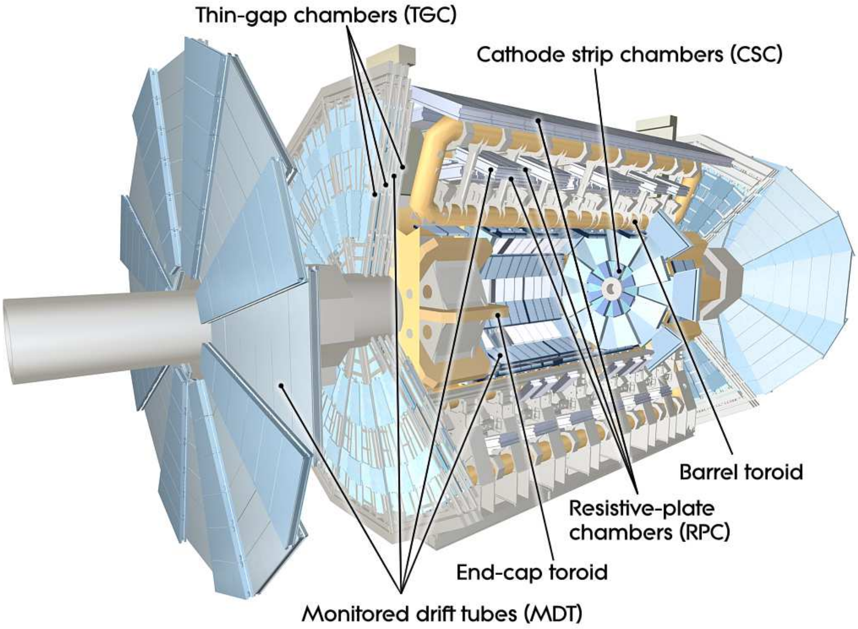

Figure 3.16: Schematic diagram of the ATLAS muon spectrometer. Figure from [89].

Chapter 4

Analysis tools

4.1 Introduction

In this Chapter a description of several tools that are common to the analyses in the following Chapters is given. In §4.2 information about the 2011 and 2012 datasets is provided. §4.3 will provide an overview of how detector level quantities are reconstructed to form physics objects used in analyses. A description of the treatment of systematic uncertainties is given in §4.4. Finally, a detailed overview of Monte Carlo (MC) generators is given in §4.5.

The author's contribution in this Chapter is the generation of $t\bar{t} + V(V = W, Z)$ MC samples. These samples are used throughout several ATLAS analyses both as a signal and a background. This work is highlighted in §4.5.3.

4.2 Datasets

The data used in the analyses in the following Chapters was collected by ATLAS during 2011 and 2012. The 2011 dataset was collected between February and October with the LHC running at a centre-of-mass energy of 7 TeV. The total recorded integrated luminosity was 5.25 fb^{-1} as shown in Figure 4.1(a) with an average of approximately 9 pp interactions per bunch crossing, $\langle\mu\rangle$, as shown in Figure 4.1(c). The maximum peak instantaneous luminosityf 3.65×10^{33} $\text{cm}^{-2}\text{s}^{-1}$. The 2012 dataset was collected between March and December at a centre-of-mass energy of 8 TeV. The recorded integrated luminosity was 21.7 fb^{-1} as shown in Figure 4.1(b) with an average of over 20 pp interactions per bunch crossing, as shown in Figure 4.1(c). The maximum peak instantaneous luminosity was 7.73×10^{33} cm^{-2}s^{-1}.

As discussed in Chapter 3 these conditions impose strong requirements on the detector design. They also provide significant challenges for efficient reconstruction of physics objects, as will be discussed in the next section, and on trigger requirements, as will be described in Chapter 5.

4.3 Definition of physics objects

Performing meaningful physics analysis requires efficient identification of physics objects and, thus, necessitates a well defined prescription for classifying detector level objects. In the following section the definitions of physics objects relevant to the rest of this thesis are described.

Object definitions can evolve over time and vary between different analysis groups. Therefore, for each object a general description of common criteria is given first before highlighting any differences for four distinct stages of ATLAS running that correspond to the four analyses described in later Chapters. The two different analysis groups are *SUSY* and *Top* and are subdivided into the following four definitions:

- *Top-2011* - $t\bar{t} + Z$ (Chapter 6),
- *SUSY-early 2011* - direct sbottom (Chapter 8),
- *SUSY-late 2011* - direct sbottom 2011 data (§9.3),
- *SUSY-2012* - direct sbottom 2012 data (§9.4)

4.3.1 Jets

Due to the short range of the strong force and colour confinement, it is not possible to observe quarks and gluons directly. Energetic partons produced in collisions hadronise creating collimated bunches of hadrons known as jets that to some extent reflect the kinematics of the underlying partons, as shown schematically in Figure 4.2.

There is no single optimal way of defining jets [98] and several different *jet-finding algorithms* exist. Formation of a jet from a single hard isolated particle should be trivial for any algorithm. However, different algorithms can have markedly different behaviour in more complicated scenarios. For example, when two hard particles are close by, when a

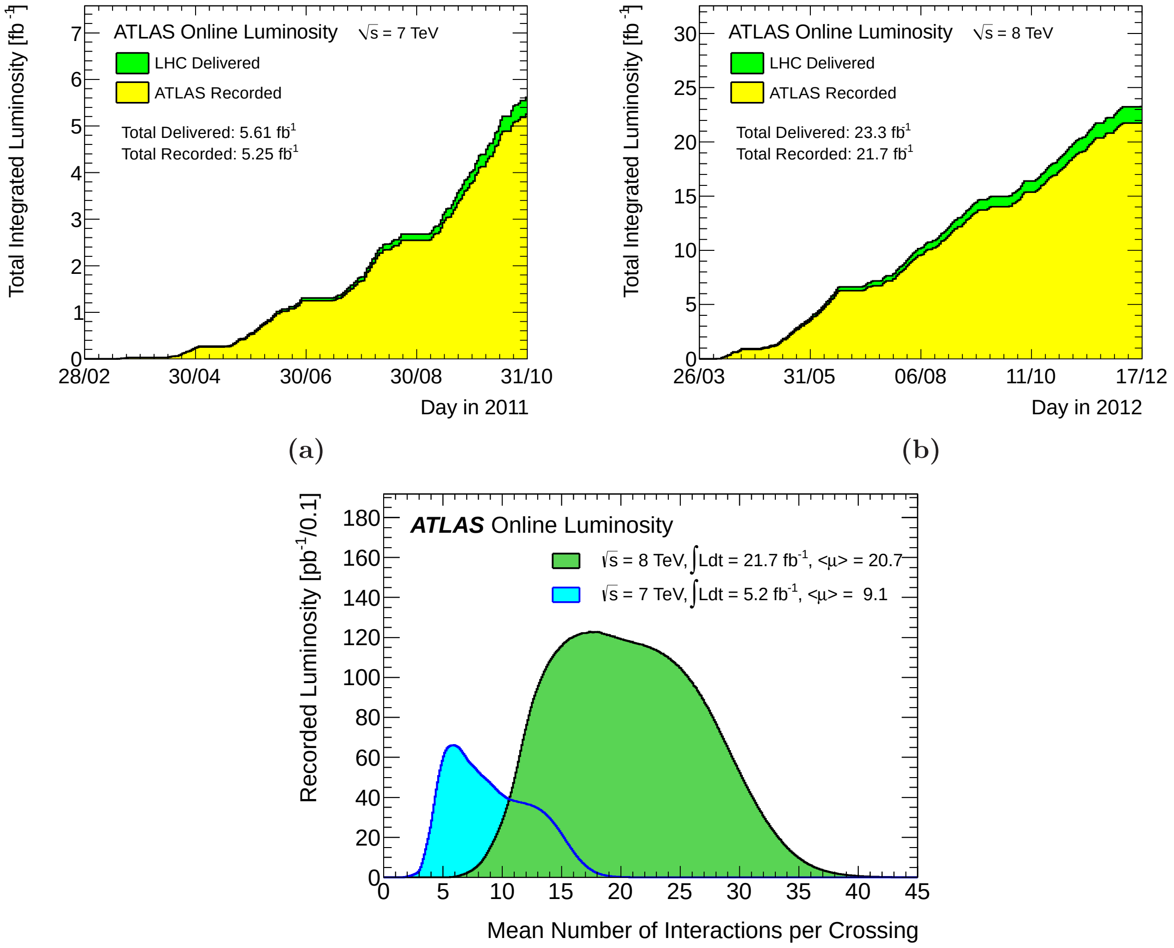

(a) **(b)**

Figure 4.1: Cumulative luminosity per day delivered to (green), and recorded by (yellow) ATLAS during stable beams in (a) 2011 data taking and (b) 2012 data taking. (c) Luminosity-weighted distribution of the mean number of interactions per crossing for the 2011 (blue) and 2012 (green) data. Figures from [96].

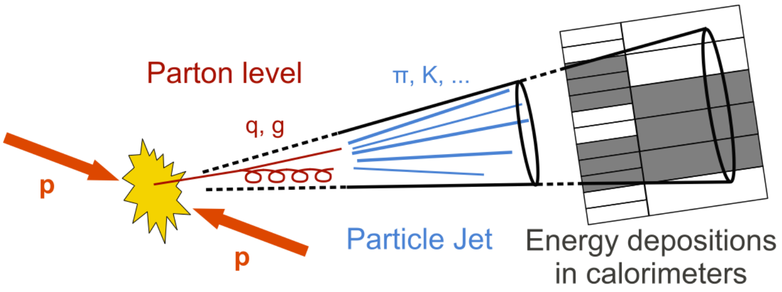

Figure 4.2: Schematic diagram of jet production and measurement. Figure from [97].

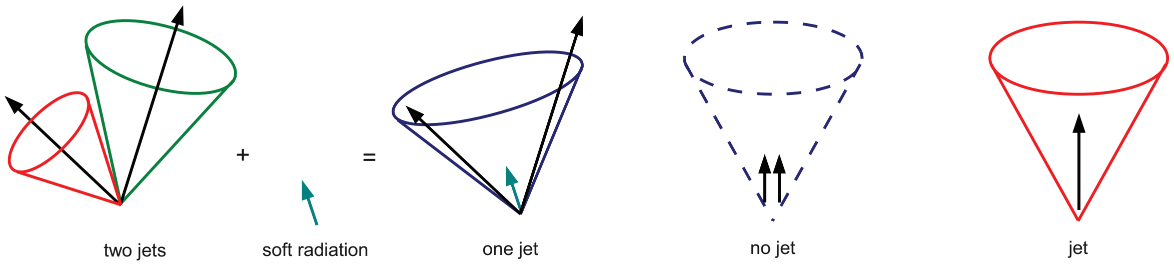

(a) (b)

Figure 4.3: Illustration of infra-red (a) and collinear (b) safety problems that an can affect an unsafe jet algorithm. Figures from [99].

parton radiates a soft gluon, or when jets are surrounded by significant noise, e.g. from pileup.

The are two important concepts that any jet-finding algorithm must be wary of. Those are *infra-red and collinear safety*, as illustrated for an unsafe algorithm in Figure 4.3(a) and (b) respectively. The result of a particular algorithm should be insensitive to hard partons undergoing collinear splittings as part of the fragmentation process and the emission of soft particles. Collinear splittings and soft emissions are hard to predict as they involve non-perturbative effects. Constructing jets in a way that is insensitive to these effects and theoretically well behaved is crucial to obtain finite perturbative results at all orders, and allow meaningful comparisons of data with theoretical predictions.

In ATLAS jets are reconstructed from energy deposits in the calorimeter cells that are supplied as input to clustering algorithms. Two types of calorimeter quantities are constructed, *calorimeter towers* and *topological cell clusters* (topoclusters). The latter are used in all the analyses in this thesis and will be described here in more detail. Figure 4.4 shows the various stages of jet reconstruction. In all that follows a successive recombination algorithm, anti-k_t [100], is used for jet-finding, with a distance parameter of 0.4.

Topoclusters are the reconstruction of three-dimensional energy deposits in the calorimeter, exploiting the fine longitudinal and transverse calorimeter segmentation. The clusters are built using a nearest-neighbour algorithm that groups together calorimeter cells with energy significance, $|E_{\text{cell}}|/\sigma$, above specific thresholds. E_{cell} is calibrated at EM scale using information derived from test beam and simulations, and σ is the electronic and expected pileup noise summed in quadrature.

The ATLAS calorimetry is non-compensating, meaning that some part of the energy

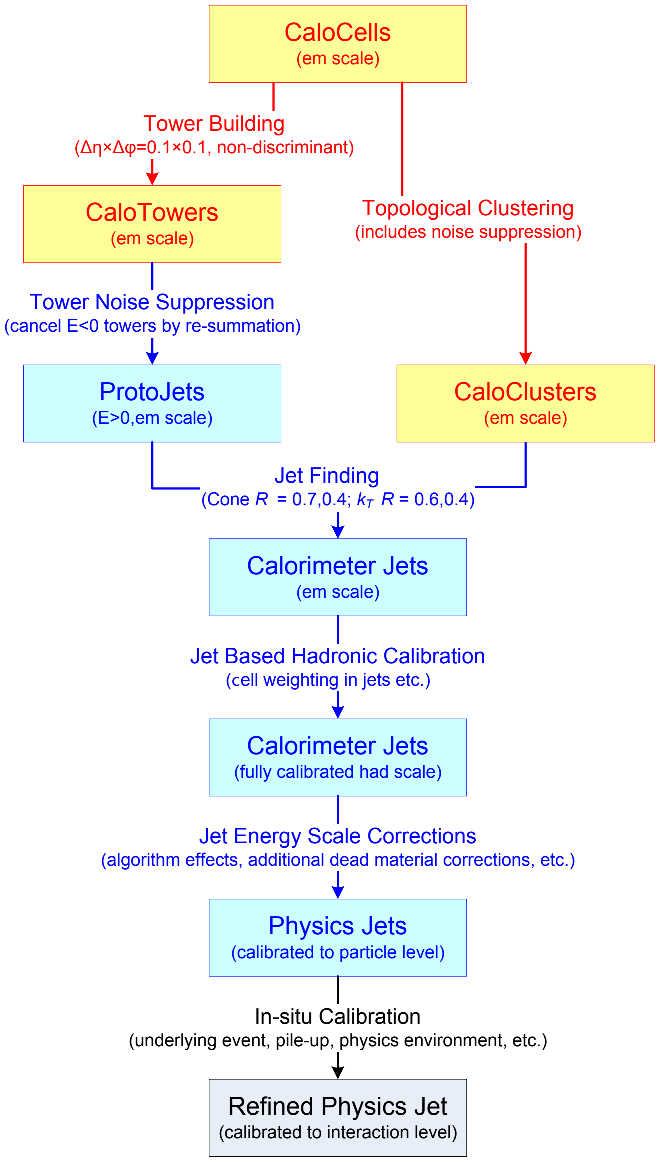

Figure 4.4: Jet reconstruction flow for calorimeter jets from towers or clusters. Figure from [89].

deposited in hadronic interactions is invisible to the detector. As a result a calibration must be applied to map the energy deposited in the calorimeter back to the true energy of the incoming hadrons. The first step is for calorimeter cell energy deposits to be calibrated to EM scale before further calibration is applied to get to the final *jet energy scale* (JES). Two JES calibration schemes are employed in ATLAS. First, the `EM+JES` scheme, where jets are reconstructed at the EM scale, then, after jet-finding, the jet energy at the hadronic scale is restored by applying correction factors obtained from simulation and validated in data [101]. Second, the *local cluster weighting* (`LCW`) scheme [102] decides whether a calorimeter topological cluster is of hadronic or EM origin and correspondingly applies either the hadronic or EM energy correction before jet-finding. All three analyses performed on 2011 data, *Top-2011*, *SUSY-early 2011* and *SUSY-late 2011*, use the `EM+JES` calibration while the stop pair analysis performed on 2012 data, *SUSY-2012*, uses the `LCW` calibration.

In order to suppress jets arising from pile-up an additional selection can be applied that requires that a given fraction of tracks within a jet originate from the primary vertex. The value of this threshold is referred to as the *jet vertex fraction* (JVF). This requirement is the default in the *Top-2011* selection, however it is not applied in any of the *SUSY* analyses.

4.3.2 b-tagging

The identification of jets resulting from the fragmentation and hadronisation of b-quarks is performed through use of *b-tagging* algorithms. These algorithms use tracking information to attempt to identify the secondary vertex due to the displacement between the primary interaction and the B-hadron decay and exploit its characteristics.

Figure 4.5 provides a schematic diagram of a b-quark decay. Displaced vertices can be identified by measuring the impact parameters of the tracks from the B-hadron decay products. The transverse impact parameter, d_0, is the distance of closest approach of the track to the primary vertex point, in the $r - \varphi$ plane. The longitudinal impact parameter, z_0, is the z coordinate of the track at the point of closest approach. Tracks from B-hadron decay products can be distinguished from tracks from the primary vertex as they have larger impact parameters [104]. It is also possible to reconstruct the secondary vertex. In this case the decay length can be used, it is defined as the distance between the secondary vertex in the jet and the primary vertex of the collision. Often the decay length significance is used, this is defined as the ratio between the measurement of the decay length and its uncertainty.

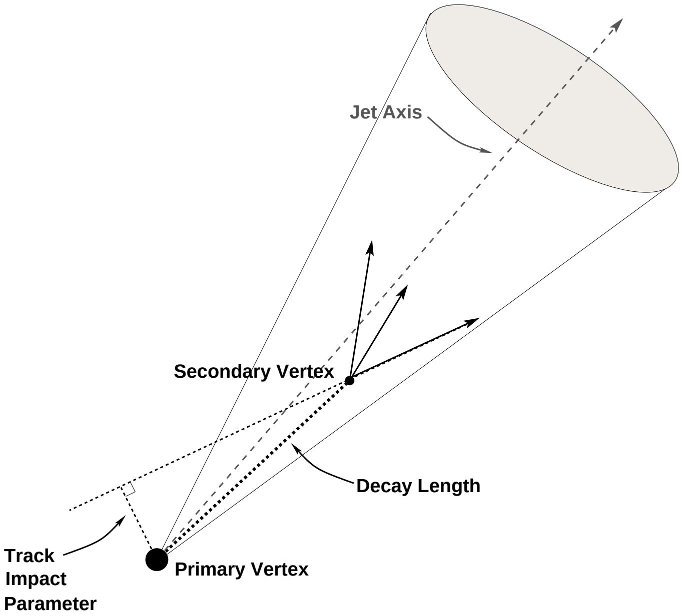

Figure 4.5: Schematic diagram of b-decay within a jet. Figure from [103].

A number of different b-tagging algorithms are available in ATLAS, the relevant ones are described below.

Secondary vertex algorithms

The `SV0` algorithm attempts to reconstruct a displaced vertex from the tracks associated to a calorimeter jet. The discriminating variable is the signed decay length significance of the reconstructed secondary vertex [105].

The `SV1` tagging algorithm is based upon the `SV0` algorithm but takes advantage of three additional properties of the vertex to increase the discriminating power: the invariant mass of all tracks associated to the vertex; the ratio of the sum of the energies of the tracks in the vertex to the sum of the energies of all tracks in the jet; and the number of two-track vertices. These variables are combined using a likelihood ratio technique [106]

Impact parameter algorithms

The `IP3D` algorithm uses the signed transverse impact parameter significance and longitudinal impact parameter significance of tracks as input to a likelihood ratio technique. These input variables are compared to pre-defined distributions for both the b- and light-jet hypotheses, taken from MC simulation, taking advantage of the correlations between the two variables [106].

Decay chain reconstruction algorithms

The `JetFitter` algorithm uses a Kalman fitter to find a common line on which the primary vertex and the b- or c-vertices lie, as well as their position on this line. This gives an approximation of the flight path for the b-hadron. The discrimination between b-, c- and light-jets is based on a likelihood using similar variables as in the `SV1` tagging algorithm along with additional variables such as the flight length significances of the vertices.

Combined algorithms

The combined `IP3D+SV1` algorithm utilises the fact that both the individual algorithms use a likelihood method. Hence, it is straightforward to combine them, summing the weights of the individual algorithms.

The `JetFitterCombNN` algorithm combines the `JetFitter` and `IP3D` algorithms based on artificial neural network techniques with MC simulated training samples and additional variables describing the topology of the decay chain [106].

The `MV1` algorithm uses a neural network to combine the jet p_{T}, jet η and inputs from the `SV0`, `IP3D+SV1`, `JetFitterCOMBNN` algorithms into a single discriminating variable [107, 108].

In the *SUSY-early 2011* selection the `JetFitterCOMBNN` algorithm is used, all other analyses use the `MV1` algorithm.

Operating points and scale factors

The above b-tagging algorithms are provided with several *operating points*. These correspond to a particular b-tagging efficiency and gluon/light quark jet rejection power for which *scale factors* to correct for differences between the tagger performance between MC and data and the corresponding systematic uncertainties are provided [107]. Figure 4.6 shows the light-jet and c-jet rejection power for various algorithms as a function of the b-tagging efficiency.

The scale factor (SF) is defined to be the ratio between the efficiencies in data (ϵ^{data}) and simulation ϵ^{MC}, for selecting b-jets (b) and light[1] (l) jets.

$$\mathrm{SF}_b(p_{\mathrm{T}}) = \frac{\epsilon_b^{\mathrm{data}}}{\epsilon_b^{\mathrm{MC}}}, \quad \mathrm{SF}_l(p_{\mathrm{T}}) = \frac{\epsilon_l^{\mathrm{data}}}{\epsilon_l^{\mathrm{MC}}}$$

---

[1] Light jets in this case include jets coming from gluons.

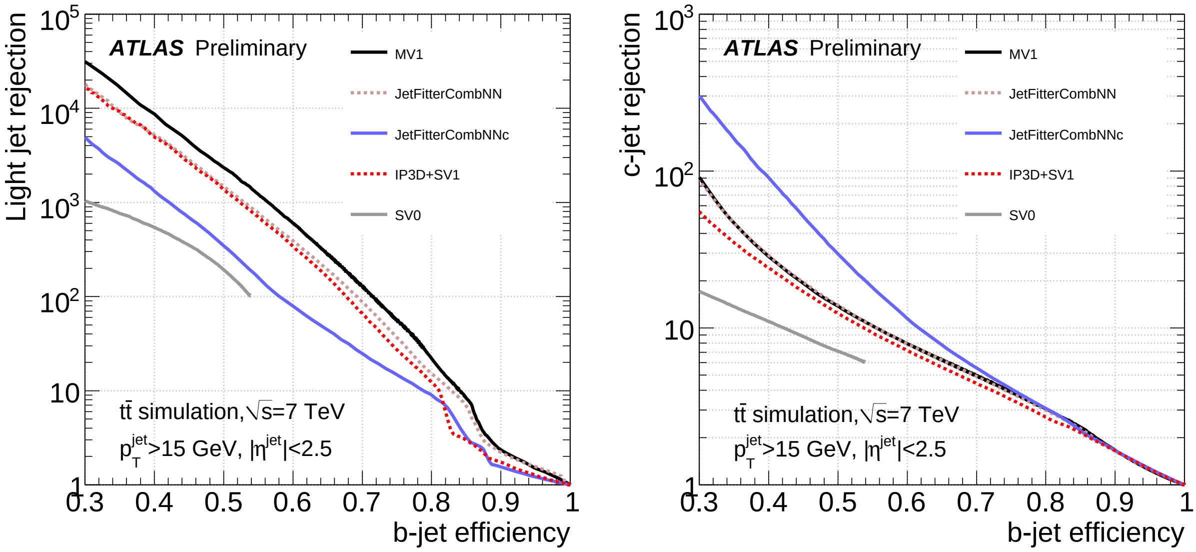

(a) **(b)**

Figure 4.6: Light-jet (a) and c-jet (b) rejection as a function of the b-tagging efficiency for various b-tagging algorithms, based on simulated $t\bar{t}$ events. Figures from [107].

The b-tagging performance is dependent on the p_T and η of the jets hence the scale factors are derived in bins of jet p_T and η. The scale factors are then used to determine a weight to assign each jet in an event and then combined to give a total weight for the event [109]. If the jet is tagged, the weight is given by

$$w_\mathrm{jet} = \mathrm{SF}_\mathrm{Flavour}(p_\mathrm{T}),$$

whereas if the jet is not tagged, the weight is given by

$$w_\mathrm{jet} = \frac{1-\epsilon^\mathrm{data}_\mathrm{Flavour}(p_\mathrm{T})}{1-\epsilon^\mathrm{MC}_\mathrm{Flavour}(p_\mathrm{T})} = \frac{1-\mathrm{SF}_\mathrm{Flavour}(p_\mathrm{T})\epsilon^\mathrm{MC}_\mathrm{Flavour}}{1-\epsilon^\mathrm{MC}_\mathrm{Flavour}(p_\mathrm{T})}.$$

The total event weight is then the product of all individual jet weights,

$$w_\mathrm{event} = \prod_\mathrm{jet} w_\mathrm{jet}.$$

The event weight w_event is included in all the MC estimations of event yields in the analyses.

Operating points used in each analysis

Top-2011: `MV1` algorithm is used at the 70% efficiency operating point for which approximately 1 in 150 light quarks or gluons are b-tagged.
SUSY-early 2011: `JetFitterCombNN` algorithm is used at 60% efficiency operating point for which approximately 1 in 420 light quarks or gluons are b-tagged.
SUSY-late 2011: `MV1` algorithm is used with two operating points at 60% (*tight*) and 75% (*loose*) efficiency where approximately 1 in 600 and 1 in 60 light quarks or gluons are b-tagged, respectively.
SUSY-2012: `MV1` algorithm is used at the 70% efficiency operating point where approximately 1 in 150 light quarks or gluons are b-tagged.

4.3.3 Electrons

Clusters of energy deposits in the electromagnetic calorimeter that can be matched with a well-measured track are identified as electron candidates. Further selection criteria to define different *quality* classifications of electron candidates are then applied to suit analysis needs. These quality cuts form three main classes of electron: `loose`, `medium` and `tight`, each with increasingly strict requirements and hence decreasing efficiency and fake rate [110]. In the analyses in the following chapters it is often required to define two electron categories *Loose* and *Tight*.

Loose electrons are defined by the `loose` definition for *SUSY-early 2011*. For all other analyses an improved definition which achieves a selection efficiency close to `loose` with a rejection power close to `medium` is used. In addition electron candidates are required to have at least 1 pixel hit and at least 7 silicon hits in the ID. Matching of the track to the calorimeter cluster is performed, ($\Delta\eta < 0.015$). Candidates are also required to have $E_{\mathrm{T}} = E_{\mathrm{cl}}/\cosh\eta > 10$ GeV and to fall within $|\eta_{\mathrm{cl}}| < 2.47$, excluding the calorimeter transition region $1.37 < |\eta_{\mathrm{cl}}| < 1.52$, where E_{cl} and η_{cl} are the energy and pseudorapidity of the electron candidate cluster, respectively. The p_{T} of the electrons in the MC is both rescaled and smeared to better match the distributions in data.

Tight electrons are required to satisfy the `tight` definition of [110] in *SUSY-early 2011*, for all other analyses a similar to `tight` but re-optimised for data collected in 2011 is used. In addition, electron candidates are required to be *isolated*, this reduces the number of electrons selected that arise from heavy hadron decays and *fake* electrons from hadrons that mimicking electron signatures. For all *SUSY-** analyses the isolation requirement is for the total transverse momenta of tracks with in a cone of $\Delta R = 0.2$ around the candidate electron to be less than 10% of the electron transverse momentum. For *Top-2011* E_{T} and η_{cluster} dependent isolation cuts are imposed on the energy in a cone of $\Delta R = 0.2$ around the electron ($E^{\Delta R=0.2}$) and on the total transverse momentum of all tracks within $\Delta R = 0.3$ of the electron ($p_{\mathrm{T}}^{\Delta R=0.3}$). The cuts are chosen such that the efficiency of the isolation requirement is 90%.

4.3.4 Muons

Muons candidates are constructed from track segments found in the muon chambers and the ID. All muon candidates are required to have a hit in the innermost pixel layer (if within acceptance), at least one hit in any pixel layer, at least 6 hits in the SCT and extension of the track in the TRT. The *SUSY* analyses utilise the `STACO` algorithm [89], whilst the *Top* analysis uses the `MuID` algorithm [111]. The p_{T} of muons in the MC are smeared to correct to the data. After smearing the acceptance requirements $p_{\mathrm{T}} > 10\,\mathrm{GeV}$ and $\eta < 2.4$ are applied. As with the electrons two classes are defined, *Loose* and *Tight*.

Muon quality cuts are again defined `loose`, `medium` and `tight` [112], each with increasingly strict requirements and hence decreasing efficiency and fake rate. *Loose* muons must also pass the `loose` selection criteria, whilst *Tight* muons must pass the `tight` criteria.

In addition, *Tight* muons must satisfy certain isolation requirements. For the *SUSY-early 2011* and *SUSY-late 2011* selections the total transverse momentum of all tracks within $\Delta R = 0.2$ of the muon candidate is required to be less than 1.8 GeV. The *SUSY-late 2011* selection also requires in addition that this total transverse momentum be less than 10% of the muon p_{T}. The *SUSY-2012* selection requires that the transverse energy within a cone of $\Delta R = 0.2$ must be less than 12% of the muon's transverse momentum and the transverse momentum of all tracks within $\Delta R = 0.3$ of the muon must also be less than 12% of the muon's transverse momentum. For the *Top-2011* selection the transverse energy within a cone of $\Delta R = 0.2$ must be less than 4 GeV and total transverse momentum of all tracks within $\Delta R = 0.3$ of the muon candidate to be less than 2.5 GeV.

4.3.5 $E_{\mathrm{T}}^{\mathrm{miss}}$

Whilst most particles produced in collisions interact with the detector to leave some signature of their presence, there are some that do not. Neutrinos leave the detector without interacting, their presence must be inferred. The momentum fraction of the incoming partons in a collision, and hence the CoM frame, in the z direction is unknown. However, modulo ISR/FSR effects, there is negligible net momentum of the incoming partons in the transverse plane. Conservation of momentum requires that if all particles produced in an event are detected the vectorial sum of their momenta should be zero. Hence, the presence of undetected particles can be inferred if an event has significant *missing transverse momentum*, $E_{\mathrm{T}}^{\mathrm{miss}}$,

$$E_{\mathrm{T}}^{\mathrm{miss}} = -\sum_{\substack{\text{visible}\\\text{paricles}}} \mathbf{p}_{\mathrm{T}} = \sum_{\substack{\text{invisible}\\\text{paricles}}} \mathbf{p}_{\mathrm{T}}. \tag{4.1}$$

This principle applies not only for detection of neutrinos but for any particles that do not interact with the detector. As discussed in §2.3.3, R-parity conserving SUSY scenarios predict the existence of a neutral weakly interacting massive LSP. Significant $E_{\mathrm{T}}^{\mathrm{miss}}$ is a key signature for searches for such SUSY scenarios. It plays an essential role in several of the analyses discussed in the following Chapters.

Several different $E_{\mathrm{T}}^{\mathrm{miss}}$ calculations are used within ATLAS, however only two are relevant to the remainder of this thesis. They are `MET_RefFinal` and `MET_Simplified20` and are closely related. In each case $E_{\mathrm{T}}^{\mathrm{miss}}$ is calculated from calorimeter cluster energy deposits calibrated to the EM scale. These clusters are then corrected to the scale of the physics object with which they are associated [113]. One of the main considerations in this choice is that it allows consistent treatment of object reconstruction systematic uncertainties to the $E_{\mathrm{T}}^{\mathrm{miss}}$ calculation.

The calculation can be separated into object-specific contributions. The final $E_{\mathrm{T}}^{\mathrm{miss}}$ calculation is given by the vectorial sum of the following *terms*:

$$\begin{aligned}\texttt{MET\_RefFinal} = {} & \texttt{MET\_RefEle} + \texttt{MET\_RefGamma} + \texttt{MET\_RefTau} + \texttt{MET\_RefJet} + \texttt{MET\_RefMuon} \\ & + \texttt{MET\_CellOut\_Eflow} + \texttt{MET\_MuonBoy},\end{aligned} \tag{4.2}$$

The terms correspond to the contributions from calorimeter cells associated with electrons, photons, hadronic taus, jets (with $p_{\mathrm{T}} > 20$ GeV) and muon calorimeter deposits, respectively. The final two terms correspond to cells not associated with any physics objects and a term to compensate for the fact that calorimetric $E_{\mathrm{T}}^{\mathrm{miss}}$ does not fully account for momenta of muons. Cases where cells are associated to multiple physics objects are resolved by choosing to assign cells to objects in the order above, highest priority first.

In 2011 data-taking `MET_RefFinal` was not fully commissioned and a simplified version was used,

$$\texttt{MET\_Simplified20} = \texttt{MET\_RefJet} + \texttt{MET\_CellOut} + \texttt{MET\_RefEle} - \sum_{\substack{\text{selected}\\\text{muons}}} \mathbf{p}_{\mathrm{T}}. \tag{4.3}$$

In keeping with the jet calibration used in 2011 the `MET_RefJet` term is calibrated to the `EM+JES` scale.

The same principle of $E_{\mathrm{T}}^{\mathrm{miss}}$ calculation can also be applied to tracks rather than calorimeter energy deposits. The transverse momenta of all tracks satisfying the quality cuts are vectorially summed to calculate the $E_{\mathrm{T}}^{\mathrm{miss\,Track}}$. The track quality requirements are as follows: p_{T} $p_{\mathrm{T}} > 500$ MeV, $|\eta| < 2.5$, $|d_0| < 1.5$ mm, $|z_0 \sin(\theta)| < 1.5$ mm, ≥ 1 pixel hit and ≥ 6 SCT hits.

4.3.6 Removal of overlapping objects

In the case of candidate objects overlapping with each other, all but one object must be removed from the event. If an electron is located within $\Delta R < 0.2$ of a jet the object is considered to be an electron and the jet is removed. After this procedure has been repeated for all electrons any leptons within $\Delta R < 0.4$ of the remaining jets are removed to suppress leptons arising from hadron decays. This overlap removal occurs after the above object definitions have been applied.

4.4 Systematic uncertainties

Several sources of systematic uncertainty affect the predicted number of simulated signal and background events. A brief description of the assessment of the uncertainties that are common to all the following analyses will now be given.

4.4.1 Lepton reconstruction and triggers

Mis-modellings of the muon or electron trigger, reconstruction and selection efficiencies in simulation are corrected to match the data using scale factors. These scale factors are derived as a function of the lepton kinematics and are taken from measurements of the efficiency in data using $Z \to \mu\mu$ or $Z \to ee$ and $W \to e\nu$ decays. The same processes are used to measure the lepton momentum scale and resolution.

4.4.2 Jet energy scale

The jet energy scale uncertainty is derived from in-situ and single pion test-beam measurements, uncertainties on the material budget of the ATLAS detector, the description of the electronic noise and the Monte Carlo modelling used in the event generation. The effect of this uncertainty is assessed by varying the p_{T}, η, flavour, pileup and nearby jet dependent calibration at a per-jet level by $\pm 1\sigma$. This gives a two point uncertainty envelope which can be used to assess the impact on selection efficiency and the shapes of kinematic distributions.

4.4.3 Jet energy resolution

The jet energy resolution (JER) and reconstruction efficiency are measured in data using techniques described in [101, 114]. An extra p_{T} and η dependant p_{T} smearing is applied to jets,to account for a possible underestimation of the jet energy resolution in the MC simulation.

4.4.4 b-jet scale factors

The b-tagging efficiencies and mis-tag probabilities are measured in data as in [107,108], and jet p_{T} dependent scale factors are applied to simulation to match the efficiencies measured in data. The uncertainties in scale factors are calculated similarly to the JES, with up and down variations for three sub-sets of the overall scale factor, the mistag rate, the b-tagging efficiency and the c- and τ-tagging efficiency. The uncertainty due to all three is calculated and combined in quadrature to give the final result.

4.4.5 $E_{\mathrm{T}}^{\mathrm{miss}}$

The systematic uncertainties on objects are propagated to the missing transverse momentum $E_{\mathrm{T}}^{\mathrm{miss}}$. In addition, the uncertainties in $E_{\mathrm{T}}^{\mathrm{miss}}$ due to the contribution from soft jets and cells which are not associated with any physics objects, including the effects of pile-up modelling, are included.

4.4.6 Luminosity

An uncertainty is assigned to the integrated luminosity of a dataset. The luminosity is determined from the counting rates measured by the ATLAS luminosity detectors. For the 2011 dataset the uncertainty on the measured luminosity is 3.9%. For the 2012 dataset the uncertainty on the measured luminosity is 3.6%.

4.5 Monte Carlo simulation

Monte Carlo simulation is an essential part of most analyses in ATLAS. It is used for comparison of the data to predictions from simulation and in estimation of SM backgrounds when data-driven techniques are not available. In searches for new physics it is required to simulate the signal process and optimise the analysis sensitivity to that process and for model-dependant interpretation of results. Additionally, the use of generator level particle information, referred to as *truth information*, can be vital for understanding the composition and behaviour of signal and background in an analysis.

There are several MC tools available for generation of a wide range of processes. As was already discussed in §3.2.3 and shown schematically in Figure 3.4, event simulation can be rather complicated at hadron colliders. Event generation can in general be separated into two parts based on the two extremes in the behaviour of QCD.

4.5.1 Running of α_S

The evolution or *running* of the strong coupling constant, shown in Figure 4.7, leads to markedly different behaviour of QCD at different distance or energy scales. Asymptotic freedom means that QCD is weakly interacting at short distance scales (high energies) so calculations of the high Q^2 hard interaction can be performed using perturbation theory. This is referred to as the *matrix element* (ME) calculation. However, at larger distance scales (lower energies) soft hadronic processes, like hadronisation and the formation of the UE, are non-perturbative and must be computed, not directly from QCD but from QCD-inspired models. This is referred to as the *parton shower* (PS).

Renormalisation group equations (RGEs) are used to evolve quantities from some reference scale to another. For α_S this running is governed by the following diffential equation:

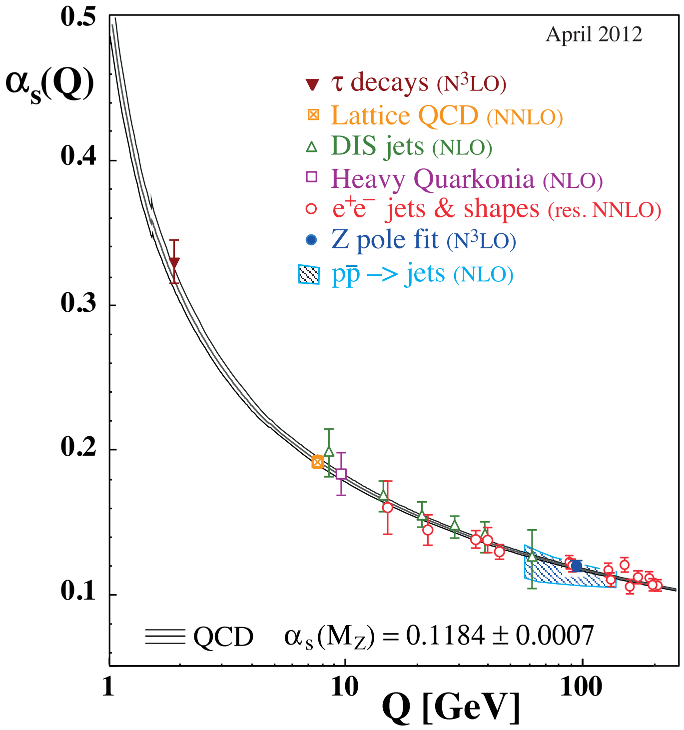

Figure 4.7: Summary of measurements of α_S as a function of the respective energy scale Q. Figure from [115].

$$\frac{d\alpha_S(\mu_R)}{d\ln\mu_R} = \underset{\text{LO}}{-\frac{\beta_0}{2\pi}\alpha_S^2} \quad \underset{\text{NLO}}{-\frac{\beta_1}{4\pi^2}\alpha_S^3} \underset{\text{NNLO}}{-\frac{\beta_2}{64\pi^3}\alpha_S^4} + \dots \tag{4.4}$$

where μ_R is the renormalisation scale usually taken to be the Q^2 scale of the hard interaction. Taking only the lowest order it is possible to solve for α_S,

$$\alpha_S(\mu_R) = \frac{\alpha_S(\mu_0)}{1 + \frac{\beta_0}{4\pi}\alpha_S(\mu_0)\ln(\mu_R^2/\mu_0^2)} \equiv \frac{4\pi}{\beta_0\ln(\mu_R^2/\Lambda_{\text{QCD}}^2)} \tag{4.5}$$

where Λ_{QCD} is the QCD scale parameter and β_0 is defined as

$$\beta_0 = 11n - \frac{2}{3}f, \tag{4.6}$$

where n is the number of colours in the theory and f is the number of flavours. If $\beta_0 < 0$ (as in the SM) the coupling decreases with increasing Q^2. This is the origin of asymptotic freedom.

If evaluated to all orders in perturbation theory the choice of scale is arbitrary, however, in practice this is is not possible. In general the scale should be set to scale of the hard interaction to avoid large logarithms which might spoil the perturbation series. But even with this choice the fact that calculations cannot be completed to infinite orders means that there is some residual dependance on the scale choice. Therefore, it is important that the uncertainty due to a particular choice of scale is evaluated when considering MC generator systematic uncertainties. Such dependancies and the corresponding systematic uncertainities are considered in §6.5.1 and §9.4.3 for the MC samples described in §4.5.3.

4.5.2 Generators and matching

Several different methods for modelling high-energy collisions have been implemented by different MC generators. Generally the ME calculation of the hard process is performed to some perturbative order, followed by parton showering and finally detector simulation.

High jet multiplicity final state processes are common backgrounds to new physics searches at a *pp* collider. In such searches the kinematic configuration of jets is often hard and well separated, which is away from the PS-dominated region and so PS alone can be inaccurate. Therefore it is essential that such processes be generated using tree-level matrix element calculations. Examples of such generators include `ALPGEN` [116] and `MADGRAPH` [117]. These generators are then interfaced with general purpose MC generators such as `PYTHIA 6.4` [118], `PYTHIA 8.1` [119] and `HERWIG 6.5` [120] which are used to shower the parton level inputs. These MC configurations are referred to as ME+PS generators. `HERWIG++` [121] and `SHERPA` [85] also use the ME+PS method but include both parts of the calculation internally.

Another class of MC generators perform ME calculations at the *next-to-leading perturbative order* (NLO) and are combined with a PS, these are referred to as NLO+PS generators. These higher order calculations are intrinsically more accurate as they include the radiation of an extra parton with full tree-level accuracy and NLO virtual corrections. Examples of such generators are `MC@NLO` [122] and `POWHEG` [123, 124]. However, it should be noted that, in certain circumstances, namely when a final state with multiple hard, well separated jets is required, ME+PS generators can be preferable to NLO+PS.

In both ME+PS and NLO+PS generators there is a problem of the overlap of phase space between the tree-level calculation and PS contributions of multi-jet final states. In the case of ME+PS generators, an overlap between the ME and PS phase-space can arise when samples are generated with additional partons at ME level, as described schematically

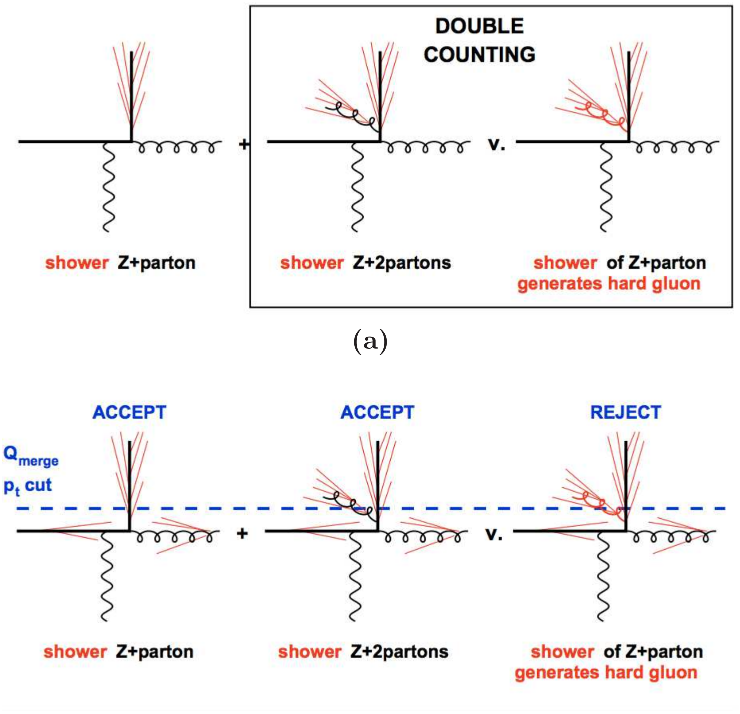

(a)

(b)

Figure 4.8: Schematic diagrams of the origin of the overlap between matrix element and parton shower in event generation with additional partons (a) and the MLM matching procedure to remove double counting (b). Figures from [125].

in Figure 4.8.

To avoid such overlaps these generators use *matching* procedures. The aim of the matching procedure is to define some means with which to merge the ME and PS contributions without this overlap. There are several different approaches to this problem. Two of the most common are the CKKW method [126–128] that applies a shower veto and therefore event reweighting and the MLM method [129, 130] based on event rejection. The latter will now be described in more detail in the context of `MADGRAPH+PYTHIA`.

MLM matching in `MADGRAPH+PYTHIA`

The original MLM method uses a cone algorithm and minimum p_T cut to cluster partons. In `MADGRAPH` three matching schemes, based upon the MLM scheme, are implemented with `PYTHIA` as the PS. These are the *cone* MLM, k_T MLM and *shower-*k_T schemes. The k_T MLM scheme will now be described in more detail.

The final-state partons in an event generated by `MADGRAPH` are clustered according to the k_T jet algorithm to obtain the "equivalent parton shower history" of the event. Only clusterings that correspond to Feynman diagrams existing in the generated matrix element are kept. For the cone jet algorithm, a minimum p_T^{ME} and ΔR is required for all partons. For the k_T scheme, the smallest k_T value is required to be above the cutoff scale `xqcut`. Events are then passed to `PYTHIA` for showering. After showering, but before hadronisation and decays, the final-state partons are clustered to form jets using the same k_T algorithm. Here the jets are clustered with a cutoff scale, `QCUT`, which must be larger than `xqcut`. These jets are then compared to the partons from the matrix element event. A jet is considered to be *matched* to a parton if the jet measure $k_T(\text{parton,jet})$ is smaller than the cutoff `QCUT`. The event is kept only if each jet is matched to a parton, except for the highest multiplicity sample, where extra jets are allowed below the k_T scale of the softest ME parton in the event. Events which do not match are rejected. Non-matched events generally arise when partons are so close that they cannot generate independent jets or when a parton is too soft to generate its own jet.

The shower-k_T scheme is identical until events are passed to `PYTHIA` where they are showered using p_T-ordered showers. For events from lower-multiplicity samples, the event is rejected if the scale of the hardest emission, Q_{hard}, is above the matching scale `QCUT`, while events from the highest multiplicity sample are rejected if Q_{hard} is greater than the scale of the softest matrix element parton in the event. One of the benefits of this matching scheme is that it allows for the matching scale `QCUT` to be set closer to the matrix element cutoff scale `xqcut` and hence is more efficient.

Typically when generating a samples with N additional partons, the generation of sub-samples with $\leq N - 1$ partons proceeds by rejecting events containing more than required number of jets, these are said to be *exclusive*. The subsample with N additional partons is said to be *inclusive* and additional jets from the PS are allowed as there will be no overlap.

Figure 4.9 shows differential jet rates, Log(Differential Jet Rate $N \rightarrow N+1$, for two scenarios in the context of generation of $t\bar{t}+Z$ `MADGRAPH+PYTHIA` samples. The differential jet rate is the scale at which the sample falls into a lower N-jet multiplicity based on the choice of `QCUT` and `qcut`. The distributions should be independent of the cutoff scales chosen as these quantities do not have physical meaning and the transition between the N-jet and $N+1$-jet samples at the cutoff should be as smooth as possible. The top row shows the k_T MLM matching scheme where `xqcut` = `QCUT` = 40 GeV, clearly there is not a smooth distribution in the differential jet rate plot and can also be seen in the leading jet p_{T} spectrum. The second row shows several choices of `QCUT` for `xqcut`= 25 GeV. The optimised parameter choice of `xqcut` = 25 GeV, `QCUT` = 30 GeV is shown in the bottom row where it is clear that the differential jet rate and p_{T} spectrum are considerably smoother.

4.5.3 MadGraph+Pythia $t\bar{t}+\mathrm{V}(=\mathrm{W}/\mathrm{Z})$

Several processes in ATLAS are generated using `MADGRAPH`. The author of this thesis was responsible for generation of simulated samples of the $t\bar{t}+W/Z$ processes. These processes are a significant background in several SUSY searches, including those in Chapters 8 and 9. In addition, $t\bar{t}+Z$ is the signal for the analysis in Chapter 6.

These samples were generated at $\sqrt{s} = 7$ and 8 TeV. Figure 4.10 shows the W/Z and top p_{T} distributions and jet multiplicity. The samples were originally generated with one additional parton and later with two additional partons. In both cases the implementation of MLM matching in `MADGRAPH+PYTHIA` uses the shower-k_T scheme, with `xqcut` = 25 GeV, `QCUT` = 30 GeV.

4.5.4 Detector simulation

Stable particles (those with lifetimessuch that $c\tau > 10$ mm) that exist after hadronisation and decays of unstable particles are fed to the ATLAS detector simulation [131]. This simulation is performed using either *full* `GEANT4` [132] simulation or a *fast* simulation in

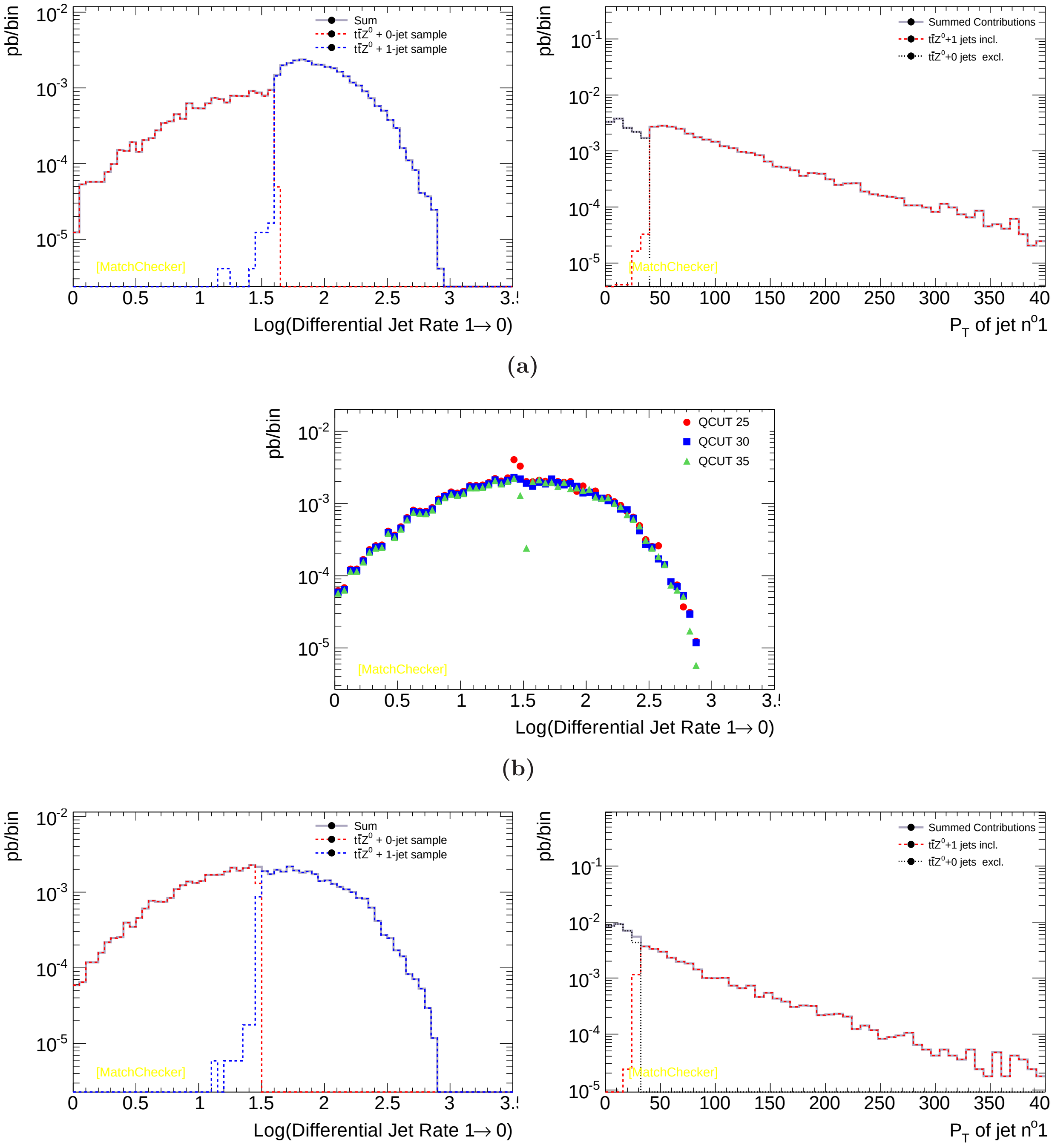

(a)

(b)

(c)

Figure 4.9: Differential jet rate and leading jet p_{T} spectrum for (a) `xqcut` $= 40$ GeV, `QCUT` $= 40$ GeV. A comparison of several `QCUT` values for `xqcut`$=25$ GeV is shown in (b) and (c) Shows the optimal choice of `xqcut` $= 25$ GeV, `QCUT` $= 30$ GeV.

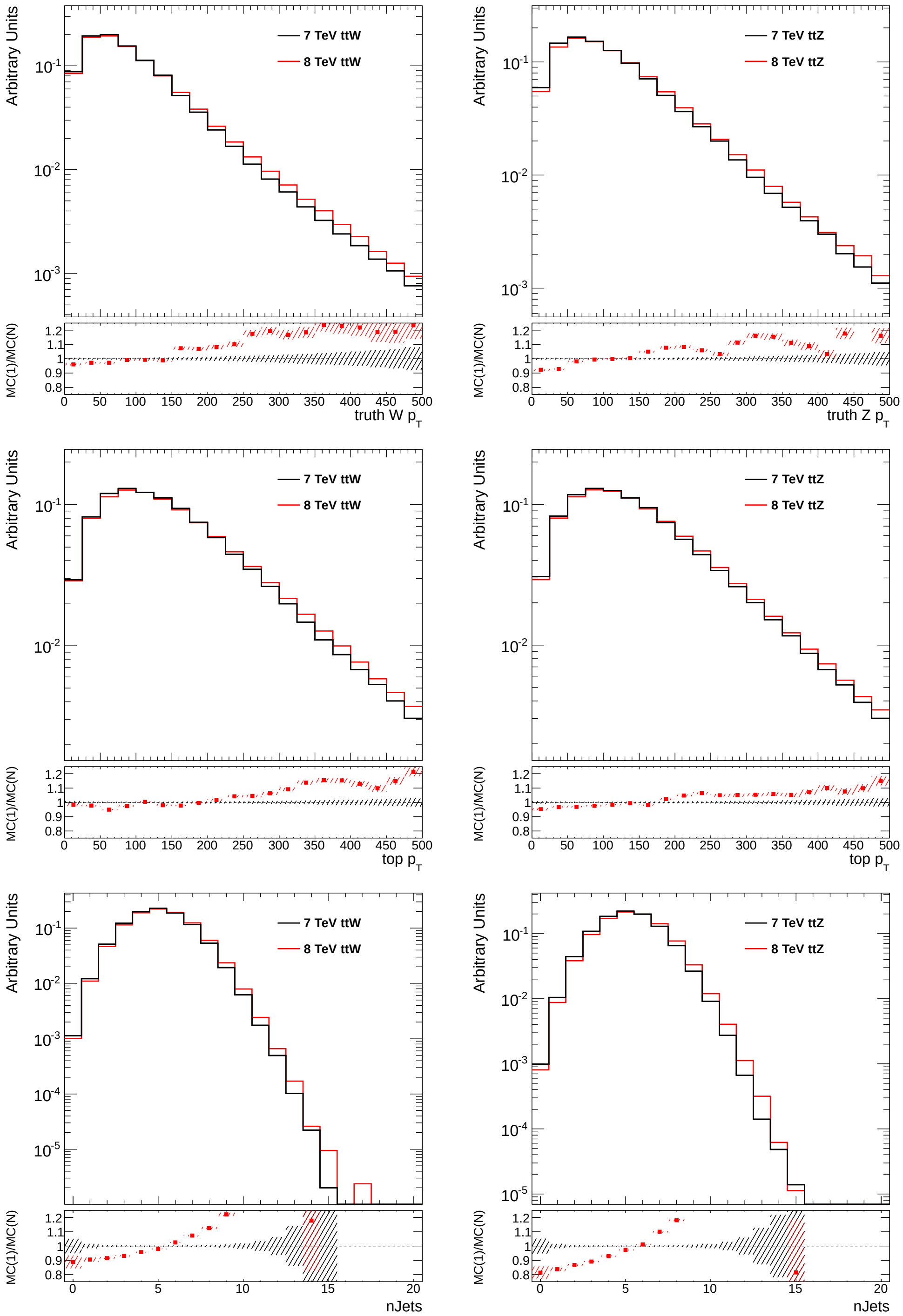

Figure 4.10: Comparison of $\sqrt{s}$ = 7 and 8 TeV samples for $t\bar{t} + W$ (Left) and $t\bar{t} + Z$ (Right). Both samples are normalised to unit area for comparison of the shape of distributions.

which calorimeter showers are simulated with a parameterised description [133] whilst all other interactions are simulated with `GEANT4`.

Following simulation of the hard interaction additional minimum bias collisions are added to simulate the multiple interactions per bunch crossing. Reconstruction of the events after digitisation of the hits in the detector uses the same software as that applied to data. In all the analyses that follow the Monte Carlo simulation is weighted to match the $\langle\mu\rangle$ distribution in the data for each year.

Chapter 5

Trigger

5.1 Introduction

This Chapter will begin by describing the ATLAS trigger system. Followed by a description of the design and implementation of a topological jet trigger algorithm based on the contransverse mass kinematic variable. Finally, an overview of studies performed to optimise the ATLAS SUSY group trigger strategy for 2011 and 2012 data taking will be given.

The author's contribution in this Chapter is the design and implementation of a topological jet trigger for SUSY searches as described in §5.3. This includes writing the trigger algorithm and thorough validation of this algorithm before it was used to collect data. In addition, the author provided justification for the allocation of trigger rate for this trigger and others through optimisation of the ATLAS SUSY Working Group trigger strategy, as described in §5.4.

5.2 ATLAS trigger system

With a nominal 40 MHz LHC bunch crossing rate and ~ 1 MB event size ATLAS is generating more information than can be recorded to disk with full granularity. As a result it is essential to have an efficient trigger system for selecting events of interest whilst rejecting those that are more abundant yet less physically significant. Approximately one W or Z boson will be produced for every 1-10 million pure-QCD events [83] as already shown in Figure 3.3.

The ATLAS trigger system, shown schematically in Figure 5.1 has a three tier structure with increasing levels of information used in reconstruction, and hence refinement of

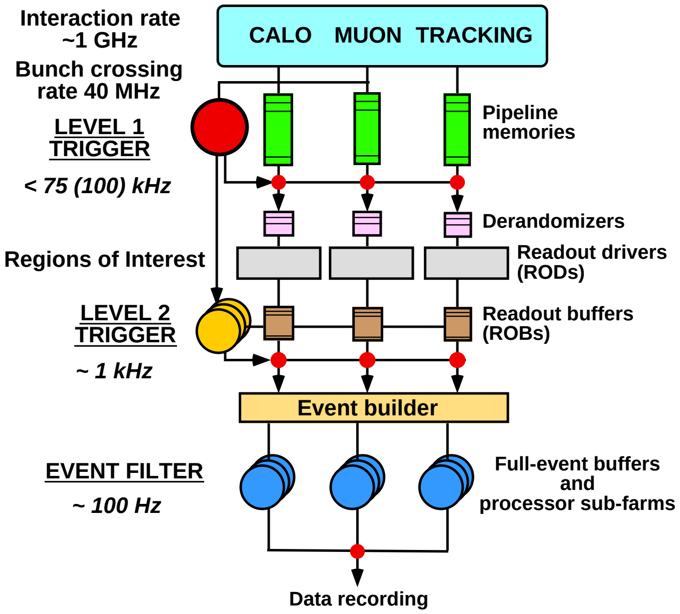

Figure 5.1: ATLAS trigger system schematic diagram. Figure from [134].

the selection criteria, at each stage.

At the lowest level, Level 1 (L1), hardware triggers use coarse calorimeter and muon information for the trigger decision. At this level the event accept rate is reduced to a maximum of 75 kHz with a latency on decision of ~2.5 μs. In the case where the trigger is passed, the raw event data is sent to the readout stream via the RODs for the next trigger level. The L1 trigger defines one or more *regions-of-interest* (RoIs), these are the positions in η and φ where the L1 trigger has identified interesting features. Results from the L1 muon and calorimeter triggers are processed by the central trigger processor (CTP), which implements trigger selections based on energy and momentum thresholds using combinations of trigger objects. This is known as a trigger *menu*.

The Level 2 (L2) trigger is software based. At this level full granularity and precision is used for the trigger decision but only within particular RoIs as identified by the Level 1 trigger. The advantage of this technique is that only ~1-4% of the event information is unpacked [135] and it is considerably quicker to analyse. The L2 menu is designed to reduce the event rate to ~2 kHz with a latency of ~40 ms.

The final trigger level is the Event Filter (EF). Offline reconstruction algorithms are used but only inside the RoIs passed on from the L2 triggers . The EF reduces the output rate to ~200 Hz, where the extra complexity in the trigger algorithms results in ~4 s of latency. Once accepted by an EF trigger an event is written to mass storage. The Level 2 and EF are collectively known as the High-Level Trigger (HLT).

During 2011 the RoI seeded EF reconstruction algorithm was replaced by a *full scan* algorithm. It was found that sufficient time was available to unpack the entire ATLAS calorimeter for jet-finding rather than just those areas within RoIs coming from L2. In this case the trigger level reconstruction is very close to that of the offline software and the efficiency is improved.

5.2.1 Trigger chains, menus and rates

Some technical aspects of the ATLAS trigger system will now be described that are required in the following discussions.

Trigger algorithms begin with a specific L1 trigger selection and typically require that additional refinements be applied to the selection at L2 and EF. This structure is defined by three separate so-called trigger *items*, one item for each level, which combine to give what is referred to as a trigger *chain*.

For example, one of the simplest configurations is a single jet trigger. At each trigger level the respective trigger items test for the existence of a jet-like object satisfying a given selection, in this case an E_{T} threshold. If the L1 item finds a jet-like object above the required threshold then the location of that RoI is passed on to L2. Here the L2 item selection requirements are applied if they are satisfied the location of the L2 RoI is passed on to the EF item. If the EF item requirements are satisfied the event will be written to permanent storage. An example in ATLAS trigger nomenclature is the trigger chain

$$\texttt{L1\_J15} \rightarrow \texttt{L2\_j25} \rightarrow \texttt{EF\_j40}. \tag{5.1}$$

The first part of the trigger item naming indicates the trigger level whilst the second part describes the object(s) being selected and the E_{T} or p_{T} threshold required. Note that increasing E_{T} or p_{T} thresholds are applied at each subsequent trigger level, this is to ensure that full efficiency is maintained between levels avoiding unnecessary trigger rate being used.

Several different trigger requirements can be combined together at each level. For example a di-jet trigger that requires two jets with a lower threshold and the additional requirement for one of these jets to satisfy a higher threshold would be written

$$\texttt{L1\_J15\_2J10} \rightarrow \texttt{L2\_j25\_2j15} \rightarrow \texttt{EF\_j30\_2j20}. \tag{5.2}$$

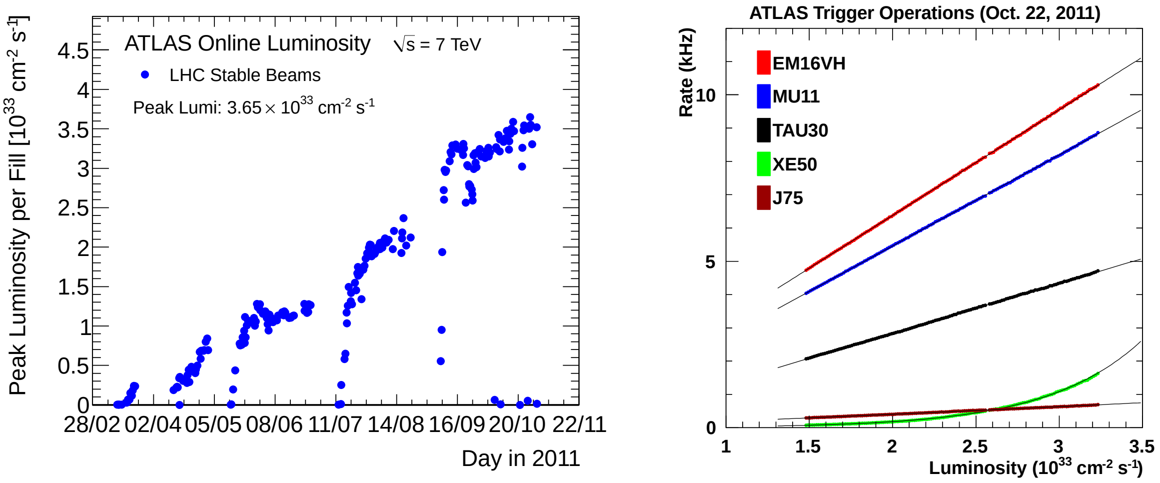

(a) (b)

Figure 5.2: (a) Peak instantaneous luminosity during 2011 data-taking. (b) Trigger rates for 2011 for various Level 1 trigger items. Figures from [96] and [136].

Also different objects can be combined to construct a trigger, for example the following electron and muon trigger

$$\texttt{L1\_EM15\_MU5} \rightarrow \texttt{L2\_e25\_mu10} \rightarrow \texttt{EF\_e40\_mu25}. \tag{5.3}$$

The different trigger objects available at each level are summarised in the following table:

Object	Level 1	HLT
jet	`J`	`j`
electron	`EM`	`e`
photon	`EM`	`g`
tau	`TAU`	`tau`
muon	`MU`	`mu`
$E_{\mathrm{T}}^{\mathrm{miss}}$	`XE`	`xe`

A record of all trigger items and how different items are linked together to form trigger chains is managed by what is referred to as a trigger *menu*. The role of the trigger menu is to define the available trigger chains and manage the distribution of the available trigger bandwidth between them at any given moment of data-taking. The trigger menu can be adapted to suit different LHC running conditions, for example different instantaneous luminosities during 2011 and 2012 data taking required significant change in the menu design to accommodate the extra rate at the high instantaneous luminosity in 2012. Figure 5.2(a) shows the peak instantaneous luminosity during 2011 data-taking and Figure 5.2(b) shows the rates of various trigger items as a function of instantaneous luminosity. This demonstrates the range of LHC running conditions that must be accommodated.

5.3 Contransverse mass trigger

The design and implementation of a topological jet trigger that uses contransverse mass as the discriminating variable is described in the following section. This trigger was developed primarily as an alternative to missing transverse energy triggers for 0-lepton SUSY searches during early ATLAS data-taking.

5.3.1 Contransverse Mass

The contransverse mass, M_{CT}, is a kinematic variable first devised in [137] and further developed in [138]. It provides a representation of the kinematic configuration of visible objects in an event. For the case where two objects undergo equal magnitude contra-linear boosts in the laboratory transverse plane, M_{CT} is an invariant quantity. Although being somewhat different in philosophy, in practise M_{CT} is rather similar to another kinematic variable, m_{T2}, described in [139, 140].

For two visible particles v_1 and v_2 the mathematical definition of M_{CT} is given by

$$M_{\mathrm{CT}}(v_1, v_2)^2 = [E_T(v_1) + E_T(v_2)]^2 - [\mathbf{p_T(v_1)} - \mathbf{p_T(v_2)}]^2, \tag{5.4}$$

in the case where particles v_1 and v_2 are massless this reduces to

$$M_{\mathrm{CT}}(v_1, v_2) = \sqrt{2p_T(v_1)p_T(v_2)[1 + \cos\Delta\varphi_{12}]}. \tag{5.5}$$

From (5.5) it is clear that M_{CT} is maximised for given $p_T(v_1)$ and $p_T(v_2)$ when the two objects considered are co-linear, i.e. $\Delta\varphi_{12}$ is small, and is minimised for two objects 'back-to-back' in the transverse plane, i.e. $\Delta\varphi_{12} = \pi$.

M_{CT} also provides information about the masses of the invisible particles in multi-step decay chains. Consider pair production of the particle δ, where both δs undergo a one-step decay, as shown in (5.6), to a visible object a and an invisible object α.

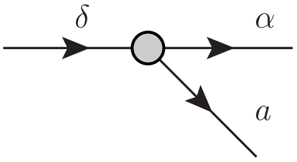

(5.6)

One can construct the contransverse mass from the four-momenta of the two visible objects, $M_{\text{CT}}(a,a)$. Over many events a distribution of this variable will exhibit a kinematic upper limit, or *endpoint*, because M_{CT} is kinematically bounded from above. The kinematic endpoint is determined by an analytical combination of the masses of the invisible particles in the decay. In our example the value of this upper limit in $M_{\text{CT}}(a,a)$ is given by

$$M_{\text{CT}}^{\text{max}}(a,a) = \frac{m(\delta)^2 - m(\alpha)^2}{m(\delta)}, \tag{5.7}$$

This has two important consequences; firstly that combinations of endpoint measurements can be used to determine the masses of the particles involved in the decay and secondly it allows M_{CT} to be used as a discriminating variable.

The presence of ISR in events can boost the CoM frame of the event in the transverse plane. As the objects used to calculate M_{CT} are no longer experiencing contra-linear boosts in the lab frame the invariance of the quantity is broken. This can result in events appearing above the kinematic endpoints which can be a problem especially for mass reconstruction. The M_{CT} technique has been developed to be able to correct for such boosts from ISR and FSR by re-boosting the CoM frame back to being at rest in the lab frame [138]. It is not possible to fully reconstruct the mass of the CoM frame so exact correction is not possible. However, the technique is formulated such that a conservative correction can be derived which when applied gives a M_{CT} value which is less than or equal to the true value of M_{CT} in the CoM frame. This is referred to as *boost-corrected contransverse mass*, $M_{\text{CT}}^{\text{corr}}$. This version of M_{CT} is the one used in the analysis described in Chapter 8.

In general, if the mass splitting between δ and α, $\Delta m = m(\delta) - m(\alpha)$, is sufficiently large it is possible to produce events with large values of M_{CT}. There are several SUSY scenarios where massive particles undergo decays of the form shown in (5.6). For example squark pair production where the squark decays to a quark and LSP, $\tilde{q} \to q\tilde{\chi}_1^0$ as shown in (5.8).

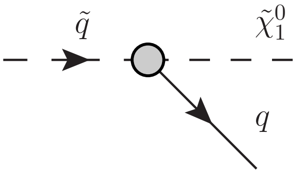

(5.8)

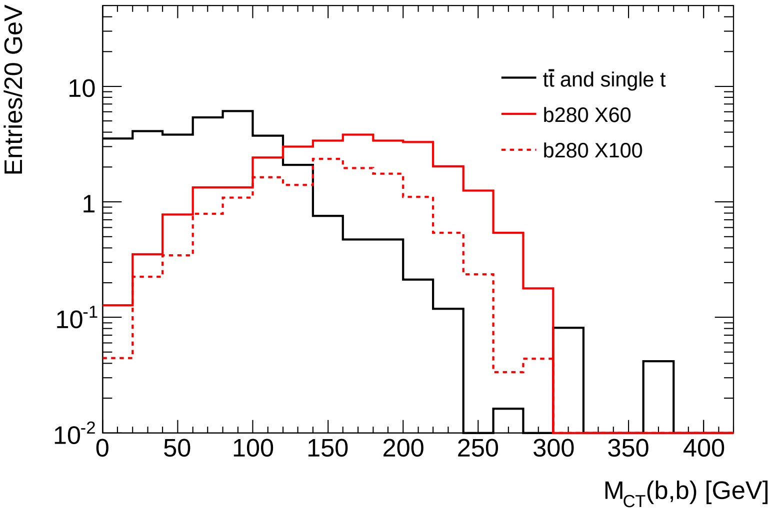

Figure 5.3: $M_{\mathrm{CT}}\,(b,b)$ for the dominant $t\bar{t}$ and single top background and two SUSY signal points; sbottom, $\tilde{b}$, pair production with $\tilde{b} \to b\tilde{\chi}_1^0$ for $m_{\tilde{b}} = 280$ GeV, $m_{\tilde{\chi}_1^0} = 60$ GeV (solid red) and $m_{\tilde{b}} = 280$ GeV, $m_{\tilde{\chi}_1^0} = 100$ GeV (dashed red).

In this case large values of M_{CT} can be obtained. However, for many SM background processes M_{CT} is expected to be low. For instance, QCD di-jet events will have M_{CT} values close to zero due to their back-to-back topology and from (5.7) it is clear that $t\bar{t}$ events have a maximum possible value of the contransverse mass between the two b-jets given by,

$$M_{\mathrm{CT}}^{\mathrm{max}}(b,b) = m_t^2 - m_W^2/m_t \sim 140\ \mathrm{GeV}. \tag{5.9}$$

From Figure 5.3 it can be seen that the endpoint in the $t\bar{t}$ distribution is clearly below that of the two SUSY signal samples.

It is clear that contransverse mass allows differentiation between SUSY signal and many standard model backgrounds, thus making it a good candidate variable on which to trigger SUSY events. This is especially true in the 0-lepton jets+$E_{\mathrm{T}}^{\mathrm{miss}}$ channel where pairs of jets constitute the visible objects that enter the M_{CT} calculation.

5.3.2 Trigger algorithm

Designing a trigger to select jets+$E_{\mathrm{T}}^{\mathrm{miss}}$ SUSY events without a $E_{\mathrm{T}}^{\mathrm{miss}}$ requirement at a hadron collider is a very challenging task. QCD multijet events have a very large cross section relative to the SUSY signal processes being targeted. More conventional selection criteria such as high jet p_{T} thresholds are not sufficient to keep the trigger rate at an acceptable level whilst maintaining efficiency for the SUSY signal, additional rejection power is required. This can be achieved by demanding, in addition to jet p_{T} requirements, that the contransverse mass, calculated from pairs of jets as the visible particles, is above a given threshold.

It is technically possible to calculate M_{CT} at trigger level but only in the HLT. The L1 trigger is hardware based and has only the capability to identify the number of jets that pass a given E_{T} threshold. It is unable to perform calculations such as those required for calculation of M_{CT}[1].

To remain as inclusive as possible a di-jet trigger is the obvious L1 seed choice for the M_{CT} trigger. Limitations on the acceptable rate of L1 jet trigger items do constrain the available options for jet thresholds and/or multiplicities. This will be discussed in more detail in §5.3.3. However, it is the available output rate at Level 2 that is most restrictive and, hence, where the additional rejection provided by an M_{CT} requirement is vital. Therefore, the format of the M_{CT} trigger chain is a di-jet L1 *seed* item followed by L2 and EF items with the addition of a M_{CT} threshold,

$$\texttt{L1\_2JA} \rightarrow \texttt{L2\_2jB\_mctX} \rightarrow \texttt{EF\_2jC\_mctY}, \tag{5.10}$$

where `A`, `B` and `C` are the L1, L2 and EF jet E_{T} thresholds respectively, `X` and `Y` are the respective L2 and EF M_{CT} thresholds.

HLT trigger algorithms operate in two stages; firstly, trigger level jets are selected with a *feature extraction algorithm* (FEX), and secondly, these jets are passed on to the *hypothesis* algorithm which applies E_T thresholds, calculates the M_{CT} values and applies the M_{CT} threshold requirement. If all the hypothesis selection requirements are satisfied the trigger item *passes* the event.

The hypothesis algorithm must be applied to pairs of jets. However it is not obvious how to select which pairs of jets should be considered in the M_{CT} calculation. There are two ways in which the L2 trigger can select these pairs. Firstly, all possible combinations of pairs of jets can be passed to the hypothesis algorithm. The trigger is passed if any of these pairs of jets satisfy the hypothesis selection requirements. The trigger items with this version of the algorithm are given the label `anymct`. Secondly, the two highest E_{T} (leading) jets are selected, only if those two jets satisfy the hypothesis selection requirements is the

---

[1] It should be noted that this functionality may be available in the future and work is ongoing in this area.

trigger passed. This version of the trigger is labelled `leadingmct`.

The `leadingmct` algorithm suffers a non-negligible loss of efficiency with respect to the offline selection. This is due to the L2 reconstruction not identifying the same two leading jets as the offline software in a non-negligible fraction of events. However this disadvantage must be balanced against the benefit of this choice which is a significantly lower trigger rate due to the more stringent selection requirement.

5.3.3 M_{CT} trigger chains

In 2011 several variations of the M_{CT} triggers ran online collecting data. During the year the instantaneous luminosity steadily increased to a maximum of ~ 3.6×10^{33} $\mathrm{cm}^{-2}\mathrm{s}^{-1}$ as can be seen in Figure 5.2. This increase in instantaneous luminosity required evolution in the trigger menu including the M_{CT} triggers. Table 5.1 shows which trigger chains were collecting data during each run periods. The rates of each EF trigger for a benchmark instantaneous luminosity of $10^{33}\mathrm{cm}^{-2}\mathrm{s}^{-1}$ are also given for comparison. The relative reduction in the rate of the triggers used for period I onwards is clear. The choice of jet E_{T} thresholds is almost entirely dominated by the available L1 seed items. At each point in time the lowest E_{T} threshold unprescaled di-jet item was chosen.

From Table 5.1 it can be seen that both types of FEX algorithms are used. The rate of the `anymct` algorithm became unmanageable for a sufficiently low M_{CT} threshold, hence the `leadingmct` algorithm was required late in 2011. The high instantaneous luminosity during this period of data-taking meant that an additional $E_{\mathrm{T}}^{\mathrm{miss}}$ requirement at L1 was necessary to keep the rate of the seed item sufficiently low whilst maintaining E_{T} thresholds that were acceptable in terms of signal efficiency.

5.3.4 Trigger Efficiencies

The more coarse energy and direction information and less sophisticated reconstruction algorithms available at trigger level lead to inefficiencies with respect to offline quantities. For example this means that a L1 jet E_{T} threshold of 30 GeV will not become fully efficient or, *turned on*, until about 45-50 GeV in an offline analysis. This also corresponds to a loss in efficiency for M_{CT}. Understanding the efficiency of the trigger with respect to offline as a function of M_{CT} is vital for the use of these triggers in analysis.

Broadly speaking the efficiency can be defined as the number of events that the trigger selects per possible triggered event as a function of some offline quantity. In this case the

Data period	L1 item	L2 items	EF item	Rate [Hz] (at 10^{33} cm^{-2}s^{-1})
A-B	`2J10_J50`	`j70_2j25_anymct150`	`j75_j30_L2anymct150`	5.42±0.68
	`2J10_J50`	`j70_2j25_anymct175`	`j75_j30_L2anymct175`	2.88±0.49
D-J	`2J10_J50`	`j70_2j25_L2anymct100`	`j75_j30_anymct150`	4.72±0.63
			`j75_j30_anymct175`	2.28±0.44
I+	`2J30_XE20`	`2j40_anymct100_xe20`	`2j45_leadingmct100_xe40`	0.42±0.19
	`2J30_XE20`	`2j50_anymct100_xe20`	`2j55_leadingmct100_xe40`	0.33±0.17

Table 5.1: The M_{CT} trigger chains, the run period at which they were taking data and the rates for EF item at an instantaneous luminosity of 10^{33} cm^{-2}s^{-1}.

efficiency is calculated using a *bootstrap* method. This method uses a lower threshold trigger with a well understood efficiency for which the events selected by the trigger whose efficiency is being calculated are always a subset of the events sexlected by this lower threshold *baseline* trigger. Thus, the baseline trigger is chosen as the reference point for comparison. The efficiency of a given trigger is calculated by measuring the fraction of events that pass both the trigger of interest and the baseline trigger to the number of events that pass the baseline trigger,

$$\epsilon = \frac{\text{no. events passing baseline } \textbf{and } M_{\mathrm{CT}} \text{ trigger}}{\text{no. events passing baseline}}. \tag{5.11}$$

This efficiency is calculated for both the `anymct` and `leadingmct` triggers. The choice of offline variable for comparison in order to best understand the trigger performance in each case is not entirely trivial. In the case of `leadingmct` the choice is more clear, one should compare to M_{CT} calculated from the two leading offline jets per event, $M_{\mathrm{CT}}\,(j_1, j_2)$. However, for `anymct` this choice is less obvious as several pairs of jets are considered. After some consideration it becomes clear that one should compare to the maximum M_{CT} of all combinations of pairs of jets in the event, $max(M_{\mathrm{CT}})$. This is analogous to the single jet trigger, the metric of comparison there is the leading jet in the event.

The efficiency plots for each trigger are shown in Figure 5.4. It can be seen that, as expected, the *anymct* trigger is significantly more efficient than the *leadingmct* version for a given M_{CT} threshold.

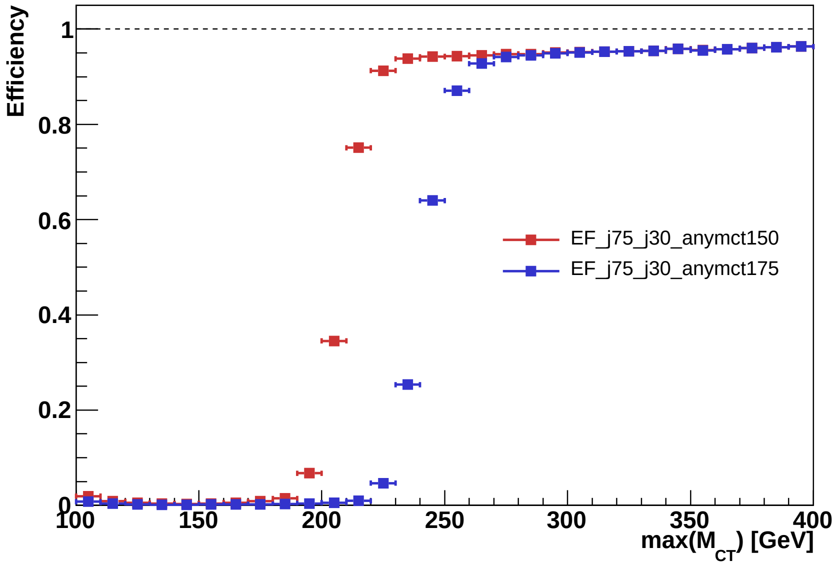

(a)

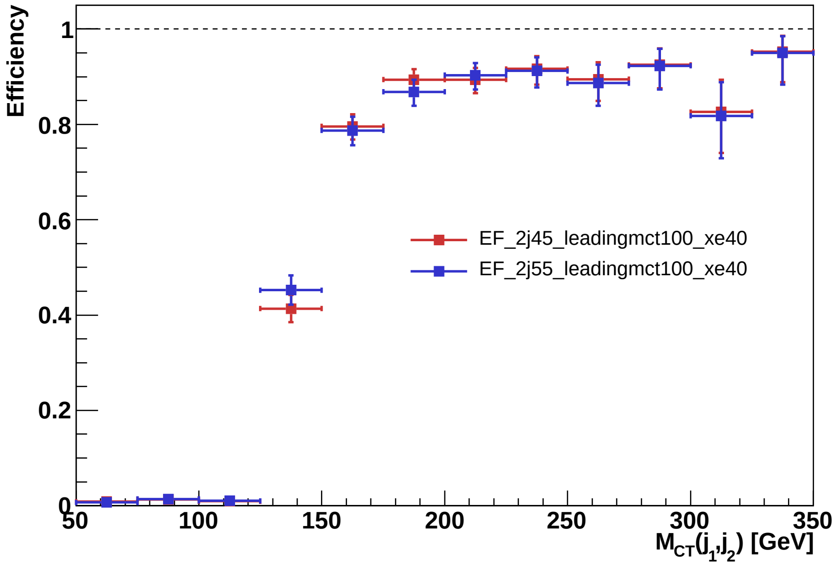

(b)

Figure 5.4: Trigger efficiencies for the *anymct* algorithm (a) and *leadingmct* algorithm (b).

Trigger item	Rate [Hz]
`EF_j75_xe55`	4.24 ±0.60
`EF_j75_j30_anymct150`	4.72 ±0.63
`EF_xe60`	3.29 ±0.53
`EF_j100_ht400`	3.31 ±0.53

Table 5.2: 2011 menu options and corresponding trigger rates at 10^{33} $\mathrm{cm}^{-2}\mathrm{s}^{-1}$.

5.4 SUSY trigger menu optimisation

In developing the M_{CT} trigger proposal it was important to justify applications for these triggers and specifically where they might perform better than the existing SUSY triggers. This meant considering several available trigger choices in the context of a number of potential SUSY signatures and analyses.

Conventional SUSY 0-lepton triggers are based on jets, $E_{\mathrm{T}}^{\mathrm{miss}}$ and combinations thereof. The two main considerations for potential new trigger items are their rate and signal efficiency, especially the relative efficiency of a given item with respect to the baseline trigger.

5.4.1 2011 SUSY inclusive 0-lepton menu optimisation

In early 2011 two SUSY scenarios were the focus of the 0-lepton searches, the mSUGRA $m_0 - m_{1/2}$ plane and the pMSSM $m_{\tilde{q}} - m_{\tilde{g}}$ plane.

Table 5.2 shows a selection of new trigger possibilities and their rates which were considered in the 2011 menu optimisation. `EF_j75_xe55` is the nominal choice and the *baseline* for comparison to potential new trigger items. Three candidates are selected for comparison; `EF_j75_j30_anymct150` which has been discussed in the preceding section and is focused on di-jet topologies; `EF_xe60`, a pure $E_{\mathrm{T}}^{\mathrm{miss}}$ trigger that for the sacrifice of a higher $E_{\mathrm{T}}^{\mathrm{miss}}$ threshold gives access to final states with lower jet p_{T}; `EF_j100_ht400` a trigger based on H_T, the scalar sum of jet p_{T}s in the event. This allows access to multi-jet topologies with potentially lower $E_{\mathrm{T}}^{\mathrm{miss}}$.

The two signal grids mentioned above were used for the trigger menu optimisation. The signal efficiencies across the mSUGRA plane for each trigger item are shown in Figure 5.5. It is most instructive to consider the unique gain in efficiency with respect to the baseline option, this is defined as the fraction of signal events selected by a new trigger item and not by the baseline. Figures 5.6(a-c) show this additional efficiency gain for each

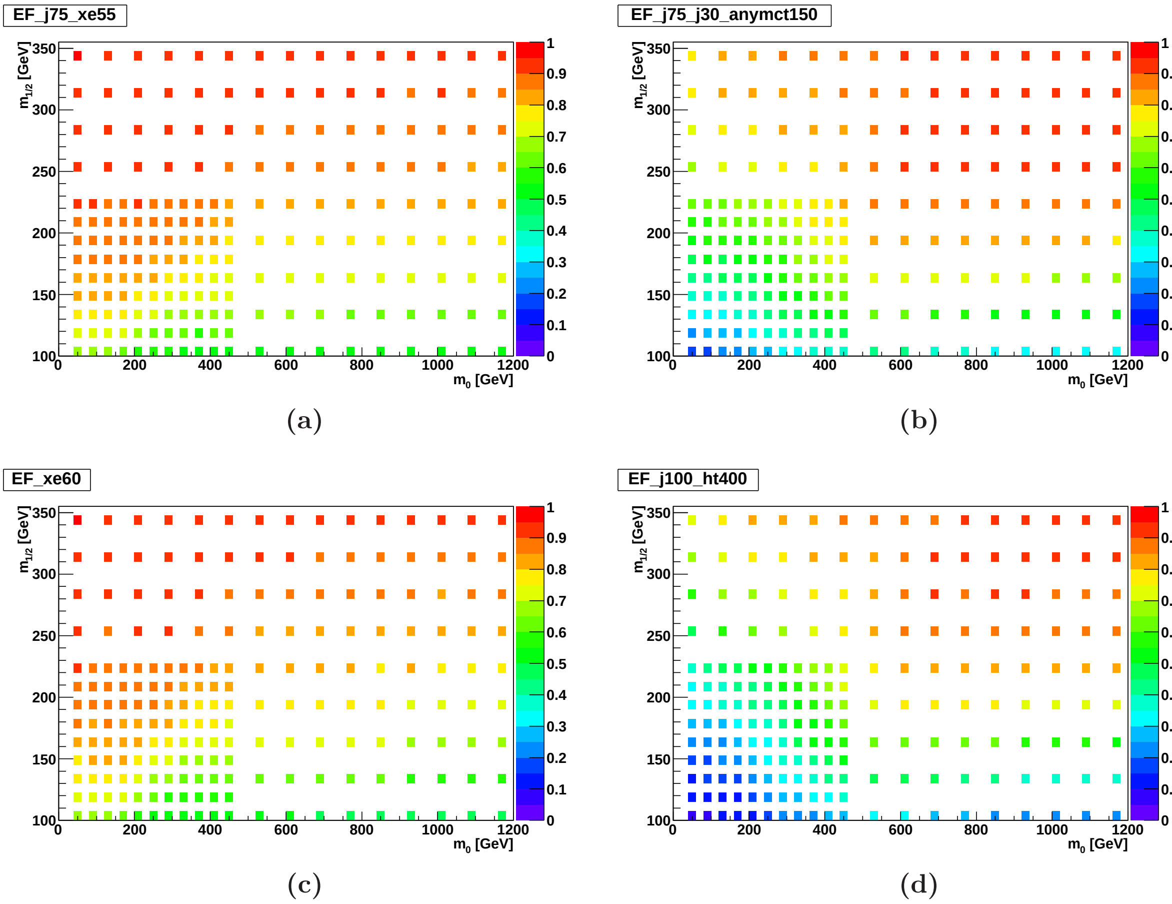

(a) **(b)**

(c) **(d)**

Figure 5.5: Signal efficiency across mSUGRA mass plane for (a) baseline `EF_j75_xe55`, (b) `EF_j75_j30_anymct150`, (c) `EF_xe60` and (d) `EF_j100_ht400`.

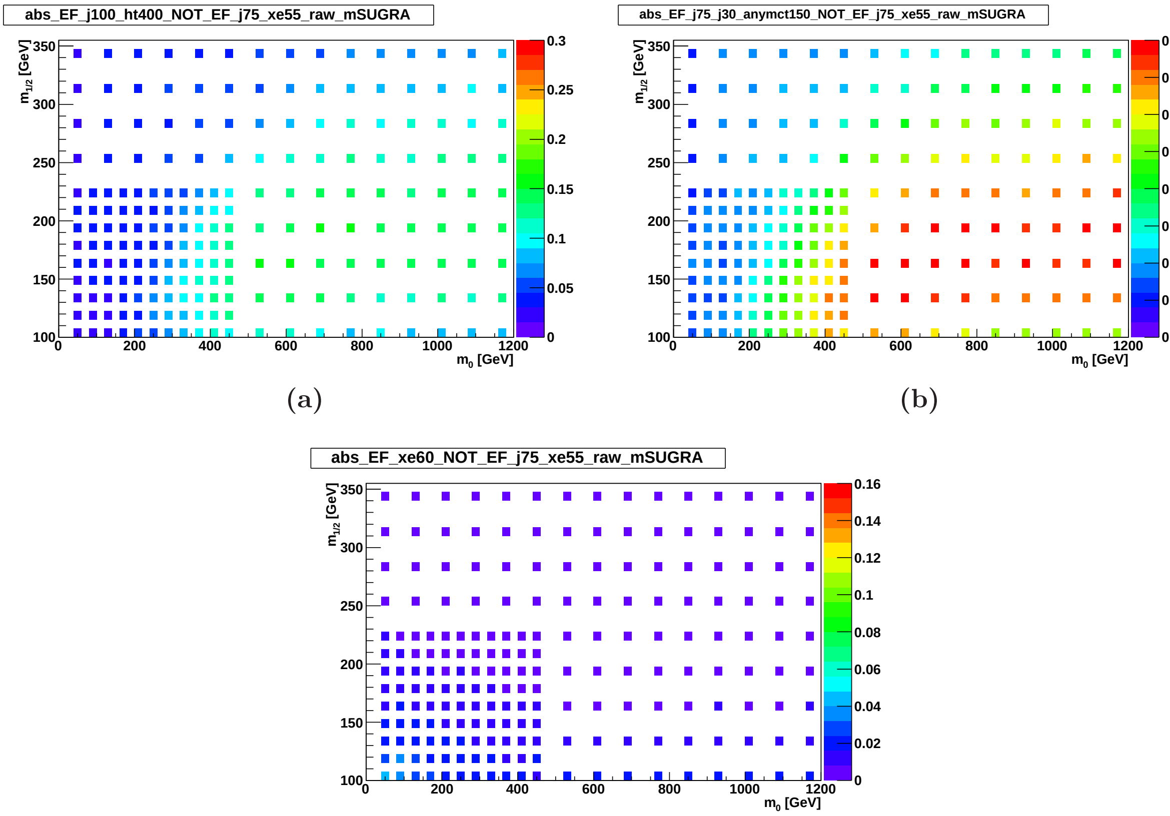

(a) **(b)**

(c)

Figure 5.6: Fractional gain in efficiency for individual items with respect to baseline trigger.

Trigger item	Rate [Hz]
`EF_b10_j75_j55_2j30`	17.7 ±3.0
`EF_b15_j100_j40_EFxe30`	12.9 ±2.5
`EF_b15_j100_j40_ht300`	9.2 ±2.1
`EF_b75_j100_EFxe20_ht200`	7.7 ±1.9
`EF_b75_j100_ht300`	6.3 ±1.8
`EF_b75_j100_EFxe30`	6.2 ±1.7
`EF_b15_4j45`	3.9 ±1.4
`EF_b15_j75_j40_xe50`	1.91 ±0.96
`EF_b15_2j55_xe50`	0.98 ±0.69
`EF_2b10_j75_2j30`	10.6 ±2.3
`EF_2b15_3L1J15`	7.8 ±2.0
`EF_2b10_4j30`	6.8 ±1.8
`EF_2b10_4j40`	2.5 ±1.1
`EF_2b15_4L1J15`	1.88 ±0.94
`EF_2b15_j75_j40_EFxe30`	0.47 ±0.47
`EF_2b15_j75_j40_ht350`	0.47 ±0.47

Table 5.3: 2012 menu options and corresponding trigger rates at 10^{34} cm^{-2}s^{-1}.

trigger item with respect to the baseline, `EF_j75_xe55`. Figure 5.6(d) shows the combined efficiency of a logical *or* between all items (excluding `EF_j75_j30_anymct150`), comparing this to Figure 5.5(a) one can see clearly the gain in signal efficiency, especially in the large m_0 low $m_{1/2}$ region.

5.4.2 2012 SUSY with b-jets 0-lepton menu optimisation

In 2012 trigger menu optimisation was particularly important for 0-lepton SUSY searches with b-jets. For 2011 most analyses had relied on the baseline jet+$E_{\mathrm{T}}^{\mathrm{miss}}$, `EF_j75_xe55`, trigger. However, with the increased instantaneous luminosity in 2012 the jet E_{T} and $E_{\mathrm{T}}^{\mathrm{miss}}$ thresholds were expected to increase significantly to maintain an acceptable trigger rate. With these higher thresholds it was important to assess alternative trigger options. Given that the signal is expected to contain real b-jets, exploiting this at trigger level provides an interesting possibility to reduce trigger rates and lower thresholds.

Table 5.3 shows several possible jet, $E_{\mathrm{T}}^{\mathrm{miss}}$, b-jet and H_T trigger combinations and their respective rates at an instantaneous luminosity of 10^{34} cm^{-2}s^{-1}. This acts as a guide for what trigger items could be allowable - as with 2011 a rate of ~1-2 Hz per item is feasible.

Trigger item	Offline selection [GeV]
`EF_j100_xe65`	$p_{\mathrm{T}}(j_0) > 150$, $E_{\mathrm{T}}^{\mathrm{miss}} > 200$
`EF_xe80`	$E_{\mathrm{T}}^{\mathrm{miss}} > 250$
`EF_b15_4j30_ht350`	$p_{\mathrm{T}}(b_0) > 50$, $p_{\mathrm{T}}(j_3) > 70$, $H_T > 500$
`EF_b15_j75_4j30_ht350`	$p_{\mathrm{T}}(b_0) > 50$, $p_{\mathrm{T}}(j_0) > 130$, $p_{\mathrm{T}}(j_3) > 50$, $H_T > 500$
`EF_b15_j75_4j30_xe30`	$p_{\mathrm{T}}(b_0) > 50$, $p_{\mathrm{T}}(j_0) > 130$, $p_{\mathrm{T}}(j_3) > 50$, $E_{\mathrm{T}}^{\mathrm{miss}} > 100$
`EF_2b15_j75_3j40_xe30`	$p_{\mathrm{T}}(b_1) > 50$, $p_{\mathrm{T}}(j_0) > 130$, $p_{\mathrm{T}}(j_2) > 50$, $E_{\mathrm{T}}^{\mathrm{miss}} > 100$

Table 5.4: 2012 menu options. Rates 5×10^{33} cm^{-2}s^{-1}.

In contrast to the studies performed in 2011, offline rather than trigger quantities are used to assess the various trigger combinations. This allows more flexibility and removes turn-on effects by applying offline thresholds that correspond to the full efficiency points of the trigger.

The trigger items chosen for comparison are given in Table 5.4 along with the corresponding offline cuts required to emulate the triggers at full efficiency. In order to determine the worth of these triggers their performance is assessed in three key SUSY with b-jets signal scenarios. These are simplified model grids for sbottom and stop quark production. Specifically, gluino-mediated sbottom production, $\tilde{g} \to b\tilde{\chi}_1^0$; sbottom pair production, with the sbottoms decaying $\tilde{b} \to b\tilde{\chi}_1^0$ with BR=100%; and $\tilde{t}$ pair production, with the stops decaying $\tilde{t} \to t\tilde{\chi}_1^0$ with BR=100%. These signal scenarios are described in more detail in Chapter 7.

The trigger selection that provides the best signal efficiency at each point on each of the three SUSY signal grids is shown on the left of Figure 5.7. The relative gain in efficiency compared to the baseline selection at each point on the signal grids is shown on the right hand side of Figure 5.7 for the following selection

$$p_{\mathrm{T}}(b_0) > 50\mathrm{GeV}, p_{\mathrm{T}}(j_0) > 130\mathrm{GeV}, p_{\mathrm{T}}(j_3) > 50\mathrm{GeV}, E_{\mathrm{T}}^{\mathrm{miss}} > 100\mathrm{GeV}. \tag{5.12}$$

From Table 5.3 it is clear that selecting events with b-jets at trigger level can provide the rate reduction required to relax other aspects of the trigger selection. Figure 5.7 demonstrates that these low thresholds can lead to improved signal efficiency with respect to the baseline trigger. It is especially clear in the small mass splitting regions where one expects softer jets and $E_{\mathrm{T}}^{\mathrm{miss}}$ that these lower thresholds can significantly increase signal efficiency.

As a result of this work the trigger items shown in Table 5.5 were included in the

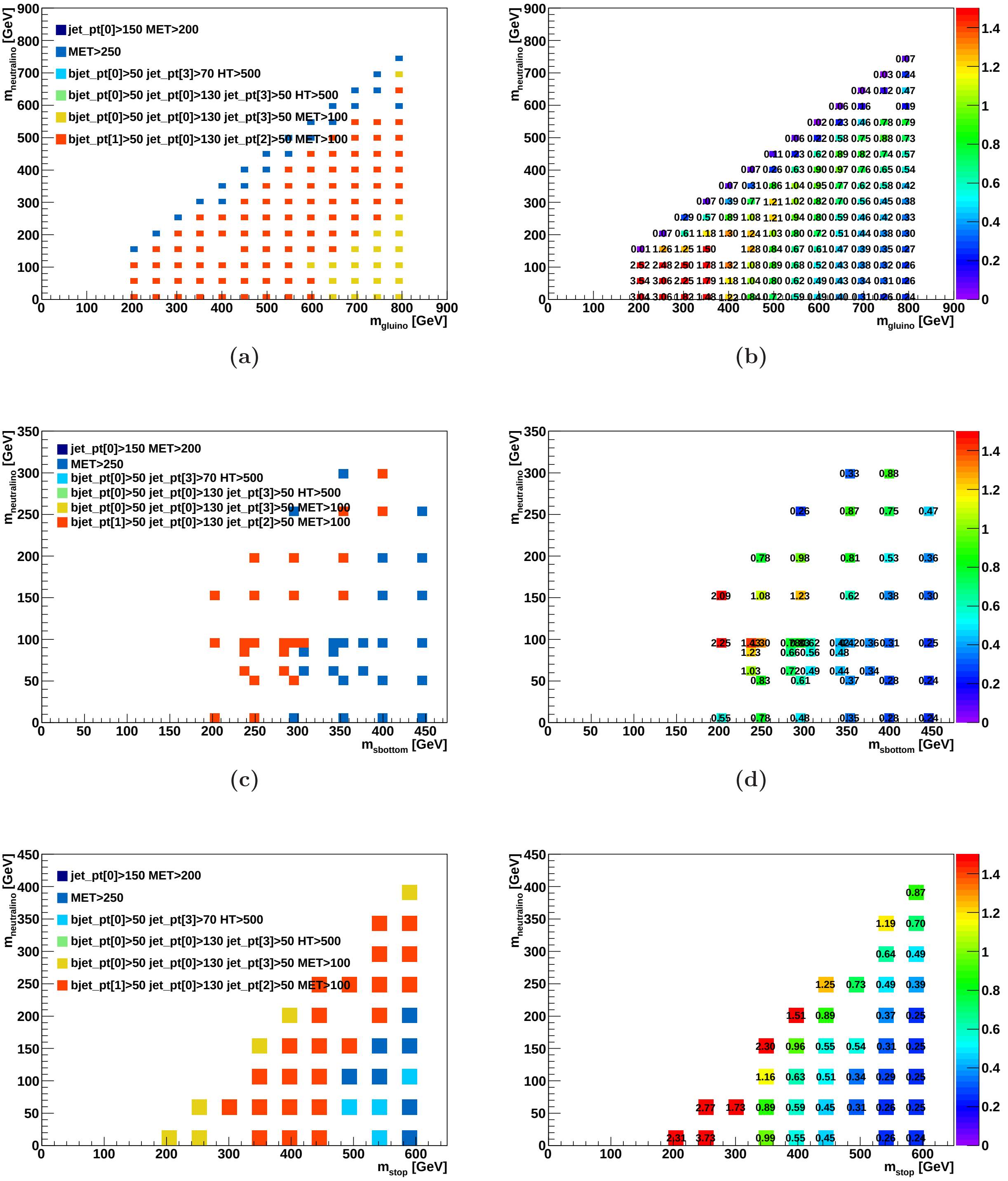

(a) (b)

(c) (d)

(e) (f)

Figure 5.7: (a,c,e) Selection giving the highest signal efficiency for the gluino-sbottom, sbottom pair and stop pair grids respectively. (b,d,f) Relative increase in efficiency compared to baseline for $p_{\mathrm{T}}(b_0) > 50$ GeV, $p_{\mathrm{T}}(j_0) > 130$ GeV, $p_{\mathrm{T}}(j_3) > 50$ GeV, $E_{\mathrm{T}}^{\mathrm{miss}} > 100$ GeV for the same signal grids.

Trigger item	Rate [Hz]
`EF_2b45_loose_j145_j45_EFxe40`	1.91±0.95
`EF_b110_loose_j110_xe55`	2.9 ±1.2
`EF_b110_loose_j110_xe60`	2.4 ±1.1
`EF_b145_medium_j145_ht400`	2.9 ±1.2
`EF_b165_medium_j165_ht500`	1.93±0.97
`EF_b35_loose_j110_2j35_EFxe80`	1.48±0.85
`EF_b45_mediumEF_j110_j45_xe60`	5.9 ±1.7
`EF_b45_medium_j145_j45_ht400`	5.3 ±1.6
`EF_b45_medium_j145_j45_ht500`	3.9 ±1.4
`EF_b55_mediumEF_j110_j55_xe60`	4.9 ±1.6
`EF_b80_loose_j80_xe55`	7.3 ±1.9
`EF_b80_loose_j80_xe60`	4.4 ±1.5

Table 5.5: 2012 menu options. Rates 10^{34} cm^{-2}s^{-1}.

trigger menu during 2012 data-taking.

Chapter 6

Search for $t\bar{t}$+Z production

6.1 Introduction

In this Chapter a search for production of $t\bar{t}$ in association with a Z boson in the 3-lepton final state is presented. The analysis uses 4.7 fb^{-1} of pp collision data collected in 2011 at $\sqrt{s} = 7$ TeV. In the targeted 3-lepton final state the Z boson is required to decay to a pair of leptons and one top quark to decay leptonically whilst the other decays hadronically. This is the first such search performed by ATLAS.

The author initiated this analysis and made major contributions to many aspects of it. This includes generation of the $t\bar{t}+Z$ signal and several background simulated samples and development of a system for estimation of generator systematic uncertainties as discussed in §6.5.1. This analysis was published in a conference note [1] which the author co-edited.

6.2 Theoretical motivation

The LHC is often described as a *"top quark factory"* [141, 142] with several million $t\bar{t}$ pairs having already been produced during 2011 and 2012 data-taking. As such, one of the principal goals of the LHC is to measure the properties of the top quark.

The properties of the top quark are interesting for many reasons. Due to its large mass and Yukawa coupling close to unity the top quark is expected to play a key role in electroweak symmetry breaking (EWSB). New physics associated with mass generation is more likely to manifest itself in the top quark sector than the lighter fermions. Several models exist that predict new particles or interactions that preferentially couple to the top quark [141]. As the top quark provides the largest contribution to quadratic divergences in corrections to the Higgs mass new physics is expected for a *natural* theory at $\sim m_t$. The top quark's large mass also opens up phase space for decay to exotic heavy states, for example Z'. The fact that the lifetime of the top $(0.5 \times 10^{-24}$ s) is shorter that the QCD interaction time ($\sim 10^{-23}$ s) means that it offers the unique opportunity to study the properties of a *bare* quark; couplings, mass and spin. Several such measurements have already been performed and are reviewed in [115, 141–143].

Since the discovery of the top quark almost two decades ago, electroweak couplings of the top quark to other SM particles have been explored at the Tevatron and LHC. These couplings can take different values in a number of BSM scenarios, such as technicolor [144] or Little Higgs [145] models. Direct measurement of electroweak couplings to the top quark can be probed in several ways, but predominantly via measurements of single top production and $t\bar{t}$ and vector boson associated production. The tbW coupling can be studied through cross section measurements of single top quarks [146–149]. Measurement of the $t\bar{t}\gamma$ cross section, can also provide a direct probe of the $tt\gamma$ coupling. Measurement of this process has been undertaken at the Tevatron [150, 151], and more recently at the LHC [152]. The CDF Collaboration has claimed 3σ evidence for $t\bar{t}\gamma$ production [151]. The $t\bar{t}+W$ process does not depend on the details of the top sector since the accompanying W boson is radiated from the initial state quarks. However, $t\bar{t}+Z$ production can directly probe the ttZ coupling.

Electroweak precision data from LEP [153–155] imposes rather strong indirect bounds on the coupling of top quarks to the Z boson. However no direct measurements of this coupling currently exist. It should be noted that the ttZ coupling cannot be constrained through measurements of $t\bar{t}$ production at hadron colliders via intermediate virtual Z bosons as the $pp \to t\bar{t}$ cross section is overwhelmed by contributions from purely QCD processes.

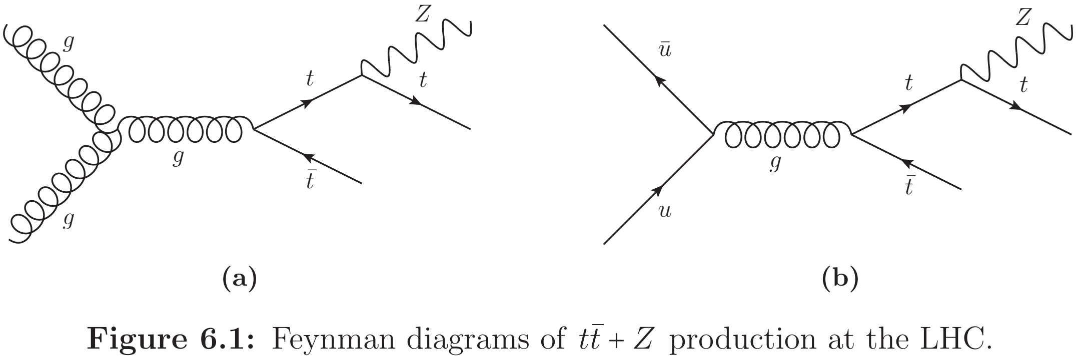

(a) (b)

Figure 6.1: Feynman diagrams of $t\bar{t}+Z$ production at the LHC.

The prospects for measurements of the ttZ coupling at hadron colliders using the $t\bar{t}+Z$ process were studied in [154, 156, 157]. The cross section for the $t\bar{t}+Z$ process is too low to have been observable at the Tevatron, hence the LHC offers a new and unique window to view this process.

The cross section for $t\bar{t}+Z$ production at $\sqrt{s}$ = 7 TeV is calculated at next-to-leading order (NLO) to be 0.14 pb [158, 159]. The k-factor, defined as the ratio of NLO and LO cross sections, is found to be 1.35 at a 14 TeV centre-of-mass energy [160], with a theoretical uncertainty of approximately 20%.

The CMS collaboration recently presented a preliminary measurement of the $t\bar{t}+Z$ cross section [161], finding $\sigma_{t\bar{t}Z} = 0.30\ ^{+0.14}_{-0.11}$ (stat) $^{+0.04}_{-0.02}$ (syst) pb with a significance of 3.66 standard deviations from the background hypothesis.

6.3 Selection

The following chapter uses the *Top-2011* object definitions. In order to select events consistent with the $t\bar{t}+Z$ final state under consideration, precisely three leptons are required. Of these three leptons one is required to have satisfied the single lepton trigger selection criteria. Additionally one opposite sign same flavour (OSSF) lepton pair is required to have an invariant mass close to m_Z (= 91.2 GeV), $|m_{l^+l^-} - m_Z| < 10$ GeV and hence be consistent with a Z boson. In the case where multiple such pairs exist, the pair whose invariant mass is closest to m_Z is assumed to be the one coming from the Z boson in what follows. Furthermore, the remaining objects in the event are required to be consistent with a $t\bar{t}$ pair in the semi-leptonic decay mode. Therefore, events must contain four jets with $p_{\mathrm{T}} > 30$ GeV and $E_{\mathrm{T}}^{\mathrm{miss}} > 30$ GeV. The signal region, denoted SR, is finally defined by the requirement that at least one of the selected jets is tagged by the MV1 algorithm. The signal is expected to contain two real b-jets in the final state. However, due to the low signal efficiency, the compounding b-tagging efficiency and already very small remaining SM background, the requirement of two b-jets leads to worse signal significance than the one b-jet requirement. Table 6.1 shows both the relative and absolute efficiencies of each cut for the simulated $t\bar{t}+Z$ sample.

To validate the MC modelling of the 3-lepton final state several control regions are defined with a somewhat looser selection than that of the signal region. Every control region must contain three leptons, two of which must form an OSSF pair and $E_{\mathrm{T}}^{\mathrm{miss}} > 30$ GeV. No requirement on the invariant mass of the OSSF pair of leptons is applied. The separate

Cut number		Relative efficiency [%]	Absolute efficiency [%]
C0	3 leptons	15.0	15.0
C1	OSSF lepton pair	100.0	15.0
C2	$E_{\mathrm{T}}^{\mathrm{miss}} > 30$ GeV	83.2	12.5
C3	4 jets $p_{\mathrm{T}} > 30$ GeV	42.1	5.2
C4	$\lvert m_{l^+l^-} - m_Z\rvert < 10$ GeV	98.6	5.2
C5	1 b-jet $p_{\mathrm{T}} > 30$ GeV	87.7	4.5

Table 6.1: The relative efficiency, with respect to the previous cut, and the absolute efficiency of all previous cuts is shown for the simulated $t\bar{t} + Z$ sample. C0 includes jet quality and trigger requirements. Only events with three leptons in the final state, resulting from decays of type $t\bar{t}(\to q\bar{q}'b\bar{b}l\nu)Z(\to ll)$, where l denotes e, μ, or a τ decaying into e or μ, are considered.

control regions are then defined by jet multiplicity requirements, control regions CRk (with $k = 1, \ldots, 3$) require events to contain precisely k jets with $p_{\mathrm{T}} > 30$ GeV and CR4Inc requires 4 jets or more with $p_{\mathrm{T}} > 30$ GeV. One additional, slightly looser, inclusive control region where two or more jets are required, CR2Inc, is defined for the purpose of having increased statistics with which to allow comparison of relevant distributions.

Table 6.2 shows the expected and observed numbers of events in CRk $(k = 1, \ldots, 4)$. Good agreement is observed between data and simulation. The control regions are dominated by the WZ+jets process. Figures 6.2 and 6.3 show the expected and observed distributions in CR2Inc for several important variables. For all distributions, good agreement is observed between data and simulation.

6.4 Backgrounds

There are few non-signal SM processes which give rise to three leptons in the final state and fewer still that contain additional jets. The dominant processes, for the signal region defined in Section 6.3, are the ‘singly resonant’ production of $t\bar{b}Z + X$ and $\bar{t}bZ + X$ with $X = jj, l\nu$ along with ‘non-resonant’ WZ+jets and ZZ+jets backgrounds. The backgrounds from these processes are estimated from Monte Carlo simulation.

Dedicated simulated samples for these backgrounds were generated for this analysis using `MADGRAPH` interfaced with `PYTHIA`. Specifically, the $(t\bar{b}Z + X$ and $\bar{t}bZ) + X(= jj, l\nu)$ processes and $WZb\bar{b}jj$ sample was generated additionally to the inclusive samples.

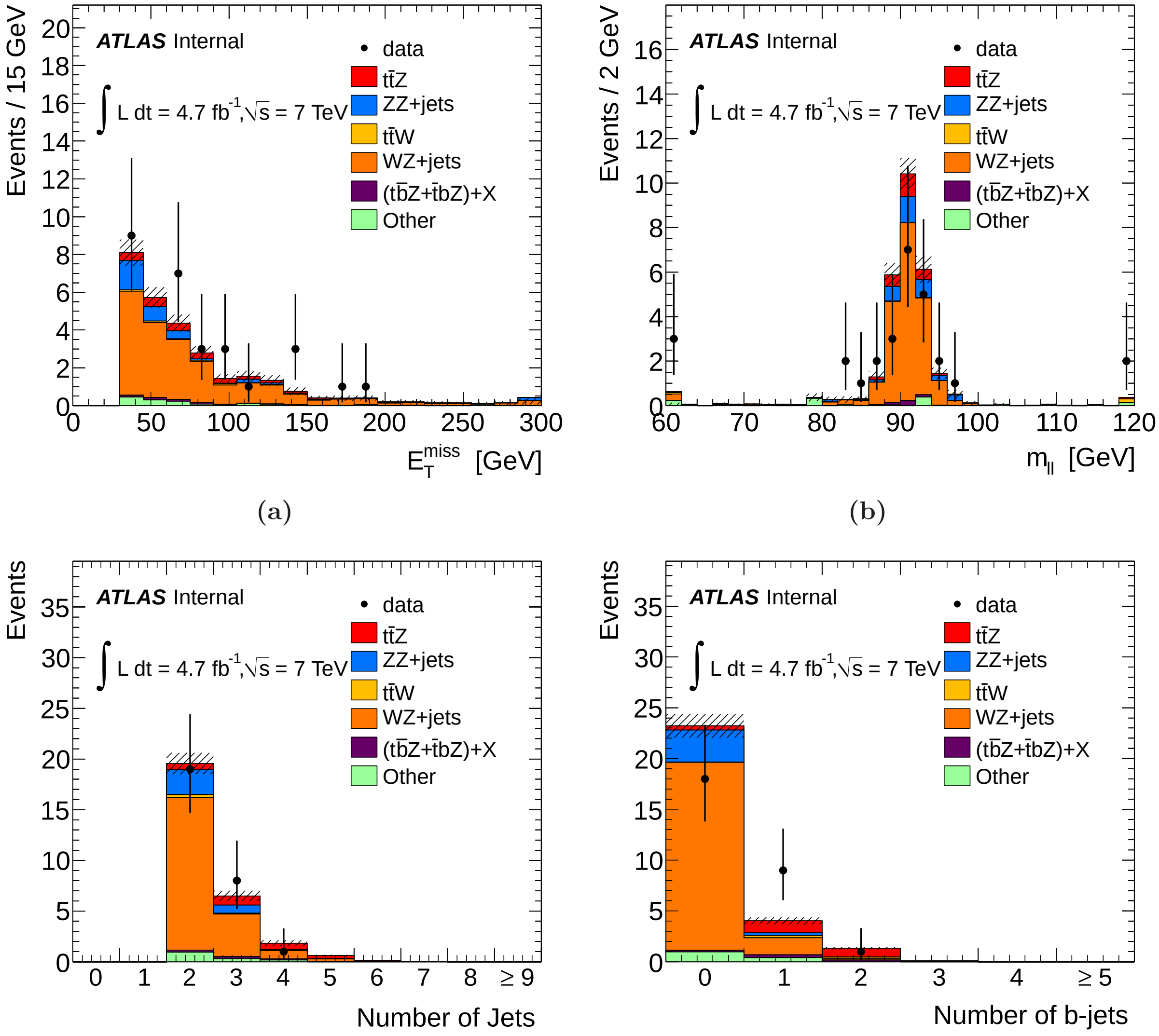

(a) (b)

(c) (d)

Figure 6.2: Expected and observed distributions of (a) $E_{\mathrm{T}}^{\mathrm{miss}}$, (b) the invariant mass of the OSSF pair of leptons, (c) the number of jets with $p_{\mathrm{T}} > 30$ GeV and (d) the number of b-tagged jets with $p_{\mathrm{T}} > 30$ GeV. Figures from [1].

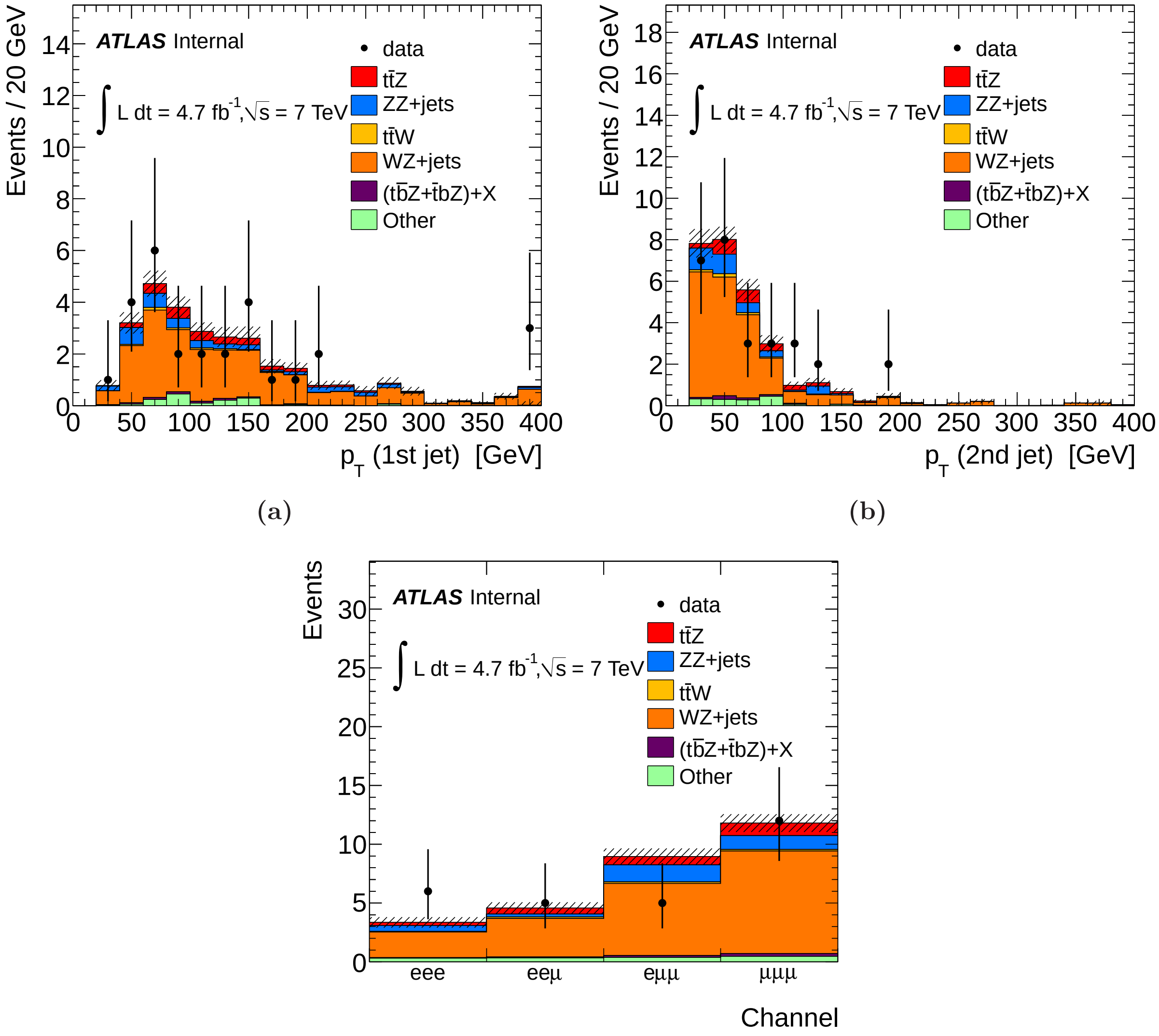

(a)

(b)

(c)

Figure 6.3: Expected and observed distributions of (a) the p_{T} of the hardest jet, (b) the p_{T} of the second hardest jet and (c) the lepton flavour combination. Figures from [1].

	CR1	CR2	CR3	CR4
$t\bar{t}+Z$	0.20 ± 0.02	0.63 ± 0.03	0.91 ± 0.04	1.04 ± 0.04
$t\bar{t}$	2.0 ± 0.3	0.64 ± 0.15	0.28 ± 0.13	< 0.07
Z+jets	0.4 ± 0.2	0.3 ± 0.2	< 1.2	0.2 ± 0.2
WZ+jets	44.5 ± 1.7	14.7 ± 1.0	4.0 ± 0.4	0.98 ± 0.19
ZZ+jets	6.3 ± 0.7	2.4 ± 0.4	0.77 ± 0.19	0.17 ± 0.06
$t\bar{t}W$	0.21 ± 0.04	0.33 ± 0.04	0.09 ± 0.02	0.032 ± 0.013
$(t\bar{b}Z+\bar{t}bZ)+jj,l\nu$	0.122 ± 0.013	0.203 ± 0.016	0.192 ± 0.016	0.155 ± 0.015
$WZbbjj$	0.14 ± 0.02	0.25 ± 0.03	0.21 ± 0.03	0.11 ± 0.02
Observed	53	19	8	1
MC Total	53.9 ± 1.9	19.5 ± 1.1	6.5 ± 0.5	2.7 ± 0.3

Table 6.2: Numbers of events observed in data and expected from the $t\bar{t}$+Z signal process and various backgrounds for the control regions CR1-4. Uncertainties shown are statistical only.

It was shown in the previous section that the WZ+jets process with three leptons in the final state is well described by simulation, by comparisons with data in control regions CR1-4.

6.4.1 Fake lepton background

In addition to backgrounds with three real leptons, there is also a background contribution from processes that have fewer than three real leptons and one or more fake leptons. In this case a 'real' lepton refers to a lepton arising from W or Z decay, a 'fake' lepton refers to those from all other sources, including in-flight decays of light or heavy hadrons, hadrons mimicking lepton signatures, and converted photons reconstructed as electrons. In a low yield multi-lepton signal region where standard model backgrounds are expected to be small, constraining the background due to events containing fake leptons is especially important.

The fake lepton background arises primarily from events with two real leptons and one additional fake lepton. These contributions can be separated into two components. Firstly, $t\bar{t}$ events in which both top quarks decay leptonically, giving two real leptons, and a third isolated lepton that could for example come from the decay of one of the b-quarks. Such an event would pass the signal region selection requirements described in Section 6.3. Secondly, events containing a real Z boson decay to a pair of leptons with one additional fake lepton arising from a jet that is mistakenly reconstructed as a lepton. These two fake lepton background contributions are estimated separately and are combined to give the final estimation of the fake lepton background contribution to the signal region.

Matrix method

Estimation of the background contribution arising from fake leptons can be provided by using the *matrix method* [162]. This method works by dividing the dataset into two categories based on *loose* and *tight* lepton definitions. The tight lepton requirements are the ones described in Section 4.3 for the *Top-2011* selection. Loose leptons have relaxed identification criteria and/or isolation requirements.

Loose electrons are defined by changing the identification criteria from the "tight" to the "medium" of [110]. The isolation requirement is relaxed such that the energy in a cone of $\Delta R = 0.2$ as well as the sum of track transverse momenta in a cone of $\Delta R = 0.3$ around the electron are required to be less than 6 GeV. The loose muon definition is identical to that of tight muons, except that the isolation requirement is removed.

For clarity we shall describe the matrix method in its simplest form where the estimation of the fake lepton contribution in a single lepton sample is undertaken. However, the method can readily be generalised for estimation of the fake lepton contribution with any number of leptons in the final state.

The method relies on determination of the real and fake efficiencies, ϵ_{real} and ϵ_{fake}, from dedicated control samples. More specifically, the efficiencies for real or fake loose leptons to also satisfy the tight criteria is defined as

$$\epsilon_{\text{real}} = \frac{N_{\text{real}}^{\text{tight}}}{N_{\text{real}}^{\text{loose}}} \quad , \quad \epsilon_{\text{fake}} = \frac{N_{\text{fake}}^{\text{tight}}}{N_{\text{fake}}^{\text{loose}}}, \tag{6.1}$$

where $N_{\text{real}}^{\text{tight}}$ and $N_{\text{fake}}^{\text{tight}}$ are the numbers of real and fake lepton events passing the tight selection criteria. The real lepton efficiency ϵ_{real} is measured using a control region consisting of events with a Z boson decaying to two leptons. The fake lepton efficiency ϵ_{fake} is measured from control regions, where the contribution of fake leptons is significantly higher. For electrons, the control region used for measuring fake rates is defined by requiring $E_{\text{T}}^{\text{miss}} < 20$ GeV, and the presence of at least one jet. For muons, the cuts $m_T(l, E_{\text{T}}^{\text{miss}}) < 20$ GeV and $E_{\text{T}}^{\text{miss}} + m_T(l, E_{\text{T}}^{\text{miss}}) < 60$ GeV, together with requiring the presence of one jet, are used to define the control region.

From these efficiencies one is able to obtain the following relations in the single lepton case. The number of events which contain one loose lepton that does not pass the tight criteria can be written as

$$N_L = (1 - \epsilon_{\text{real}})N_{\text{real}}^{\text{loose}} + (1 - \epsilon_{\text{fake}})N_{\text{fake}}^{\text{loose}}, \tag{6.2}$$

where $N_{\text{real}}^{\text{loose}}$ and $N_{\text{fake}}^{\text{loose}}$ are the number of events containing real and fake leptons that pass the loose lepton requirements, and the number of events selected using the tight lepton requirements can be written as

$$N_T = \epsilon_{\text{real}}N_{\text{real}}^{\text{loose}} + \epsilon_{\text{fake}}N_{\text{fake}}^{\text{loose}}. \tag{6.3}$$

The two previous relations may be represented in the form of a two dimensional matrix

$$\begin{pmatrix} N_{\text{T}} \\ N_{\text{L}} \end{pmatrix} = \begin{pmatrix} \epsilon_{\text{real}} & \epsilon_{\text{fake}} \\ (1 - \epsilon_{\text{real}}) & (1 - \epsilon_{\text{fake}}) \end{pmatrix} \begin{pmatrix} N_{\text{real}}^{\text{loose}} \\ N_{\text{fake}}^{\text{loose}} \end{pmatrix}. \tag{6.4}$$

One can then invert the matrix to obtain equations for $N_{\text{real}}^{\text{loose}}$ and $N_{\text{fake}}^{\text{loose}}$ in terms of the measurable quantities N_{T}, N_{L}, ϵ_{real} and ϵ_{fake}. Then taking the expression for $N_{\text{fake}}^{\text{loose}}$ and simply rearranging (6.1) one can obtain the number of fake leptons passing the tight selection requirements

$$N_{\text{fake}}^{\text{tight}} = \frac{\epsilon_{\text{fake}}}{\epsilon_{\text{real}} - \epsilon_{\text{fake}}}[\epsilon_{\text{real}}N_L - (1 - \epsilon_{\text{real}})N_T]. \tag{6.5}$$

Estimation of backgrounds arising from fake leptons

1-lepton matrix method for Z+jets background estimate Estimation of the fake lepton background due to events with two leptons originating from the Z boson, which are assumed to be real, and one other isolated lepton is performed using the single lepton matrix method. A loose lepton sample is defined by events containing an OSSF pair of tight leptons (l^+l^-) whose invariant mass satisfies $|m_{l^+l^-} - m_Z| < 10$ GeV, together with a loose lepton that fails the tight requirements. Formula (6.5) is then used to obtain the fake lepton background estimate. No events are found in data in the loose lepton sample. The 68% confidence level (CL) upper limit for a mean of a Poisson distribution with no observed events (from a Neyman confidence interval construction) is 1.14. A conservative limit on the number of Z+jets events with a fake lepton can be estimated by taking $N^{\text{loose}} = 1.14$, $N^{\text{tight}} = 0$, $\epsilon_{\text{fake}} = 0.50$, corresponding to the largest measured fake efficiency as a function of lepton η and p_{T}, and $\epsilon_{\text{real}} = 0.80$, the corresponding real lepton efficiency. The resulting estimate for the number of Z+jets events with three leptons, one of which being a fake, in the signal region is $0.0^{+1.5}_{-0.0}$. A different criterion for loose electrons, in which no isolation requirement is applied, gives an estimate of $0.0^{+0.8}_{-0.0}$ for this background.

Non-Z background estimate The fake lepton background coming from events that do not contain a Z boson candidate is estimate with a *sideband method*. The number of events expected in the signal region is estimated by extrapolating from a control region with identical selection criteria to the signal region except the requirement that an OSSF lepton pair has an invariant mass not compatible with a Z boson, $|m_{l^+l^-} - m_Z| > 10$ GeV. The extrapolation from the control region to the signal region is made using a transfer factor. The transfer factor between the sideband and the signal region is defined as

$$f = \frac{N(|m_{l^+l^-} - m_Z| < 10\text{ GeV})}{N(|m_{l^+l^-} - m_Z| > 10\text{ GeV})}. \tag{6.6}$$

The value of f is calculated using $t\bar{t}$ simulated events (with no jet or $E_{\mathrm{T}}^{\mathrm{miss}}$ requirement to minimise the statistical uncertainty) to be $f = 0.34 \pm 0.09\ (\text{stat.}) \pm 0.03\ (\text{syst.})$. The systematic uncertainty is dominated by the electron efficiency scale factor and jet energy scale uncertainties. No events are found in data in this control region. The number of events expected in the control region from the $t\bar{t}+Z$ signal process and backgrounds with three real leptons is found to be negligible. A 68% CL upper limit of 1.14 on the number of fake lepton background events in the sideband control region is set. The resulting estimate of the fake lepton background (excluding $Z(\rightarrow ll) + X$ events with fake leptons) is $0.0^{+0.4}_{-0.0}$.

The total fake lepton background is given by the sum of the contributions from events with and without a Z boson, giving $0.0^{+1.6}_{-0.0}$ events. This estimate is used for the primary result. However, the remainder of this section outlines several methods for validating the fake background estimate. The justification for this particular choice is that it provides a data driven estimation. This is important due to the MC generator uncertainties that exist, especially in final states that require the presence of several additional partons in order to satisfy the selection criteria.

Methods for validation of the fake lepton background estimate

3-lepton matrix method As previously discussed the matrix method can be extended to estimate the fake contribution for any number of leptons in the final state. For our signal selection requirement of three leptons an eight-dimentional matrix method can be formulated. For each of three leptons (ordered, say, in p_{T}), in a data sample with loose lepton criteria applied, the lepton may either pass the tight selection (T), or the loose but not the tight (L) selection. One then writes

$$\begin{pmatrix} N_{\mathrm{TTT}} \\ N_{\mathrm{TTL}} \\ \dots \\ N_{\mathrm{LLL}} \end{pmatrix} = \mathbf{M} \begin{pmatrix} N_{\mathrm{RRR}} \\ N_{\mathrm{RRF}} \\ \dots \\ N_{\mathrm{FFF}} \end{pmatrix}. \tag{6.7}$$

Here $N_{LLL}, N_{TTL}, \dots$ denote the numbers of events in which the i-th lepton satisfies the tightness criterion T_i (with T_i either L or T), while $N_{RRR}, N_{RRF}, \dots$ denote the numbers of events in the loose sample for which the i-th lepton is real or fake. The matrix $\mathbf{M}$ is then given by

$$\mathbf{M} = \begin{pmatrix} r_1 r_2 r_3 & r_1 r_2 f_3 & \cdots & f_1 f_2 f_3 \\ r_1 r_2 (1 - r_3) & r_1 r_2 (1 - f_3) & \cdots & f_1 f_2 (1 - f_3) \\ \cdots & & & \\ (1 - r_1)(1 - r_2)(1 - r_3) & (1 - r_1)(1 - r_2)(1 - f_3) & \cdots & (1 - f_1)(1 - f_2)(1 - f_3) \end{pmatrix}, \tag{6.8}$$

where r_i and f_i are the real and fake efficiencies for lepton i[1]. The matrix $\mathbf{M}$ can be inverted to obtain $N_{RRR}, N_{RRF}, \dots$ from the measured numbers $N_{LLL}, N_{LLT}, \dots$. The fake lepton background contribution in the signal region can then be computed as the contribution to N_{TTT} from all terms with at least one fake lepton.

Only two events are found in data which satisfy signal region selection but contain three leptons, at least one of which fails the tight selection. The resulting estimate of the fake lepton background is 2.4 ± 1.9 (stat.) ${}^{+1.6}_{-0.4}$ (syst.). The systematic uncertainty is computed from the uncertainty in the fake lepton efficiencies. The method is repeated with an even looser criterion for loose electrons, where no isolation requirement is applied, this gives an estimate of 0.6 ± 0.5 (stat.) for the fake lepton background. No additional events enter the loose sample with the looser requirement. However, a lower value of f results in a smaller central value for the estimate.

Monte Carlo prediction for fake lepton backgrounds The data driven estimates of the fake lepton background can be compared to the estimate purely from Monte Carlo simulation. No events in simulated samples pass the signal region selection, and estimates of $0.0^{+1.2}_{-0.0}$ events for the Z+jets background, and $0.00^{+0.07}_{-0.00}$ for the $t\bar{t}$ background are obtained.

---

[1] Shorthand for $\epsilon_{\mathrm{fake}}(i)$ and $\epsilon_{\mathrm{fake}}(i)$ in the description of the single lepton method.

	CR1	CR2	CR3	CR4
Fakes (DD, 3-lepton MM)	-0 ± 3	-3 ± 2	2 ± 3	2.4 ± 1.9
Fakes (DD, 1-lepton MM)	0.1 ± 1.4	0.5 ± 1.1	-0.1 ± 0.4	-0.16 ± 0.16
Fakes (DD, sideband)	2.0 ± 0.8	1.0 ± 0.6	0.7 ± 0.5	0 ± 0
Fake Background (MC)	2.4 ± 0.4	0.9 ± 0.3	0.30 ± 0.14	0.2 ± 0.2

Table 6.3: The fake background estimates from the data-driven (DD) 3-lepton Matrix Method, 1-lepton Matrix Method, the Z sideband method, and Monte Carlo simulation for the four control regions CRi, $i = 1, \ldots, 4$.

These are compatible with estimates from the data driven methods.

A comparison of estimates of the fake backgrounds in control regions CRi ($i = 1, \ldots, 4$) obtained using the various methods described above is shown in Table 6.3. It can be seen that the estimation from the 3-lepton matrix method and from the purely Monte Carlo simulation driven method are both compatible with each other and compatible with the estimate from the combination of the two single lepton approximation methods, hence validating the method that is used for the fake lepton background estimation in what follows.

6.5 Systematic uncertainties

Several sources of systematic uncertainty effect the predicted number of simulated signal and background events. A discussion of systematic uncertainties common to all analyses is given in §4.4. The affect of these uncertainties and discussion of additional systematic uncertainties that are specific to this analysis only are given in the following section.

The dominant systematic uncertainties in this measurement come from MC statistics, b-tagging, jet energy scale, corrections to e and μ identification and reconstruction efficiencies, jet vertex fraction and MC generator uncertainties. These are summarised in Table 6.4.

6.5.1 MC generator systematics

An additional important systematic uncertainty for this analysis is the MC generator uncertainty. This enters the cross section upper limit calculation through the signal selection efficiency. The uncertainty on the renormalisation scale and factorisation scales are de-

Systematic uncertainty	Background	Signal
Luminosity	4%	4%
b-tagging	5%	5%
e trigger efficiency	2%	<1%
e reco. and identification efficiency	5%	5%
e energy scale	<1%	<1%
e energy resolution	<1%	<1%
μ trigger efficiency	2%	<1%
μ reco. efficiency	2%	2%
μ momentum scale	<1%	<1%
μ momentum resolution	<1%	<1%
Jet energy scale	5%	7%
Jet reco efficiency	<1%	<1%
$E_{\mathrm{T}}^{\mathrm{miss}}$ cell out and soft jet	1%	<1%
$E_{\mathrm{T}}^{\mathrm{miss}}$ pileup	1%	<1%
JVF	5%	6%
Renormalisation & factorisation scale	-	10%
ISR/FSR	-	6%
MC driven background normalisation	50%	-
Total	51%	17%

Table 6.4: Systematic uncertainties in the signal region for $t\bar{t}Z$ signal and background yields estimated from Monte Carlo simulation. The uncertainties are relative to the nominal value and expressed in percent. In cases where asymmetric shifts were obtained for a single systematic uncertainty, the average of the absolute values of the shifts with respect to the nominal value was taken.

termined by considering variations around the nominal value. Dedicated MC samples are generated with the nominal scale fixed at $\mu_R = \mu_F = 2m_t + m_Z$, then with each scale is then varied up and down independently multiplying by a factor of 2 and 0.5, respectively. The largest effect comes from the downward variation of the factorisation scale. The resulting overall uncertainty is 10%, estimated by taking the largest variation in the selection efficiency.

The uncertainty on the signal selection efficiency due to potential Monte Carlo mismodeling of initial and final state radiation (ISR/FSR) is also studied. Alternative MC samples with more or less ISR and FSR activity are produced by varying the Pythia parameters controlling the parton shower (PS). The ISR variations are constrained by the ATLAS measurement of $t\bar{t}$ production with a veto on additional central jet activity in pp collisions [163]. The resulting effect on the signal selection efficiency leads to an overall uncertainty of 6.2% which is used in the final result.

$t\bar{t} + Z$ scale variation systematics

Figure 6.4 shows various kinematic distributions obtained with the scale variations described above. It can be seen from the ratios that the variation around the nominal value is most apparent in the jet p_T distribution.

Figure 6.5 shows the number of events remaining after each of the analysis cuts and the corresponding percentage differences are shown in Table 6.5. One can see that the largest difference comes from the downward variation of the factorisation scale where at the 4-jet requirement the efficiency is ~ 7% lower than the nominal value and this grows to ~ 10% after the full selection is applied.

$t\bar{t} + Z$ ISR/FSR variation systematics

Monte Carlo samples were generated for different ISR, FSR and PS variations of parameters in `PYTHIA`. These samples correspond to variations of the following parameters in `PYTHIA`:

- PARP(64): Multiplicative factor for the transverse momentum evolution scale for use as a scale in α_s and parton distributions.
- PARP(67): Multiplicative factor for the Q^2 scale of the hard scattering to define the maximum parton virtuality allowed in Q^2-ordered space-like showers.
- PARP(72): Λ value used in running α_s for time-like parton showers, except for showers in the decay of a resonance.

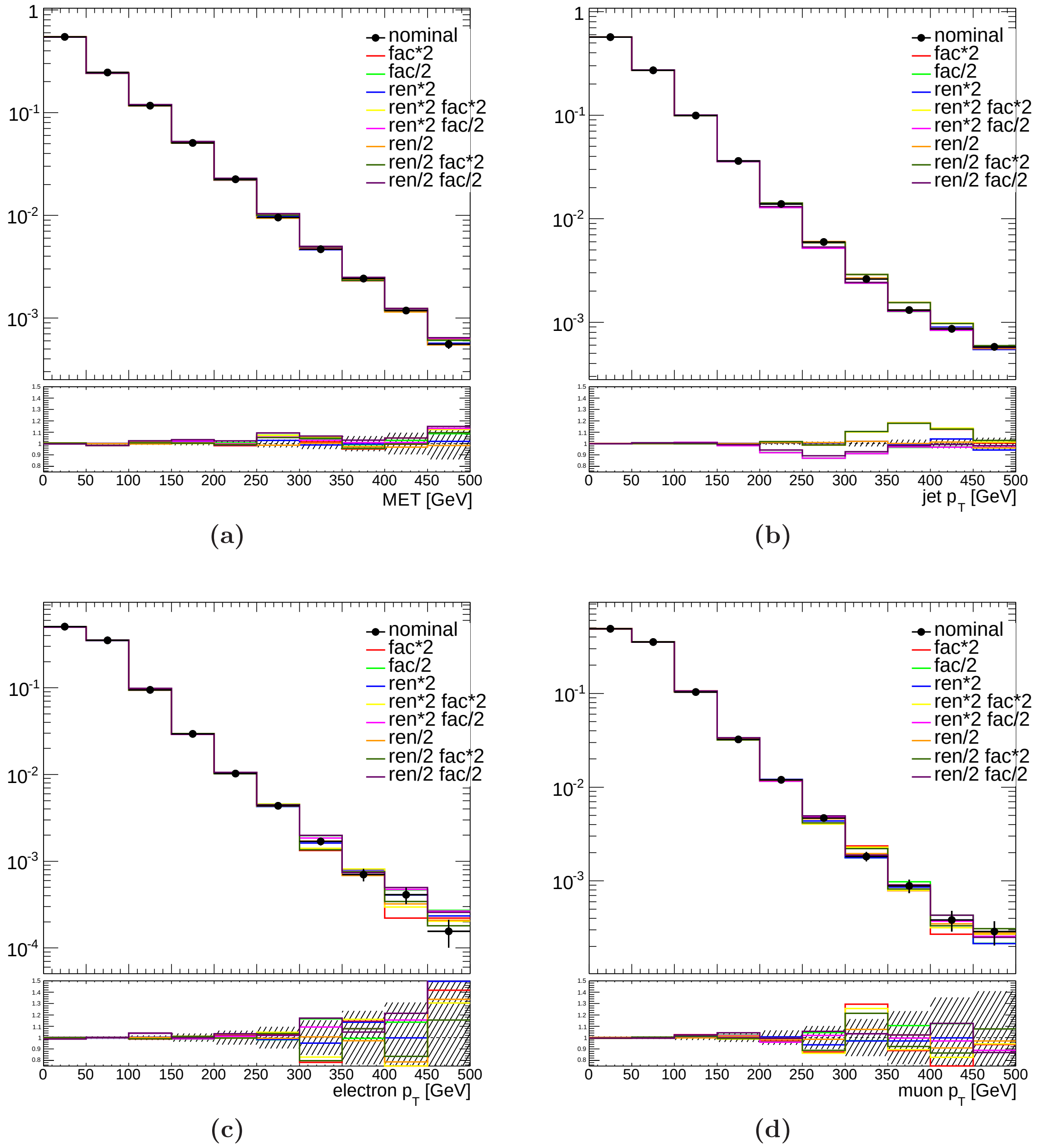

(a) **(b)**

(c) **(d)**

Figure 6.4: Kinematic distributions with scale variations compared to the distribution for the nominal fixed scale for the $t\bar{t}+Z$ signal sample. The hatched area on the ratio histogram shows the expected statistical uncertainty from the limited size of generated samples.

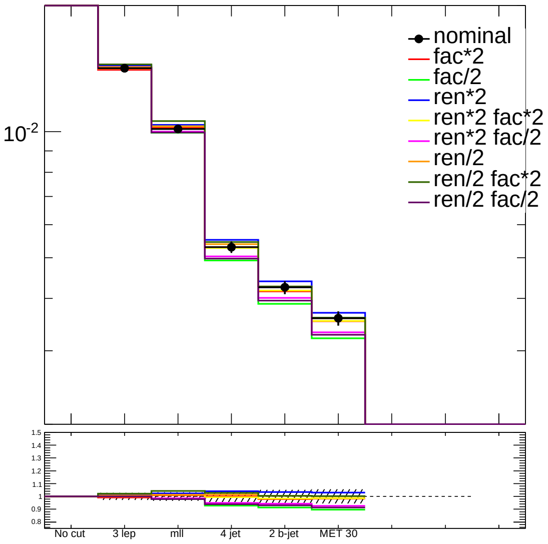

Figure 6.5: Fraction of the total number of events passing each stage of signal selection for several scale variations. The hatched area on the ratio histogram shows the expected statistical uncertainty from the limited size of generated samples.

- PARJ(82): Invariant mass cut-off, m_{min}, of parton showers, below which partons are not assumed to radiate.

Dedicated samples are used to compare selection efficiencies for the various samples. Figure 6.6 shows kinematic distributions obtained with the ISR/FSR/PS variations mentioned above. Figure 6.7 shows the number of events remaining after each of the analysis cuts and the corresponding percentage differences are shown in Table 6.6. One can see that the largest difference comes from the PS variation where, from the 4-jet requirement onwards, the efficiency is ~ 7% lower than the nominal value.

6.5.2 Other systematic uncertainties

An uncertainty on the cross section for the WZ+jets background of 50% is assigned. This is based on Berends-Giele scaling [164], and assuming a 24% uncertainty per additional jet [165]. The same 50% uncertainty is also applied for the $(t\bar{b}Z + \bar{t}bZ) + X$, $X = jj, l\nu$ background process assuming that the uncertainty is similar for this process.

All the considered systematic uncertainties estimated from Monte Carlo simulation in the signal region are shown in Table 6.4 for both the signal and background yields.

Scale Variation	3 lepton	$\lvert m_{ll} - m_Z\rvert < 10$ GeV	4 jet	2 b-jet	$E_T^{miss} > 30$ GeV
Nominal(efficiency)	0.01417	0.01016	0.0053	0.0043	0.0036
μ_R $2\mu_F$	0.91	0.92	-0.051	-2.2	-1.6
μ_R $\mu_F/2$	.15	-2.2	-7.1	-8.7	-10
$2\mu_R$ μ_F	.5	2.3	4	3.3	3
$2\mu_R$ $2\mu_F$	0.063	1.4	-0.58	-1.7	-1.4
$2\mu_R$ $\mu_F/2$	.6	-1.5	-5	-5.6	-7.5
$\mu_R/2$ μ_F	.6	1.3	1.5	0.47	0.012
$\mu_R/2$ $2\mu_F$	.1	4.4	2.9	0.5	0.31
$\mu_R/2$ $\mu_F/2$	.082	-2	-6.2	-7.1	-8.7

Table 6.5: Percentage difference with respect to the nominal value at each stage of the selection for different scale variations.

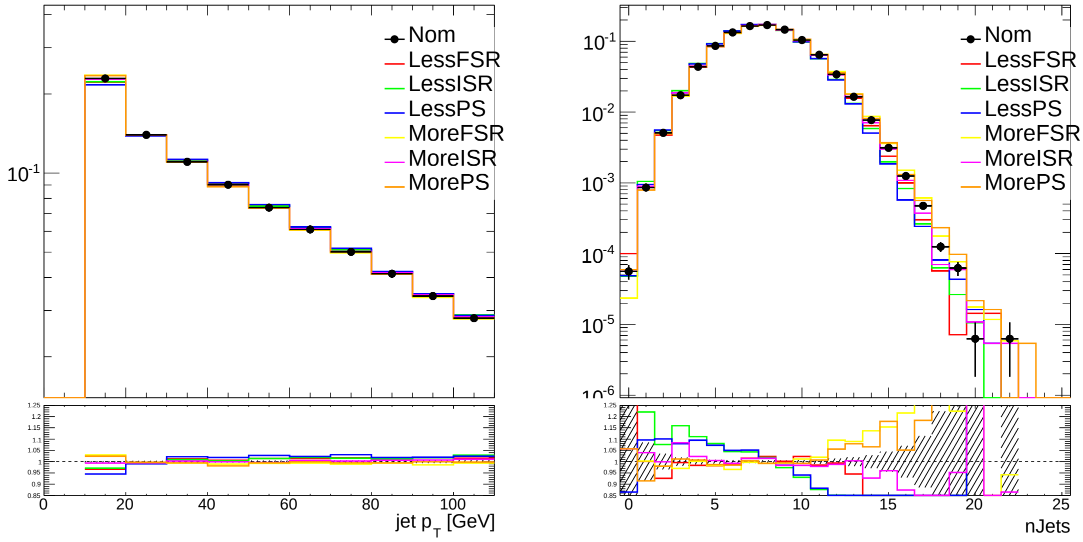

(a)

(b)

Figure 6.6: Kinematic distributions with ISR, FSR and PS variations compared to the distribution for the nominal Pythia parameters $t\bar{t}+Z$ signal sample. The hatched area on the ratio histogram shows the expected statistical uncertainty from the limited size of generated samples.

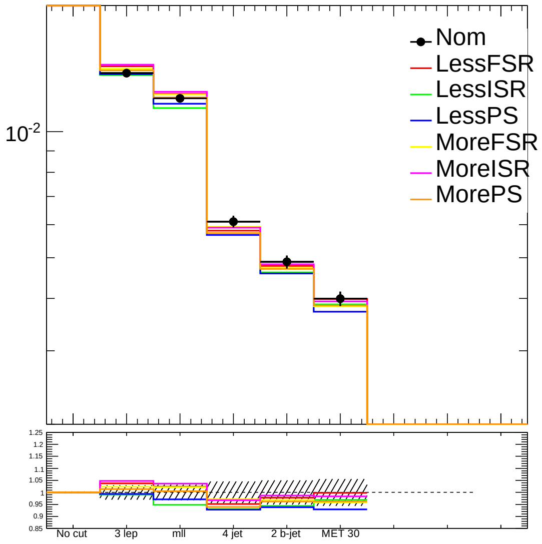

Figure 6.7: Fraction of the total number of events passing each stage of signal selection for several ISR, FSR and PS variations. The hatched area on the ratio histogram shows the expected statistical uncertainty from the limited size of generated samples.

6.6 Results

The number of signal region events expected from simulation and observed in data are shown in Table 6.7. The expected number of signal events in the signal region is 0.85 ± 0.04 (stat.) ± 0.14 (syst.). The expected number of background events from SM processes with three real leptons, obtained from simulation, is 0.28 ± 0.05 (stat.) ± 0.14 (syst.). The expected fake lepton background is $0.0^{+1.6}_{-0.0}$. If central value for the fake lepton estimation is taken to be zero the signal to background ratio is 3.0. One event is observed in the data.

Figure 6.8 shows a number of key distributions with the full signal region selection applied. The one observed event in data is clearly compatible with that of the expected signal and is consistent with the standard model expectation. Figure 6.9 shows an event display of the only candidate event found in data passing all selection cuts of the signal region. This event has $E_{\mathrm{T}}^{\mathrm{miss}} = 78.3$ GeV, the invariant mass of the two selected muons is found to be 90.7 GeV, the transverse mass of the missing transverse momentum with the selected electron is 66.8 GeV. The event has two jets which are b-tagged and two more which are not b-tagged. The invariant mass of the pair of jets which are not b-tagged is 82.5 GeV.

Scale Variation	3 lepton	$\|m_{ll} - m_Z\| < 10$ GeV	4 jet	2 b-jet	$E_T^{miss} > 30$ GeV
Nominal(efficiency)	0.014	0.012	0.0061	0.0049	0.004
Less FSR	3.8	2.5	-4.8	-2.2	-0.2
Less ISR	-1	-5.1	-6.9	-5.6	-3.1
Less PS	-0.59	-2.9	-7.1	-6.2	-7
More FSR	2.4	2.1	-2.8	-3.1	-4.1
More ISR	4.7	3.6	-3.2	-1.3	-1.6
More PS	1.4	0.48	-6.1	-3.8	-3.8

Table 6.6: Percentage difference with respect to the nominal value at each stage of the selection for different ISR, FSR and PS variations.

	SR
$t\bar{t}Z$	0.85 ± 0.04
WZ+jets	0.06 ± 0.04
ZZ+jets	0.014 ± 0.014
$t\bar{t}W$	0.011 ± 0.008
$(t\bar{b}Z + \bar{t}bZ) + X(=jj, l\nu)$	0.125 ± 0.013
$WZbbjj$	0.065 ± 0.016
Observed	1
MC Total	1.13 ± 0.06

Table 6.7: Numbers of events observed in data and expected from the $t\bar{t}Z$ signal process and various backgrounds for the signal region. The uncertainties shown are statistical only. No events passing the selections are found in the Z+jets and $t\bar{t}$ simulated samples.

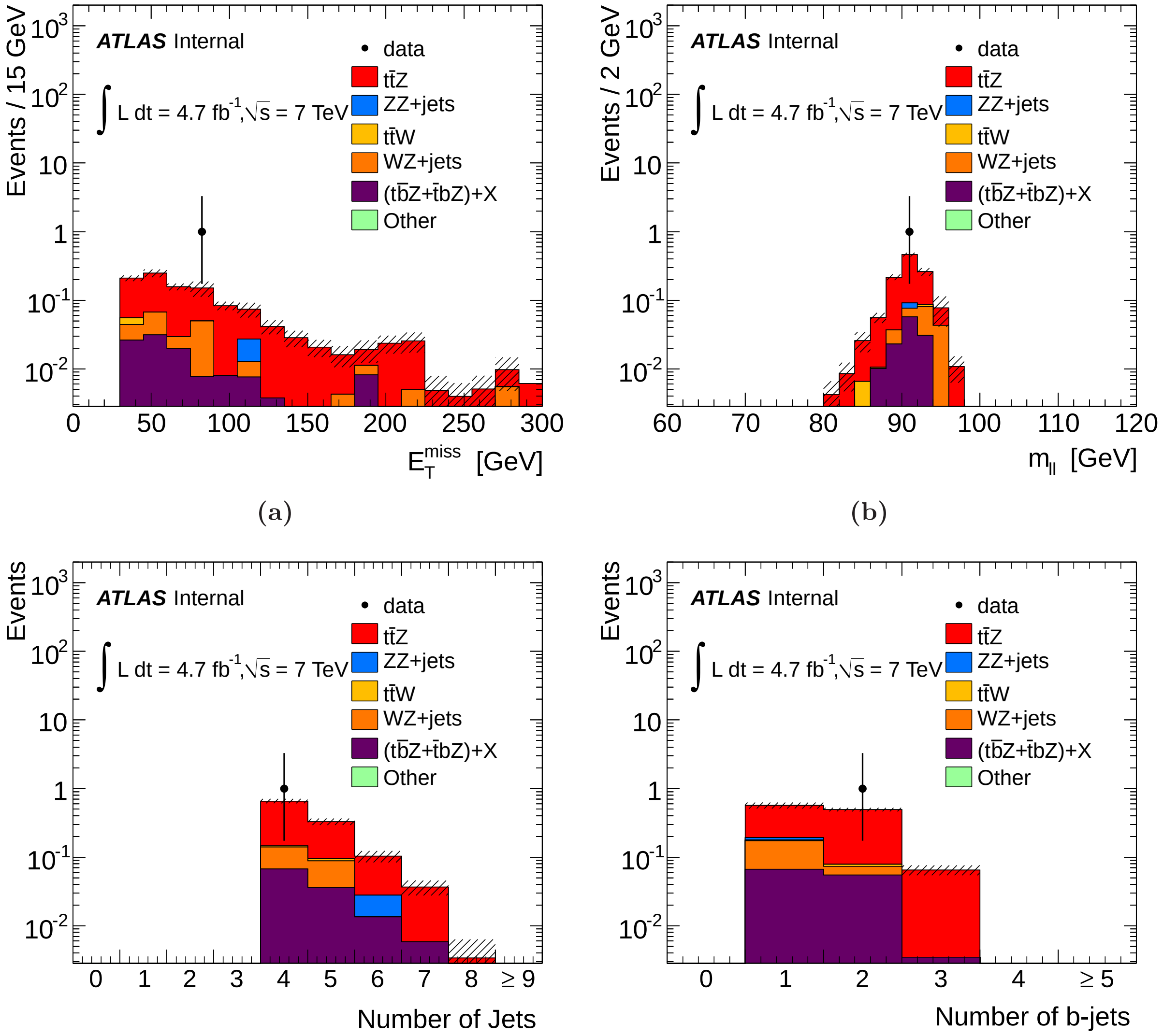

(a)

(b)

(c)

(d)

Figure 6.8: *Continued overleaf.*

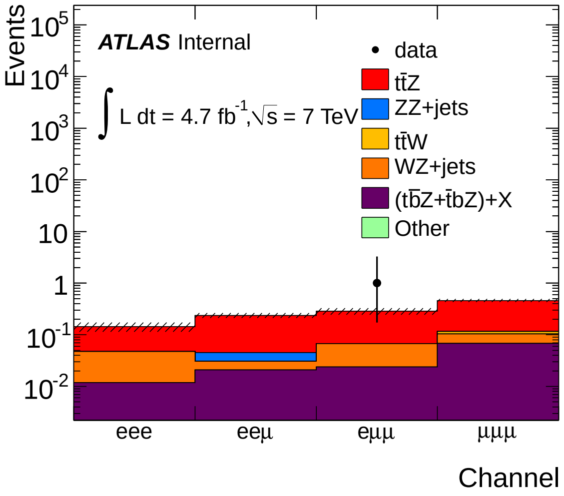

(e)

Figure 6.8: Expected and observed distributions of (a) $E_{\mathrm{T}}^{\mathrm{miss}}$, (b) the invariant mass of the OSSF pair of leptons, (c) the number of selected jets with $p_{\mathrm{T}} > 30$ GeV, (d) the number of b-tagged jets and (e) the lepton flavour combination, for the signal region selection. Figures from [1].

The result can be translated into a 95% probability upper limit on the $t\bar{t}+Z$ production cross section, $\sigma_{t\bar{t}Z}$. For this purpose, a Bayesian prescription is used, as implemented in Ref. [166]. A flat prior probability distribution is assumed for the number of signal events, and a Poisson likelihood $P(n|s,b,\theta_i)$ is used where n is the number of observed events, s the expected number of signal events, b the expected number of background events and θ_i are nuisance parameters corresponding to the dominant systematic uncertainties: the jet energy scale, b-tagging scale factor and jet vertex fraction scale factor uncertainties.

To derive the 95% probability upper limit on the $t\bar{t}+Z$ production cross section, the efficiency[2] ϵ is computed using $t\bar{t}+Z$ simulated events, and the posterior distribution of

$$\sigma = \frac{s}{\epsilon_{MC} \times \mathcal{L}} \tag{6.9}$$

is computed, where $\mathcal{L} = 4.7\ \mathrm{fb}^{-1}$ is the integrated luminosity of the analysed dataset.

The 95% probability upper limit on the number of signal events is 4.1, with an efficiency of $\epsilon_{MC} = (0.13 \pm 0.02)\%$. The observed upper limit on the $t\bar{t}+Z$ production cross

---

[2] The efficiency ϵ as defined here includes also detector acceptance effects.

section is 0.71 pb with an expected upper limit of 0.74 pb.

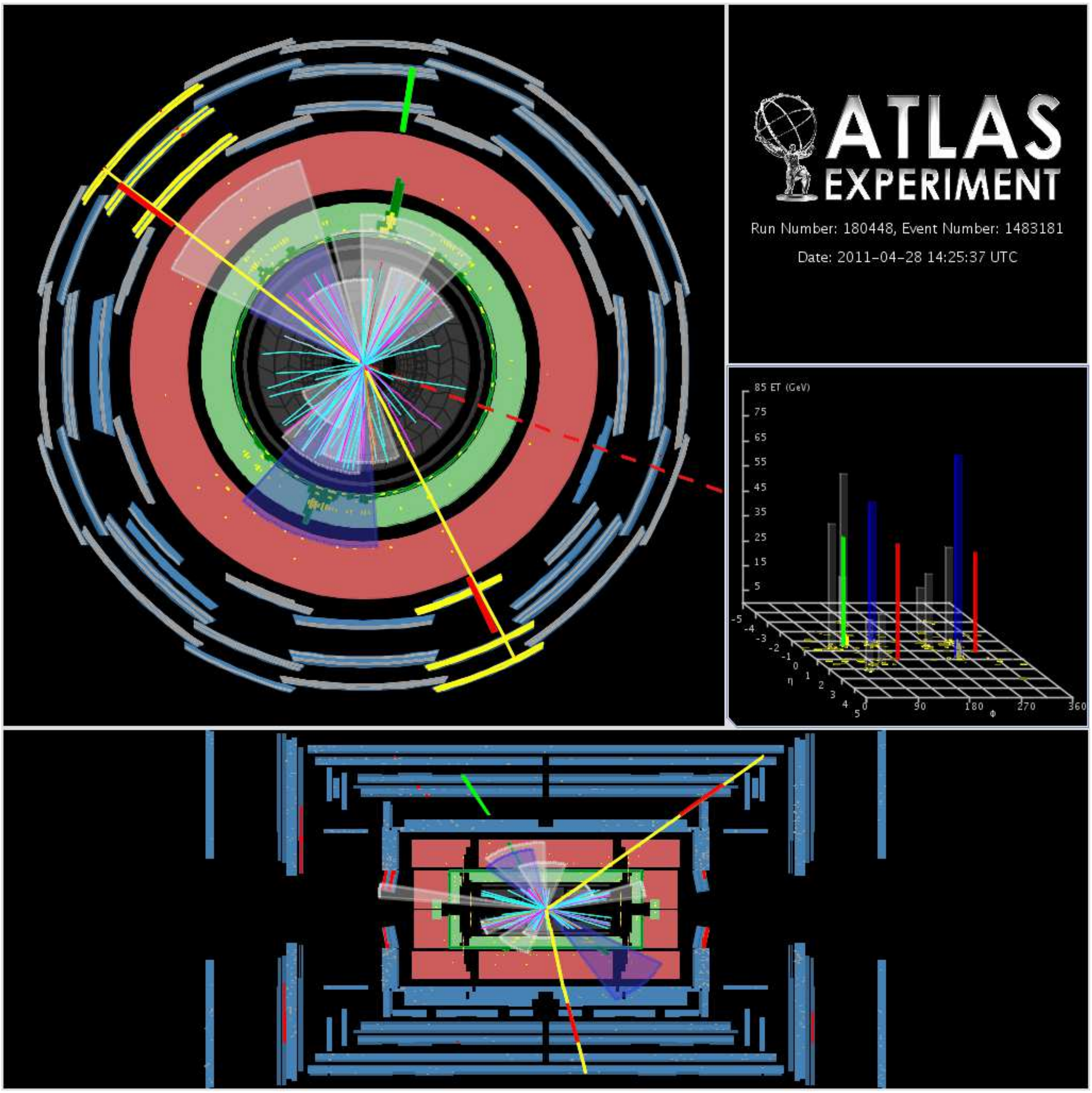

Figure 6.9: The only candidate event in data found in the signal region. The event is in the $e\mu\mu$ channel. The thick green line indicates the selected electron. The two thick red lines with associated tracks (light blue) represent the selected muons. The red arrow indicates the direction of the $E_{\mathrm{T}}^{\mathrm{miss}}$. The b-jets are highlighted with by blue cones/towers. The expected signal-to-background ratio in the signal region is 3.0, taking zero as the estimate of the fake lepton background. Figures from [1].

6.7 Summary and conclusion

Using 4.7 fb^{-1} of $\sqrt{s} = 7$ TeV pp collision data collected by ATLAS, a search for $t\bar{t} + Z$ production in the three lepton final state was performed. In a signal region requiring three leptons, a missing transverse momentum of 30 GeV and four jets with $p_{\mathrm{T}} > 30$ GeV, one of which is b-tagged, 0.85 ± 0.04 (stat.) ± 0.14 (syst.) signal events were expected. The background from events containing three leptons from W and Z bosons in this signal region was estimated from simulation as 0.28 ± 0.05 (stat.) ± 0.14 (syst.). In addition, a fake lepton background of $0.0^{+1.6}_{-0.0}$ events was estimated by a data driven method. One candidate event whose kinematical properties are consistent with a $t\bar{t} + Z$ event was found in data, in agreement with expectations from the Standard Model. The result was translated to a 95% probability upper limit of 0.71 pb on the $t\bar{t} + Z$ production cross section, consistent with the NLO Standard Model prediction of 0.14 pb.

Chapter 7

Third generation SUSY searches

7.1 Introduction

In Chapters 8 and 9 two analyses that search for the direct pair production of the supersymmetric partners to the bottom and top quarks are described. This Chapter will introduce the SUSY signals being targeted and motivation for these searches. Furthermore, there are several aspects of the analyses that are common to both, such as methods for background estimation and determination of systematic uncertainties. To avoid repeated discussion of these techniques in what follows they are summarised in this Chapter.

7.2 Introduction to searches

An overview of the theoretical motivation for searches for the supersymmetric partners to third generation quarks will be given, followed by a description of relevant signal models and finally an overview of previous third generation squark searches.

7.2.1 Theoretical motivation

Due to the larger masses of the SM third generation quarks significant mixing of the left- and right-handed squarks can occur. This can lead to significantly lighter mass eigenstates which has important implications for naturalness.

Mixing

The left- and right-handed third generation squarks can mix to produce mass eigenstates, the lightest of which can, in the case of maximal mixing, be significantly lighter than the first and second generation quarks. The sbottom and stop mixing in the MSSM enters through following stop mass terms in the Lagrangian:

$$\mathcal{L}_{\text{stop masses}} = -\left(\tilde{t}_L^* \tilde{t}_R^*\right) \mathbf{m}^{\mathbf{2}}_{\tilde{\boldsymbol{t}}} \begin{pmatrix} \tilde{t}_L \\ \tilde{t}_R \end{pmatrix}, \tag{7.1}$$

where

$$\mathbf{m}^{\mathbf{2}}_{\tilde{\boldsymbol{t}}} = \begin{pmatrix} m(\tilde{t}_L)^2 & m(t)(A_t - \mu\cot\beta) \\ m(t)(A_t - \mu\cot\beta) & m(\tilde{t}_R)^2 \end{pmatrix}. \tag{7.2}$$

The matrix can be diagonalised in the $L--R$ basis to get the mass eigenstates:

$$\begin{pmatrix} \tilde{t}_1 \\ \tilde{t}_2 \end{pmatrix} = \begin{pmatrix} \cos\theta_{\tilde{t}} & -\sin\theta_{\tilde{t}} \\ \sin\theta_{\tilde{t}} & \cos\theta_{\tilde{t}} \end{pmatrix} \begin{pmatrix} \tilde{t}_L \\ \tilde{t}_R \end{pmatrix} \tag{7.3}$$

where $m^2_{\tilde{t}_1} < m^2_{\tilde{t}_2}$ and $\theta_{\tilde{t}}$ is the stop mixing angle. The large top quark Yukawa coupling effects the RGE evolution of parameters down the electroweak scale such that the third generation squark masses can be significantly smaller than the those of the first two generations. The m^2_t terms in the diagonal elements of (7.2) mitigate this effect somewhat, but the off-diagonal entries can still induce a significant mixing which reduces the lighter top-squark squared-mass eigenvalue. Hence, models often predict that $\tilde{t}_1$ is the lightest squark of all, and that it is predominantly right-handed [20].

A very similar prescription applies for the sbottom mixing, where

$$\mathbf{m}^{\mathbf{2}}_{\tilde{\boldsymbol{b}}} = \begin{pmatrix} m(\tilde{b}_L)^2 & m(b)(A_b - \mu\cot\beta) \\ m(b)(A_b - \mu\cot\beta) & m(\tilde{b}_R)^2 \end{pmatrix}. \tag{7.4}$$

The size of mixing in the sbottom sector depends on the size of $\tan\beta$. If it is small ($<\sim 10$) there is not a large effect from the mixing terms as the bottom Yukawa term is much smaller than that of the top. However, even in the case of small $\tan\beta$, because $\tilde{b}_L$ is part of the $\tilde{t}_L$ doublet, it can be significantly lighter than the other left-handed down-type squarks after renormalisation group evolution to the electro-weak scale.

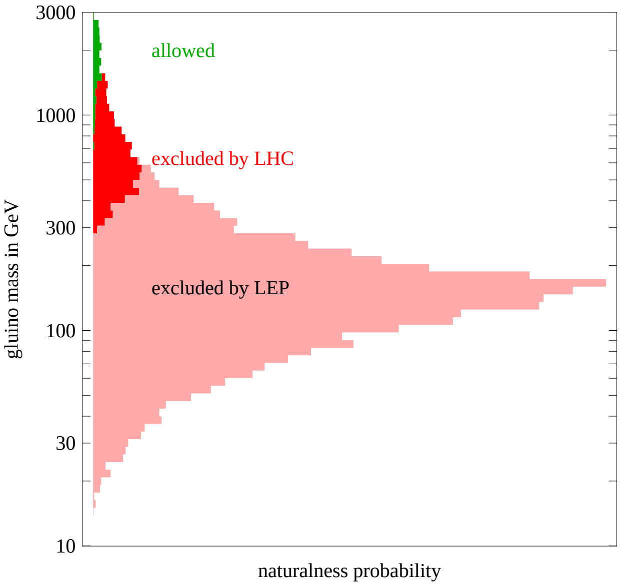

(a)

Figure 7.1: "Naturalness probability distribution" for the gluino mass in the CMSSM. Only its tail was allowed after LEP, and the tail of the tail remains allowed after first LHC data. Figure from [169].

Naturalness

Providing a solution to the hierarchy problem is one of the fundamental motivations for SUSY as an extension to the SM. However, the exclusion of low mass scale sparticles introduces a new *fine tuning* problem for SUSY models. One of the chief motivations for sparticles with masses <~ 1 TeV is that they naturally render $M_W \ll M_{Pl}$ without the need to fine tune parameters to keep M_W small [167].

To avoid increasingly precise fine-tuning of parameters, the effective scale of supersymmetry breaking must not be arbitrarily separated from the electroweak breaking scale. Imposing this "naturalness" criterion, corresponds to placing an upper limit on superparticle masses in the TeV range [168]. The amount of fine tuning required for a particular set of SUSY model parameters can be quantitatively assessed by the following metric:

$$\left| \frac{a_i}{M_Z^2} \frac{\partial M_Z^2(a_i)}{\partial a_i} \right| < \Delta, \tag{7.5}$$

where $M_Z^2(a_i)$ is the Z mass squared as a function of the parameters of the theory a_i. The purpose of (7.5) is to avoid unnatural tuning of the physical parameters of the theory by requiring that a variation of any of the parameters a_i does not correspond to a variation

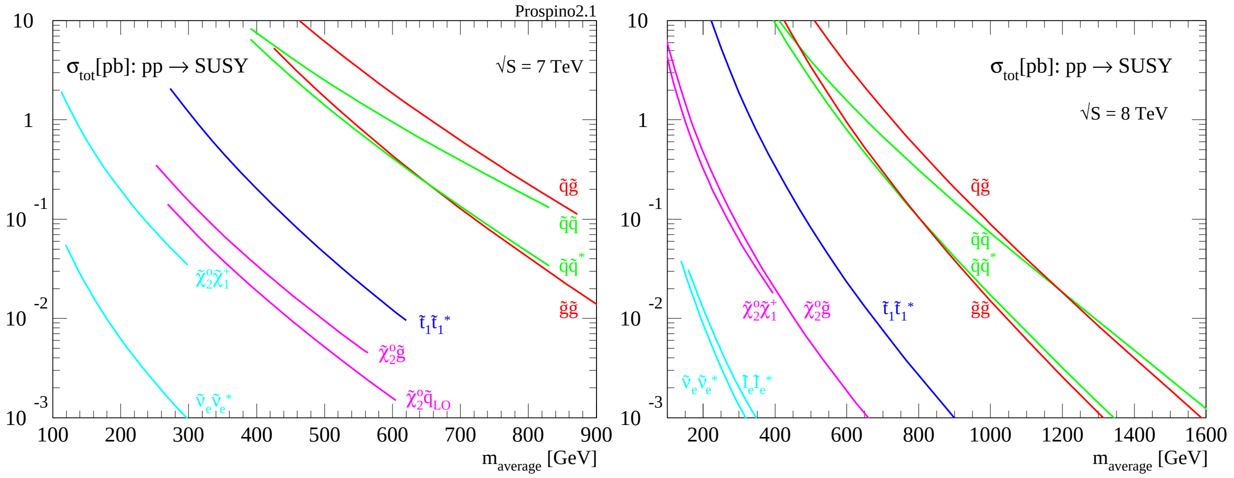

(a) **(b)**

Figure 7.2: Sparticle production cross sections at NLO as a function of the sparticle mass (or average mass for e.g. multiple squarks), m_{average}, (a) at $\sqrt{s} = 7$ TeV and (b) at $\sqrt{s} = 8$ TeV. Figures from `Prospino2.1` [170].

of M_Z^2 more than Δ-times larger.

Figure 7.1 provides an indication of how much SUSY phase space can be ruled out my imposing naturalness arguments. It illustrates the "naturalness probability" as defined in [169] for a range of gluino masses in the CMSSM. The regions excluded by LEP and now the LHC are shown, only a tiny fraction of the phase space now remains and what does remain has a very low naturalness probability.

7.2.2 Signal models

As already discussed, large mixing in the MSSM can result in mass eigenstates for the lightest sbottom and stop, $\tilde{b}_1$ and $\tilde{t}_1$, that are significantly lighter than those of the first and second generation squarks. Consequently, the ~TeV scale exclusion on first and second generation squarks masses does not restrict the possibility to produce $\tilde{b}_1$ and $\tilde{t}_1$ at low masses and considerable cross sections at the LHC.

In the signal models considered in the following, there are two different production modes of third generation squarks: *gluino mediated production* and *direct pair production*. Gluino mediated production refers to production of $\tilde{b}_1$ and $\tilde{t}_1$ in the gluino decay. Figure 7.2 shows the production cross section for several SUSY processes at both $\sqrt{s} = 7$ TeV and $\sqrt{s} = 8$ TeV. It is clear that for a given mass scale first and second generation squark and

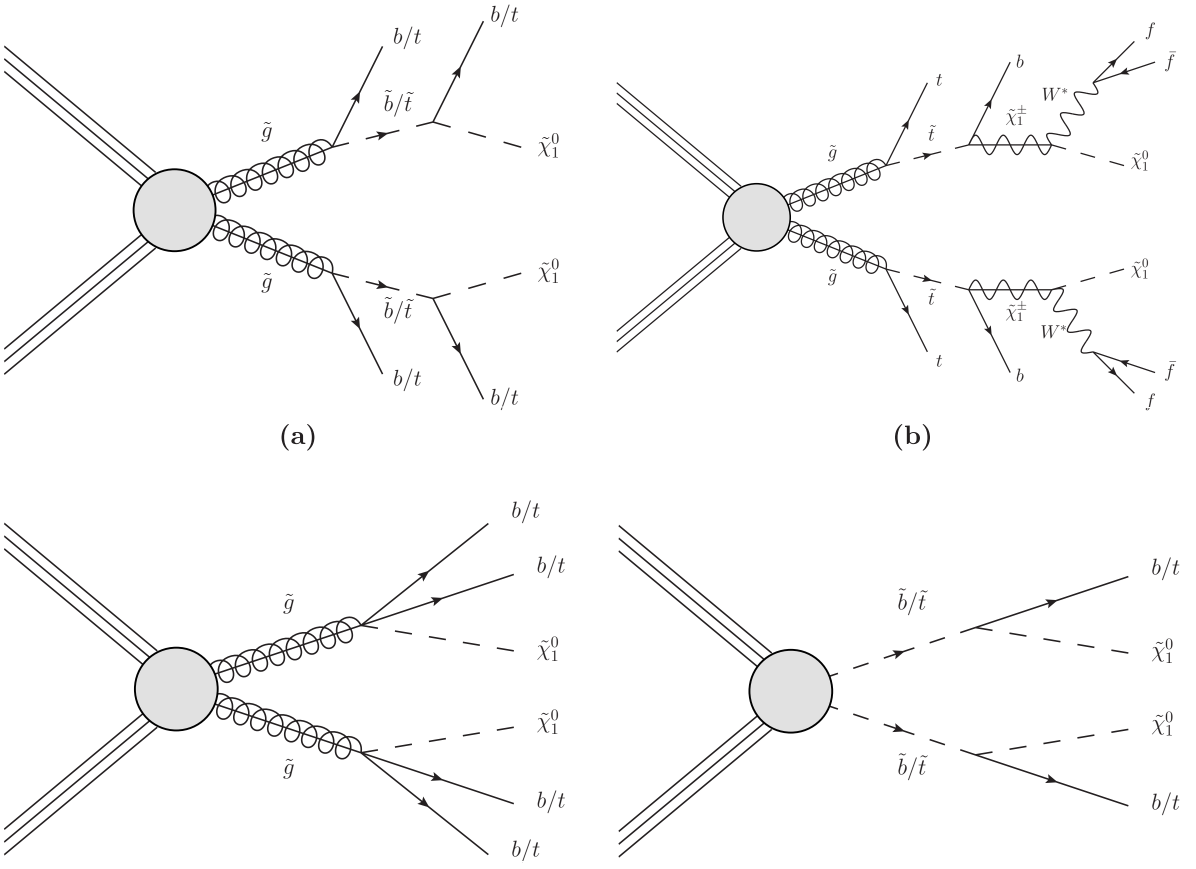

(a) **(b)**

(c) **(d)**

Figure 7.3: Feynman diagrams for (a) gluino mediated sbottom, (b) gluino mediated stop, (c) gluino mediated off-shell stop (d) direct stop production.

gluino pair production has a considerably larger cross section than stop pair production. However, with ~ TeV scale exclusion of gluino masses the production cross section of allowed gluino masses becomes comparable to that of direct third generation squark pair production. Therefore, searches for gluino mediated stop and sbottom production is most relevant for early searches, with direct production searches becoming more important with increased luminosity.

Decay

Gluino pair production can mediate sbottom and stop production through the following gluino decay modes, $\tilde{g} \rightarrow \tilde{b}_1 b$ and $\tilde{g} \rightarrow \tilde{t}_1 t$. Of central importance to the final phenomenology for gluino mediated production as well as direct pair production are, of course, the decay modes of the sbottom and stop. Depending on the sparticle mass spectra many different decay modes are available. However, only a small number of specific scenarios are considered here. The only scenario for the $\tilde{b}_1$ decay considered is decay via $\tilde{b}_1 \to b\tilde{\chi}_1^0$. Two different scenarios are considered for the $\tilde{t}_1$ decay. Firstly, analogous to the $\tilde{b}_1$ decay mode, decay via $\tilde{t}_1 \to t\tilde{\chi}_1^0$; secondly, decay via an intermediate chargino, $\tilde{t}_1 \to b\tilde{\chi}_0^{\pm}$. In gluino mediated production, where $\tilde{g} \to \tilde{b}_1 b \to bb\tilde{\chi}_1^0$ or $\tilde{g} \to \tilde{t}_1 t \to tt\tilde{\chi}_1^0$, the case where the $\tilde{b}_1$ or $\tilde{t}_1$ is off-shell can be considered. This gives rise to an effective 3-body decay of the gluino. Thus, one has the decay modes, $\tilde{g} \to bb\tilde{\chi}_1^0$ or $\tilde{g} \to tt\tilde{\chi}_1^0$. The corresponding Feynman diagrams for the previously described processes are given in Figure 7.3.

7.2.3 Previous sbottom and stop searches

The focus of the remaining Chapters is searches for direct pair production of sbottom and stop squarks. To provide a wider context to these searches a brief review of existing results from analyses targeting gluino mediated stop and sbottom production will now be given.

Results are interpreted in four SUSY signal scenarios that can be divided into two categories; *phenomenological MSSM* models and *simplified models*. The idea in both categories is to impose restrictions on the available sparticle phase space such that only a small number of processes contribute in any given model.

The phenomenological MSSM model goes some way to simplifying the signal model. All particles other than the gluino, sbottom, (stop and chargino) and neutrino have their masses set very high. In this case, gluino pair production, sbottom (stop) pair production and gluino-sbottom(-stop) associated production are the only contributing processes. With the neutralino (and chargino) masses fixed there are only two remaining relevant parameters, $m_{\tilde{g}}$ and $m_{\tilde{b}_1}$ ($m_{\tilde{t}_1}$). Variation of these variables provides a range of kinematics. Results can straightforwardly be presented in the relevant 2-dimensional mass plane.

Simplified models [171, 172] go one step further and generally restrict the sparticle phase space such that only one process is produced. All other sparticles are decoupled by setting their masses to very high values leaving only two or three masses free. Variation of these masses give rise to a wide range of kinematics. This strategy has the benefit that the interpretation of results is unambiguous. It is then possible provide re-interpretation of more complicated models by taking linear combinations of several simplified models and assigning each different production cross sections and branching ratios.

The signal models for relevant ATLAS and CMS searches will now be described in more detail:

Gluino-sbottom: Within the framework of the phenomenological MSSM the $\tilde{b}_1$ is set to be the lightest squark and all others are set much heavier than the gluino, giving the spectrum $m_{\tilde{g}} > m_{\tilde{b}_1} > m_{\tilde{\chi}_1^0}$. this way only a few processes contribute. Sbottoms can only be produced via gluino mediation and direct pair production, diagrams (a) and (d) in Figure 7.3. The gluino decays via $\tilde{g} \to \tilde{b}_1 b$ with a branching ratio of 100% and the sbottom via $\tilde{b}_1 \to b\tilde{\chi}_1^0$ with a branching ratio of 100% with $m_{\tilde{\chi}_1^0}$ is set to 60 GeV. Exclusion limits are set in the $m_{\tilde{g}} - m_{\tilde{b}_1}$ plane.
Gluino-stop: Similar to the gluino-sbottom model, except this time the $\tilde{t}_1$ is the lightest squark. In this particular scenario the $\tilde{t}_1$ is assumed to decay exclusively via $\tilde{t}_1 \to b\tilde{\chi}_0^{\pm}$. The neutralino mass is set to 60 GeV and here the chargino mass is set to 120 GeV. The Feynman diagram for the gluino-mediated production mode is given in Figure 7.3 (a). Results are interpreted in the $m_{\tilde{g}} - m_{\tilde{t}}$ plane.
Gbb: A simplified model scenario is constructed where $m_{\tilde{g}} < m_{\tilde{b}_1}$ resulting in a 3-body decay of the gluino via an off-shell sbottom. With all other squark masses set much larger than the gluino mass the only contributing process is gluino pair production with $\tilde{g} \to bb\tilde{\chi}_1^0$ with a branching ratio of 100%, as shown in the diagram of Figure 7.3 (c). Event kinematics are not affected by the sbottom mass and only parameters of interest become the gluino and neutralino masses, so results are interpreted in the $m_{\tilde{g}} - m_{\tilde{\chi}_1^0}$ plane.
Gtt: This model is entirely analogous to the Gbb simplified model scenario replacing the sbottom with a stop , as shown in the diagram of Figure 7.3 (c).

Figures 7.4 (a) and (b) show the exclusion limits set by the ATLAS search looking for events containing three b-jets using the $\sqrt{s} = 7$ TeV data in the gluino-sbottom and gluino-stop scenarios. Figures 7.4 (c) and (d) show the ATLAS and CMS exclusion limits, respectively, in the Gbb scenario using the $\sqrt{s} = 8$ TeV dataset. The ATLAS search again looks for events containing three b-jets. There are two complimentary CMS searches, one considering the events containing large $E_{\mathrm{T}}^{\mathrm{miss}}$ and H_T and another using the α_{T} kinematic variable. Figures 7.4 (e) and (f) show the exclusion limits for a number of ATLAS and CMS SUSY searches, respectively, that have interpreted their results in the Gtt model.

The results discussed in this section do not impose direct constraints on the direct sbottom and stop searches that are discussed in detail in the following two Chapters. This is because in the direct sbottom and direct stop pair production simplified models the gluino is decoupled and the exclusion limits applied here do not apply.

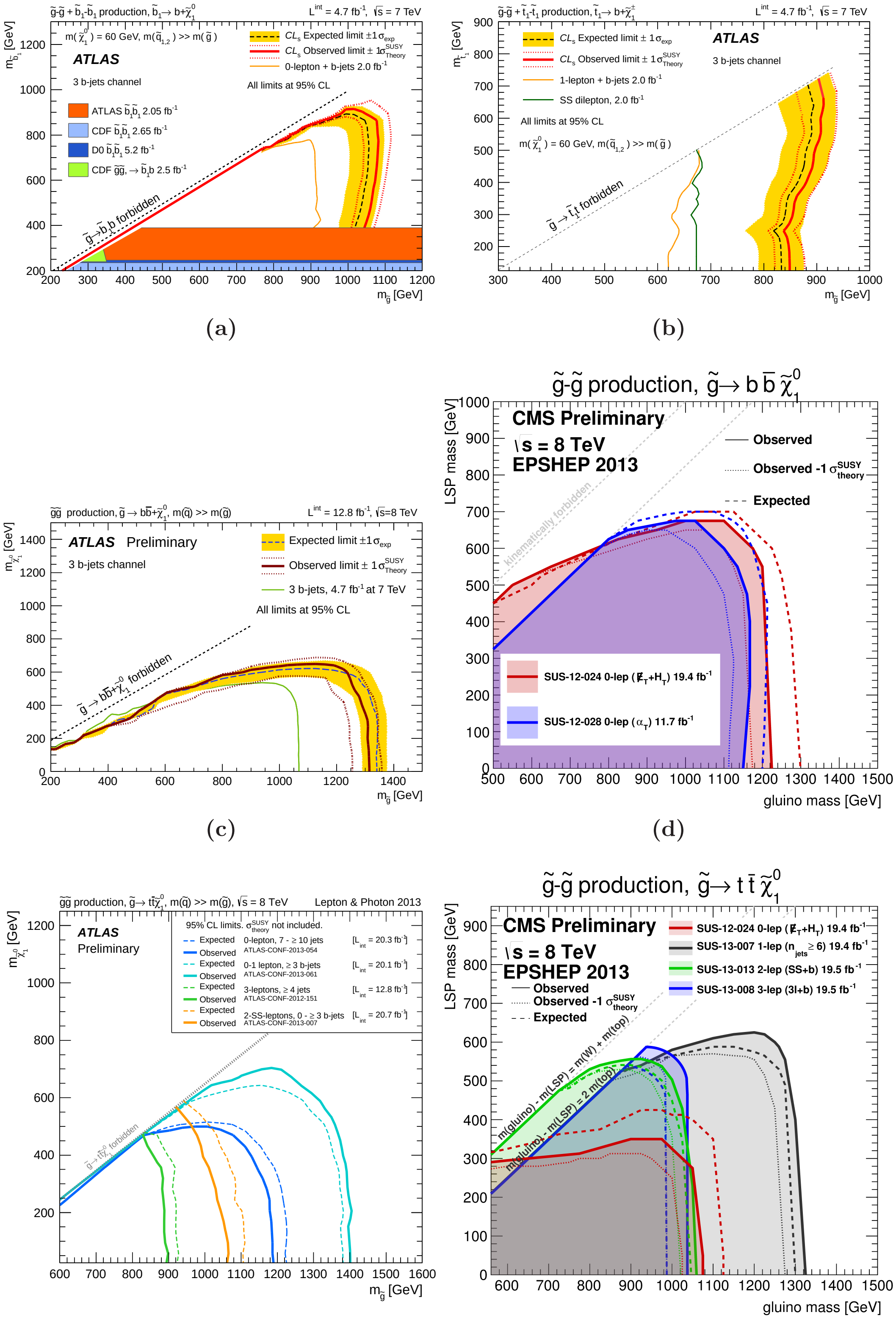

(a) (b)

(c) (d)

(e) (f)

Figure 7.4: Exclusion limits on gluino mediated sbottom and stop production with 2011 $\sqrt{s}$ = 7 TeV and 2012 $\sqrt{s}$ = 8 TeV data. Figures from [173], [174], [77] and [76].

7.3 Background estimation techniques

Almost all SUSY searches expect some level of contamination from SM processes in their signal regions. Precise estimation of the expected contribution from these backgrounds and their corresponding uncertainties is essential in such searches. A well developed understanding of SM backgrounds is mandatory for both confidence in claims for observation of new physics and claims for exclusion of particular signal models. In this section two background estimation techniques are described that are common to the analyses that will be described fully in Chapters 8 and 9.

7.3.1 Transfer factor method

An approach used in many SUSY analyses is the *transfer factor method*. This approach is referred to as *semi-data-driven* as it combines information taken both from data and MC simulation. The general principal is to define a *control region* where some part of the selection is orthogonal to the signal region selection. Control regions are usually defined to select one particular background process that is expected to contribute in the signal region. Once defined, a control region can be used to compare expectation from simulation to the data. Good agreement provides validation of the MC performance for a given selection.

With a control region defined and the MC description of the process under consideration validated, there can be some confidence in extrapolating from the control region to the signal region using the MC. This is where the transfer factor arises. It is defined to be the ratio between the number of events expected from the MC in the signal region to the number of events expected from the MC in the control region. Normalising this ratio to the number of events observed in the data and subtracting away contributions from the other backgrounds, provides an estimation of the number of events expected in the signal region for this background process. This procedure can be summarised by the following expression

$$N_{\mathrm{SR}}^{\mathrm{Bkg(data)}} = \frac{N_{\mathrm{SR}}^{\mathrm{Bkg(MC)}}}{N_{\mathrm{CR}}^{\mathrm{Bkg(MC)}}} \times \left(N_{\mathrm{CR}}^{\mathrm{data}} - N_{\mathrm{CR}}^{\mathrm{Non\text{-}Bkg(MC)}} \right), \tag{7.6}$$

where SR and CR refer to the signal region and control region respectively.

One of the major attractions of this technique is that some systematic uncertainties are expected to cancel out in the ratio. In general, the more kinematically similar the control region and signal region are the greater the cancellation. In practice, when defining a control region selection, there is often trade-off between maximising the similarity of the kinematic requirements of the two regions and maintaining sufficient numbers of events that statistical uncertainties do not become dominant. Another consideration is the signal contamination in the control region. This technique is only applicable if the signal contamination in the control region is negligible.

The transfer factor technique is used extensively to estimate, for example, the $t\bar{t}$, W+jets or Z+jets backgrounds in the following analyses.

7.3.2 Multi-jet background estimation

QCD has a low selection efficiency but very large cross section compared to the signal models being considered. Hence, this is an extremely important background to constrain. In the following searches the QCD multi-jet and all-hadronic $t\bar{t}$ backgrounds are estimated using the data-driven *jet smearing method* which is briefly described here. More details of the method can be found in [175].

Overview of the method

QCD events that enter the signal region are assumed to have acquired $E_{\mathrm{T}}^{\mathrm{miss}}$ due to mis-measurement of one or more jets in the event. The concept of the jet smearing method is to estimate the QCD background from such events by emulating this mis-measurement. The momentum of jets in clean, well measured data events (with low $E_{\mathrm{T}}^{\mathrm{miss}}/\frac{1}{2}\sqrt{\Sigma E_T}$) are *smeared* to generate *pseudoevents* with possibly large $E_{\mathrm{T}}^{\mathrm{miss}}$ and $E_{\mathrm{T}}^{\mathrm{miss}}/\frac{1}{2}\sqrt{\Sigma E_T}$ values that can pass the signal region selection requirements. The different stages of the method are as follows:

1 Low $E_{\mathrm{T}}^{\mathrm{miss}}/\frac{1}{2}\sqrt{\Sigma E_T}$ *seed* events with the same number of jets as in the analysis are selected from data.

2 A smearing function is constructed using a sample of simulated jet events. This is referred to as the jet *response*, R, it is calculated in bins of $p_T(j^{\mathrm{true}})$ and defined to be

$$R = \frac{p_T(j^{\mathrm{reco}})}{p_T(j^{\mathrm{true}})}. \tag{7.7}$$

Separate response functions are constructed for b-tagged and non-b-tagged jets. They are expected to have markedly different responses due to the large number of neutrinos and muons in heavy flavour jets hence it is important to smear each jet with its corresponding response.

3 The momentum of jets in the seed events selected in (1) are smeared, randomly sampling from either b-tagged or non-b-tagged response as defined in (2). The response function used is dependent on the b-tag weight of the jet. This operation is repeated many times (typically $\sim 10,000$ times) per seed event to randomly generate configurations where $E_{\mathrm{T}}^{\mathrm{miss}}$ comes from fluctuating jets.

4 Once a large sample of pseudo-events is generated, these are passed through the analysis cuts to give distributions of the QCD estimation for any variable of interest. These distributions are then normalised within a QCD enriched control region, subtracting the non-QCD component taken from Monte Carlo. For the sbottom and stop searches the control region is constructed by selecting events with the signal region cuts but with the QCD rejection cuts reversed.

The response function

The response function is derived using `PYTHIA` di-jet samples. The shape of the response is constructed by calculating the response R for each jet in 20 GeV bins of $p_{\mathrm{T}}(j^{\mathrm{true}})$, where R is defined as in (7.7). The p_{T} of any neutrinos within $\Delta R(j,\nu) < 0.4$ of the jet are added back to the $p_{\mathrm{T}}(j^{\mathrm{true}})$ as well as any other objects within a cone of $\Delta R < 0.4$ that contribute to any of the $E_{\mathrm{T}}^{\mathrm{miss}}$ terms. This ensures that the full true jet momentum is taken into account.

Examples of the two-dimensional response taken from the stop pair analysis using 2012 data are shown in Figure 7.5. The larger number of neutrinos present in heavy flavour jets results in a broader low side tail for their response as can be seen more clearly in Figure 7.6. These distributions are again taken from the 2012 data stop analysis and compares the response functions in different truth p_{T} ranges for reconstructed b-tagged jets, non-b-tagged jets and all jets.

Validation in data

To validate the response function in data, two analyses are performed. The first, referred to as the *di-jet balance* analysis, is used to validate the Gaussian core of the response. The second, referred to as the *mercedes* analysis, is used to validate the tails of the response. In both the di-jet balance and Mercedes analyses events are selected with single jet triggers.

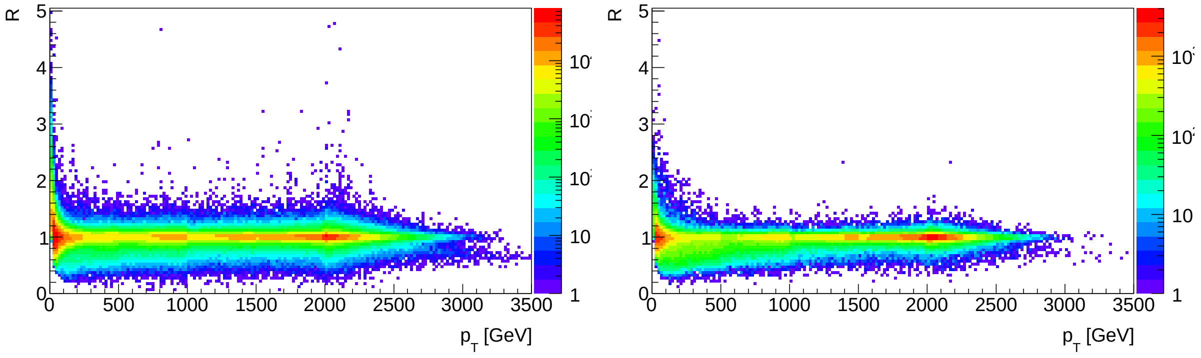

(a) (b)

Figure 7.5: The response function binned in true p_{T} as calculated using `PYTHIA` di-jet samples for untagged jets (left) and tagged jets (right).

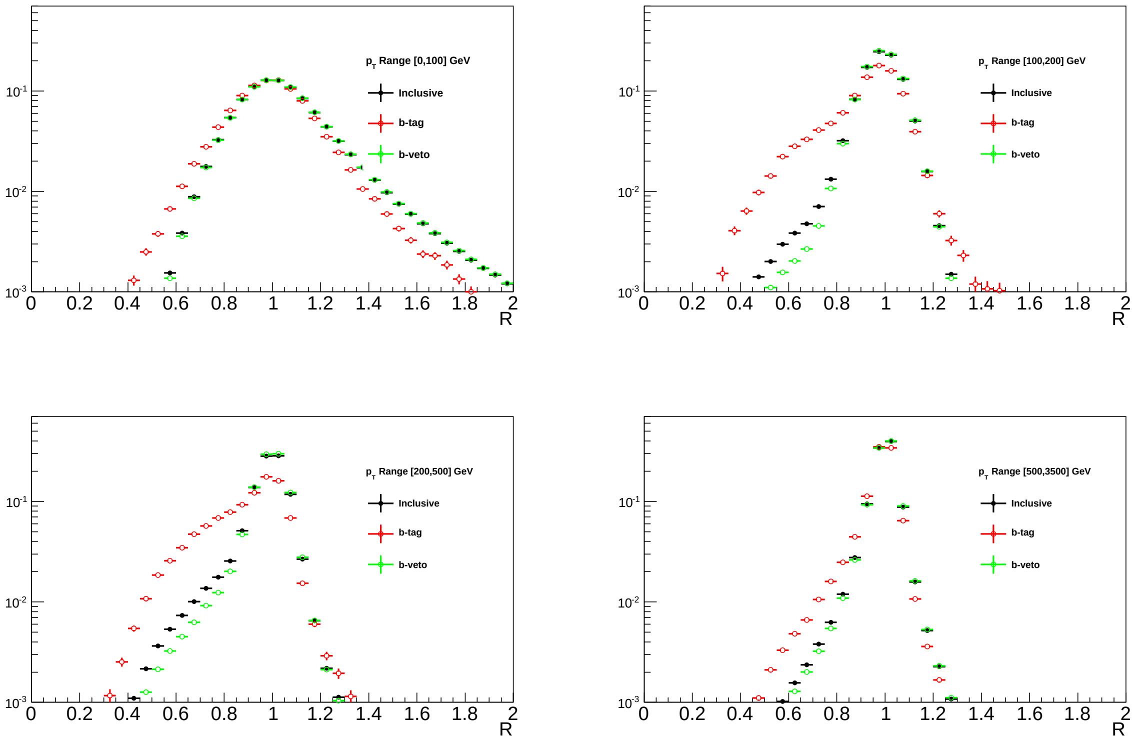

Figure 7.6: Plots of the response function for b-tagged jets (red), non-b-tagged jets (green) and all jets (black) using MC samples in the truth p_{T} ranges $[0, 100]$ GeV (top left), $[100, 200]$ GeV (top right), $[200, 500]$ GeV (bottom left), $[500, 3500]$ GeV (bottom right).

Trigger items with online jet p_T thresholds of $55 - 460$ GeV are used and it is required that the leading offline jet p_{T} is above the respective turn-on plateau value. The b-tag and non-b-tag cases are treated separately in each analysis.

Di-jet balance The MC modelling of the Gaussian component, σ_R, of the response is investigated using the di-jet balance $A(p_T(1), p_T(2))$, defined as follows for 2 jets with $p_T(1), p_T(2)$:

$$A(p_T(1), p_T(2)) = \frac{p_T(1) - p_T(2)}{p_T(1) + p_T(2)} \tag{7.8}$$

This is a useful quantity as the width of $A(p_T(1), p_T(2))$, denoted by σ_A, is related to σ_R by means of:

$$\sqrt{2}\sigma_A = \frac{\sigma_{P_T}}{P_T} = \sigma_R \tag{7.9}$$

$A(p_T(1), p_T(2))$ is calculated in events with exactly two jets that satisfy the following selection cuts:

- 2 jets with $p_{\mathrm{T}}(1) > 70$ GeV and $p_{\mathrm{T}}(2) > 40$ GeV
- A veto on any third jet with $p_{\mathrm{T}} > 30$ GeV
- $\min_{i=1,2} |\Delta\varphi(j_i, E_{\mathrm{T}}^{\mathrm{miss}})| < 0.3$ to ensure that the $E_{\mathrm{T}}^{\mathrm{miss}}$ is associated to one of the jets.

The di-jet balance distribution derived from the pseudodata and data is binned in p_{T} and fitted with a Gaussian. An example taken from the 2012 data stop analysis is shown in Figures 7.7(a) and (b). The mean of the Gaussian is set to 0 and the width and normalisation are fitted. The difference between the data and pseudodata widths can be treated with a p_{T} dependent correction which is convoluted with the response as derived from the Monte Carlo. Figure 7.7 (c) shows the fitted gaussian widths are a function of average p_{T}.

Mercedes Analysis The tails of the response function are validated in data using a sample of three-jet events where the $E_{\mathrm{T}}^{\mathrm{miss}}$ can be unambiguously associated with one of the jets, and hence, can be attributed to the fluctuation of that jet. Such events are known as Mercedes events because of their resemblance to the three-pronged Mercedes logo. Figure 7.8 shows two examples of the parallel and anti-parallel selection from 2011 data.

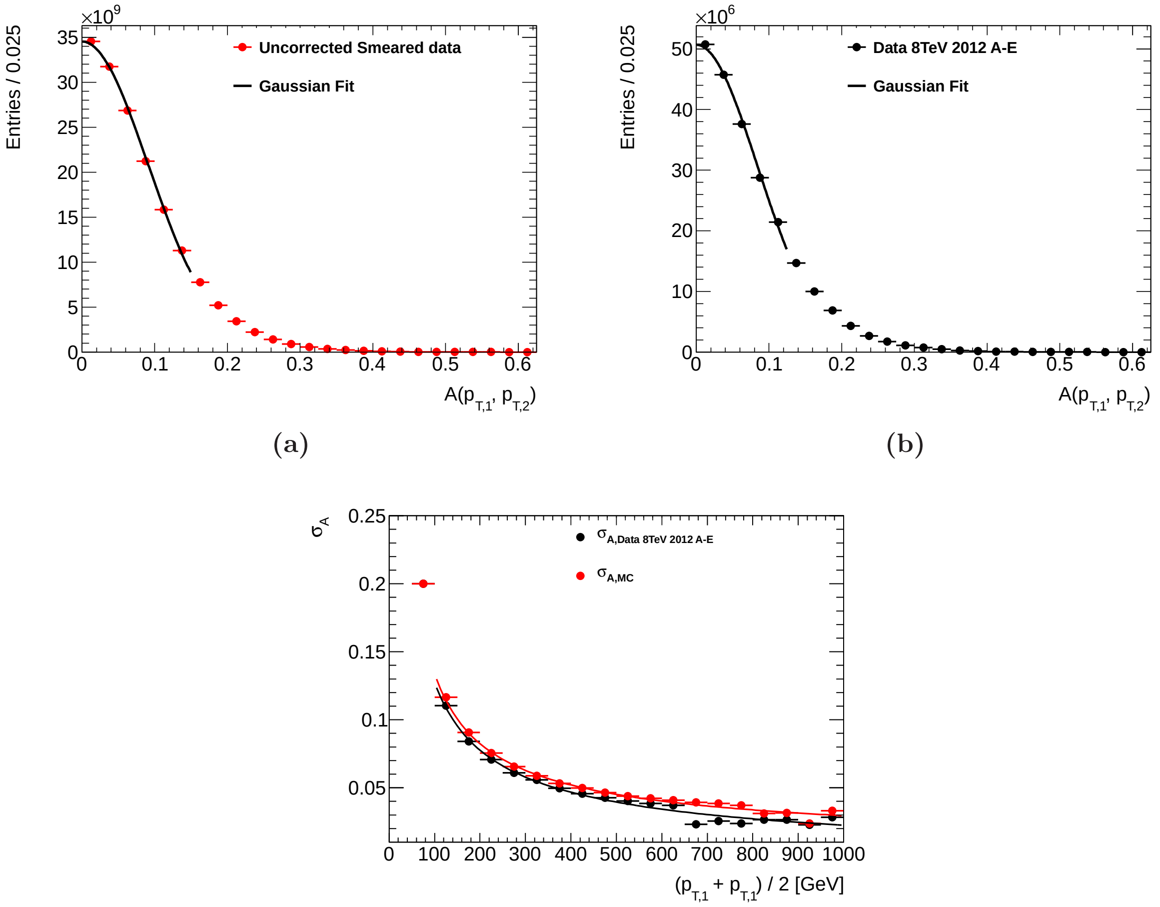

(a) **(b)**

(c)

Figure 7.7: An example of the fit to the di-jet balance A is shown for $140 < p_{\mathrm{T}} < 160\,\mathrm{GeV}$ in the smeared pseudodata (a) and the data (b). The widths $\sigma_A(p_T)$ of the balance distribution as derived from the data and the smeared events, shown as a function of average p_{T} (c).

The true transverse momentum vector of the jet can be estimated by adding back the $E_{\mathrm{T}}^{\mathrm{miss}}$ vector. The response of this jet (R_2) is then given by:

$$R_2 \simeq \frac{\vec{p}_{\mathrm{T}}^{J} \cdot (\vec{p}_{\mathrm{T}}^{J} + \vec{E}_{\mathrm{T}}^{\mathrm{miss}})}{|\vec{p}_{\mathrm{T}}^{J} + \vec{E}_{\mathrm{T}}^{\mathrm{miss}}|^2}, \tag{7.10}$$

where $\vec{p}_{\mathrm{T}}^{J}$ is the reconstructed p_{T} of the jet associated with the $E_{\mathrm{T}}^{\mathrm{miss}}$. A sample of events where the $E_{\mathrm{T}}^{\mathrm{miss}}$ is associated with a single jet is selected by applying the following cuts:

- At least three jets with $p_{\mathrm{T}} > 130, 40, 40\,\mathrm{GeV}$
- $E_{\mathrm{T}}^{\mathrm{miss}} > 30\,\mathrm{GeV}$ which is parallel or anti-parallel to one, and only one, of the jets. To ensure this the jets are ordered in $\varphi_i = \Delta\varphi(j_i, E_{\mathrm{T}}^{\mathrm{miss}}); i = 1..n$ and two configurations are considered:
    - Parallel: In this case the $E_{\mathrm{T}}^{\mathrm{miss}}$ is a product of an under fluctuation and one requires that $|\varphi_1| < 0.1$. To rule out the cases where the source of the $E_{\mathrm{T}}^{\mathrm{miss}}$ is ambiguous it is required to be well separated from the other jets in φ by requiring $|\varphi_1| < \pi - |\varphi_n|$, and $|\varphi_{(n-1)}| > 0.5$.
    - Anti-Parallel: Here the $E_{\mathrm{T}}^{\mathrm{miss}}$ is the product of a jet energy over-estimate and so is required to be on the opposite side of the event from one of the jets. This topology is enforced by requiring $\pi - |\varphi_n| < |\varphi_1|$, $\pi - |\varphi_1| < 0.1$ and $\pi - |\varphi_{(n-1)}| > 0.5$.

To reduce the $Z \to \nu\nu + jj$ contamination of the control region the p_{T} of the two leading non-fluctuating jets are required to be larger than 130 GeV and 40 GeV. Figure 7.9 shows the R_2 distribution for b-tagged jets and non-b-tagged jets respectively as measured with data and using the jet smearing method, taken from the 2012 data stop analysis.

Source of systematic uncertainties

There are several systematic uncertainties in the method which must be evaluted and extrapolated into the final estimation in the signal regions. The uncertainties and their treatment will now be described.

Uncertainty on the correction to the Gaussian component

The correction to the Gaussian component is validated in data, however the size of the correction is varied up and down such that the smeared widths lie above and below the data to provide an estimation of the uncertainty on this correction. For

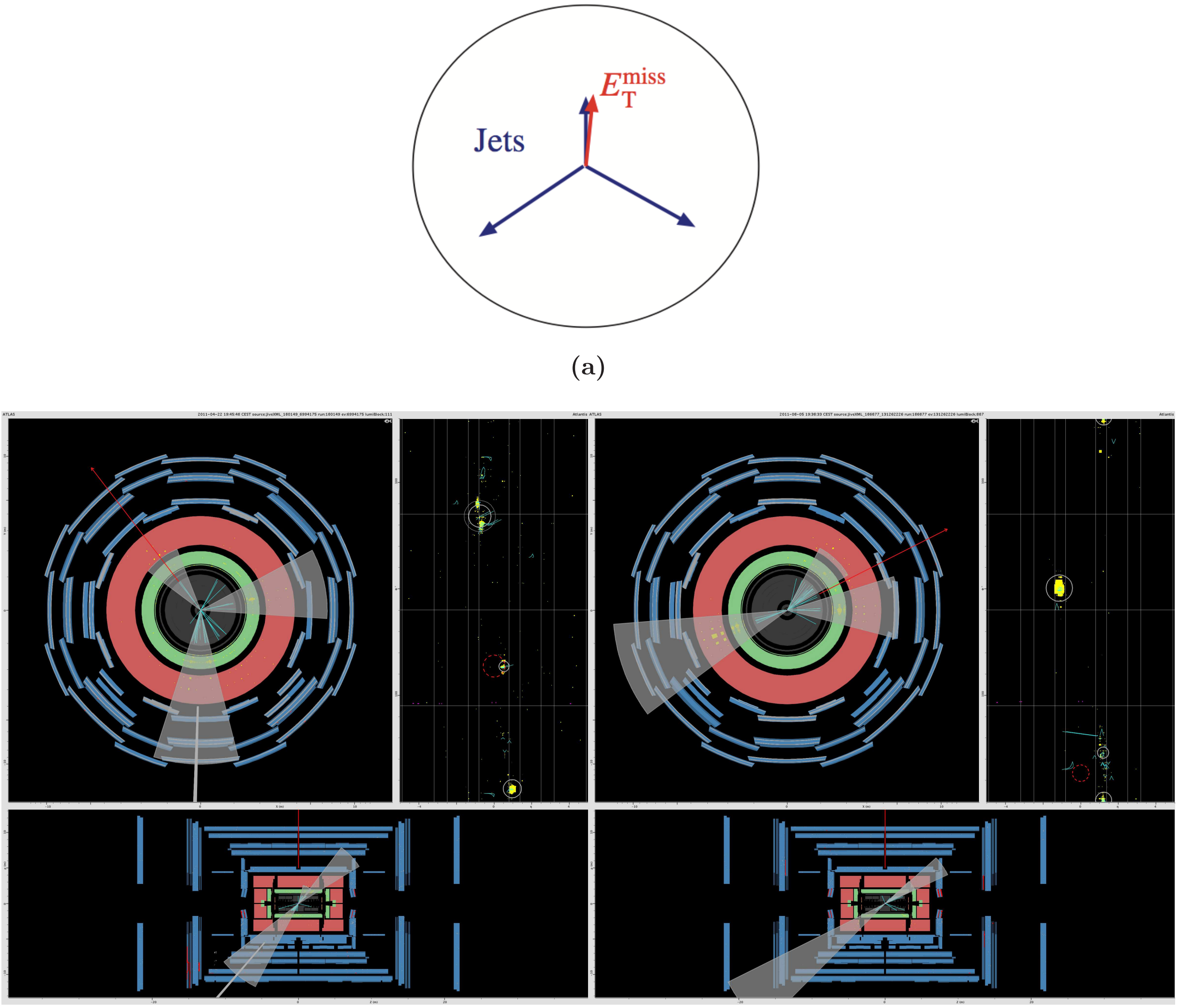

(a)

(b) **(c)**

Figure 7.8: (a) Schematic diagram of a Mercedes event. (b) A Mercedes event in the parallel configuration and (c) one in the anti-parallel configuration taken from 2011 data.

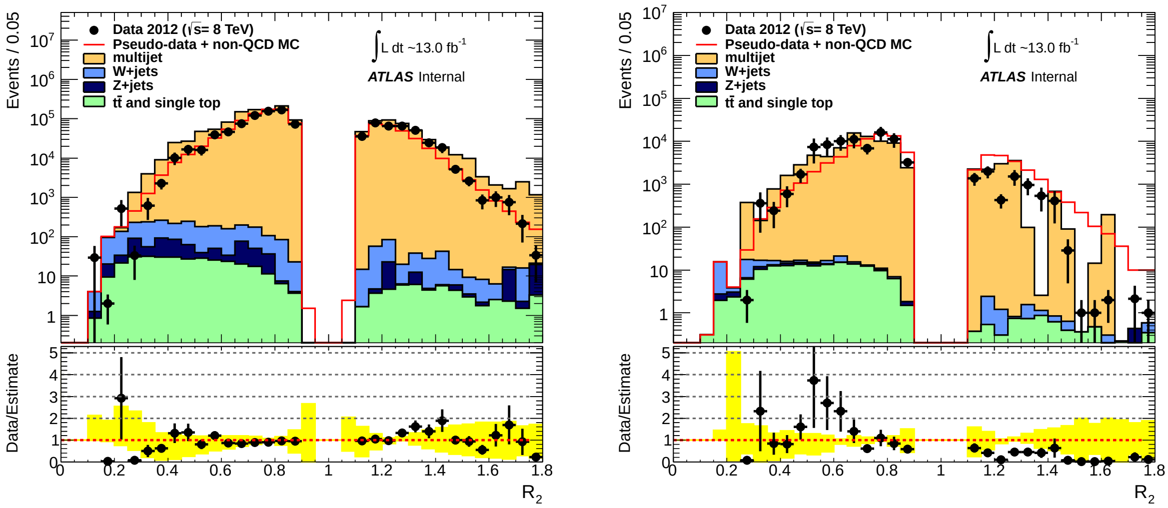

Figure 7.9: Events in the tails of the R_2 distribution as measured in Mercedes events for non-b-tagged jets (left) and b-tagged jets (right).

each variation, the corresponding estimate of the yield is calculated and the difference with respect to the nominal value is quoted as the uncertainty.

Tail uncertainty

To evaluate the uncertainty due to imperfect modelling of the tail component, the analysis is repeated after modifying the low side tail of the response function. The tail is scaled up and down by factors which push the smeared estimate above and below the R_2 distribution as calculated using the data. The estimated yield using these scaled responses is calculated and the differences with respect to the nominal yield are used as systematic uncertainties.

The total uncertainty on the estimate is calculated by adding the different components described above in quadrature. The exact value of the uncertainty is analysis dependent but is approximately 100% for the searches described in this thesis. This value is fairly large, however the estimated yield is often very small and these large uncertainties have very little impact on the final interpretation of the results.

7.4 Statistical interpretation

In order to assess the compatibility of the observed data with a particular model of new physics a well defined statistical treatment is essential. Claims of discovery or exclusion of a particular signal model can only be obtained with a rigorous mathematical framework.

In the analyses described in the following chapters the results are interpreted in terms of exclusion limits in the $m_{\tilde{t}_1} - m_{\tilde{\chi}_1^0}$ or $m_{\tilde{b}_1} - m_{\tilde{\chi}_1^0}$ planes. A framework called `HistFitter` [176], developed by the ATLAS SUSY group, is used for the statistical interpretation of results in Chapter 9. A subtly different framework was used in Chapter 8 but the underlying statistical treatment is the same.

The statistical model used is based on the profile likelihood ratio method [177]. The likelihood is constructed for each signal region and is the product of Poisson distributions, one for the signal region, P_{SR}, and another constraining the systematic uncertainties, C_{Syst}. In addition, it is possible to include a Poisson distribution for a control region, P_{CR}, in order to constrain specific backgrounds. A possible likelihood function is therefore:

$$L(\mathbf{n}|\mu, \mathbf{s}, \mathbf{b}, \alpha) = P_{\mathrm{SR}} \times P_{\mathrm{CR}} \times C_{\mathrm{Syst}}(\theta^0, \theta). \tag{7.11}$$

Each Poisson function P_i reflects the measured number of events, $\mathbf{n_i}$, in the region i and the expected number of events for signal $\mathbf{s}$ and background $\mathbf{b}$. Normalisation factors μ_{X} for background or signal are free parameters to adjust the magnitude of these contributions. The nuisance parameters α parameterise the systematic uncertainties on both the signal and the background using Gaussian distributions.

The inputs to the fit are; the expected and observed number of events in the control regions; transfer factors that can be used to propagate the event count from the control region to signal regions; fixed background estimates in the signal regions from either data driven or MC estimates.

Gaussian PDFs are used to model the systematic uncertainties, each having nominal values θ^0 around which θ can be varied when maximising the likelihood. Theoretical and background uncertainties are taken into account as well as detector uncertainties on the signal. Correlations between nuisance parameters can be treated properly as 1) overall scale factors fully correlated across the different regions and the different components (like luminosity), 2) scale factors fully correlated across the different regions but independent per component (like theory uncertainties), and 3) fully uncorrelated variables (like Monte Carlo statistical errors) with one parameter per bin. Table 7.1 summarises the systematic uncertainties considered in the likelihood.

The current ATLAS recommendation is not to directly consider the theoretical uncertainties on the signal yield in the limit setting machinery itself. Instead the limit-setting process is repeated with signal yields corresponding to the nominal cross-section $\pm 1\sigma^{\mathrm{SUSY}}_{\mathrm{Theory}}$

Name	Treatment
Luminosity	Fully correlated
MC statistics	Uncorrelated
Physics process modelling	
Pileup	Fully correlated
Total cross-section	Correlated per process
Generator	Correlated per process
ISR, FSR	Correlated per process
Parton Shower	
QCD jet smearing	
Object modeling	
JES	Fully correlated
JER	
Soft $E_{\mathrm{T}}^{\mathrm{miss}}$ scale	
Soft $E_{\mathrm{T}}^{\mathrm{miss}}$ resolution	
b-tagging	

Table 7.1: Summary of systematic uncertainties included in the likelihood.

where the term $\sigma_{\mathrm{Theory}}^{\mathrm{SUSY}}$ corresponds to the uncertainty arising from the choice of normalisation and factorisation scales as well as the PDF uncertainties. The latter also includes a variation of the strong coupling.

Chapter 8

Search for direct sbottom pair production

8.1 Introduction

In this Chapter a search for direct pair production of the supersymmetric partner to the bottom quark (sbottom) using 2.05 fb^{-1} of $\sqrt{s}$ = 7 TeV pp collision data collected by ATLAS is described. It is the first search of its kind to be performed by ATLAS.

The author initiated this analysis and was responsible for the introduction and development of the contransverse mass variable, used for discrimination between signal and background. The author's major contributions are optimisation of the signal region, described in §8.4, and estimation of the leptonic $t\bar{t}$ and W+jets backgrounds, described in §8.6.3. This analysis was published in a paper [2].

8.2 Existing experimental limits

The analysis targets sbottom pair production in the $\tilde{b} \to b\tilde{\chi}_1^0$ decay mode, shown in Figure 8.1. The final state is two b-jets and $E_{\mathrm{T}}^{\mathrm{miss}}$ coming from the undetected neutralinos.

Limits on this process have been set by previous experiments; CDF and D0 at the Tevatron [178, 179] and at LEP [180]. The exclusion limits from the most recent CDF and D0 results are shown in Figure 8.2.

The physics object definitions used are the *SUSY-early 2011* criteria described in §4.3.

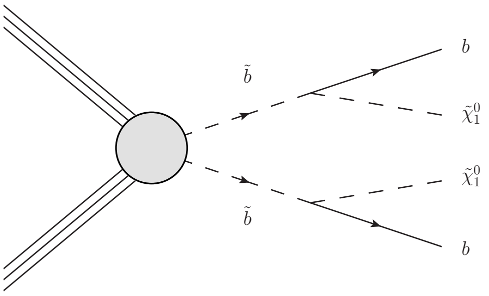

Figure 8.1: Feynman diagram of direct sbottom pair production signal being considered.

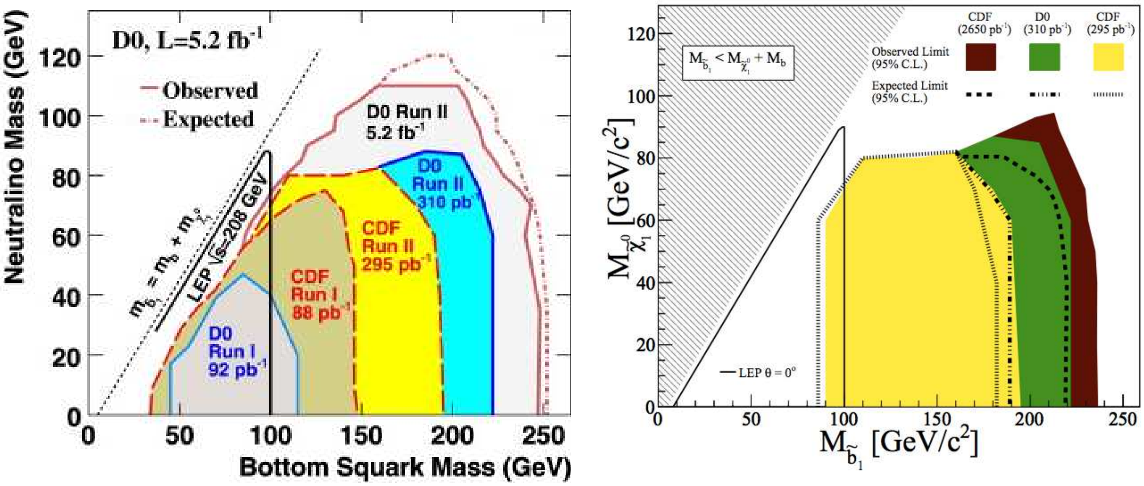

Figure 8.2: Limits on direct sbottom pair production from the Tevatron experiments, D0 [179] and CDF [178].

8.3 Dataset and simulated samples

This analysis uses *pp* collision data recorded by ATLAS during 2011. The dataset corresponds to an integrated luminosity of 2.05 fb^{-1}. The final state under consideration contains jets and $E_{\mathrm{T}}^{\mathrm{miss}}$, thus a combined single jet and $E_{\mathrm{T}}^{\mathrm{miss}}$ trigger is used to select events. At the event filter level this trigger requires events to contain at least one jet with $p_{\mathrm{T}} > 75$ GeV and $E_{\mathrm{T}}^{\mathrm{miss}} > 45$ GeV at EM scale. To be in the full efficiency region of the trigger, events must contain one offline jet with $p_{\mathrm{T}} > 130$ GeV and offline $E_{\mathrm{T}}^{\mathrm{miss}} > 120$ GeV at `EM+JES` scale.

Monte Carlo simulation samples are used for estimation of key standard model backgrounds, signal optimisation studies and setting exclusion limits. The Monte Carlo samples used in this study are simulated with the ATLAS full `GEANT4` simulation and are summarised in Table 8.1 along with their cross sections. When several generators are listed, the first corresponds to the one used for the default estimate and the remainder are used only for systematic studies.

QCD `PYTHIA6` with ATLAS MC10 tune settings [181] and modified `MRST2007LO*` PDF [182].

W/Z + jets `ALPGEN` interfaced with `JIMMY` [183]. Cross sections are computed with NNLO accuracy using `FEWZ` [184, 185] and the `CTEQ6L1` PDF. Additional samples are produced to simulate the contribution from Wbb, Wcc and Zbb.

Top pair production `MC@NLO` with final state parton showers and the underlying event simulated via interfaces to `HERWIG` and `JIMMY` respectively and the `CTEQ6.6` NLO PDF. The $t\bar{t}$ cross section is normalised to the NLO value including next-to-leading-log resummation corrections (NLO+NLL) [186].

Diboson and $t\bar{t}$+X WW, WZ and ZZ events are generated using `HERWIG` and the event yield normalised to NLO. Events of $t\bar{t}$ produced in association with W/Z or $b\bar{b}$ are not included in the standard top pair samples described above. Additional samples generated with `ALPGEN` interfaced with `HERWIG` are used for $t\bar{t}+b\bar{b}$. `MADGRAPH` interfaced with `PYTHIA6` is used to generate $t\bar{t}+W/Z$. In all cases, LO cross section values are used to normalize the event yield.

SUSY `HERWIG++` using the simplified model particle spectrum calculated with `MADGRAPH`. All sparticle masses except those involved in the production and decay are set very high to effectively decouple the particle spectrum. The `MRST2007LO*` PDF [187] is used. Samples are normalised to next-to-leading order (NLO) cross section predictions calculated using `PROSPINO` [188].

All MC samples are simulated with an average of 8 minimum bias interactions per bunch crossing. Contributions from out-of-time pileup have also been taken into account.

Production process	$\sigma\times$ BR in nb (perturbative order)	Generator
Dijet (QCD) ($\hat{p}_{\mathrm{T}}$ >8 GeV/c)	10.47×10^6 (LO)	`PYTHIA`, `ALPGEN`
$W\to\ell\nu$ (+jets)	31.4 (NNLO)	`ALPGEN`
$Z\to\nu\bar{\nu}$ (+jets)	5.82 (NNLO)	`ALPGEN`
$Z\to\ell^+\ell^-$ (+jets)	3.20 (NNLO)	`ALPGEN`
Diboson (WW, WZ, ZZ)	7.1×10^{-2} (NLO)	`HERWIG`, `ALPGEN`
$t\bar{t}$	0.164 (NLO + NLL)	`MC@NLO`, `POWHEG` `ALPGEN`, `ACERMC`
single t	0.85 (NLO + NLL)	`MC@NLO`
$t\bar{t}$+$b\bar{b}$	0.9×10^{-3} (LO)	`ALPGEN`, `ACERMC`
$t\bar{t}$+W/Z	0.4×10^{-3} (LO)	`MADGRAPH+PYTHIA`

Table 8.1: Summary of simulated samples for standard model backgrounds.

8.4 Signal region optimisation

In this analysis the main discrimination between signal and background is provided by the contransverse mass, M_{CT}, kinematic variable which has already been described in §5.3.1. With the final state of two b-jets and $E_{\mathrm{T}}^{\mathrm{miss}}$, after QCD rejection cuts the dominant background is $t\bar{t}$. M_{CT} is used in this analysis as it is particularly good at discriminating between the signal and $t\bar{t}$ background.

Taking (5.7) and adapting it to the case of $t\bar{t}$ production ($\delta = t$, $\alpha = W$) the kinematic endpoint in $M_{\mathrm{CT}}(b,b)$ is given by

$$M_{\mathrm{CT}}^{\max}(b,b) = \frac{m(t)^2 - m(W)^2}{m(t)} \simeq 140\ \mathrm{GeV}. \tag{8.1}$$

In the sbottom signal model ($\delta = \tilde{b}_1$, $\alpha = \tilde{\chi}_1^0$) the endpoint is given by

$$M_{\mathrm{CT}}^{\mathrm{max}}(b,b) = \frac{m(\tilde{b}_1)^2 - m(\tilde{\chi}_1^0)^2}{m(\tilde{b}_1)}, \tag{8.2}$$

which for relatively large mass splittings, $\Delta m = m_{\tilde{b}_1} - m_{\tilde{\chi}_1^0}$, values of $M_{\mathrm{CT}}^{\mathrm{max}}(b,b)$ larger than the $t\bar{t}$ kinematic limit can be achieved. Hence, $M_{\mathrm{CT}}(b,b)$ acts as a very effective discriminating variable. The boost-corrected version of the contransverse mass variable is used in the analysis in order to conservatively correct for unwanted boosts of the reference frame due to ISR [138].

M_{CT} should ideally be constructed using the two b-jets in the event. However, in order to inform our choice of the final jet selection three M_{CT} definitions are considered for optimisation, each differing in the choice of jet pairs used to reconstruct the M_{CT} observable.

1 $M_{\mathrm{CT}}(b_1, b_2)$: the two highest p_{T} b-tagged jets are used; only events where b_1 and b_2 are first and second leading jet, respectively, are selected.

2 $M_{\mathrm{CT}}(j_1, j_2)$: the first and second leading jets are used, regardless of whether they are tagged jets; the selected events must have at least two b-tagged jets with p_{T} above 50 GeV.

3 $M_{\mathrm{CT}}(b_1', b_2')$: the two highest p_{T} b-tagged jets, regardless of their position in the p_{T}-ordered jet list.

Figure 8.3 shows the M_{CT} distributions in MC for the three definitions with two representative signal samples and the $t\bar{t}$ background. Definition 2, $M_{\mathrm{CT}}(j_1, j_2)$, is found to be less effective for discrimination because it is easy to select the wrong combination of jet pairs to construct M_{CT}, this means the kinematic endpoint is not preserved. Definitions 1 and 3 give similar performance. However, the signal model under consideration is expected to have exactly two b-jets in the final state and these jets will have a significant p_{T} if Δm is sufficiently large. Additional jets from initial and final state radiation (of all flavours) are also expected but these jets will be significantly softer in p_{T}. For this reason an exclusive 2 jet selection is chosen where a veto on the p_{T} on the third jet of $p_{\mathrm{T}} < 50$ GeV is imposed. This gives good background rejection whilst maintaining signal efficiency.

The signal regions are defined by incremental M_{CT} thresholds in order to maximise signal efficiency whilst rejecting SM background. Increasing thresholds maintains sensitiv-

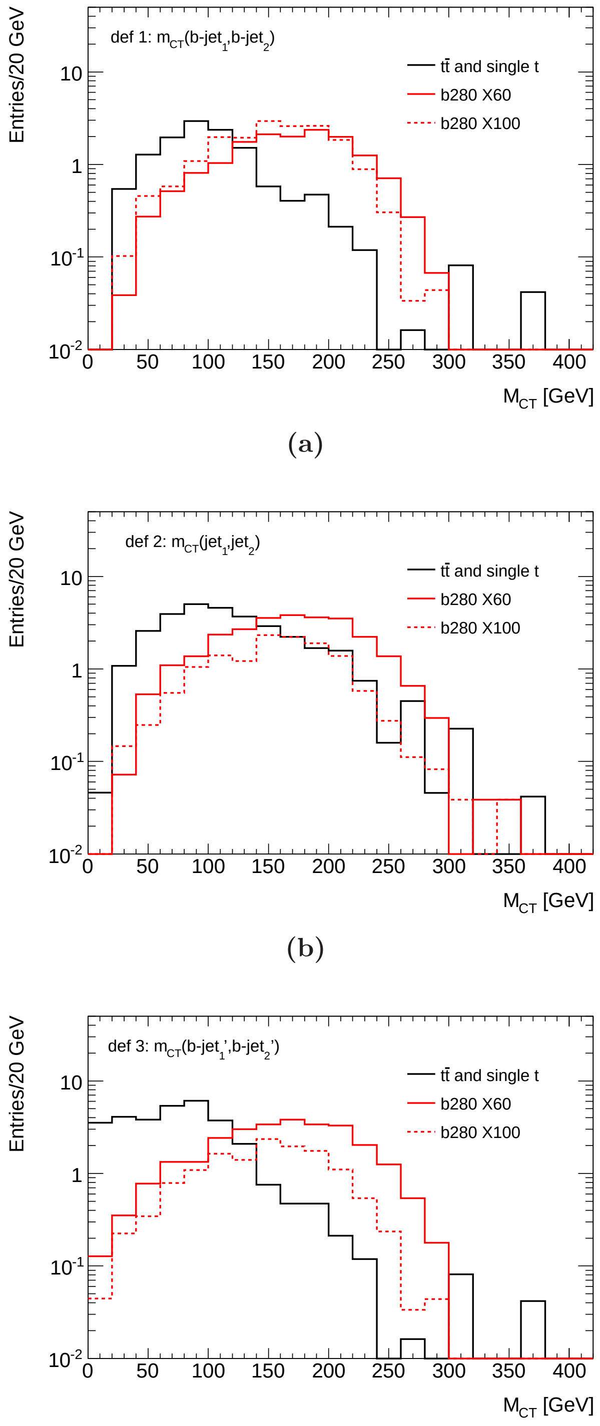

(a)

(b)

(c)

Figure 8.3: Distributions of M_{CT} constructed using the first and second leading jets only if they are b-tagged (a), the first and second leading jets regardless of b-tagging requirements (b) and the two leading b-tagged jets (c). Two representative signal samples are compared to $t\bar{t}$ background distribution.

ity across a range of sbottom and neutralino masses. The lowest threshold is M_{CT} above 100 GeV, where top pair production peaks.

It is important to understand the tails of the $M_{\mathrm{CT}}(b,b)$ distribution for the dominant $t\bar{t}$ background. For $t\bar{t}$ $M_{\mathrm{CT}}(b,b)$ is expect to be bounded from above at ~ 140 GeV. However, some events are found above this threshold. Figure 8.4 (top) shows the MC truth composition of the $t\bar{t}$ sample after requiring exactly two b-tagged jets as a function of M_{CT}.

When the two b-jets used in calculating $M_{\mathrm{CT}}(b,b)$ correspond to the two b-quarks originating from the top decays the kinematic endpoint is clearly preserved. The $M_{\mathrm{CT}}(b,b)$ tail is dominated by events where one of the two leading b-tagged jets is actually a c-jet arising from the hadronic decay of one of the W bosons. In this case the kinematic limit of ~140 GeV no longer applies. The composition is also shown in the bottom two plots of Figure 8.4, where semi-leptonic (b) and di-leptonic (c) $t\bar{t}$ contributions are considered separately. As expected the tail is dominated by semi-leptonic $t\bar{t}$ events.

8.5 Event selection

In order to enter the signal region events must satisfy event cleaning and data quality requirements. These include rejecting events with poorly reconstructed jets and requiring the event has a primary vertex with ≥ 5 tracks. Events must satisfy the trigger requirements described in §8.3 and there must be at least one jet with $p_{\mathrm{T}} > 75$ GeV and $E_{\mathrm{T}}^{\mathrm{miss}} > 45$ GeV. Offline the leading jet is required to have $p_{\mathrm{T}} > 130$ GeV and $E_{\mathrm{T}}^{\mathrm{miss}} > 130$ GeV is required to be in the fully efficient region of the trigger. To isolate the 0-lepton final state events that contain electrons with $p_{\mathrm{T}} > 20$ GeV or muons with $p_{\mathrm{T}} > 10$ GeV are vetoed. Rejection of the dominant QCD background is achieved by imposing topological constraints on the orientation of jets and $E_{\mathrm{T}}^{\mathrm{miss}}$ and the relative magnitude of $E_{\mathrm{T}}^{\mathrm{miss}}$ compared to the hadronic activity in the event. The azimuthal angle between the leading two jets and $E_{\mathrm{T}}^{\mathrm{miss}}$ is required to be larger than 0.4 and the ratio of $E_{\mathrm{T}}^{\mathrm{miss}}$ to m_{eff} is required to be larger than 0.25, where m_{eff} is defined to be the scalar sum of $E_{\mathrm{T}}^{\mathrm{miss}}$ and jet momenta in the event. It is then required that events contain exactly two b-jets. This serves to suppress the W+jets and Z+jets backgrounds whilst having a high efficiency for the SUSY signal. The remaining dominant background is $t\bar{t}$. Finally the signal regions are defined by incremental $M_{\mathrm{CT}}(b,b)$ cuts. The selection is summarised in Table 8.2.

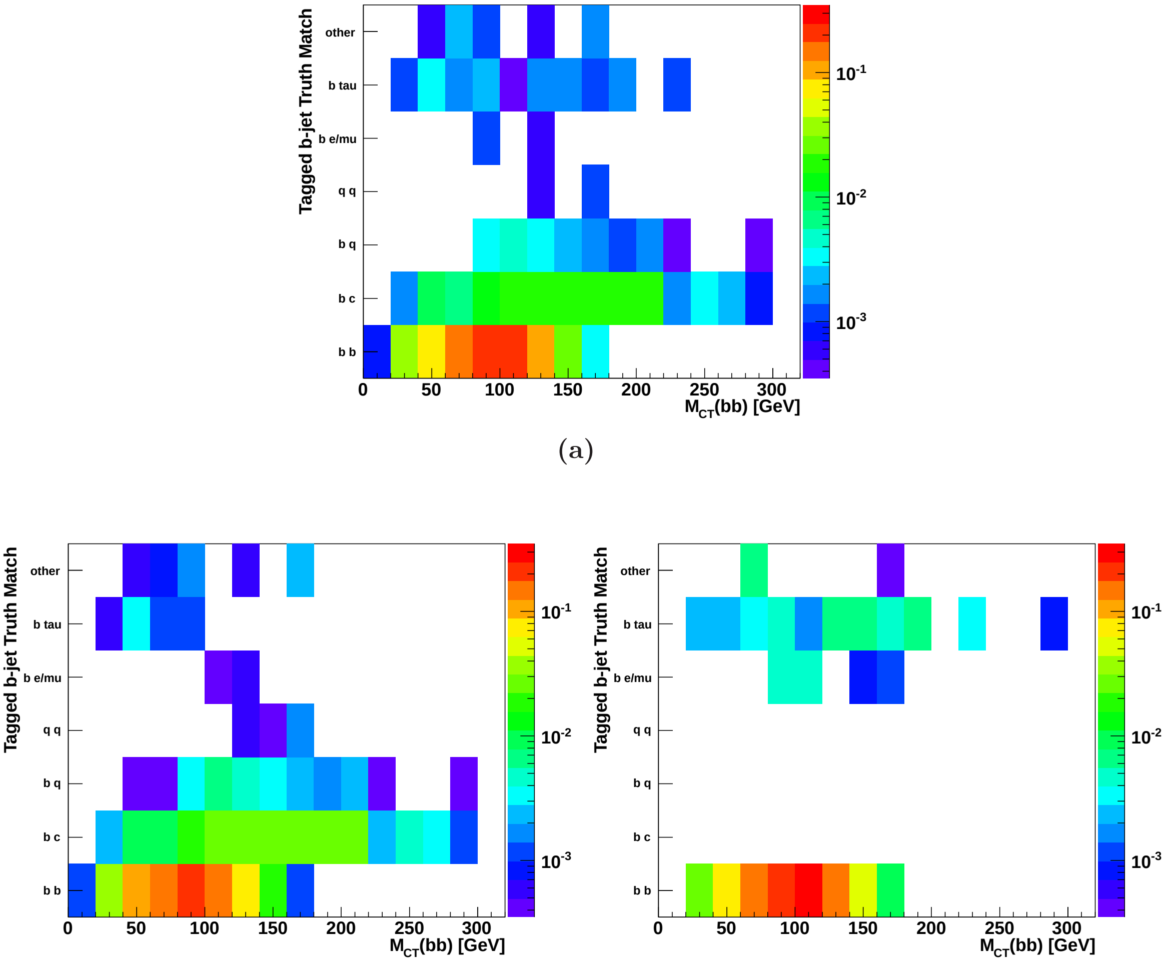

(a)

(b)

(c)

Figure 8.4: (a) Composition of the $t\bar{t}$ sample after requiring 2 b-tagged jets and exclusive selection as a function of M_{CT}. Also shown for the semi-leptonic (b) and dilepton (c) components separately.

Lepton veto: e: $p_{\mathrm{T}} > 20$ GeV, μ: $p_{\mathrm{T}} > 10$ GeV
== 2 jets $p_{\mathrm{T}} > 130, 50$ GeV
veto 3^{rd} jet, $p_{\mathrm{T}} > 50$ GeV
$E_{\mathrm{T}}^{\mathrm{miss}} > 130$ GeV
$E_{\mathrm{T}}^{\mathrm{miss}}/M_{\mathrm{eff}} > 0.25$
minimum $\Delta\varphi(E_{\mathrm{T}}^{\mathrm{miss}}, jet_{1,2}) > 0.4$ rad, $\Delta\varphi(E_{\mathrm{T}}^{\mathrm{miss}}, jet_{3}) > 0.2$ rad
== 2 b-jets $p_{\mathrm{T}} > 50$ GeV
$M_{\mathbf{CT}}$ **>100/150/200 GeV**

Table 8.2: Definition of the three signal regions, each characterised by different M_{CT} thresholds.

8.6 Background estimation

Estimation of the SM backgrounds purely from MC lead to significant systematic uncertainties due to the generator modelling and can suffer from limited statistics. As such, dedicated control regions are defined to use the data to aid estimation of the dominant backgrounds. A 1-lepton control region is defined for validation of the MC for the $t\bar{t}$, single t and production of a W in association with heavy flavour jets (W+HF) backgrounds. A 2-lepton control region is defined for validation of the background from production of a Z in association with heavy flavour jets (Z+HF). In both cases estimation of the contribution of these backgrounds in the signal regions use the semi-data-driven *transfer factor* method, described in §7.3.1. The QCD background is estimated using the data-driven jet smearing method.

8.6.1 QCD background estimation

Estimation of the QCD background is provided by the jet smearing method, previously discussed in §7.3.2. Although the probability that a QCD event contains heavy flavour jets and that one or more of those jets gives rise to significant $E_{\mathrm{T}}^{\mathrm{miss}}$ is small, the comparatively large QCD cross section means that this is a very important background to constrain.

The di-jet balance analysis is used to derive corrections to the gaussian core of the response function in order to better describe the data. The *Mercedes* analysis is used to validate the tails of the response function. It was found that the low side tail of the response function would better describe the data with a small correction to increase the tail component.

The estimation is validated in a QCD enriched control region that is defined by reversing the cut on the angle between the two leading jets and the $E_{\mathrm{T}}^{\mathrm{miss}}$: $\Delta\varphi(E_{\mathrm{T}}^{\mathrm{miss}}, jet_{1,2}) < 0.4$. This gives a control sample to validate the technique and calculate the normalisation of the QCD estimate. The normalisation is taken to be the ratio of the number of events in data, subtracting the contribution of non-QCD SM backgrounds from MC, to the number of *pseudodata* events passing the selection cuts.

Selection	Total
2 b-jets jets	1.77±0.90
M_{CT} >100 GeV	1.58±0.80
M_{CT} >150 GeV	1.40±0.29
M_{CT} >200 GeV	0.09±0.05

Table 8.3: Estimate of the QCD background for 2.05 fb^{-1} from jet smearing method for the 2-jet exclusive selections in the various Signal regions.

The estimate of the QCD background in each of the signal regions using this method is given in Table 8.3.

8.6.2 Leptonic $t\bar{t}$ and $\mathrm{W + HF}$ control region

The control region is defined by reversing the lepton veto and instead selecting events that contain exactly one lepton. The same pre-selection requirements are imposed as for the signal region except the jet+$E_{\mathrm{T}}^{\mathrm{miss}}$ trigger is replaced by single electron and single muon triggers. The jet selection is loosened to require at least two jets rather than exactly two jets to increase statistics. An additional requirement that the transverse mass between the lepton and $E_{\mathrm{T}}^{\mathrm{miss}}$, $m_T(l, E_{\mathrm{T}}^{\mathrm{miss}})$, be between 40 and 100 GeV is imposed. The lower bound reduces the contribution from QCD events containing a fake lepton whilst the upper bound reduces possible signal contamination and also reduces the contribution from di-leptonic $t\bar{t}$. The latter keeps the composition of the background closer to that of the signal regions. The $E_{\mathrm{T}}^{\mathrm{miss}}$ threshold is reduced and the QCD rejection cuts dropped completely, again to increase statistics. The 1-lepton control region selection is summarised in Table 8.4

The upper threshold of 100 GeV on m_{T} is introduced to reduce the fraction of events that enter the control region from di-leptonic $t\bar{t}$ where one of the leptons is lost. Figures 8.5 (a) and (b) shows the composition of the $t\bar{t}$ sample in terms of semi-leptonic and di-leptonic

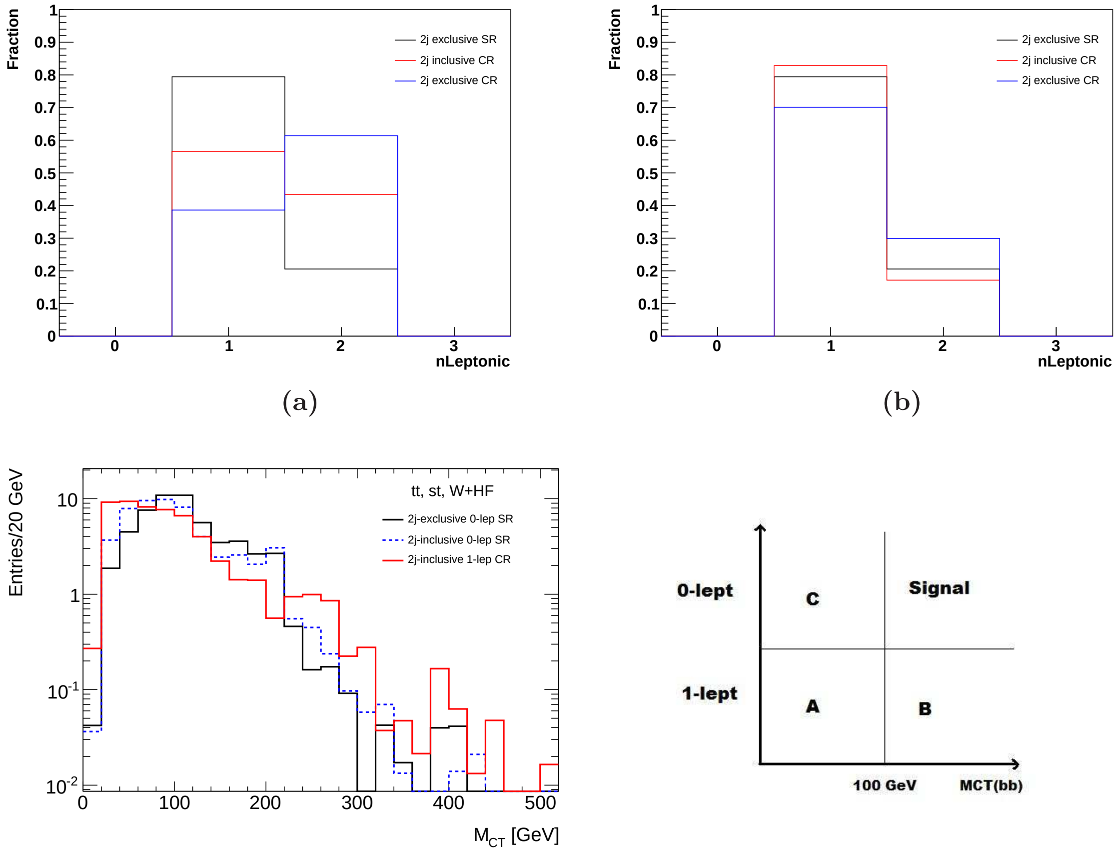

(a) (b)

(c) (d)

Figure 8.5: Background composition in the signal and control regions after the full selections are applied except the M_{CT} requirement, with (a) no m_{T} requirement and (b) requiring $40 < m_{\mathrm{T}} < 100$ GeV. (c) Shape comparison for the M_{CT} distribution in the signal region and control regions. (d) Illustration of control regions in M_{CT} VS N lepton employed for the determination of the top and W+HF background.

== 1 lepton: e/μ: $p_{\mathrm{T}} > 25$ GeV
>= 2 jets $p_{\mathrm{T}} > 130, 50$ GeV veto 3^{rd} jet, $p_{\mathrm{T}} > 50$ GeV
$E_{\mathrm{T}}^{\mathrm{miss}} > 80$ GeV
== 2 b-jets $p_{\mathrm{T}} > 50$ GeV
$40 < m_T(l, E_{\mathrm{T}}^{\mathrm{miss}}) < 100$ GeV
$M_{\mathbf{CT}}$ **>100/150/200 GeV**

Table 8.4: Definition of the 1-lepton control region.

$t\bar{t}$ fractions with and without the m_{T} requirement. The composition of signal region and control region is closer with the m_{T} requirement. It is desirable to keep the background composition as similar as possible to the signal region in order to reduce reliance on the MC to extrapolate between the two regions.

The use of a fully data-driven estimation of these backgrounds using the *ABCD* method was considered. In this method four regions are defined in a 2-dimensional space where extrapolations between each can give a purely data-driven estimate. Figure 8.5(d) shows the four regions. They are defined by two regions in lepton multiplicity and two regions separated by the $M_{\mathrm{CT}}(b,b) = 100$ GeV boundary. Region B is designed to have kinematics close to those of the signal region, while the requirement of 1-lepton ensures negligible signal contamination. However, for this method to work, the $M_{\mathrm{CT}}(b,b)$ distribution must have the same shape in both the signal region and 1-lepton control region. Figure 8.5(c) shows there is a systematic difference in shape and therefore the *ABCD* cannot be employed here, the *transfer factor* method is used instead.

Taking (7.6) and applying it in this case, the number of top and W+HF events in the signal regions ($N_S R^{top+W+HF}$) can be estimated from the following relation,

$$N_{SR}^{top+(W+HF)} = \left(\frac{N_{SR}}{N_{CR}}\right)_{MC}^{top+(W+HF)} \times [N_{CR}^{data} - N_{CR}^{Z,MC} - N_{CR}^{others,MC} - N_{CR}^{QCD}]. \qquad (8.3)$$

The QCD multijet background in the 1-lepton control region, N_{CR}^{QCD}, is estimated using the 1-dimensional implementation of the *matrix method* described in §6.4.1. $N_{CR}^{others,MC}$ indicates the diboson and $t\bar{t} + W/Z/b\bar{b}$ background contributions that are estimated from MC. As discussed in §7.3.1 this approach allows some cancellation of the JES, b-tagging and theoretical systematic uncertainties.

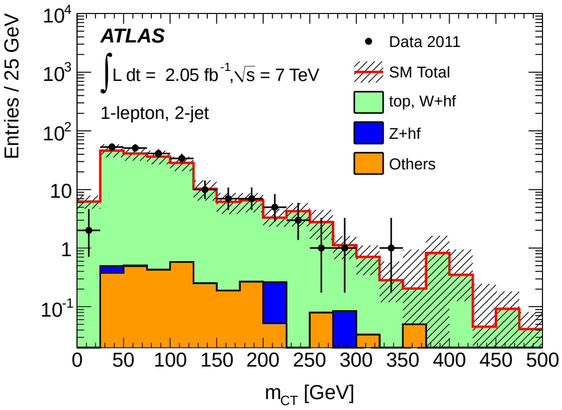

Figure 8.6: Distribution of M_{CT} (b,b) in the 1-lepton control region. Figure from [2].

Figure 8.6 shows a comparison of the data with SM expectation for the full 1-lepton control region selection except the $M_{\mathrm{CT}}(b,b)$ cuts. The agreement is very good, validating the capability of the MC to reproduce the data in this regime and hence in the signal region.

8.6.3 Z + HF control region

The signal region contains a contribution of approximately 25% from Z+HF ($Z \to \nu\nu$) before any $M_{\mathrm{CT}}(b,b)$ cut is applied. This rises up to approximately 35% in the higher $M_{\mathrm{CT}}(b,b)$ signal regions after the contribution from $t\bar{t}$ is reduced. It is very hard to define a control region dominated by Z+HF but orthogonal to the signal region. Instead, a 2-lepton control region is used to select $Z \to ll$ events. The transverse momenta of the leptons is then vectorially subtracted from the $E_{\mathrm{T}}^{\mathrm{miss}}$ to emulate $Z \to \nu\nu$ events, this is referred to as $Z \to l'l'$. Other than this modification a very similar approach to that of the previous subsection is taken to estimate this background, again using the *transfer factor method.*

The control region is defined by requiring exactly two opposite sign same flavour leptons. The leptons' transverse momenta are vectorially subtracted from the $E_{\mathrm{T}}^{\mathrm{miss}}$ in order the mimic the $Z \to \nu\nu$ topology. This modified $E_{\mathrm{T}}^{\mathrm{miss}}$ must be greater than 50 GeV. At least two jets with $p_{\mathrm{T}} > 80, 50$ GeV are required. Finally the invariant mass of the lepton pair is required to be compatible with a Z: $81 < m_{ll} < 101$ GeV. The selection is summarised in Table 8.5.

Using the *transfer factor method* the estimated number of events in the signal region is given by the relation

== 2 leptons: $ee/\mu\mu$: $p_{\mathrm{T}} > 25/20$ GeV
>= 2 jets $p_{\mathrm{T}} > 80, 50$ GeV
$E_{\mathrm{T}}^{\mathrm{miss(leptoncorrected)}} > 50$ GeV
== 2 b-jets $p_{\mathrm{T}} > 50$ GeV
$81 < m_{ll} < 101$ GeV
$M_{\mathbf{CT}}$ **>100/150/200 GeV**

Table 8.5: Definition of the 2-lepton control region.

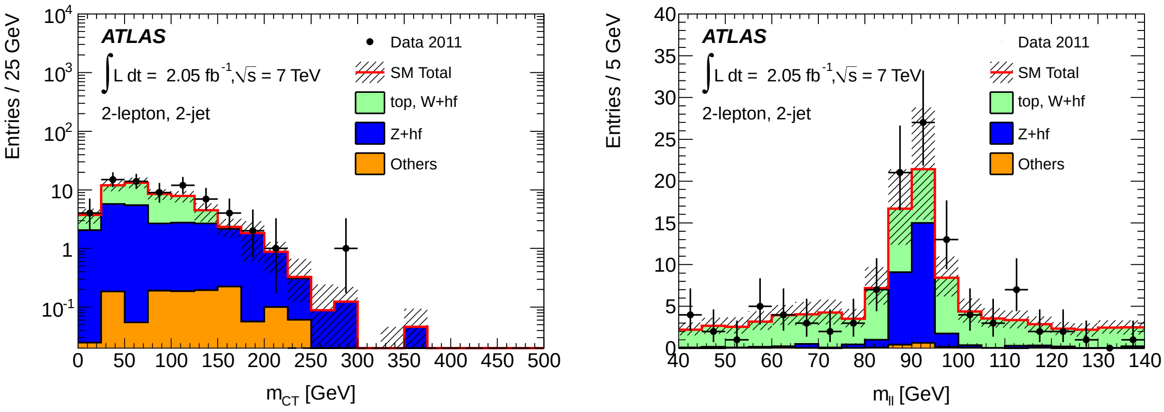

Figure 8.7: Distributions of $M_{\mathrm{CT}}(b,b)$ (left) and $m_{l^+l^-}$ (right) in the 2-lepton control region. Figures from [2].

$$N_{SR}^{Z\to\nu\nu+jets} = \left(\frac{N_{SR}^{Z\to\nu\nu+jets}}{N_{CR}^{Z\to l'l'+jets}}\right)_{MC} \times [N_{CR}^{data} - N_{CR}^{top,MC} - N_{CR}^{others,MC} - N_{CR}^{QCD}]. \quad (8.4)$$

Figure 8.7 shows the $M_{\mathrm{CT}}(b,b)$ and $m_{l^+l^-}$ distributions in the two 2-lepton control region for the full selection without any M_{CT} cuts applied. Z+HF and single top and $t\bar{t}$ production constitute approximately half of the events each, the other backgrounds are negligible and no signal contamination is expected. Note that the contribution from single top and $t\bar{t}$ is estimated from MC but is scaled by a transfer factor derived from the m_{ll} sidebands. The value of this is found to be 1.1 with an uncertainty of about 30% due to b-tagging uncertainties. Excellent agreement between the data and SM expectation is observed, validating the MC estimate of this background.

8.6.4 Other backgrounds

Several other SM processes that contribute to the final state are considered such as diboson and associated production of $t\bar{t}$ with W, Z bosons or $b\bar{b}$. These processes only make up a small fraction of the signal region yields and predictions are taken purely from MC.

8.7 Systematic uncertainties

Several sources of systematic uncertainties are considered in the analysis. The dominant contributions come from uncertainties in the $t\bar{t}$ background MC modelling, b-tagging efficiency, JES and JER.

In the QCD estimate the uncertainties considered are those due to modelling of the gaussian core and lowside tail, along with the JES and b-tagging uncertainties. The lowside tail and b-tagging uncertainties dominate, resulting in an uncertainty on the final estimate of 50%-100% in the signal region depending on the M_{CT} selection.

The important systematic uncertainties in the top and W+HF estimation are the residual (not cancelled in the transfer factor ratio) JES, b-tagging, lepton identification and theory uncertainties. The dominant contribution comes from the top theoretical uncertainties. These are estimated using dedicated `ACERMC` samples with variations in the amount of ISR and FSR, and through comparison of the default `Alpgen` samples with `MC@NLO`. The theory uncertainty on the estimate is between 10% and 15% depending on the M_{CT} selection. Other important contributions come from b-tagging efficiencies and JES which range from 5%-10% and 5%-15%, respectively, also subject to the M_{CT} selection.

In the $Z \rightarrow \nu\nu$+HF estimate the systematic uncertainties considered are JES, b-tagging efficiency and theory. The dominant contribution comes from the residual JES uncertainty which ranges from 15%-20% depending on the M_{CT} selection. The uncertainty on b-tagging efficiency is 4%-7% depending on the M_{CT} selection.

The systematic uncertainty on the background expectation due to the finite data statistics in the control regions varies from 21% to 44%, increasing with the M_{CT} selection applied.

8.8 Results and interpretation

The number of events observed in data compared to the expectation from SM backgrounds is shown in Table 8.6 and the correspondiing M_{CT} and $E_{\mathrm{T}}^{\mathrm{miss}}$ distributions are shown in

M_{CT}	top, W+HF	Z+HF	Others	Total SM	Data
0	67 ± 10	23 ± 8	3.6 ± 1.5	94 ± 16	96
100	36 ± 10	23 ± 9	3.1 ± 1.6	62 ± 13	56
150	12 ± 5	12 ± 6	2.7 ± 0.9	27 ± 8	28
200	3.2 ± 1.6	3.9 ± 3.2	1.0 ± 0.9	8.1 ± 3.5	10

Table 8.6: Number of events observed and expected from SM backgrounds for an integrated luminosity of 2.05 fb^{-1}.

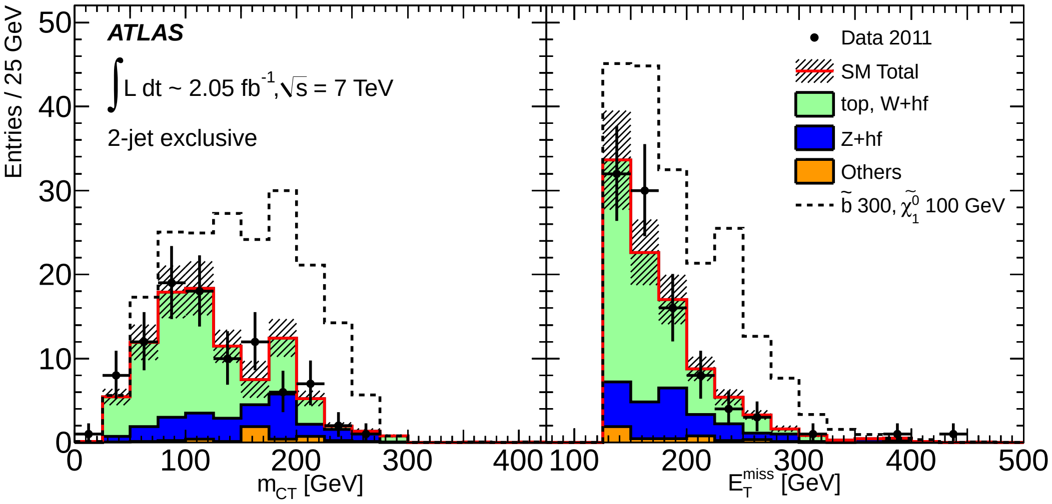

Figure 8.8: Distribution of the $M_{\mathrm{CT}}(b,b)$ (left) and $E_{\mathrm{T}}^{\mathrm{miss}}$ (right) with all the signal region selection applied except the M_{CT} selection. Figure from [2].

Figure 8.8. The quoted errors include the full systematic uncertainties. No significant excess is observed, the observation is consistent with the SM expectation.

The results are interpreted in terms of 95% confidence level upper limits using the CL$_s$ prescription. At each point on $m_{\tilde{b}} - m_{\tilde{\chi}_1^0}$ plane the signal region giving the best expected sensitivity is used. Figure 8.9 shows the corresponding exclusion limits in the $m_{\tilde{b}} - m_{\tilde{\chi}_1^0}$ plane. The dashed blue line shows the expected exclusion limit and the dark green dashed lines correspond to the ±1σ uncertainty on the expected limit. The red line indicates the observed exclusion and the yellow band shows the ±1σ theoretical uncertainty on the signal cross section.

The quoted exclusion is conservatively chosen to be that of the -1σ signal cross section band. For a massless neutralino sbottom masses are excluded up to 390 GeV. For neutralino mass of 120 GeV sbottom masses are excluded for $275 < m_{\tilde{b}} < 350$ GeV.

It is also possible to set model independent limits on the effective cross section, σ_{eff},

M_{CT}	σ_{eff}(Expected) [fb]	σ_{eff}(Observed) [fb]
100	15.2	13.4
150	9.2	9.6
200	4.7	5.6

Table 8.7: Expected and observed 95% confidence level upper limits on the effective cross section for new physics.

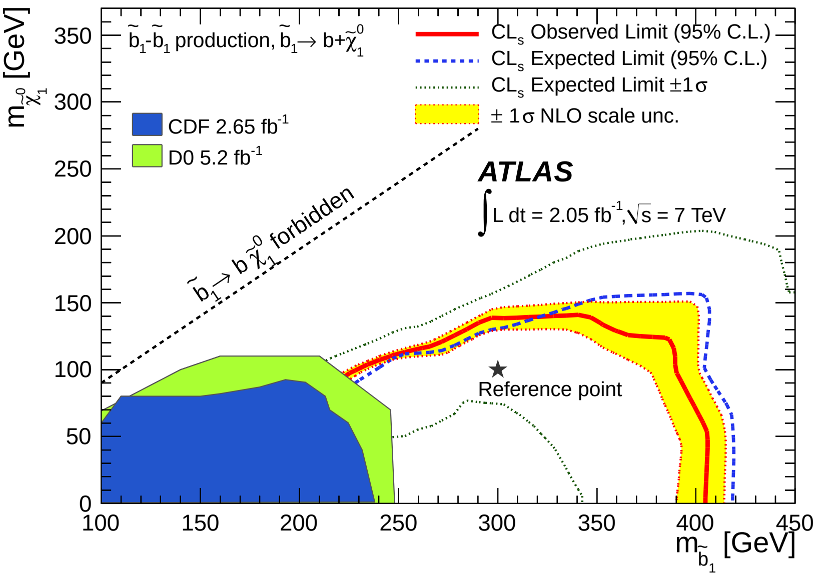

Figure 8.9: Expected and observed exclusion limits in the $m_{\tilde{b}_1} - m_{\tilde{\chi}_1^0}$ plane. Figure from [2].

(including acceptance and efficiency corrections) for new physics in each signal region. The 95% confidence level upper limits are given in Table 8.7.

8.9 Summary and conclusions

This search for sbottom quark direct pair production was performed using 2.05 fb^{-1} of $\sqrt{s}$ = 7 TeV ATLAS data collected in 2011. The search was dedicated on the $\tilde{b}_1 \to b\tilde{\chi}_1^0$ decay mode assuming a branching ratio of 100%. No significant excess was observed in the data and exclusion limits at the 95% confidence level were set. These limits significantly extend the reach of previous searches.

Chapter 9

Search for direct stop pair production

9.1 Introduction

In this Chapter searches for direct pair production of the supersymmetric partner to the top quark (stop) are described. The first uses 4.7 fb^{-1} of $\sqrt{s}$ = 7 TeV pp collision data collected by ATLAS in 2011 and the second uses 20.5 fb^{-1} of $\sqrt{s}$ = 8 TeV pp collision data collected by ATLAS in 2012.

As well as being responsible for initiating these analyses, the author's contributions in this Chapter are the introduction of a key new discriminating variable for rejection of the dominant $t\bar{t}$ background, described in §9.2.1, and general signal region optimisation, described in §9.4.2. The author was also responsible for estimation of the QCD background, described in §9.3.3 and §9.4.3; generation of the $t\bar{t}$+W/Z background and estimation of the corresponding generator systematic uncertainties, described in §9.4.3. The analysis using 2011 data was published in a paper [3] and the analysis using 2012 data was published as a conference note [4]. The author co-edited the internal documentation in both cases.

9.2 Analysis strategy

Both analyses target the scenario where the lightest stop decays $\tilde{t}_1 \rightarrow t\tilde{\chi}_1^0$, as shown in Figure 9.1, with a branching ratio taken to be 100%. The analyses focus on the 0-lepton final state, and hence the all-hadronic $t\bar{t}$ decay mode. The final state under consideration consists of six jets, b-jets and significant $E_{\mathrm{T}}^{\mathrm{miss}}$.

The analysis strategy is the same for both analyses. A general overview of the selection procedure is given here, more detail is provided in the following sections.

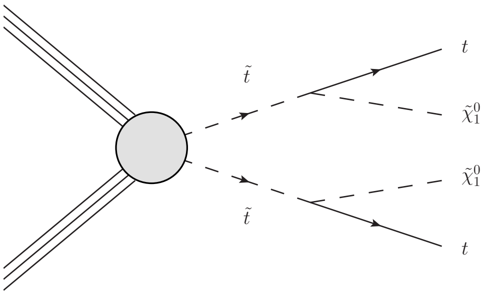

Figure 9.1: Feynman diagram of direct stop pair production signal being considered.

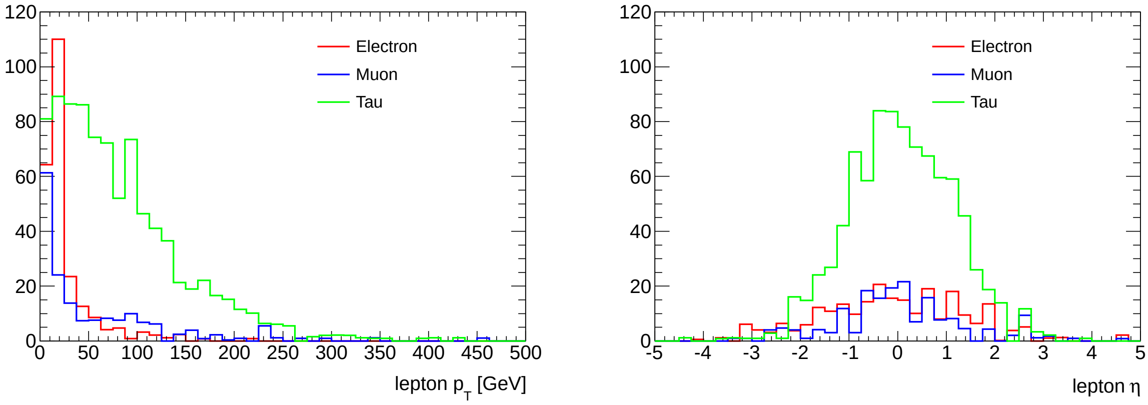

Figure 9.2: The true p_{T}, η, and flavour of the lepton originating from the top decay. This is taken from $sqrts$ = 7 TeV semi-leptonic and di-lepton $t\bar{t}$ MC samples after a basic preselection requiring 6 jets and $E_{\mathrm{T}}^{\mathrm{miss}} > 150$ GeV.

Firstly, events must satisfy trigger requirements based on some criteria on the leading jet p_{T} and/or $E_{\mathrm{T}}^{\mathrm{miss}}$. Then events containing leptons are vetoed and, in order to identify events consistent with all-hadronic $t\bar{t}$, the event is required to contain at least six jets. To reject the QCD background some $E_{\mathrm{T}}^{\mathrm{miss}}$ preselection threshold is applied. Furthermore, cuts on the azimuthal angle between the leading three jets and $E_{\mathrm{T}}^{\mathrm{miss}}$ are applied and the direction of $E_{\mathrm{T}}^{\mathrm{miss}}$ (calculated by the calorimetry) is required to coincide with that of the missing transverse momentum calculated from tracks in the event, $E_{\mathrm{T}}^{\mathrm{miss\,Track}}$. To reject a significant amount of W/Z+jets background events are required to contain at least one b-jet. The exact b-jet requirements differ between the 2011 and 2012 analyses and are described in more detail in §9.3 and §9.4.

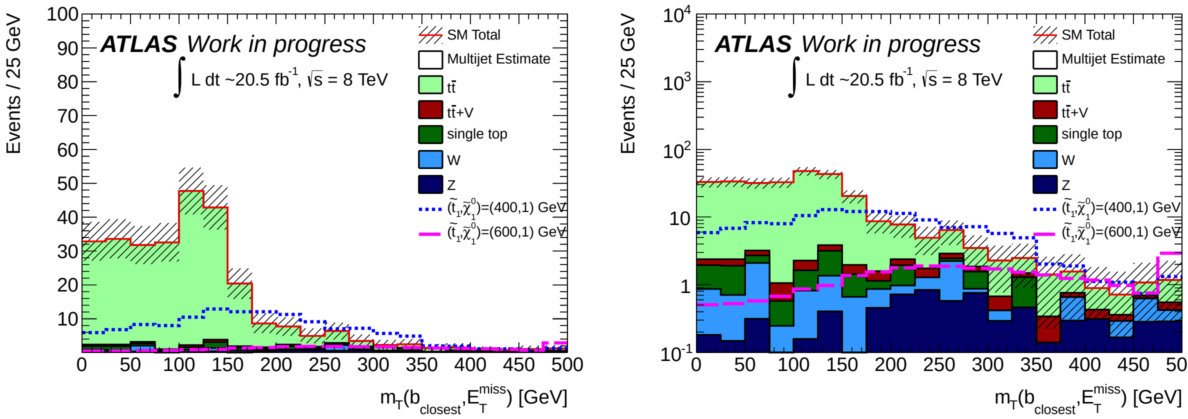

Figure 9.3: Distribution of $m_T(b, E_{\mathrm{T}}^{\mathrm{miss}})$ with the 2012 signal region selection, except the cut on this variable, on a linear (Left) and logarithmic (Right) scales.

9.2.1 Semi-leptonic $t\bar{t}$ rejection

The remaining dominant background is semi-leptonic $t\bar{t}$ where the lepton has either gone out of acceptance, been mis-identified or is a τ lepton that decays hadronically and is reconstructed as a jet. The relative contributions of each component are shown in Figure 9.2.

Transverse mass

A kinematic variable has been developed and optimised specifically for this analysis to remove the majority of the remaining leptonic $t\bar{t}$ background whilst maintaining high signal efficiency. The variable exploits the kinematic constraints on the decay products of the top quark.

In a W boson decay $W \to l\nu$ the transverse mass between the lepton and $E_{\mathrm{T}}^{\mathrm{miss}}$, $m_T(l, E_{\mathrm{T}}^{\mathrm{miss}})$, is bounded from above by m_W. Analogously, in a top decay, $t \to bW$, the transverse mass between the b-quark and W boson is bounded from above by m_t. In the high $E_{\mathrm{T}}^{\mathrm{miss}}$ regime that this analysis focuses upon it is a reasonable assumption that the majority of the transverse momentum of the leptonically decaying W is imparted to the neutrino. Hence, if the assumption $p_{\mathrm{T}}(W) \simeq E_{\mathrm{T}}^{\mathrm{miss}}$ is made, the following relation is obtained

$$m_T(b, E_{\mathrm{T}}^{\mathrm{miss}}) \equiv \sqrt{2 p_{\mathrm{T}}(b) E_{\mathrm{T}}^{\mathrm{miss}} (1 - \cos \Delta\varphi_{b E_{\mathrm{T}}^{\mathrm{miss}}})} \leq m_t. \tag{9.1}$$

As two b-quarks are present in $t\bar{t}$ events there is an ambiguity in the identification of which b-jet is associated to the leptonic side of the decay. It was found that selecting the b-jet closest to the $E_{\mathrm{T}}^{\mathrm{miss}}$ in φ is a suitable choice. The stop signal model is not bounded from above at m_t, hence, a large increase in sensitivity can be achieved by cutting on this variable. Figure 9.3 gives an impression of the discriminating power possible with this variable.

$t\bar{t}$ reconstruction

Further requirements for events to be consistent with the fully-hadronic $t\bar{t}$ decay mode can be imposed. Reconstruction of the two top quarks can be achieved by collecting together two sets of three-jet objects, based on their consistency with the $t\bar{t}$ topology. Although several methods for allocating jets to two top quarks are available, one of the simplest is used in these analyses. It is referred to as the ΔR_{min} method and the algorithm is defined as follows:

- Find the two jets closest in ΔR. Combine them to form a W candidate.
- Find the next jet closest in ΔR to the W. Combine this with the jets from the W candidate to form a top quark candidate. The mass of this candidate is referred to as $m(t_1)$.
- Repeat these steps with the remaining jets in order to construct a second top quark candidate. The mass of this candidate is referred to as $m(t_2)$.

The mass of both reconstructed top candidates can then be considered in the selection criteria optimisation. The difference between the truth and reconstructed top candidates in the MC is shown in Figure 9.4 for lepton+jets $t\bar{t}$ events and a signal sample. The reconstructed masses provide additional discrimination between the signal and semi-leptonic $t\bar{t}$ background but also removes a large fraction of any remaining W/Z+jets background.

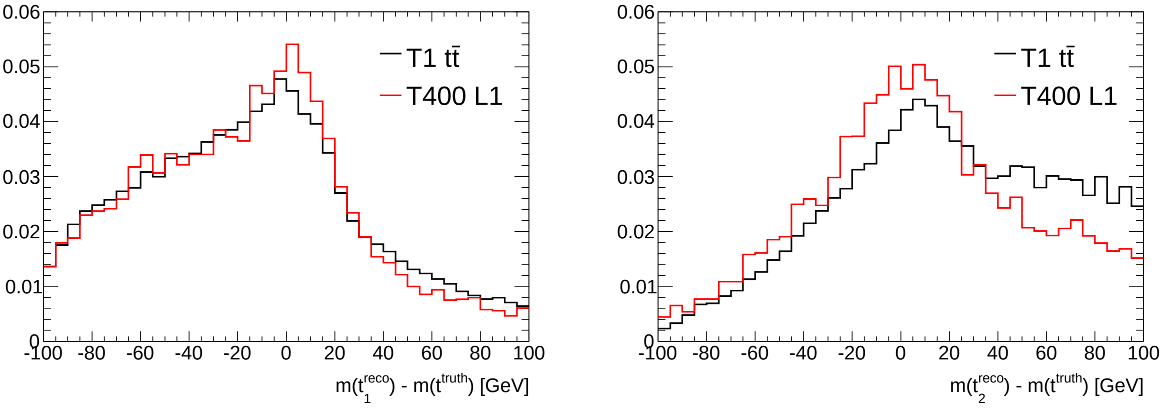

Figure 9.4: The mass difference between the reconstructed and true top candidates in $t\bar{t}$ MC using the $\Delta R_{\min}$ method. The black curve shows the lepton+jets $t\bar{t}$ MC, and the red curve shows the $m_{\tilde{t}_1} = 400\,\text{GeV}$, $m_{\tilde{\chi}_1^0} = 1\,\text{GeV}$ signal MC.

9.3 Stop pair search using 2011 data

This analysis is the first stop pair production search performed by ATLAS in the 0-lepton final state. The *SUSY-late 2011* object definitions of §4.3 were used.

9.3.1 Dataset and simulated samples

The analysis uses the full dataset collected by ATLAS during 2011, this corresponds to 4.7 fb^{-1} of $\sqrt{s} = 7$ TeV pp collisions. The data were collected using two combined single jet and $E_{\mathrm{T}}^{\mathrm{miss}}$ triggers, in order to cope with the increasing pileup conditions the $E_{\mathrm{T}}^{\mathrm{miss}}$ threshold was increased mid-way through data-taking, see Table 9.1. For events to satisfy the trigger at EF level, they were required to contain at least one jet with $p_{\mathrm{T}} > 75$ GeV and $E_{\mathrm{T}}^{\mathrm{miss}} > 45, 55$ GeV at EM scale. To be in the full efficiency region of the triggers offline the leading jet is required to have $p_{\mathrm{T}} > 130$ GeV and $E_{\mathrm{T}}^{\mathrm{miss}} > 150$ GeV.

Table 9.1: Triggers used for 2011 data periods $D - M$.

2011 Period	Trigger Chain	L2 Chain	L1 Seed
$D - K$	`EF_j75_xe45`	`L2_j50_xe20`	`L1_J50_XE20`
$L - M$	`EF_j75_xe55`	`L2_j70_xe35`	`L1_J50_XE35`

Simulated samples are used for several purposes throughout the analysis. Predominantly they are used for estimation of the SUSY signal, the main SM backgrounds during optimisation, to understand the shape of the semi-leptonic $t\bar{t}$ background in the final semi-data-driven estimate and the final estimation for subdominant backgrounds. The exact choice of MC generators and settings used for this analysis will now be described. A summary of the samples used and their corresponding cross sections are given in Table 9.2. Where more than one generator is listed the first used for the final estimation and the remainder are considered in the estimation of systematic uncertianties.

QCD `PYTHIA6` with ATLAS MC11 tune settings [181] and modified `MRST2007LO*` PDF [182].

W/Z + jets `ALPGEN` interfaced with `JIMMY`. Cross sections are computed with NNLO accuracy using `FEWZ` [184, 185] and the `CTEQ6L1` PDF. Additional samples are produced to simulate the contribution from $W + bb$, $W + cc$ and $Z + bb$.

Top pair production `ALPGEN` is interfaced with `HERWIG` and `JIMMY`. The $t\bar{t}$ cross section is normalised to the NLO value including next-to-leading-log resummation corrections (NLO+NLL) [186].

DiBoson and $t\bar{t} + X$ WW, WZ and ZZ events are generated using `HERWIG` and the event yield is normalised to the NLO cross sections. Events of $t\bar{t}$ produced in association with W/Z or $b\bar{b}$ are not included in the standard top pair samples described above. Additional samples generated with `ALPGEN` interfaced with `HERWIG` is used for $t\bar{t} + b\bar{b}$. `MADGRAPH` interfaced with `PYTHIA6` is used to generate $t\bar{t} + W/Z$. In all cases, LO cross section values are used to normalize the event yield.

SUSY `HERWIG++` is used to generate the signal samples with the $\tilde{t}_1 \to t\tilde{\chi}_1^0$ branching ratio set to 100%. All sparticle masses except those involved in the production and decay are set very high to effectively decouple the particle spectrum. The $\tilde{t}\tilde{t}^*$ production cross section is calculated to `NLO+NLL` accuracy using the `NLL-fast` [189] program with the `MSTW2008NLO` and `CTEQ10` PDF sets taking the average of the two as the quoted value. Theoretical uncertainties on the cross section due to variations in the renormalisation and factorisation scale, α_s and PDF are also calculated by `NLL-fast`.

Production process	$\sigma\times$ BR in nb (perturbative order)	Generator
Dijet (QCD) ($\hat{p}_{\mathrm{T}}$ >8 GeV/c)	10.47×10^6 (LO)	`PYTHIA`, `ALPGEN`
$W \to \ell\nu$ (+jets)	31.4 (NNLO)	`ALPGEN`
$Z \to \nu\bar{\nu}$ (+jets)	5.82 (NNLO)	`ALPGEN`
$Z \to \ell^+\ell^-$ (+jets)	3.20 (NNLO)	`ALPGEN`
Diboson (WW, WZ, ZZ)	7.1×10^{-2} (NLO)	`HERWIG`, `ALPGEN`
$t\bar{t}$	0.167 (NNLO)	`ALPGEN`, `MC@NLO`, `POWHEG`, `ACERMC`
single t	0.085 (NLO+NLL)	`MC@NLO`
$t\bar{t}$+$b\bar{b}$	0.9×10^{-3} (LO)	`ALPGEN`, `ACERMC`
$t\bar{t}$+W/Z	0.4×10^{-3} (LO)	`MADGRAPH+PYTHIA`

Table 9.2: Summary of simulated samples for standard model backgrounds.

9.3.2 Event selection

The general analysis strategy has already been outlined in §9.2 and will now be discussed in more detail. Standard ATLAS event cleaning cuts are applied, including the requirement for the primary vertex in each event to have ≥ 5 tracks, that events containing poorly reconstructed jets are vetoed. Cuts are also applied to remove events with fake $E_{\mathrm{T}}^{\mathrm{miss}}$ induced by jets associated with calorimeter noise, non-collision backgrounds and cosmic-ray or poorly reconstructed muons.

The signal region selection begins by isolating events with the 0-lepton final state, vetoing events containing electrons with $p_{\mathrm{T}} > 20$ GeV or muons with $p_{\mathrm{T}} > 10$ GeV. Events are required to contain at least six jets with $p_{\mathrm{T}} > 130, 30, ..., 30$ GeV, the leading jet selection being driven by the trigger. Again, driven by the trigger requirements, events must have $E_{\mathrm{T}}^{\mathrm{miss}} > 150$ GeV.

The signal model under consideration is expected to contain two real b-jets from the $t\bar{t}$ decay. However due to non-negligible inefficiencies that exist in the b-tagging algorithms it is not necessarily optimal to require two b-jets. A significance based optimisation was performed and the selection that gives the best sensitivity is the requirement for events to contain *either* two b-jets tagged with the `loose` b-tagging efficiency operating point *or* just one b-jet tagged with the `tight` b-tagging efficiency operating point. In this case `loose` corresponds to 75% efficiency and `tight` to 60% efficiency.

Rejection of any residual QCD background is performed by requiring that the azimuthal angle between the leading three jets and the $E_{\mathrm{T}}^{\mathrm{miss}}$ is larger than $\pi/5$ and that the direction of the track-based $E_{\mathrm{T}}^{\mathrm{miss}}$ is within $\pi/3$ of the direction of the calorimeter–based $E_{\mathrm{T}}^{\mathrm{miss}}$.

Having already selected events containing at least six jets the ΔR_{min} $t\bar{t}$ reconstruction algorithm, described in §9.2.1, can be employed. Once two 3-jet objects corresponding to the reconstructed top quarks are identified, cuts can be placed on the invariant mass of these combined objects. This helps reject any remaining W/Z+jets background as well as removing some of the dominant semi-leptonic $t\bar{t}$ background which is only expected to contain one well reconstructed hadronically decaying top quark.

After the previous selection requirements are imposed, the dominant remaining background is semi-leptonic $t\bar{t}$. As can be seen from Figure 9.2, for these events to pass the lepton veto the lepton must either be out of acceptance or mis-identified due to events where the W decays to a τ lepton which decays hadronically and is reconstructed as a jet. In fact it is the latter that gives the largest contribution. To reject this background a τ

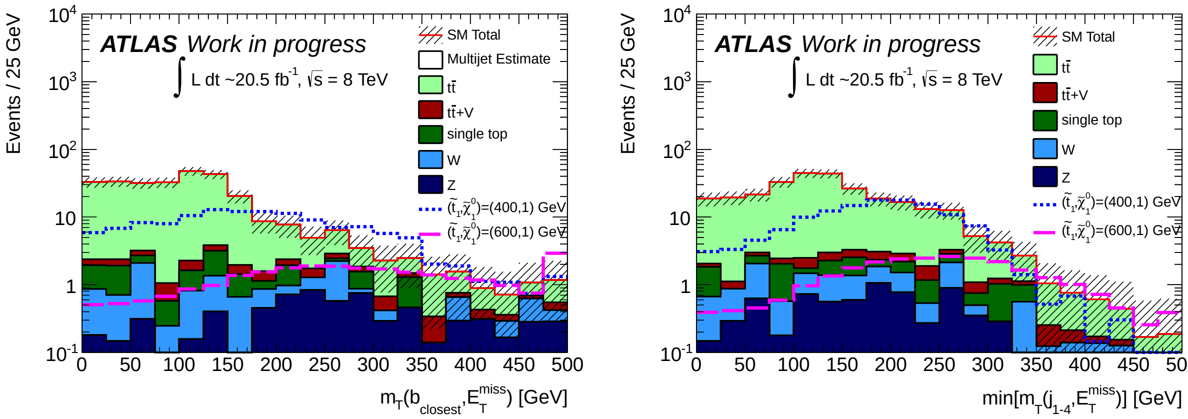

Figure 9.5: Distributions of $m_T(b_{\text{closest}}, E_{\text{T}}^{\text{miss}})$ and $\min\left[m_{\text{T}}\left(\text{j}_{1-4}, E_{\text{T}}^{\text{miss}}\right)\right]$.

candidate veto is applied. τ candidates are identified as jets with low track multiplicity that are close to the direction of the $E_{\text{T}}^{\text{miss}}$ in φ and have $m_T(\tau_{\text{candidate}}, E_{\text{T}}^{\text{miss}})$ consistent with a $W \to \tau\nu$ decay. Events are rejected if these requirements are satisfied.

Further rejection of the semi-leptonic $t\bar{t}$ background is achieved through use of kinematic variables similar to the transverse mass variable described in §9.2.1. In the case where two `loose` b-tagged jets are present the closest b-jet to the $E_{\text{T}}^{\text{miss}}$ in φ is selected and events are required to have $m_T(b_{\text{closest}}, E_{\text{T}}^{\text{miss}}) > 175$ GeV. In the case of only one `tight` b-tagged jet being present the ambiguity of whether the identified b-jet is associated with the leptonic or hadronic t decay makes this variable less useful. Instead the minimum transverse mass between the leading four jets and the $E_{\text{T}}^{\text{miss}}$, $\min\left[m_{\text{T}}\left(\text{j}_{1-4}, E_{\text{T}}^{\text{miss}}\right)\right]$, is used. This behaves very similarly to the previous transverse mass definition as can be seen in Figure 9.5. These events are required to have $\min\left[m_{\text{T}}\left(\text{j}_{1-4}, E_{\text{T}}^{\text{miss}}\right)\right] > 175$ GeV.

Finally, the signal regions are defined by incremental $E_{\text{T}}^{\text{miss}}$ thresholds. The signal region selection was extensively optimised and thresholds of 150 GeV and 260 GeV are used, the higher threshold giving increased sensitivity to larger stop masses. The full selection that defines the two signal regions, SRA and SRB, is summarised in Table 9.3.

9.3.3 Background estimation

Estimation of the QCD background is again performed using the jet smearing method, previously described in §7.3.2. The dominant semi-leptonic $t\bar{t}$ background is estimated using the *transfer factor* method, outlined in §7.3.1, using a 1-lepton control region to

<table>
<tr><td colspan="2">1 tight b-tagged jet OR 2 loose b-tagged jets</td></tr>
<tr><td colspan="2">$E_{\mathrm{T}}^{\mathrm{miss,track}} > 30\,\mathrm{GeV}$ and $\left|\Delta\varphi\left(E_{\mathrm{T}}^{\mathrm{miss}}, E_{\mathrm{T}}^{\mathrm{miss,track}}\right)\right| < \frac{\pi}{3}$</td></tr>
<tr><td colspan="2">$\min\left|\Delta\varphi\left(\mathrm{jet}^{0-2}, E_{\mathrm{T}}^{\mathrm{miss}}\right)\right| > 0.2\,\pi$</td></tr>
<tr><td colspan="2">$80 < m(t_1),\, m(t_2) < 270$ GeV</td></tr>
<tr><td colspan="2">Veto events with a τ candidate based on $m_{\mathrm{T}}\left(\tau\,\mathrm{candidate}, E_{\mathrm{T}}^{\mathrm{miss}}\right)$</td></tr>
<tr><td colspan="2">Events with 1 tight b-tagged jet: $\min\left[m_{\mathrm{T}}\left(\mathrm{j}_{1-4}, E_{\mathrm{T}}^{\mathrm{miss}}\right)\right] > 175\,\mathrm{GeV}$
Events with 2 loose b-tagged jets: $m_{\mathrm{T}}\left(b_{\mathrm{closest}}, E_{\mathrm{T}}^{\mathrm{miss}}\right) > 175\,\mathrm{GeV}$</td></tr>
<tr><td>SRA</td><td>SRB</td></tr>
<tr><td>$E_{\mathrm{T}}^{\mathrm{miss}} > 150\,\mathrm{GeV}$</td><td>$E_{\mathrm{T}}^{\mathrm{miss}} > 260\,\mathrm{GeV}$</td></tr>
</table>

Table 9.3: Summary of signal region selection criteria.

Leading jet $p_T > 130\,\mathrm{GeV}$, ≥ 6 jets $p_T > 30\,\mathrm{GeV}$
$E_{\mathrm{T}}^{\mathrm{miss}} > 150\,\mathrm{GeV}$
1 tight b-tagged jet or 2 loose b-tagged jets
$E_{\mathrm{T}}^{\mathrm{miss,track}} > 30\,\mathrm{GeV}$
$\left|\Delta\varphi\left(E_{\mathrm{T}}^{\mathrm{miss}}, E_{\mathrm{T}}^{\mathrm{miss,track}}\right)\right| > \frac{\pi}{3}$ **or** $\min\left|\Delta\varphi\left(\mathrm{jet}^{0-2}, E_{\mathrm{T}}^{\mathrm{miss}}\right)\right| < 0.2\pi$

Table 9.4: Selection criteria for the QCD control region.

validate the MC modelling of the $t\bar{t}$ process in this regime.

QCD background estimation

As in the sbottom pair analysis, selection efficiency of backgrounds due to QCD or all-hadronic $t\bar{t}$ events is expected to be very low, but due to the potentially huge cross sections of these processes it is important that they are well constrained. Events can contribute to the signal region if they contain significant $E_{\mathrm{T}}^{\mathrm{miss}}$ arising from mis-measurement of one or more jets in the event. Once again the *jet smearing method* is used for estimation of this background. The estimate is normalised to data in a QCD enriched control region.

From the di-jet balance analysis the gaussian core of the response was determined to be narrower in MC than in data, so a correction is applied.

The *Mercedes* analysis is used to validate the tails of the response function. The agreement between data and the smeared estimate using the MC derived response is very good and no additional correction is applied to the tails of the response function.

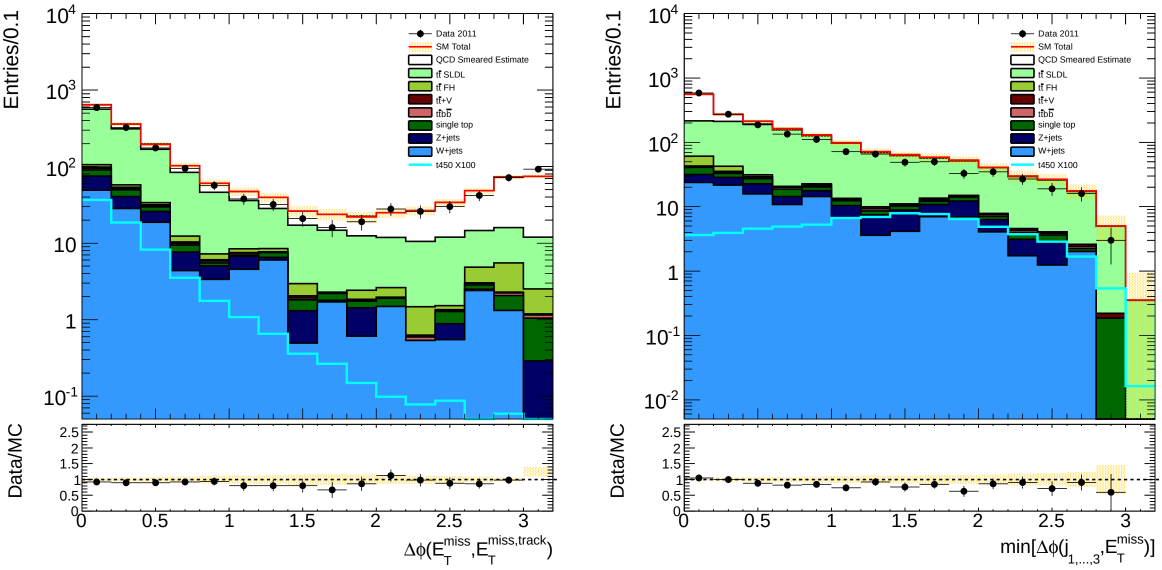

(a) **(b)**

Figure 9.6: Distributions in the QCD control region prior to the reversed QCD rejection cuts.

A QCD enriched control region is used to normalise the estimate from the *pseudodata* to the data. The control region is defined by reversing the QCD rejection criteria outlined in the previous section. Specifically, events are required to satisfy either of the reversed $\left|\Delta\varphi\left(E_{\mathrm{T}}^{\mathrm{miss}}, E_{\mathrm{T}}^{\mathrm{miss,track}}\right)\right|$ or $\min\left|\Delta\varphi\left(\mathrm{jet}^{0-2}, E_{\mathrm{T}}^{\mathrm{miss}}\right)\right|$ selections defined in Table 9.3. In order to increase statistics the selection requirements for $t\bar{t}$ rejection are removed. The selection is summarised in Table 9.4.

The method is validated in the control region through comparison of the estimate to the data for several important variables. Of crucial importance is that the method can reproduce the $\left|\Delta\varphi\left(E_{\mathrm{T}}^{\mathrm{miss}}, E_{\mathrm{T}}^{\mathrm{miss,track}}\right)\right|$ and $\min\left|\Delta\varphi\left(\mathrm{jet}^{0-2}, E_{\mathrm{T}}^{\mathrm{miss}}\right)\right|$ variables as these are key to the overall normalisation. The two variables are shown in Figure 9.6 with the full control region selection applied except the requirements on each variable. The estimate is clearly able to provide an accurate estimation of these variables. With the full control region selection applied several other key variables are shown in Figures 9.7 and 9.8. All variables are well reproduced by the jet smearing estimate.

The estimation of the QCD and all-hadronic $t\bar{t}$ background in the signal regions is derived by taking the smearing estimate normalised to data in the control region. The multi-jet yield as estimated using the jet smearing method is given in Table 9.14 for each

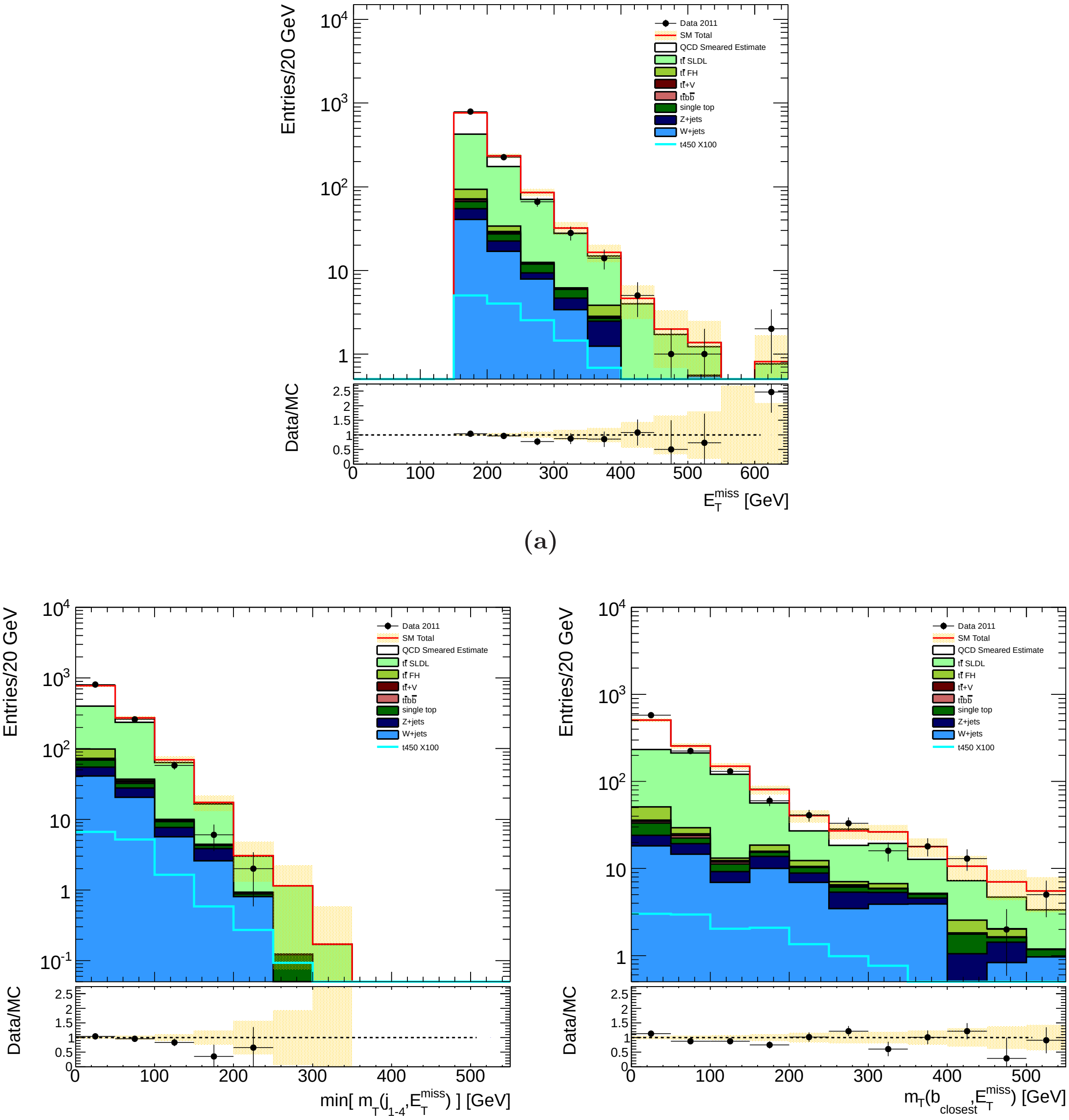

(a)

(b)

(c)

Figure 9.7: *Continued overleaf.*

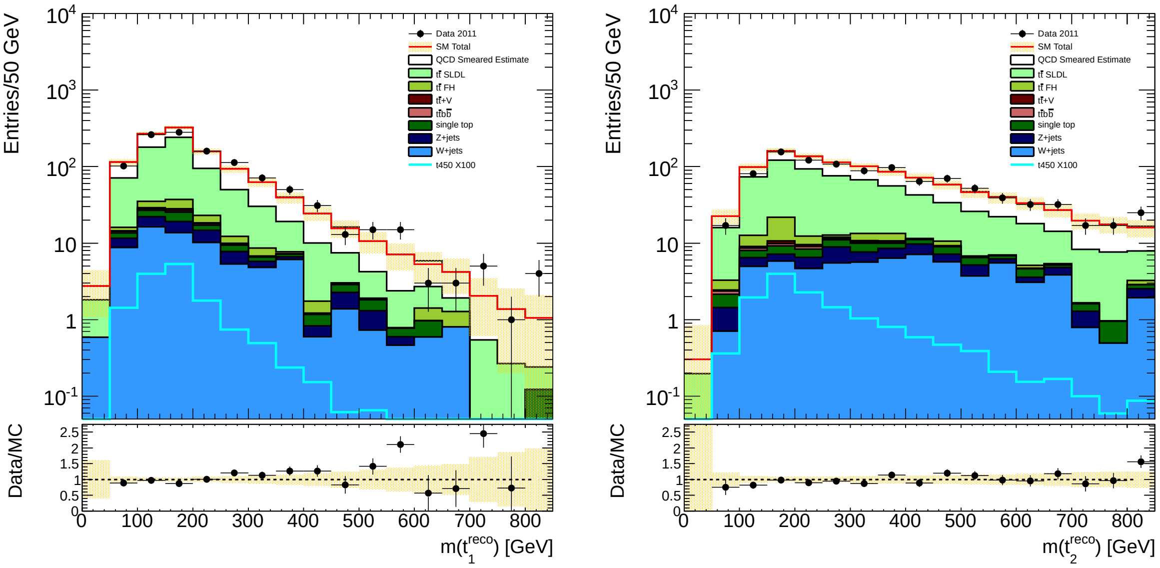

(d) **(e)**

Figure 9.7: Distributions of key variables in the QCD control region.

of the signal regions. The systematic uncertainty assigned is 100% which is predominantly due to variations in the gaussian core and the lowside tail.

Signal Region	Jet Smearing Estimate	% of SR
$E_{\mathrm{T}}^{\mathrm{miss}} > 150\,\mathrm{GeV}$	0.2 ± 0.2	2%
$E_{\mathrm{T}}^{\mathrm{miss}} > 260\,\mathrm{GeV}$	0.015 ± 0.015	< 1%

Table 9.5: Estimated background in the signal regions of QCD multijet and all-hadronic $t\bar{t}$ processes from the jet-smearing method.

Semileptonic $t\bar{t}$ background estimation

The dominant background in the signal region is $t\bar{t}$ where one of the W decays to leptons. Figure 9.2 shows that the signal region is composed predominantly of events where the W boson decays to a τ which decays hadronically and is reconstructed as a jet. In order to replicate this topology a control region is defined with very similar selection requirements to the signal region except that the lepton veto is reversed and instead, exactly one lepton is required. The lepton is then added to the jet collection and treated as a jet in all the remaining selection criteria, emulating a hadronic τ. The MC modelling of the $t\bar{t}$

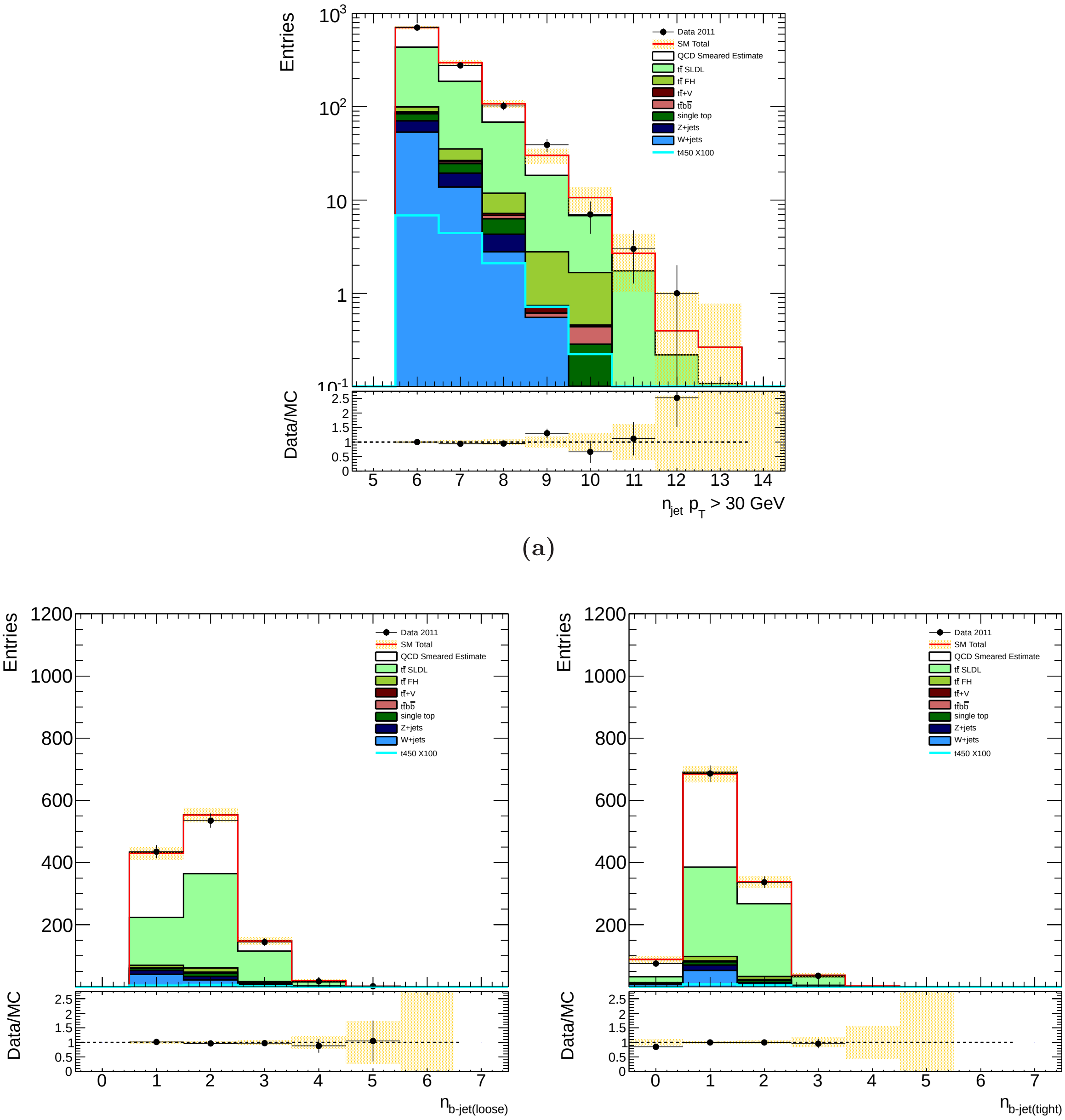

(a)

(b)

(c)

Figure 9.8: Distributions of jet multiplicity (a) and distributions of the *b*-jet multiplicity for the “loose” 75% (b) and “tight” 60%(c) operating points in the QCD control region.

single electron or muon trigger
exactly 1 signal lepton, which is then treated as a jet
$E_{\mathrm{T}}^{\mathrm{miss}} > 150\,\mathrm{GeV}$
Leading jet with $p_{\mathrm{T}} > 130\,\mathrm{GeV}$
≥ 6 jets with $p_{\mathrm{T}} > 30\,\mathrm{GeV}$
$\min\left\|\Delta\varphi\left(\mathrm{jet}^{0-2}, E_{\mathrm{T}}^{\mathrm{miss}}\right)\right\| > 0.1\pi$
$m(t_1) < 600\,\mathrm{GeV}$ OR $m(t_2) < 600\,\mathrm{GeV}$
$40 < m_{\mathrm{T}}\left(\ell, E_{\mathrm{T}}^{\mathrm{miss}}\right) < 120\,\mathrm{GeV}$
1 tight b-tagged jet OR 2 loose b-tagged jets

Table 9.6: Summary of the selection for the 1-lepton control region.

background is validated in this control region and the *transfer factor* technique is used to extrapolate from the control region to the signal region to provide the final estimate.

It is especially important to have a partially data-driven estimate of this background because the MC modelling of additional partons in high jet multiplicity $t\bar{t}$ events is known to have large uncertainties. For events to enter the signal region they must satisfy the 6-jet selection, for semi-leptonic $t\bar{t}$ this means that at least one jet from ISR or FSR must be present.

The 1-lepton control region is defined by requiring that either a single electron or single muon trigger be satisfied and that the event contains exactly one lepton that passes the signal lepton criteria. From this stage onwards the lepton is considered as a jet in the selection and definition of variables. In keeping with the signal region, events must contain $E_{\mathrm{T}}^{\mathrm{miss}} > 150$ GeV, leading jet $p_{\mathrm{T}} > 130$ GeV and six jets with $p_{\mathrm{T}} > 30$ GeV. The QCD rejection criteria along with the reconstructed top mass selection are slightly loosened to increase statistics. Additionally, the transverse mass between the lepton and $E_{\mathrm{T}}^{\mathrm{miss}}$ is required to be within the window $40 < m_T(l, E_{\mathrm{T}}^{\mathrm{miss}}) < 120$ GeV, the lower bound to reject the QCD background from fake leptons and the upper bound to reduce possible signal contamination and to remain orthogonal to the 1-lepton stop search. Finally, identical b-tagging requirements to the signal region are imposed. The 1-lepton control region selection is summarised in Table 9.6.

The *transfer factor* method can also be thought of as defining a scale factor with which to normalise the MC predictions to the data. The scale factor, $SF_{t\bar{t}}$, is defined as

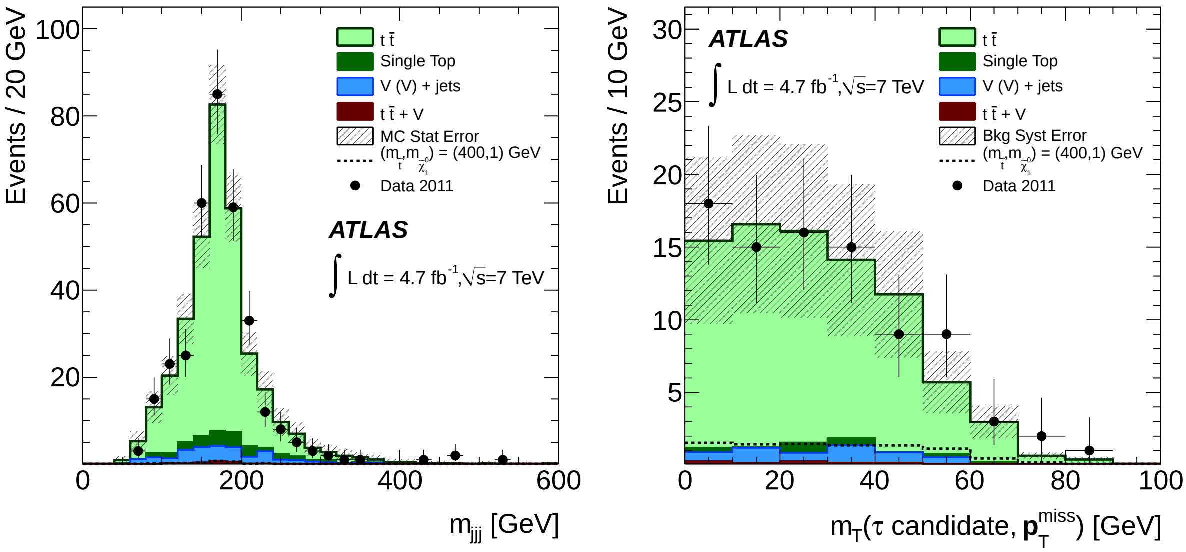

(a) **(b)**

Figure 9.9: (a) Three-jet invariant mass distribution of the hadronic top-quark candidate in the 1-lepton control region. (b) $m_T(\tau, E_{\mathrm{T}}^{\mathrm{miss}})$ distribtion in the τ enhanced validation region. Both distributions have the $t\bar{t}$ scale factor applied. Figures from [3].

follows

$$N_{SR}^{t\bar{t}} = \left(\frac{N_{SR}^{MC}}{N_{CR}^{MC}}\right) \times \left[N_{CR}^{data} - N_{others}^{MC}\right] = \left(\frac{N_{CR}^{data} - N_{others}^{MC}}{N_{CR}^{MC}}\right) \times N_{SR}^{MC} = SF_{t\bar{t}} \times N_{SR}^{MC}. \qquad (9.2)$$

The scale factor obtained is 0.66 ± 0.05 where the error quoted is statistical only. Figure 9.9 (a) shows the invariant mass of the reconstructed hadronic top in the 1-lepton control region after the scale factor has been applied. The scale factor is also validated in a τ enriched validation region that has selection identical to the signal region but reversing the τ candidate veto and relaxing the m_T requirements to increase statistics. Figure 9.9 (b) shows the transverse mass of τ candidates with $E_{\mathrm{T}}^{\mathrm{miss}}$ in this validation region, the agreement between the SM expectation and the data is very good.

9.3.4 Systematic uncertainties

Several sources of systematic uncertainty are considered in the analysis, the dominant contributions are summarised in Table 9.7. The uncertainty in the JES, JER, cell-out $E_{\mathrm{T}}^{\mathrm{miss}}$

SRA	Generator	ISR/FSR	b-tag	Fakes	JES	JER	MC Stats
Leptonic $t\bar{t}$	23.5%	10.9%	4.9%	0.4%	7.3%	2.2%	7.5%
Other	33.4%	–	5.5%	8.1%	27.5%	15.2%	13.2%
Total BG	26.7%	7.3%	5.1%	2.9%	13.9%	6.5%	6.6%

SRB	Generator	ISR/FSR	b-tag	Fakes	JES	JER	MC Stats
Leptonic $t\bar{t}$	5.1%	6.8%	4.2%	0.3%	9.4%	9.5%	16.8%
Other	37.4%	–	4.6%	8.9%	41.6%	3.5%	20.3%
Total BG	20.8%	3.5%	4.3%	4.5%	25.1%	6.6%	9.9%

Table 9.7: The symmetrised systematic uncertainties for each signal region separated into contributions from the dominant leptonic $t\bar{t}$ and other backgrounds.

term and b-tagging efficiency are estimated for all backgrounds and the signal. A MC generator uncertainty is also considered for the $t\bar{t}$ and W/Z+jets backgrounds along with other theoretical uncertainties. The dominant systematic uncertainties on the $t\bar{t}$ estimate are due to MC generator modelling, JES, limited MC statistics and b-tagging efficiency. The total uncertainty on the $t\bar{t}$ estimation is 30% and 27% in signal regions A and B respectively. For the W/Z+jets estimation an additional theoretical uncertainty on the fraction of events containing heavy flavour jets of 55% is applied. The other dominant systematic uncertainties are again due to MC generator modelling, JES, limited MC statistics and b-tagging efficiency. The total uncertainty on all non-$t\bar{t}$ backgrounds is 51% and 47% in SRA and SRB respectively.

9.3.5 Results and interpretation

Table 9.8 shows the number of events observed in data for each signal region compared to the SM expectation. The agreement between observation and expectation is very good and no significant excess is observed in the data. Figure 9.10 shows the $E_{\mathrm{T}}^{\mathrm{miss}}$ distribution with the full signal region selection applied, good agreement between the data and SM expectation is observed.

The results are interpreted in terms of a model-independent 95% confidence level upper limit on the visible cross section, shown in Table 9.8. Interpretation is also provided as 95% confidence level exclusion limits of the stop pair signal model in the $m_{\tilde{t}_1}$–$m_{\tilde{\chi}_1^0}$ plane. Figure 9.11 shows the expected and observed exclusion limits. The yellow shaded region indicates the $\pm1\sigma$ exclusion due to experimental uncertainties on the expected limit. The dashed red lines indicate the $\pm1\sigma$ exclusion due to uncertainty on the signal cross section

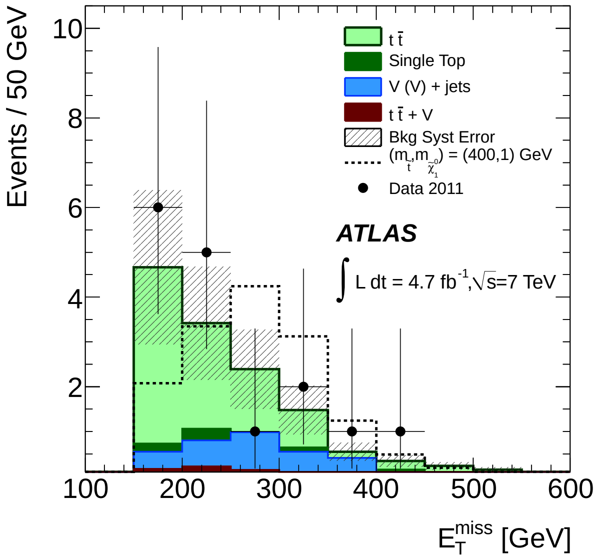

Figure 9.10: The $E_{\mathrm{T}}^{\mathrm{miss}}$ distribution in data compared to the SM expectation for SRA. Figure from [3].

on the observed exclusion. The exclusion quoted is conservatively chosen to be the that of the -1σ theoretical uncertainty on the observed limit. Correspondingly, stop masses are excluded between 370 and 465 GeV for a neutralino mass of ~ 0 GeV and a stop mass of 445 GeV is excluded for neutralino masses below 50 GeV.

9.3.6 Summary

A search for direct stop quark pair production was performed using 4.7 fb^{-1} of $\sqrt{s} = 7$ TeV pp collision data collected by ATLAS during 2011. The stop quarks are assumed to decay via $\tilde{t}_1 \to t\tilde{\chi}_1^0$ with a branching ratio of 100%. No excess was observed above the SM expectation and the result is interpreted in terms of 95% confidence level exclusion limits in the $m_{\tilde{t}_1} - m_{\tilde{\chi}_1^0}$ plane.

	SRA	SRB
$E_{\mathrm{T}}^{\mathrm{miss}}$	> 150 GeV	> 260 GeV
$t\bar{t}$	9.2 ± 2.7	2.3 ± 0.6
$t\bar{t} + W/Z$	0.8 ± 0.2	0.4 ± 0.1
Single top	0.7 ± 0.4	$0.2\ ^{+\ 0.3}_{-\ 0.2}$
Z+jets	$1.3\ ^{+\ 1.1}_{-\ 1.0}$	$0.9\ ^{+\ 0.8}_{-\ 0.7}$
W+jets	$1.2\ ^{+\ 1.4}_{-\ 1.0}$	0.5 ± 0.4
Diboson	$0.1\ ^{+\ 0.2}_{-\ 0.1}$	$0.1\ ^{+\ 0.2}_{-\ 0.1}$
Multi-jets	0.2 ± 0.2	0.02 ± 0.02
Total SM	$13.5\ ^{+\ 3.7}_{-\ 3.6}$	$4.4\ ^{+\ 1.7}_{-\ 1.3}$
SUSY $(m_{\tilde{t}_1}, m_{\tilde{\chi}_1^0}) = (400, 1)$ GeV	14.8 ± 4.0	8.9 ± 3.1
Data (observed)	16	4
Visible cross section [fb] (upper limit)	2.9 (2.5)	1.3 (1.3)

Table 9.8: The numbers of expected events for the SM backgrounds and an example SUSY signal point.

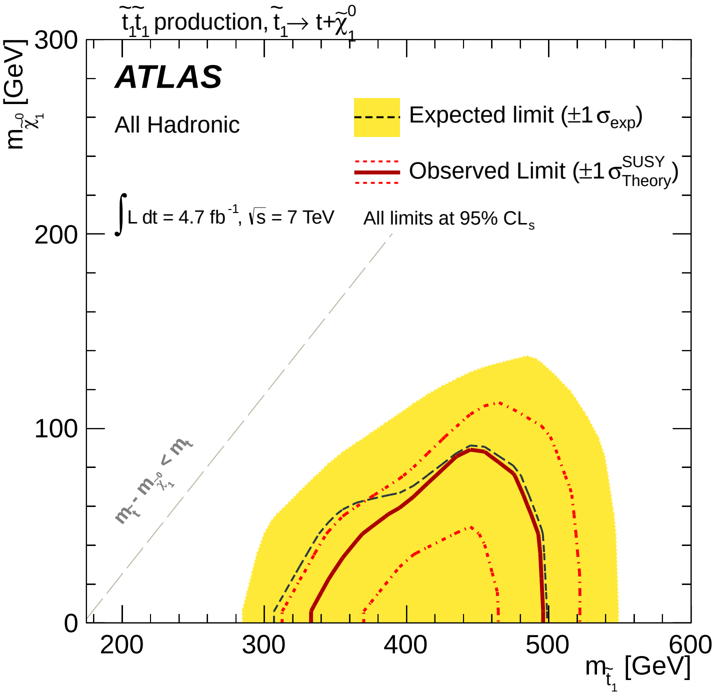

Figure 9.11: Expected and observed 95% CL$_s$ exclusion limits in the plane of $m_{\tilde{\chi}_1^0}$ vs. $m_{\tilde{t}_1}$. Figure from [3].

9.4 Stop pair search using 2012 data

In this section a search for direct stop quark pair production using 20.5 fb^{-1} of $\sqrt{s} = 8$ TeV *pp* collision data collected by ATLAS during 2012 is described. This analysis is an update to the analysis described in the previous section, §9.3.

9.4.1 Dataset and simulated samples

The full 2012 dataset corresponding to 20.5 fb^{-1} of $\sqrt{s} = 8$ TeV *pp* collisions is used in this analysis. The data was collected using two $E_{\mathrm{T}}^{\mathrm{miss}}$ triggers, one of which only considered events that were not in the first 3 bunches of the bunch train in order to cope with the pileup conditions, see Table 9.9. For events to satisfy the trigger they were required to have $E_{\mathrm{T}}^{\mathrm{miss}} > 80$ GeV at EM scale. To be in the full efficiency region of the triggers the offline $E_{\mathrm{T}}^{\mathrm{miss}}$ is required to be above 150 GeV for the jet selection applied in §9.4.2.

2012 Period	Trigger Chain	L2 Chain	L1 Seed
Period A-Run 203680	`EF_xe80T_tclcw_loose`	`L2_xe45T`	`L1_XE40_BGRP7`
Run 203719-Period L	`EF_xe80_tclcw_loose`	`L2_xe45`	`L1_XE40`

Table 9.9: Triggers used for 2012 data periods $A - L$.

Simulated samples are used for several purposes throughout the analysis, predominantly for estimation of the main SM backgrounds during optimisation and to understand the shape of the semi-leptonic $t\bar{t}$ and Z+jets background in the final semi-data-driven estimates and for estimation of the SUSY signal and subdominant SM backgrounds. The exact choice of MC generators and settings used for this analysis will now be described and is summarised along with the corresponding cross section in Table 9.10. Where more than one generator is listed, the first is used for the main estimaition and the others for systematic uncertainty calculations.

QCD Events are generated using `PYTHIA8`.

Top pair production `POWHEG` is used to generate events with generator level lepton filter and `MC@NLO` for the all-hadronic decay mode. The inclusive $t\bar{t}$ cross section is calculated with `HATHOR 1.2` [190] using `MSTW2008NNLO` [83] PDFs.

Production process	$\sigma\times$ BR in nb (perturbative order)	Generator
Dijet (QCD) ($\hat{p}_{\mathrm{T}}$ >8 GeV/c)	72.85×10^6 (LO)	`PYTHIA8`
$W \to \ell\nu$ (+jets)	36.5 (NNLO)	`ALPGEN`
$Z \to \nu\bar{\nu}$ (+jets)	6.70 (NNLO)	`SHERPA`
$Z \to \ell^+\ell^-$ (+jets)	3.72 (NNLO)	`ALGEN`
Diboson (WW, WZ, ZZ)	25.3×10^{-3} (NLO)	`SHERPA`
$t\bar{t}$	0.238 (NNLO)	`POWHEG`, `MC@NLO`, `ACERMC`, `ALPGEN`
single t	0.052 (NLO+NLL)	`MC@NLO`
$t\bar{t}$+W/Z	437×10^{-6} (NLO)	`MADGRAPH+PYTHIA`

Table 9.10: Summary of simulated samples for standard model backgrounds.

Single top production `MC@NLO` is used for single-top production in the s- and Wt channels, `ACERMC` [191] is used for the t-channel. The cross sections are calculated with `MC@NLO`.

W/Z+jets Events generated using `SHERPA` using separate samples for different heavy flavour jet content. Cross section calculated by `DYNNLO` [192] with the `MSTW2008NNLO` PDF set.

$t\bar{t}$+W/Z `MADGRAPH` interfaced with `PYTHIA6` is used for generation of $t\bar{t}$+W/Z associated production. The cross sections are normalised to NLO cross sections [159, 193].

DiBoson WW, WZ and ZZ events are generated using `Sherpa` and are normalised to the NLO calculations from `MCFM` [194] using `MSTW2008NLO` PDFs.

SUSY `HERWIG++` is used to generate the signal samples with the $\tilde{t}_1 \to t\tilde{\chi}_1^0$ branching ratio set to 100%. All sparticle masses except those involved in the production and decay are set very high to effectively decouple the particle spectrum. The stop is chosen to be mostly the partner of the right-handed top quark and the neutralino to be almost a pure bino. The signal samples were generated with `HERWIG++`. The $\tilde{t}\tilde{t}^*$ production cross section is calculated to `NLO+NLL` accuracy using the `NLL-fast` [189] program with the `MSTW2008NLO` and `CTEQ10` PDF sets taking the average of the two as the quoted value. Theoretical uncertainties on the cross section due to variations in the renormalisation and factorisation scale, α_s and PDF are also calculated by `NLL-fast`.

9.4.2 Event selection

The analysis strategy has already been described in §9.2, but a more detailed overview of the 2012 analysis selection will be given here. An overview of the signal region optimisation procedure is also provided.

Optimisation

The first stage in identifying the signal region selection is to perform an optimisation using the selection from the 2011 data analysis as the starting point. The optimisation procedure is a simple cut-based approach. A number of relevant kinematic variables, each with a set of allowed thresholds to be considered, are provided as the input to the optimisation. Each variable is allowed to vary, within its range, independently with respect to the others. For each combination of variables and thresholds the number of background events, B, and the number of signal events, S (for every point on the signal grid) is calculated from MC. These numbers are then passed into the following significance calculation:

$$S = \sqrt{B^2 + \Delta B^2 + \Delta S^2}. \tag{9.3}$$

Where ΔB and ΔS are the systematic error on the background and signal respectively. For the purposes of this optimisation it is sufficient to estimate these uncertainties with a flat value. In the following, the systematic uncertainty on the background and signal are both assumed to be 25%.

Once the significance is calculated for each signal point for a given cut, it is stored and then compared to the next cut. If the new cut gives a better significance it is kept for that particular signal point, if not, the previous one is kept. Once all combinations of variables and thresholds have been considered the optimisation in complete. The result is a signal grid, where at each signal point the cut giving the best significance and the corresponding significance value are assigned.

The selections considered in rows 1-4 of Figure 9.12 correspond to A-D in Table 9.11. In each case the items in bold refer to the variables used for optimisation while the preceding non-bold selection criteria are the pre-selection cuts. The first optimisation (A) considers changes in the leading jet p_{T} and $E_{\mathrm{T}}^{\mathrm{miss}}$. A clear preference is shown for the lowest jet p_{T} threshold and, as expected, incremental $E_{\mathrm{T}}^{\mathrm{miss}}$ thresholds give the best sensitivity across the range of stop masses. The optimisation performed in Table 9.11(B) is designed to check the best b-jet selection. Combinations of 1 or 2 b-jets satisfying the loose and tight efficiency

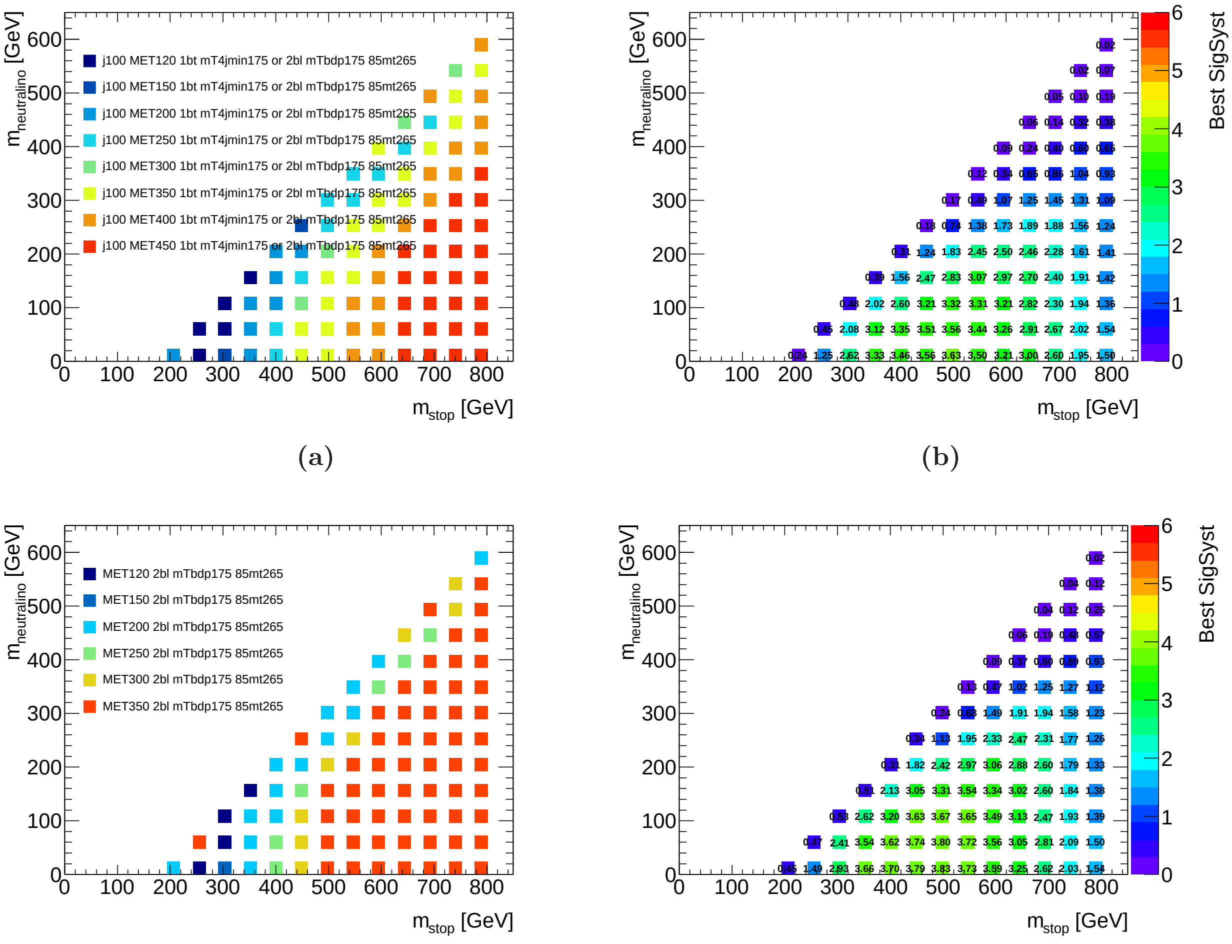

(a) (b)

(c) (d)

Figure 9.12: *Continued overleaf.*

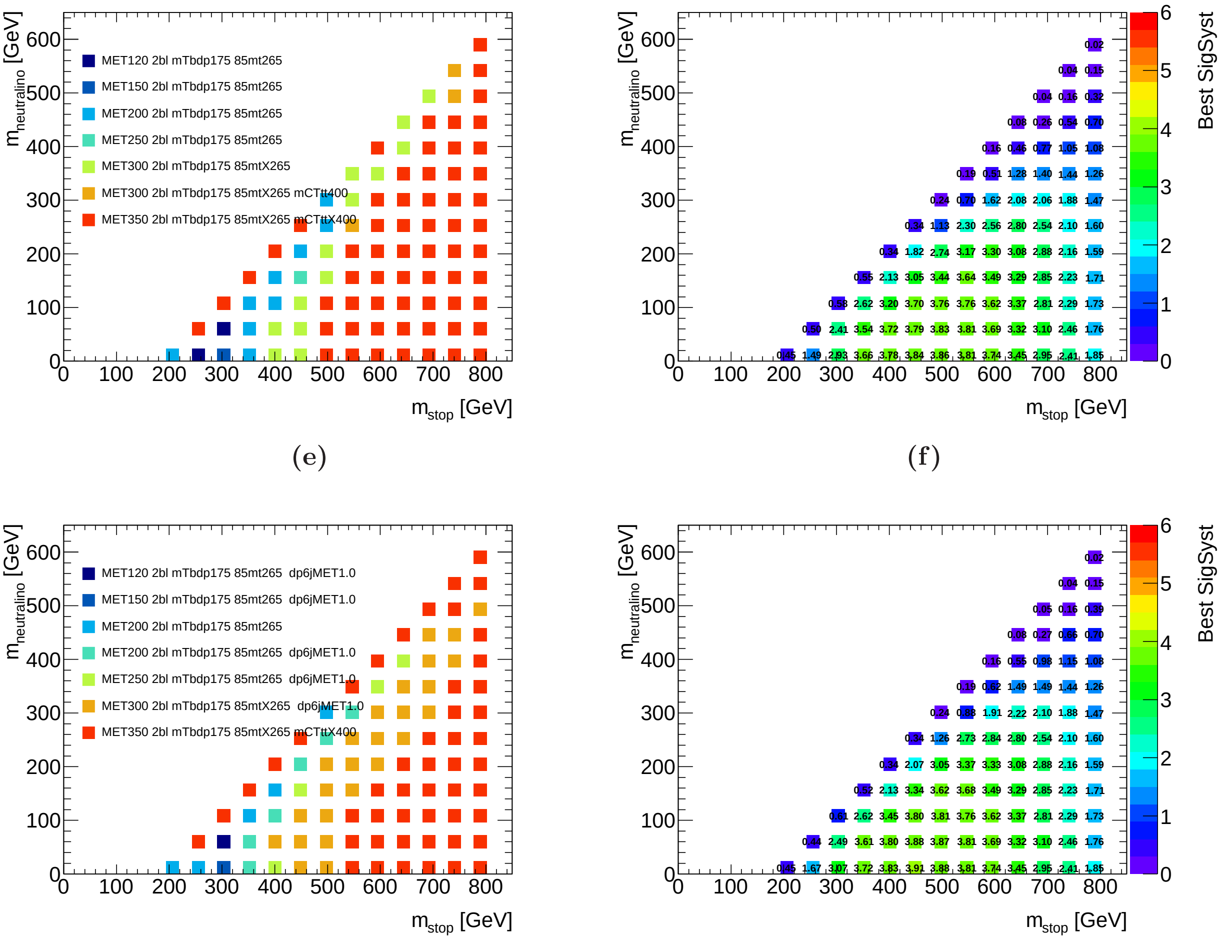

(e) (f)

(g) (h)

Figure 9.12: The left column signifies which set of cuts give the best significance at each point and the right column shows the corresponding significance. Rows 1-4 correspond to the selections A-D in Table 9.11.

A	(≥ 2 loose b-jets && $m_{\mathrm{T}}\left(b_{\mathrm{closest}}, E_{\mathrm{T}}^{\mathrm{miss}}\right) > 175\,\mathrm{GeV}$ or ≥ 1 tight b-jet && $\min\left[m_{\mathrm{T}}\left(\mathrm{j}_{1\text{-}4}, E_{\mathrm{T}}^{\mathrm{miss}}\right)\right] > 175\,\mathrm{GeV}$) $85 < m(t_1),\, m(t_2) < 265\,\mathrm{GeV}$
	jet $\boldsymbol{p_{\mathrm{T}}} \in [\mathbf{100, 125, 150, 175}]\,\mathbf{GeV}$ **$\boldsymbol{E_{\mathrm{T}}^{\mathrm{miss}}} \in [\mathbf{120, 150, 200, 250, 300, 350, 400, 450}]\,\mathbf{GeV}$**
B	jet $p_{\mathrm{T}} > 100\,\mathrm{GeV}$ $85 < m(t_1), m(t_2) < 265\,\mathrm{GeV}$
	b-jets $\in$ [≥ 2 loose, ≥ 2 tight, ≥ 1 tight,(≥ 2 loose or ≥ 1 tight)] **$\mathbf{m_T} \in \left[\boldsymbol{m_{\mathrm{T}}}\left(\boldsymbol{b}_{\mathrm{closest}}, \boldsymbol{E}_{\mathrm{T}}^{\mathrm{miss}}\right) > \mathbf{175}, \mathbf{min}\left[\boldsymbol{m_{\mathrm{T}}}\left(\mathbf{j_{1\text{-}4}}, \boldsymbol{E}_{\mathrm{T}}^{\mathrm{miss}}\right)\right] > \mathbf{175}\right]\,\mathbf{GeV}$** **$\boldsymbol{E}_{\mathrm{T}}^{\mathrm{miss}} \in [\mathbf{120, 150, 200, 250, 300, 350}]\,\mathbf{GeV}$**
C	jet $p_{\mathrm{T}} > 100\,\mathrm{GeV}$ $85 < m(t_1), m(t_2) < 265\,\mathrm{GeV}$ ≥ 2 loose b-jets $m_T \in \left[m_{\mathrm{T}}\left(b_{\mathrm{closest}}, E_{\mathrm{T}}^{\mathrm{miss}}\right) > 175, \min\left[m_{\mathrm{T}}\left(\mathrm{j}_{1\text{-}4}, E_{\mathrm{T}}^{\mathrm{miss}}\right)\right] > 175\right]\,\mathrm{GeV}$
	$\boldsymbol{M}_{\mathrm{CT}}(\mathbf{t}, \mathbf{t}) \in [\mathbf{0, 400}]\,\mathbf{GeV}$ **$\boldsymbol{E}_{\mathrm{T}}^{\mathrm{miss}} \in [\mathbf{120, 150, 200, 250, 300, 350}]\,\mathbf{GeV}$**
D	jet $p_{\mathrm{T}} > 100\,\mathrm{GeV}$ $85 < m(t_1), m(t_2) < 265\,\mathrm{GeV}$ ≥ 2 loose b-jets $m_T \in \left[m_{\mathrm{T}}\left(b_{\mathrm{closest}}, E_{\mathrm{T}}^{\mathrm{miss}}\right) > 175, \min\left[m_{\mathrm{T}}\left(\mathrm{j}_{1\text{-}4}, E_{\mathrm{T}}^{\mathrm{miss}}\right)\right] > 175\right]\,\mathrm{GeV}$
	$\boldsymbol{M}_{\mathrm{CT}}(\mathbf{t}, \mathbf{t}) \in [\mathbf{0, 400}]\,\mathbf{GeV}$ **$\mathbf{min}[\boldsymbol{\Delta\varphi}(\mathbf{j_{1\text{-}6}}, \boldsymbol{E}_{\mathrm{T}}^{\mathrm{miss}})] \in [\mathbf{0, 1.0}]$** **$\boldsymbol{E}_{\mathrm{T}}^{\mathrm{miss}} \in [\mathbf{120, 150, 200, 250, 300, 350}]\,\mathbf{GeV}$**

Table 9.11: Various selections used for optimisation of the signal regions.

requirements were considered along with a different choice of m_T cut. A clear preference for two loose b-jets and the corresponding $m_{\mathrm{T}}\left(b_{\mathrm{closest}}, E_{\mathrm{T}}^{\mathrm{miss}}\right)$ cut is shown.

Finally, the selections of Table 9.11(C) and 9.11(D) look to more unconventional optimisation criteria. The variables considered are $M_{\mathrm{CT}}(t,t)$ and $min[\Delta\varphi(j_{1\text{-}6}, E_{\mathrm{T}}^{\mathrm{miss}})]$ shown in Figure 9.13. Here some gains in significance are observed but limited W+jets MC statistics meant that it is hard to trust any conclusions. In the final selection these variables were not used.

Signal regions

Following the optimisation procedure described in the previous section the following signal regions are defined. The selection begins with the requirement that the appropriate $E_{\mathrm{T}}^{\mathrm{miss}}$

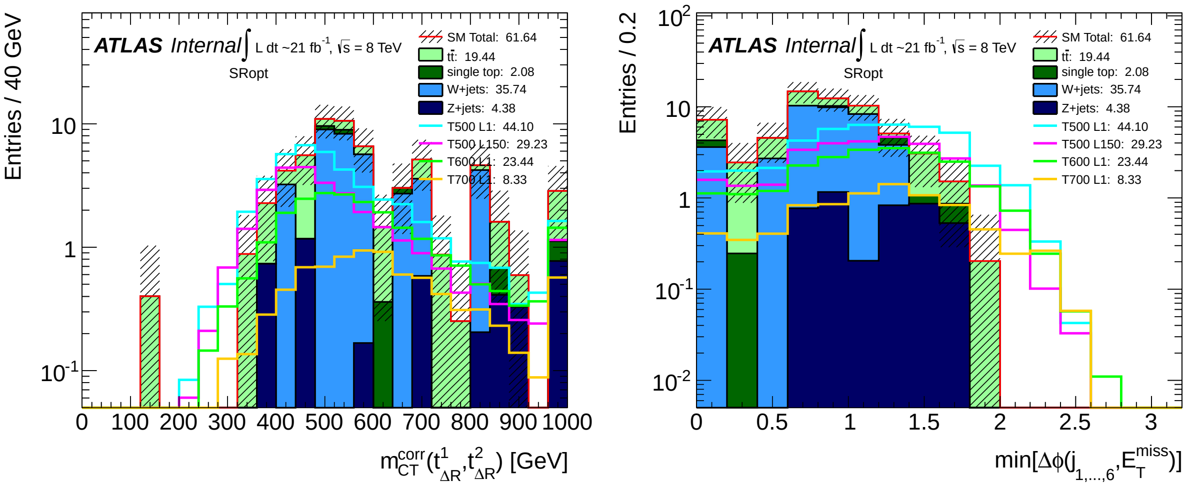

(a) **(b)**

Figure 9.13: $M_{\rm CT}(t,t)$ (a) and $min[\Delta\varphi(j_{1-6}, E_{\rm T}^{\rm miss})]$ (b) distributions with the pre-selection of Table 9.11(C) applied.

trigger be satisfied, and standard event cleaning cuts that have already been described in §9.3.2 are applied. Isolation of the SUSY signal begins by vetoing events that contain either an electron or muon with $p_{\rm T} > 10$ GeV. In order to be in the full efficiency region of the trigger the offline $E_{\rm T}^{\rm miss}$ is required to be above 150 GeV. To select events consistent with a fully-hadronic $t\bar{t}$ decay six jets are required with $p_{\rm T} > 80, 80, 35, ..., 35$ GeV. Two selection criteria designed to reject the QCD background due to events with poorly measured jets which give rise to significant $E_{\rm T}^{\rm miss}$ are applied: the difference between the direction in φ of the track-based and calorimeter-based $E_{\rm T}^{\rm miss}$ calculations must be smaller than $\pi/3$; and the azimuthal angle between the $E_{\rm T}^{\rm miss}$ and leading three jets is required to be greater than $\pi/5$. After the above selection the remaining dominant background is semi-leptonic $t\bar{t}$ events. To remove events where the leptonic W decays $W \to \tau\nu$ and the τ then decays hadronically, τ-candidates jets are identified. If a jet has low track multiplicity (≤ 4 tracks) and is close in φ to the $E_{\rm T}^{\rm miss}$ then it is identified as a τ-candidate and the event is removed. Furthermore, events are required to contain two b-tagged jets, where 70% b-tagging efficiency operating point is used. The $m_T(b_{\rm closest}, E_{\rm T}^{\rm miss})$ is required to be larger than 175 GeV. Two hadronic top quarks are reconstructed using the $\Delta R_{\rm min}$ method described in §9.2.1. The invariant masses of the reconstructed tops are required to be consistent with the top mass, $80 < m_{jjj} < 270$ GeV.

Finally, the three signal regions are defined by incremental $E_{\rm T}^{\rm miss}$ thresholds. The

Lepton veto		
$E_{\mathrm{T}}^{\mathrm{miss}} > 150$ GeV		
jet $p_{\mathrm{T}} > 80, 80, 35, ..., 35$ GeV		
$E_{\mathrm{T}}^{\mathrm{miss,track}} > 30\,\mathrm{GeV}$ and $\left\|\Delta\varphi\left(E_{\mathrm{T}}^{\mathrm{miss}}, E_{\mathrm{T}}^{\mathrm{miss,track}}\right)\right\| < \frac{\pi}{3}$		
$\min\left\|\Delta\varphi\left(\mathrm{jet}^{0-2}, E_{\mathrm{T}}^{\mathrm{miss}}\right)\right\| > 0.2\,\pi$		
Veto events with a τ candidate		
2 loose b-tagged jets		
$m_{\mathrm{T}}\left(b_{\mathrm{closest}}, E_{\mathrm{T}}^{\mathrm{miss}}\right) > 175\,\mathrm{GeV}$		
$80 < m(t_1),\, m(t_2) < 270$		
Signal Region I	Signal Region II	Signal Region III
$E_{\mathrm{T}}^{\mathrm{miss}} > 200\,\mathrm{GeV}$	$E_{\mathrm{T}}^{\mathrm{miss}} > 300\,\mathrm{GeV}$	$E_{\mathrm{T}}^{\mathrm{miss}} > 350\,\mathrm{GeV}$

Table 9.12: Summary of the signal region selection criteria.

thresholds are optimised to give the best sensitivity over a range of stop and neutralino masses. The full signal region selection is summarised in Table 9.12.

9.4.3 Background estimation

The dominant backgrounds are semi-leptonic $t\bar{t}$ and Z+jets. The $t\bar{t}$ background is estimated using a dedicated 1-lepton control region in which a profile likelihood fit is performed to obtain the normalisation in each signal region. This procedure is described in more detail in §9.4.5. The Z+jets background is estimated using the *transfer factor* method with a dedicated 2-lepton control region. The QCD background is again estimated using the *jet smearing* method and normalised in a QCD enriched control region. There is an irreducible background due to $t\bar{t} + Z(\to \nu\bar{\nu})$ but this process has a very small cross section and it is not possible to define a suitable control region. The $t\bar{t} + W/Z$ backgrounds are estimated purely using MC, but several generator level systematic uncertainties are considered.

QCD control region

The jet smearing method is once more employed to estimate the QCD background. The estimate is normalised and validated to data in a QCD-enriched control region. The cuts applied in the control region, summarised in Table 9.13, are aimed to enhance the QCD and all-hadronic $t\bar{t}$ contributions.

Figure 7.5 shows the 2D response for b-tagged and non-b-tagged jets and Figure 7.6

jet(1,2) $p_T > 80, 80\,\text{GeV}$, ≥ 6 jets $p_T > 35\,\text{GeV}$
$E_{\mathrm{T}}^{\mathrm{miss}} > 160\,\text{GeV}$
2 loose b-tagged jets
$E_{\mathrm{T}}^{\mathrm{miss,track}} > 30\,\text{GeV}$
$\left\lvert\Delta\varphi\left(E_{\mathrm{T}}^{\mathrm{miss}}, E_{\mathrm{T}}^{\mathrm{miss,track}}\right)\right\rvert > \frac{\pi}{3}$ **or** $\min\left\lvert\Delta\varphi\left(\text{jet}^{0-2}, E_{\mathrm{T}}^{\mathrm{miss}}\right)\right\rvert < 0.2\pi$

Table 9.13: Selection criteria for the QCD control region.

Signal Region	Jet Smearing Estimate	% of SR
SRI ($E_{\mathrm{T}}^{\mathrm{miss}} > 200\,\text{GeV}$)	0.12 ± 0.12	0.7%
SRII ($E_{\mathrm{T}}^{\mathrm{miss}} > 300\,\text{GeV}$)	0.01 ± 0.01	0.2%
SRIII ($E_{\mathrm{T}}^{\mathrm{miss}} > 350\,\text{GeV}$)	0.004 ± 0.004	0.2%

Table 9.14: Estimated background in the signal regions of QCD multi-jet and all-hadronic $t\bar{t}$ processes from the jet-smearing method.

the response for tagged and non-tagged jets for a range of truth jet p_{T} slices. The gaussian core of the response function is validated in using the di-jet balance validation region. Unlike the previous analyses no correction is applied to the gaussian core of the response function as the MC response is slightly wider than the data. The tails of the response function are again validated in the *Mercedes* validation region. Figure 7.9 shows the R_2 distributions for both non-b-tagged and b-tagged for the smearing estimate and the data.

Since the high $\left\lvert\Delta\varphi\left(E_{\mathrm{T}}^{\mathrm{miss}}, E_{\mathrm{T}}^{\mathrm{miss,track}}\right)\right\rvert$ and low $\min\left\lvert\Delta\varphi\left(\text{jet}^{0-2}, E_{\mathrm{T}}^{\mathrm{miss}}\right)\right\rvert$ regions are used to normalise the smeared events it is crucial that these variables are well described. Figure 9.14 shows these distributions using the normalisation derived from the control region without a cut on each variable applied. Good agreement between the data and smeared estimate is observed. Figures 9.15 and 9.16 show distributions of several key kinematic variables for the signal region. The smearing distributions reproduce the data to a very reasonable level and well within a conservative 100% uncertainty applied to this estimation in the signal region.

The estimation of the QCD and all-hadronic $t\bar{t}$ background in the signal regions is derived by taking the smearing estimate normalised to data in the control region. The multi-jet yield as estimated using the jet smearing method is given in Table 9.14 for each of the signal regions.

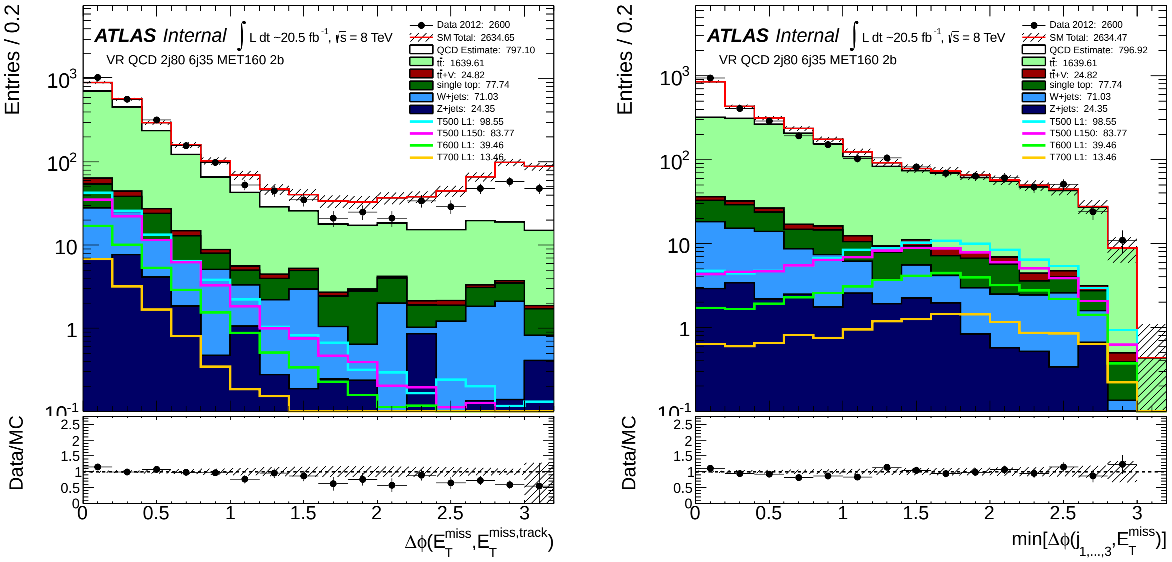

Figure 9.14: Distributions in the QCD control region prior to reversed QCD rejection cuts. Hashed bars are the MC statistical uncertainty.

$t\bar{t}$ estimation

In order to estimate the $t\bar{t}$ background a control region is defined to be enriched with semi-leptonic $t\bar{t}$ events. The final estimation of the $t\bar{t}$ contribution in the signal region is extracted by a simultaneous fit to the control regions and signal regions where the normalisation of the $t\bar{t}$ is extracted from the fit.

The control region is defined by reversing the signal region lepton veto and instead requiring events to pass a single lepton trigger and contain exactly one lepton which satisfies the signal lepton definition. The lepton is then treated as a jet to emulate the dominant component of the $t\bar{t}$ background in the signal region coming from leptonic W decays to a τ lepton which decays hadronically and is reconstructed as a jet. The lepton is then included in all jet-based selection criteria.

The jet selection is identical to that of the signal region, the QCD rejection requirement is loosened to requiring $\min\left|\Delta\varphi\left(\text{jet}^{0-2}, E_{\mathrm{T}}^{\text{miss}}\right)\right| > 0.1\pi$. The $m_T(b_{\text{closest}}, E_{\mathrm{T}}^{\text{miss}})$ requirement and τ-candidate veto are dropped entirely. The reconstructed top mass window is loosened such that only one of the reconstructed hadronic tops must have $m_{jjj} < 600$ GeV. An additional requirement that the transverse mass between the lepton and $E_{\mathrm{T}}^{\text{miss}}$, $m_{\mathrm{T}}(\ell, E_{\mathrm{T}}^{\text{miss}})$, be in the window $40 < m_{\mathrm{T}}(\ell, E_{\mathrm{T}}^{\text{miss}}) < 120\,\text{GeV}$ is imposed. The lower limit rejects the QCD background whilst the upper limit reduces signal contamination and ensures that the control region is orthogonal to the 1-lepton direct stop search

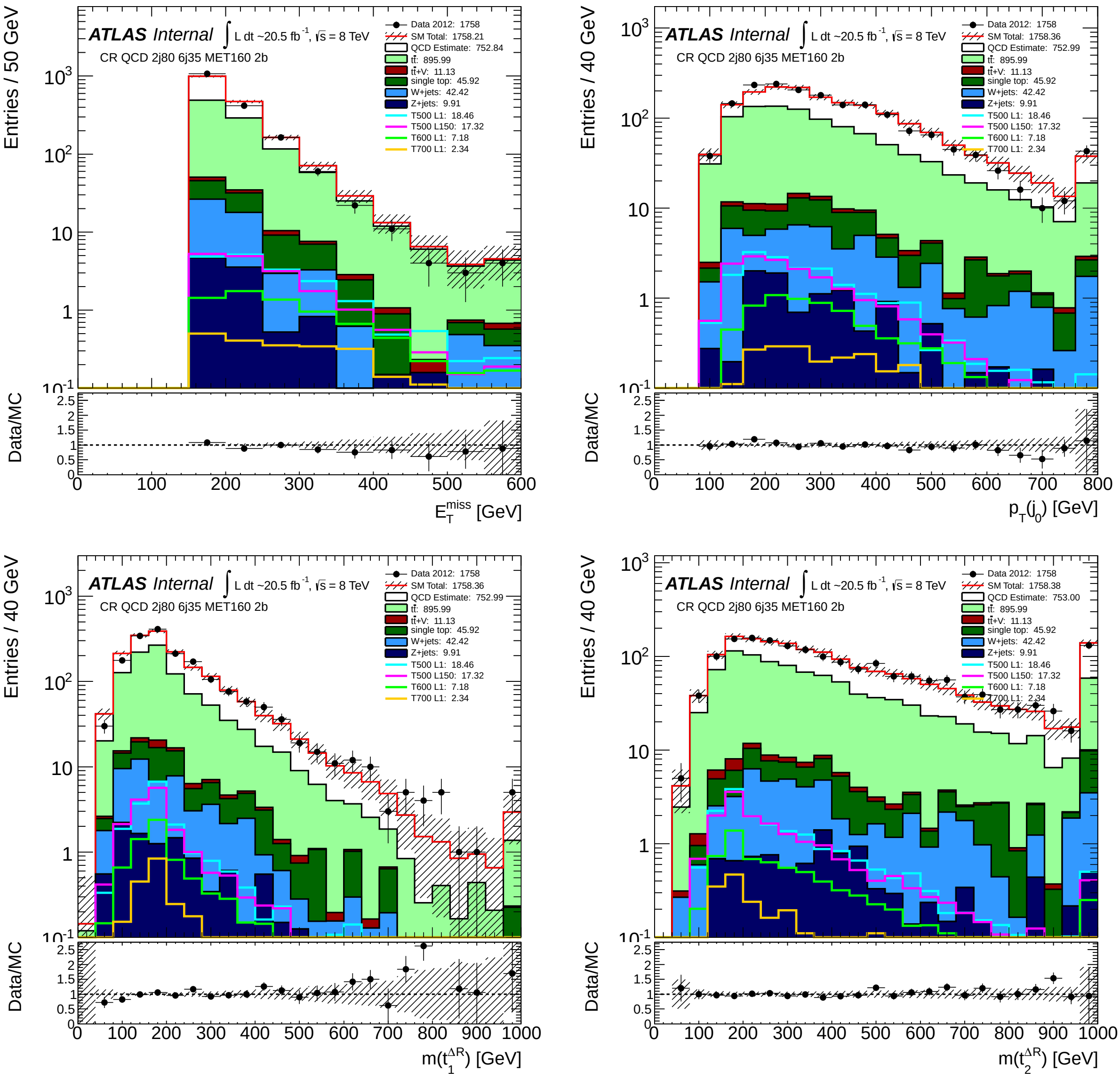

Figure 9.15: *Continued overleaf.*

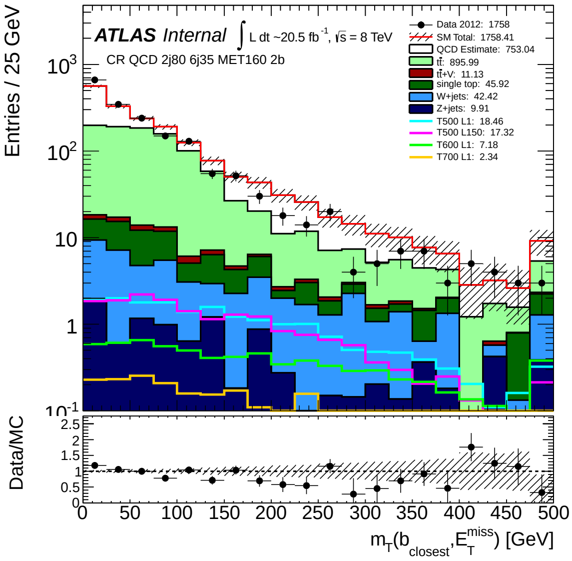

Figure 9.15: Distributions of key variables in the QCD control region. Hashed bars are the MC statistical uncertainty.

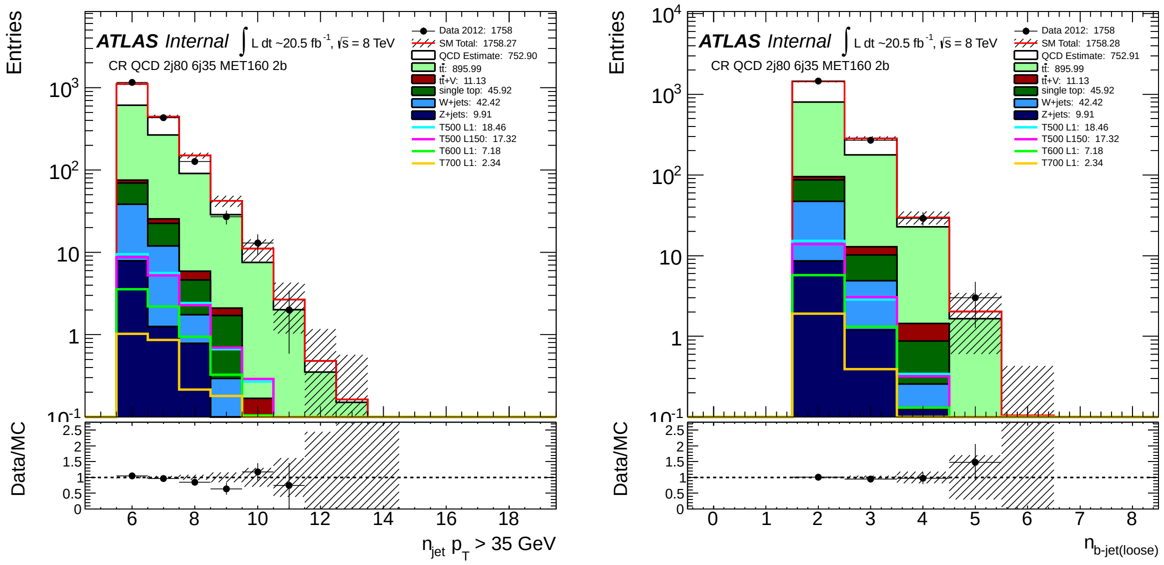

Figure 9.16: Distributions of jet multiplicity for jets with $p_T > 35\,\text{GeV}$ (left) and b-jet multiplicity for the "loose" 70% operating point (right) in the QCD control region. Hashed bars are the MC statistical uncertainty.

single electron or muon trigger
exactly 1 signal lepton, which is then treated as a jet
$E_{\mathrm{T}}^{\mathrm{miss}} > 100\,\mathrm{GeV}$
Leading 2 jets with $p_{\mathrm{T}} > 80\,\mathrm{GeV}$
≥ 6 jets with $p_{\mathrm{T}} > 35\,\mathrm{GeV}$
$\min\left\|\Delta\varphi\left(\mathrm{jet}^{0-2}, E_{\mathrm{T}}^{\mathrm{miss}}\right)\right\| > 0.1\pi$
$m(t_1) < 600\,\mathrm{GeV}$ OR $m(t_2) < 600\,\mathrm{GeV}$
$40 < m_{\mathrm{T}}\left(\ell, E_{\mathrm{T}}^{\mathrm{miss}}\right) < 120\,\mathrm{GeV}$
2 loose b-tagged jets

Table 9.15: Summary of the selection for the 1-lepton control region.

signal region. Finally, three control regions are defined each with identical $E_{\mathrm{T}}^{\mathrm{miss}}$ selection to the three signal regions. The $t\bar{t}$ control region selection is summarised in Table 9.15.

Figure 9.17 shows the comparison of the SM expectation and the data in the 1-lepton control region. The yellow band in the ratio corresponds to the systematic uncertainty on the estimate. Good agreement is observed between the data and the expectation.

Z+jets estimation

The Z+jets background is estimated using the *transfer factor* method, employing a dedicated 2-lepton control region. It is hard to identify a selection orthogonal to the signal region that is dominated by $Z(\rightarrow \nu\bar{\nu})$+jets. So instead a 2-lepton control region is defined which is dominated by $Z(\rightarrow ll)$+jets events, the lepton momenta is then vectorially subtracted from the $E_{\mathrm{T}}^{\mathrm{miss}}$ to emulate the $Z(\rightarrow \nu\bar{\nu})$ topology.

Events are required to satisfy a di-lepton trigger and contain two same flavour opposite sign signal leptons. In order to reduce contamination from di-lepton $t\bar{t}$ events $E_{\mathrm{T}}^{\mathrm{miss}} <$ 50 GeV is required. To further enhance the Z+jets contribution the invariant mass of the lepton pair is required to be $81 < m_{ll} < 101$ GeV. Identical jet selection requirements are imposed to keep the control region as kinematically similar to the signal region as possible. The transverse momenta of the leptons is vectorially subtracted from the $E_{\mathrm{T}}^{\mathrm{miss}}$ calculation in order to treat the leptons as neutrinos. This corrected $E_{\mathrm{T}}^{\mathrm{miss}}$ is then required to be $E_{\mathrm{T}}^{\mathrm{miss}} > 70$ GeV and the same b-tagging selection as the signal region is applied. The selection is summarised in Table 9.16.

Figure 9.18 provides a comparison between the data and the SM expectation in the

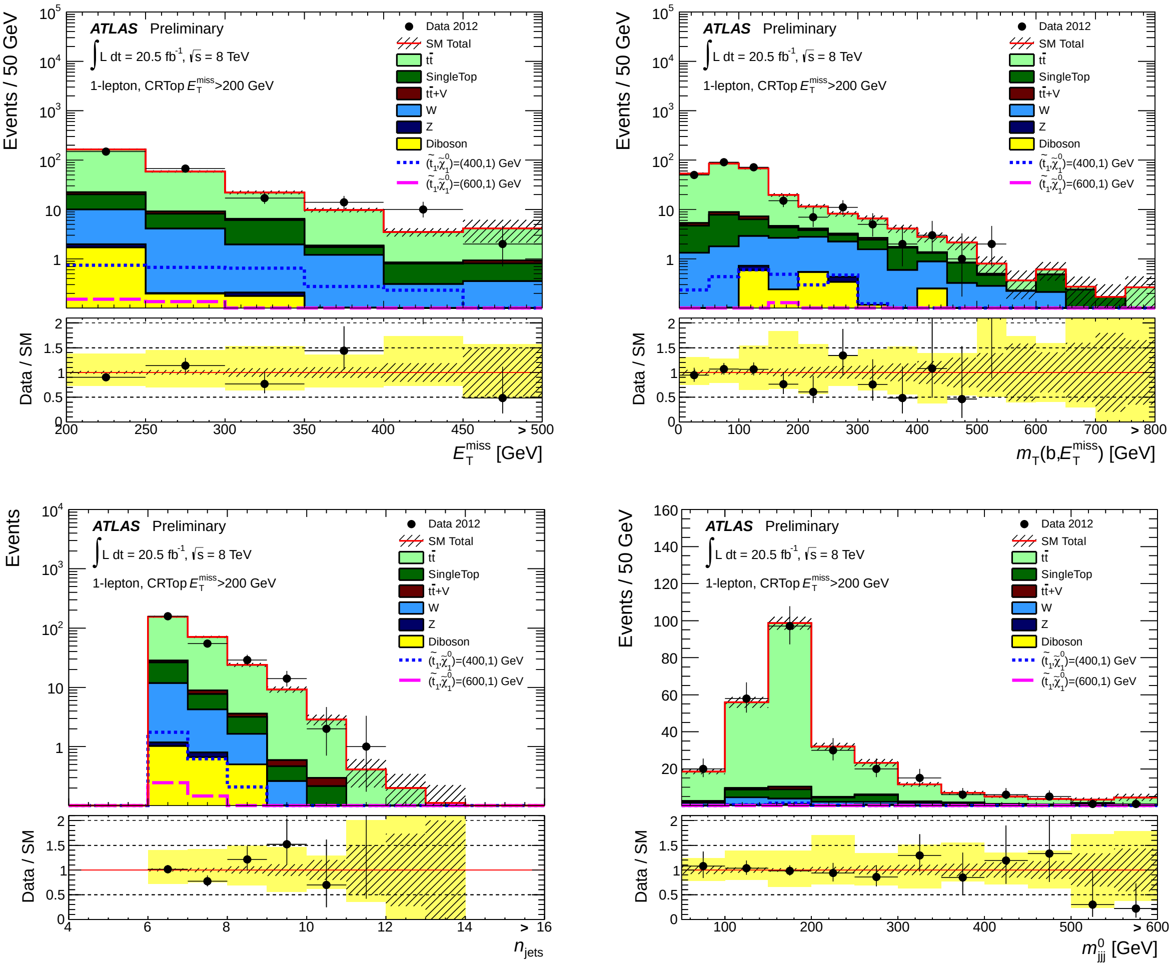

Figure 9.17: Key distributions in the 1-lepton control region. Figures from [4].

di-lepton trigger
exactly 2 signal electrons or muons with p_{T} >20, 20 GeV and 20,10 GeV.
$E_{\mathrm{T}}^{\mathrm{miss}} < 50$ GeV
$\lvert m_{ll} - m_Z \rvert < 10$ GeV
≥ 6 jets with $p_{\mathrm{T}} > 80, 80, 30, ..., 30$ GeV
$E_{\mathrm{T}}^{\mathrm{misscorr}} > 70$ GeV
loose b-tagged jets

Table 9.16: Summary of the selection for the 2-lepton control region.

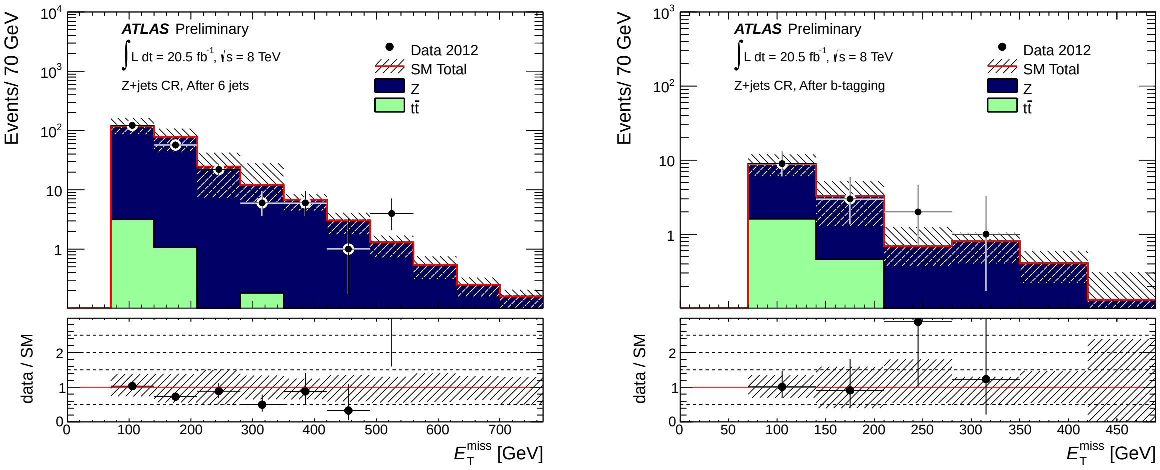

Figure 9.18: The $E_{\mathrm{T}}^{\mathrm{miss}}$ distribution in the Z+jets control region without the requirement on the number of b-tagged jets (Left) and after all selection requirements (Right). The uncertainty band around the Standard Model expectation is the combination of statistical and systematic uncertainties. Figures from [4].

2-lepton control region. Good agreement is observed both before (Left) and after (Right) the b-tagging requirements. The normalisation of the Z+jets MC estimate is scaled up by a factor of 1.06 ± 0.35 as derived from the data in this control region.

$t\bar{t}$ validation region

In order to validate the 1-lepton $t\bar{t}$ control region, an additional *validation region* is used. This region is formed by applying all of the cuts in the lowest $E_{\mathrm{T}}^{\mathrm{miss}}$ signal region except the $m_{\mathrm{T}}\left(b_{\mathrm{closest}}, E_{\mathrm{T}}^{\mathrm{miss}}\right)$ and τ-candidate veto cuts. A window of $50 < m_{\mathrm{T}}\left(b_{\mathrm{closest}}, E_{\mathrm{T}}^{\mathrm{miss}}\right) < 150$ GeV is selected, the lower threshold keeps the QCD background at a negligible level, whilst the upper threshold makes the region orthogonal to the signal region minimises signal contamination. Figure 9.19(a) shows the number of jets without any requirement on possible τ-candidates, 9.19(b) shows the same plot with the τ candidate veto applied and 9.19(c) with the τ-candidate veto reversed. The good agreement between the observation in data and the MC expectation for each of the three validation regions shows that there is no bias due to the fraction of τ+jets events in the sample.

$t\bar{t}$ + W/Z estimation

The $t\bar{t} + V (V = W, Z)$ processes, although having relatively small cross sections, become a significant background in the tighter signal regions. In particular $t\bar{t} + Z, (Z \to \nu\nu)$ is an

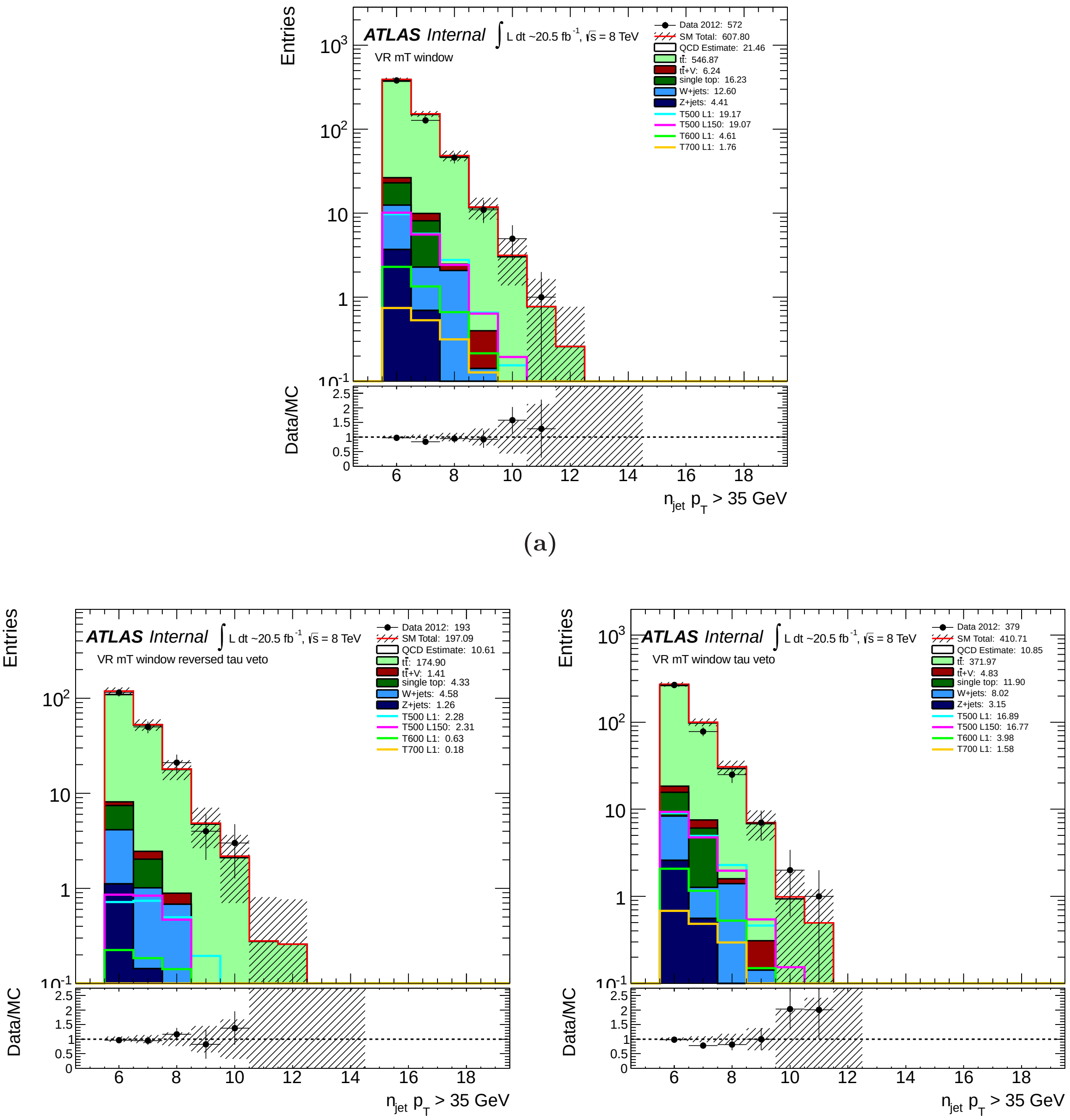

(a)

(b) **(c)**

Figure 9.19: Jet multiplicity distributions in the $t\bar{t}$ validation region with no τ-candidate selection (a), the τ-candidate veto applied (b) and the τ-candidate veto reversed (c).

Process	Reference	$\sigma_{NLO}[fb]$	Nominal scale, μ_0	Scale Range	Scale Uncertainty	PDF Uncertainty
$t\bar{t}+W^+$	[193]	161	m_t	$[\mu_0/4, 4\mu_0]$	$^{+12\%}_{-20\%}$	$^{+7\%}_{-8\%}$
$t\bar{t}+W^-$	[193]	71	m_t	$[\mu_0/4, 4\mu_0]$	$^{+16\%}_{-21\%}$	$^{+6\%}_{-8\%}$
$t\bar{t}+W^+$	[159]	142.6	$m_t + m_W/2$	$[\mu_0/2, 2\mu_0]$	$^{+10\%}_{-11\%}$	–
$t\bar{t}+W^-$	[159]	60.5	$m_t + m_W/2$	$[\mu_0/2, 2\mu_0]$	$^{+11\%}_{-12\%}$	–
$t\bar{t}+Z$	[159]	205.7	$m_t + m_Z/2$	$[\mu_0/2, 2\mu_0]$	$^{+9\%}_{-13\%}$	–

Table 9.17: Summary of NLO cross section and theoretical uncertainty calculations from Campbell et al. [193] and Garzelli et al. [159]. In all cases the renormalisation scale, μ_R, and factorisation scale, μ_F, are set equal to a common scale, $\mu = \mu_R = \mu_F$.

irreducible background to $\tilde{t} \rightarrow t + E_{\mathrm{T}}^{\mathrm{miss}}$ searches. Due to the low cross section it is very hard to define a suitable control region for this background. As a result the estimate is taken purely from MC. Several sources of systematic uncertainty due to the MC generator modelling of these processes are considered.

NLO cross section calculations for these processes have been performed for $t\bar{t}+W$ [193] and for both $t\bar{t}+W$ and $t\bar{t}+Z$ [159] at $\sqrt{s} = 8$ TeV. These calculations include theoretical uncertainties on the cross section due to the choice of nominal renormalisation and factorisation scale. In [193] the theoretical uncertainty due to the choice of PDF is also considered. These values and their respective uncertainties are summarised in Table 9.17.

The central value for the $t\bar{t}+W$ cross section is taken from [193] and the $t\bar{t}+Z$ cross section from [159]. The scale and PDF uncertainty envelope from [193] is chosen for the final quoted uncertainties for both $t\bar{t}+W$ and $t\bar{t}+Z$. This choice is driven by the larger, and more conservative, scale variation range and the consistent PDF variation which is not quoted in [159]. Although [193] does not quote these uncertainties for $t\bar{t}+Z$ [159] shows that the scale uncertainties are of the same size for $t\bar{t}+W$ and $t\bar{t}+Z$ so the same uncertainty is quoted for both processes. The largest uncertainty per variation is chosen and then symmetrised, hence a 21% scale uncertainty and 8% PDF uncertainty is assigned. Adding these in quadrature the final theoretical uncertainty on the cross section is 22%.

Table 9.18 shows a summary of the $t\bar{t}+V$ samples, the number of events generated and their cross sections. The table also shows the theory calculation for the NLO cross section in each case and hence the corresponding k-factor for the generated samples. The

Sample	N events	σ_{LO} (MC) [pb]	σ_{NLO} [pb]	k-factor	Reference
ttbarWExcl	400k	0.104100	–	1.18	–
ttbarWj ttbarWjExcl	400k	0.053372	–	1.18	–
ttbarWjjIncl	400k	0.041482	–	1.18	–
	1.2M	0.199	0.232	–	[193]
ttbarZExcl	400k	0.067690	–	1.34	–
ttbarZj ttbarZjExcl	400k	0.045357	–	1.34	–
ttbarZjjIncl	400k	0.039772	–	1.34	–
	1.2M	0.1528	0.2057	–	[159]

Table 9.18: List of MC samples, the number of events generated, their cross sections and k-factors.

samples are all produced with `MADGRAPH`+`PYTHIA` with the `AUET2B` tune and `CTEQ6L1` PDF.

Although the cross section is known to NLO the MC generation is performed at LO, hence a significant shape uncertainty is expected. As these processes have been generated with several additional partons the uncertainty due to parton shower is likely to be reduced but is not negligible.

The generator uncertainties can be separated into the following contributions:

- Renormalisation and factorisation scale (variation in MG)
- ISR (coherent variation in MG and `PYTHIA`)
- FSR (variation in `PYTHIA`)
- MLM matching scale (variation in MG)

Each variation is expected to be independent so they are to be combined in quadrature.

Table 9.19 shows the details of which parameters are changed in `MADGRAPH` and/or `PYTHIA` for each systematic variation. For each variation a new sample is generated with 100k events at generator level. These samples can then be used to assess impact of each variation on kinematic distributions and signal region selection cuts.

Figure 9.20 shows a selection of relevant kinematic variables with no selection applied to give an impression of the systematic variation in shape for different uncertainties. Note the large dependence on both the number of jets and H_T in Figure 9.20 due to the ISR variations. Figure 9.21 shows the efficiency at each stage of a simplified version of the

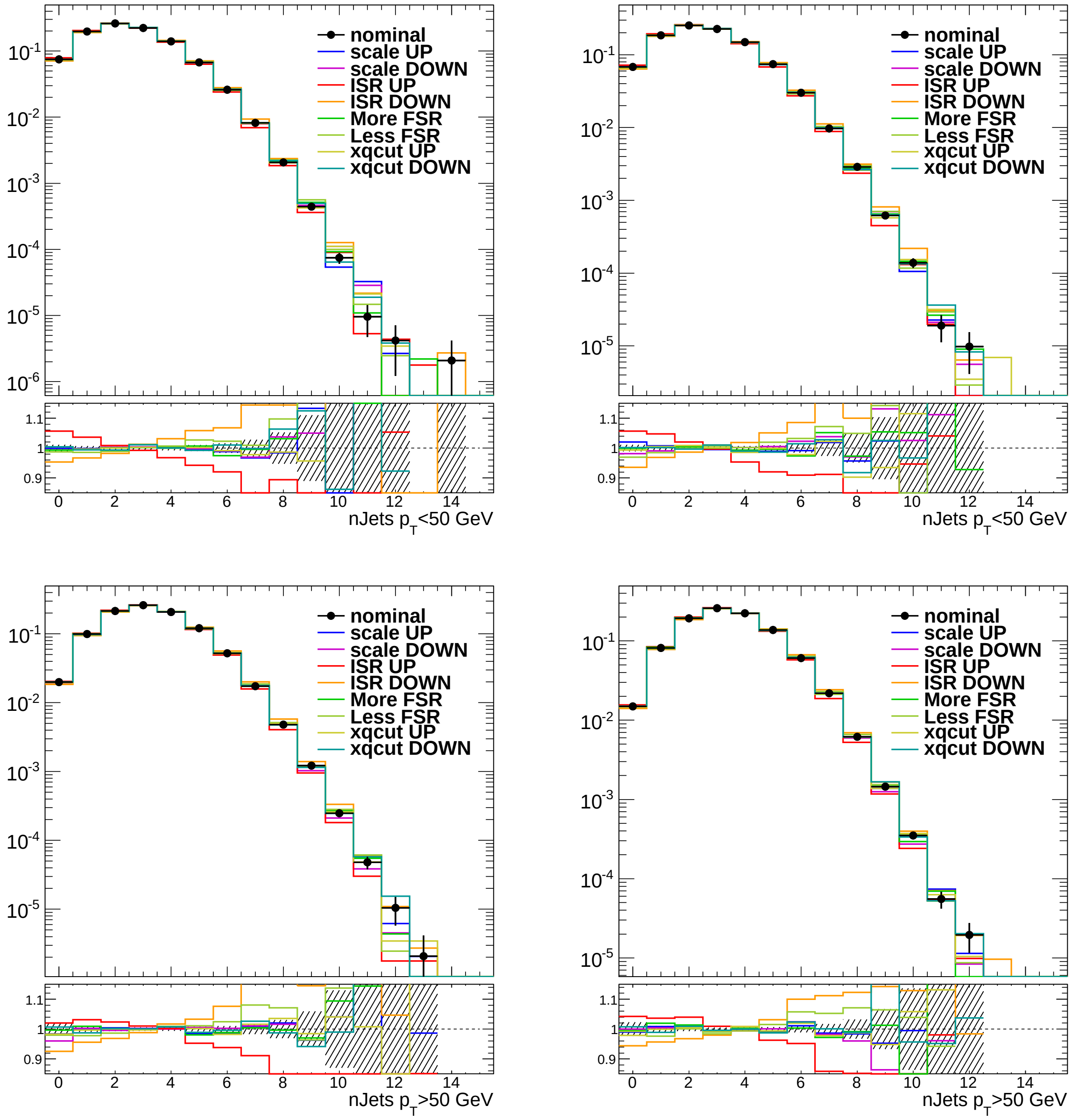

Figure 9.20: *Continue overleaf.*

Variation	`MADGRAPH` parameters	`PYTHIA` parameters
Nominal	scalefact=1.0,xqcut=20 GeV	PARP(64)=0.68, PARP(72)=0.527, PARJ(82)=0.83
scale UP	scalefact=2.0	–
scale DOWN	scalefact=0.5	–
ISR UP	alpsfact=2.0	PARP(64)=4.0,
ISR DOWN	alpsfact=0.5	PARP(64)=0.25,
More FSR	–	PARP(72)=0.7905, PARJ(82)=0.5
Less FSR	–	PARP(72)=0.2635, PARJ(82)=1.66
xqcut UP	xqcut=25 GeV	–
xqcut DOWN	xqcut=15 GeV	–

Table 9.19: Summary of each systematic variation. The fist row shows the nominal settings and all subsequent rows show the modified parameter values for each variation, the "–" symbol denotes that all the relevant parameters remain unchanged.

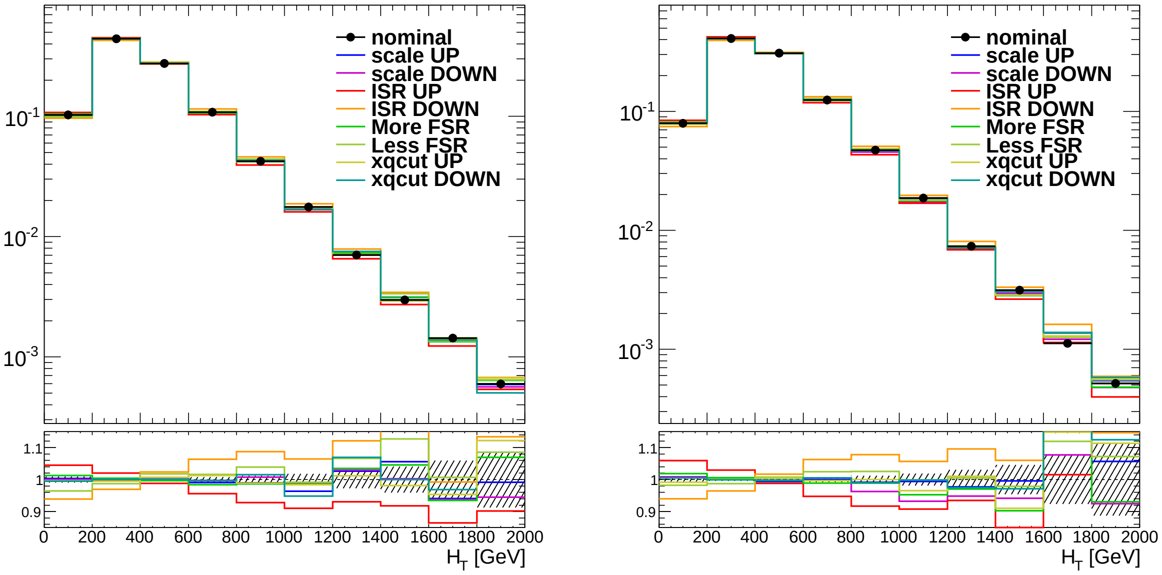

Figure 9.20: Kinematic distributions for $t\bar{t}$+W (left) and $t\bar{t}$+Z (right) for each systematic variation. The hatched band represents the statistical uncertainty on the nominal sample.

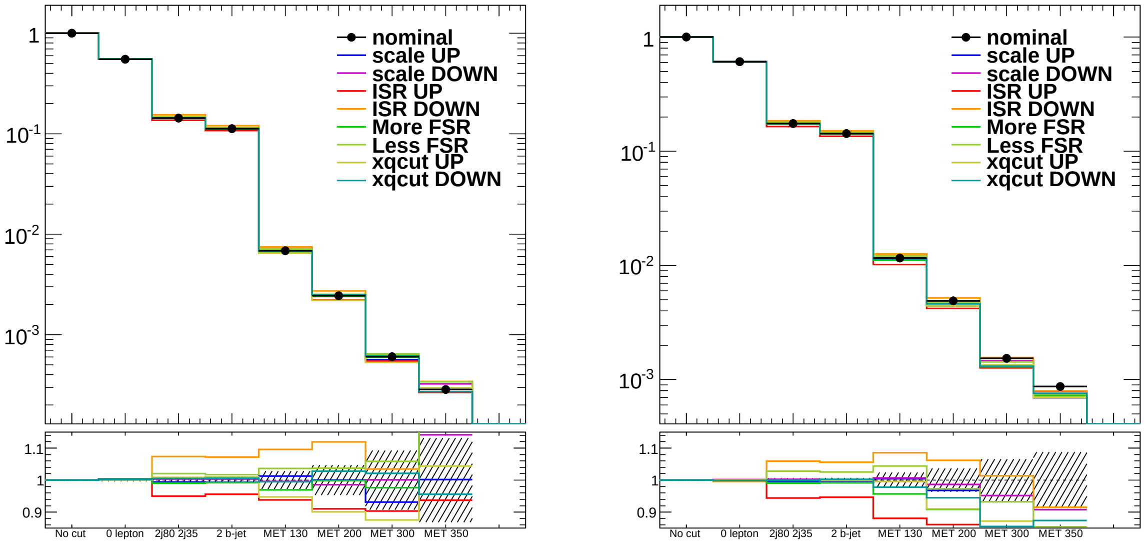

Figure 9.21: Cut efficiency for $t\bar{t}+W$ (left) and $t\bar{t}+Z$ (right) for each systematic variation. The hatched band represents the statistical uncertainty on the nominal sample.

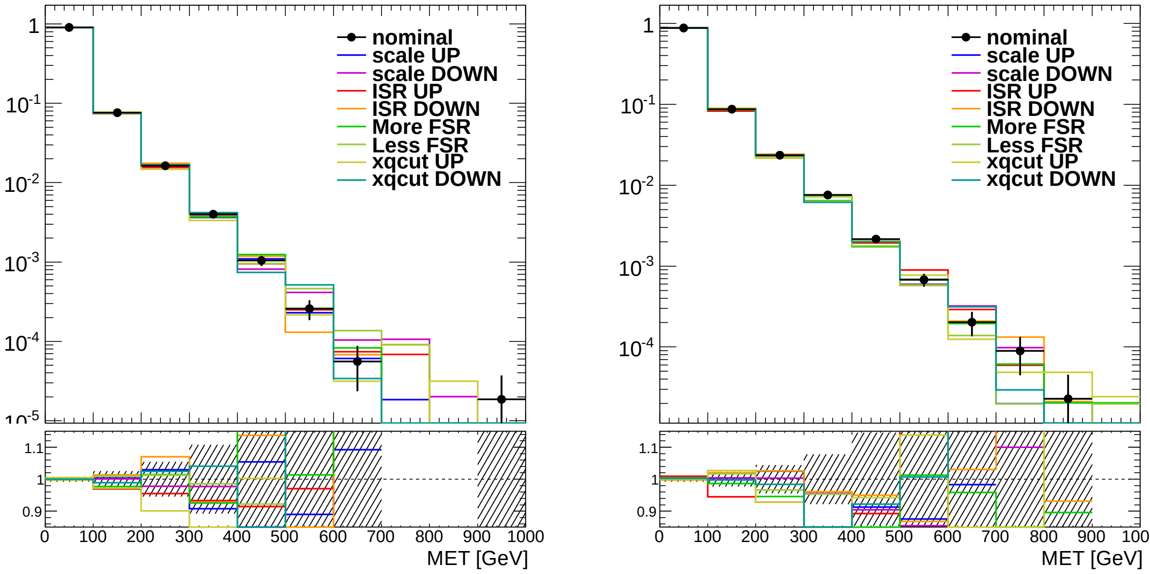

Figure 9.22: $E_{\mathrm{T}}^{\mathrm{miss}}$ distribution for $t\bar{t}+W$ (left) and $t\bar{t}+Z$ (right) for each systematic variation. The hatched band represents the statistical uncertainty on the nominal sample.

Variation	0 lepton	2j80 6j35	2 b-jet	MET130	MET200	MET300	MET350
scale	0.1%	0.3%	0.1%	0.1%	0.9%	5.1%	5.4%
ISR	0.2%	5.8%	5.5%	10.3%	10.1%	9.7%	4.8%
FSR	0%	1.9%	1.7%	4.4%	3.2%	4.6%	0.5%
xqcut	0%	0%	0.2%	0.9%	1.8%	0.5%	3%
Total	0.3%	6.1%	5.7%	11.2%	10.8%	11.9%	7.8%

Table 9.20: Summary of contribution of each systematic variation at each stage of the signal region selection. The uncertainties have been symmetrised taking the full envelope of the variation and centering on the nominal value.

signal region selection. Again it is clear that the ISR variation has the largest effect on the selection efficiency, especially at the jet selection stage. Figure 9.22 shows $E_{\mathrm{T}}^{\mathrm{miss}}$ distribution after a requirement of a lepton veto, $p_{\mathrm{T}} > 80, 80, 35, ..., 35$ GeV and 2 b-jets. Although the statistics are very limited there does not appear to be a strong dependence in the shape of the $E_{\mathrm{T}}^{\mathrm{miss}}$ for any variation.

Table 9.20 summarises the contribution of each variation at each stage of the selection and the total combined uncertainty. The largest uncertainty comes at the $E_{\mathrm{T}}^{\mathrm{miss}} > 300$ GeV cut and is 11.9% and, as expected, is dominated by the ISR variation. The decrease in uncertainty at the $E_{\mathrm{T}}^{\mathrm{miss}} > 350$ GeV cut is likely to be due to a lack of statistics. Hence a total uncertainty of 12% would be quoted using this method. In the final limit calculation a more conservative uncertainty of 30% on the LO→NLO k-factor is applied to cover the shape uncertainty.

9.4.4 Systematic uncertainties

Several sources of systematic uncertainties are considered in the analysis. Each uncertainty is treated as a nuisance parameter in the profile likelihood fit, which will be described in more detail later in §9.4.5. Table 9.21 gives a summary of the dominant systematic uncertainties on the signal region yields.

The important systematic uncertainties on reconstructed objects arise due to uncertainties on the JES, JER and b-tagging efficiency. In the leptonic control regions the uncertainty on lepton identification and momentum and energy scale are also considered. A significant uncertainty on the $t\bar{t}$ and Z+jets background estimates comes from theoretical uncertainty in the shape and normalisation of these processes. The systematic uncertainties on the $t\bar{t} + W/Z$ processes have already been discussed in §9.4.3.

Uncertainty	**SR1**	**SR2**	**SR3**
Total	18%	33%	45%
Background sample sizes (data and simulation)	10%	17%	21%
Jet energy scale and resolution	10%	10%	25%
$t\bar{t}$ theory	10%	19%	22%
Z+jets theory	4%	8%	8%
$t\bar{t} + W/Z$ theory	5%	8%	10%

Table 9.21: The total systematic uncertainty on the background in each of the three signal regions and a list of the dominant contributions to the uncertainty. The individual uncertainties can be correlated.

Theoretical uncertainty on $t\bar{t}$ background estimation arises due to the fixed order of the matrix element calculation, uncertainties in the hadronisation and fragmentation and from the amount of initial and final state radiation produced by the generator. These uncertainties can affect the shape of distributions and hence the extrapolation of the MC from control region to signal region and the normalisation of the samples. The latter is reduced by employing a semi-data-driven background estimation technique. The generator uncertainties are assessed through comparison of the nominal sample to other generators/parton showers and to samples where the renormalisation and factorisation scale in `POWHEF` are varied and to `ACERMC` samples where the amount of ISR/FSR is varied.

Similarly the theoretical uncertainty on the Z+jets estimate is assessed by comparing the nominal samples with additional samples generated with variations of the renormalisation and factorisation scale. An additional uncertainty on the normalisation for Z+jets on the number of additional partons and the flavour content of the additional jets is considered.

9.4.5 Results and interpretation

As previously discussed in §7.4 a profile likelihood combined fit of the signal region and $t\bar{t}$ control region is performed to extract the final estimate of the SM background expectation. The number of events in each control and signal region is treated with a Poisson probability density function. The statistical and systematic uncertainties on the expected yields are included in the probability density function as nuisance parameters, constrained to be Gaussian with a width given by the size of the uncertainty. In total seventeen nuisance parameters are included in the fit and correlations between the control region and signal

Number of events	**SR1**	**SR2**	**SR3**
Observed	15	2	1
Expected background	17.5 ± 3.2	4.7 ± 1.5	2.7 ± 1.2
Expected $t\bar{t}$	9.8 ± 2.6	1.9 ± 1.3	0.9 ± 0.7
Expected $t\bar{t} + W/Z$	1.7 ± 1.0	0.7 ± 0.4	0.51 ± 0.30
Expected Z+jets	2.1 ± 1.0	1.2 ± 0.5	0.8 ± 0.4
Expected W+jets	1.2 ± 0.8	0.32 ± 0.29	$0.19^{+0.23}_{-0.19}$
Expected single-top	1.5 ± 0.9	0.5 ± 0.4	$0.3^{+0.5}_{-0.3}$
Expected multijet	0.12 ± 0.12	0.01 ± 0.01	< 0.01
Expected diboson	1.2 ± 1.2	< 0.22	< 0.22
Fit input expectation $t\bar{t}$	9.9	1.7	0.6

Table 9.22: The observed numbers of events in the three signal regions, and the background expectations.

region are taken into account. A likelihood is formed by the product of these probability density functions and the constraints on the nuisance parameters. The $t\bar{t}$ background normalisation is allowed to vary in the fit and is adjusted to maximize the likelihood.

Table 9.22 shows the number of events observed in data compared to the SM expectation in each signal region. The $t\bar{t}$ expectation before and after the fit is shown. No significant deviation from the SM expectation is observed.

Figure 9.23 shows the $E_{\mathrm{T}}^{\mathrm{miss}}$ and $m_{\mathrm{T}}(b, E_{\mathrm{T}}^{\mathrm{miss}})$ distributions with the full signal region selection applied except the cut on that variable. The observation is consistent with the SM expectation in both cases.

The result is interpreted in terms of 95% confidence level exclusion limits in the $m_{\tilde{t}_1} - m_{\tilde{\chi}_1^0}$ plane, assuming a branching ratio $\tilde{t}_1 \rightarrow t\tilde{\chi}_1^0 = 100\%$. The resulting exclusion limits are show in Figure 9.24 (a). The yellow band signifies the $\pm 1\sigma$ uncertainties on the expected exclusion limit for all uncertainties other than the theoretic uncertainty on the signal. The dashed red lines signify the uncertainty on the observed exclusion limit due to the theoretical uncertainty on the signal cross section. The -1σ uncertainty on the observed limit is conservatively chosen to be the quoted exclusion reach. For a nearly massless neutralino stop masses between 320 and 660 GeV are excluded. For neutralino mass of 150 GeV, stop masses are excluded between 400 and 620 GeV. This result significantly extends previous limits described in §9.3.

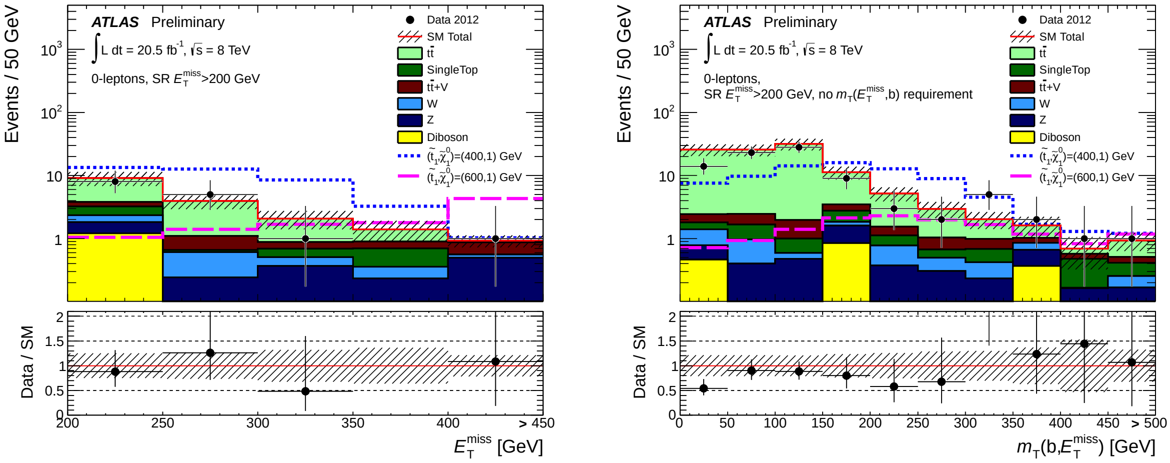

Figure 9.23: Distributions of $E_{\mathrm{T}}^{\mathrm{miss}}$ (left) and $m_{\mathrm{T}}(b, E_{\mathrm{T}}^{\mathrm{miss}})$ (right) after all selection requirements except for the one on the variable being plotted. The rightmost bin includes all overflow. For the $m_{\mathrm{T}}(b, E_{\mathrm{T}}^{\mathrm{miss}})$ distribution, $E_{\mathrm{T}}^{\mathrm{miss}} >$ 200 GeV has been applied. The SM expectation shown here is the input to the SM background fit. The uncertainty band around the SM expectation combines statistical and systematic uncertainties. Figures from [4].

It is also possible to convert the model-dependant cross section upper limit into an upper limit of the branching ratio for $\tilde{t}_1 \to t\tilde{\chi}_1^0$ in the $m_{\tilde{t}_1} - m_{\tilde{\chi}_1^0}$ plane. This interpretation is shown in Figure 9.24 (b). For a stop quark mass of 400 GeV and neutralino mass of 1 GeV branching ratios above 54% are excluded in this signal model.

9.5 Summary and conclusions

Two analyses have been reported, both targeting direct stop quark production with the $\tilde{t}_1 \to t\tilde{\chi}_1^0$ decay of the stop in the 0-lepton final state. These searches have used the full 2011 and 2012 datasets collected by ATLAS at $\sqrt{s} = 7$ TeV and $\sqrt{s} = 8$ TeV respectively. No significant excesses were found in either case and exclusion limits in terms of the $m_{\tilde{t}_1} - m_{\tilde{\chi}_1^0}$ plane are set. Figure 9.25 shows the exclusion limits set by both these analyses and the other $\tilde{t}_1 \to t\tilde{\chi}_1^0$ searches performed by ATLAS including leptonic final states. The most recent analysis, using 2012 data, sets the most stringent exclusion limits for a nearly massless neutralino, with stop masses excluded up to 620 GeV.

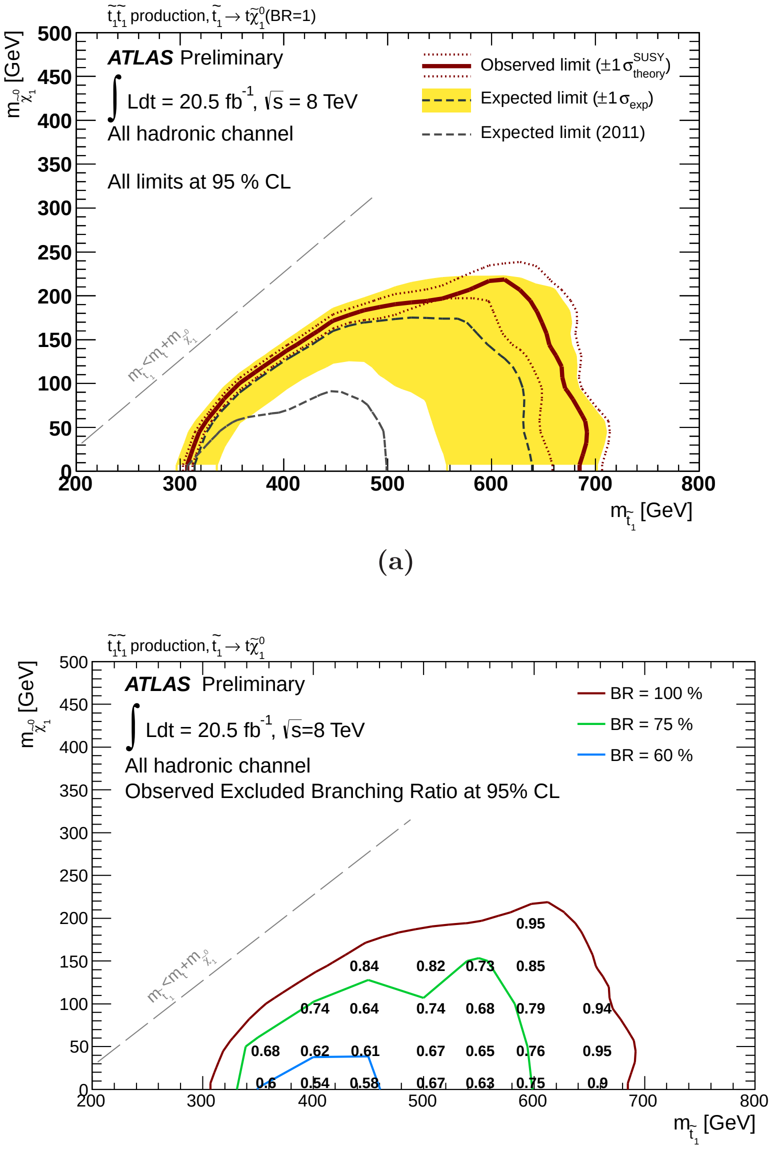

(a)

(b)

Figure 9.24: (a) Expected and observed exclusion limits at 95% CL for the model of $(pp \to \tilde{t}_1\tilde{t}_1^* \to t\tilde{\chi}_1^0\bar{t}\tilde{\chi}_1^0)$ with 100% branching ratio of $\tilde{t}_1 \to t\tilde{\chi}_1^0$. (b) Excluded (at 95% CL) branching fractions for $\tilde{t}_1 \to t\tilde{\chi}_1^0$ in the model where $pp \to \tilde{t}_1\tilde{t}_1^*$. Figures from [4].

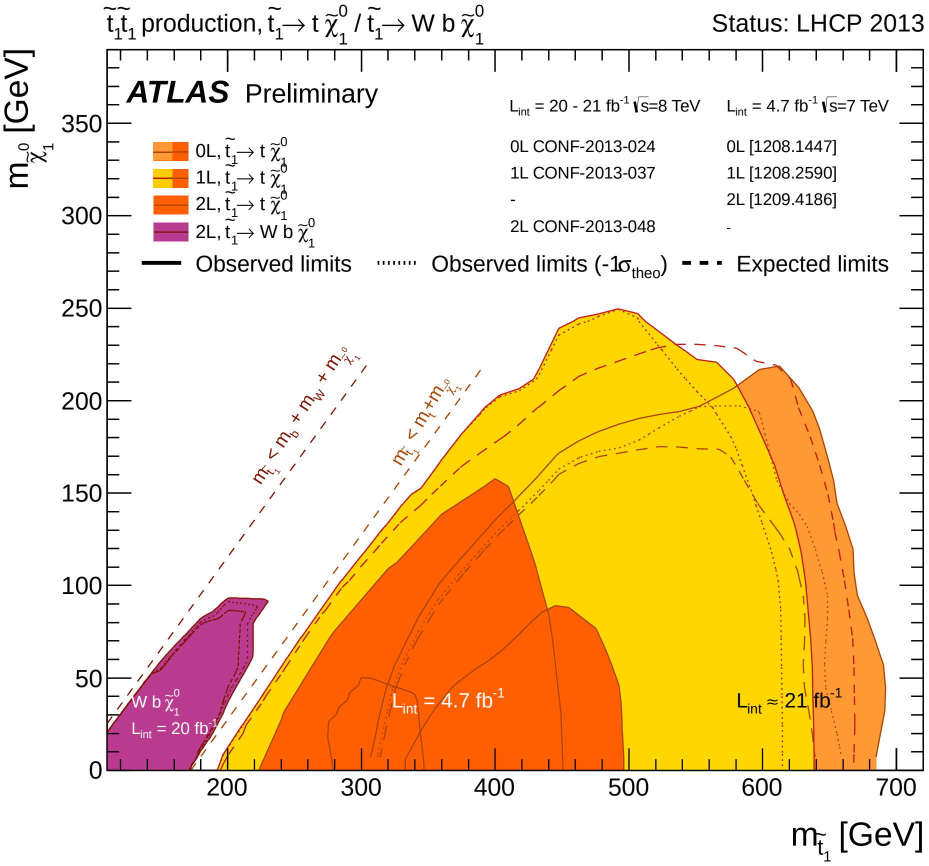

Figure 9.25: Summary of all ATLAS stop results including the $\tilde{t}_1 \rightarrow t\tilde{\chi}_1^0$ decay mode. Figure from [77].

Chapter 10

Summary

The LHC and its detectors have now experienced more than two years of greatly successful data taking. The results of measurements and searches performed using this data have already made remarkable progress in high energy particle physics. The discovery of a Higgs boson is arguably the highlight of the LHC results so far and represents a significant milestone. This thesis has used data collected during 2011 and 2012 to perform a number of analyses.

The analysis described in Chapter 6 was a search for $t\bar{t} + Z$ production in the three lepton final state which was performed using 4.7 fb^{-1} of $\sqrt{s} = 7$ TeV pp collision data collected by ATLAS. In a signal region requiring three leptons, a missing transverse momentum of 30 GeV and four jets with $p_{\mathrm{T}} > 30$ GeV and one b-tagged jet, one candidate event whose kinematical properties are consistent with a $t\bar{t} + Z$ event was found in data. This was in agreement with the SM expectation and the result was translated to a 95% probability upper limit of 0.71 pb on the $t\bar{t} + Z$ production cross section, consistent with the NLO Standard Model prediction of 0.14 pb.

Chapter 8 outlined a search for direct pair production of the supersymmetric partner to the bottom quark using 2.05 fb^{-1} of $\sqrt{s} = 7$ TeV data. The search is focused on the $\tilde{b}_1 \to b\tilde{\chi}_1^0$ decay mode assuming a branching ratio of 100%. No significant excess was observed in the data and exclusion limits at the 95% confidence level were set. For a massless neutralino sbottom masses are excluded up to 390 GeV. For a neutralino mass of 120 GeV sbottom masses are excluded for $275 < m_{\tilde{b}} < 350$ GeV. These limits significantly extended the reach of previous searches.

In Chapter 9 two searches for direct pair production of the supersymmetric partner to the top quark were described. One performed using 4.7 fb^{-1} of $\sqrt{s} = 7$ TeV data collected during 2011 and the other using 20.5 fb^{-1} of $\sqrt{s} = 8$ TeV data collected during 2012. In both cases the stops are assumed to decay via $\tilde{t}_1 \to t\tilde{\chi}_1^0$ with a branching ratio of 100%. No significant excess above the SM expectation was observed in either dataset and the result is interpreted in terms of 95% confidence level exclusion limits in the $m_{\tilde{t}_1} - m_{\tilde{\chi}_1^0}$ plane. In the 2011 data analysis stop masses are excluded between 370 and 465 GeV for a neutralino mass of ~ 0 GeV and a stop mass of 445 GeV is excluded for neutralino masses below 50 GeV. In the 2012 analysis, for a nearly massless neutralino stop masses between 320 and 660 GeV are excluded. For a neutralino mass of 150 GeV, stop masses are excluded between 400 and 620 GeV. This result excludes top squarks up to higher masses than in previous searches. From the 2012 data result, the model-dependant cross section upper limit was converted into an upper limit of the branching ratio for $\tilde{t}_1 \to t\tilde{\chi}_1^0$ in the $m_{\tilde{t}_1} - m_{\tilde{\chi}_1^0}$ plane. For a stop quark mass of 400 GeV and neutralino mass of 1 GeV branching ratios above 54% are excluded.

Several searches for new physics have been performed using the data collected during 2011 and 2012 and whilst no significant deviation from the SM expectation has so far been observed there is much work left to do. The shutdown of the LHC until early 2015 and the corresponding increase in centre of mass energy that will be available when it comes back online will facilitate the most stringent tests of the SM to date. The lack of any observation of any new physics at this increased centre of mass energy would be a very interesting result in itself. Amongst other things it will cast into doubt the suitability of many SUSY scenarios as extensions to the SM.

References

[1] *Search for $t\bar{t}Z$ production in the three lepton final state with* 4.7 fb^{-1} *of* $\sqrt{s} = 7$ *TeV pp collision data collected by the ATLAS detector*, Tech. Rep. ATLAS-CONF-2012-126, CERN, Geneva, Aug, 2012.

[2] ATLAS Collaboration Collaboration, G. Aad et al., *Search for scalar bottom pair production with the ATLAS detector in pp Collisions at* $\sqrt{s} = 7$ *TeV*, Phys.Rev.Lett. **108** (2012) 181802, `arXiv:1112.3832 [hep-ex]`.

[3] ATLAS Collaboration, *Search for a supersymmetric partner to the top quark in final states with jets and missing transverse momentum at* $\sqrt{s} = 7$ *TeV with the ATLAS detector*, Phys. Rev. Lett. **109** (2012) 211802, `arXiv:1208.1447 [hep-ex]`.

[4] *Search for direct production of the top squark in the all-hadronic ttbar + etmiss final state in 21 fb-1 of p-pcollisions at sqrt(s)=8 TeV with the ATLAS detector*, Tech. Rep. ATLAS-CONF-2013-024, CERN, Geneva, Mar, 2013.

[5] T. Aoyama, M. Hayakawa, T. Kinoshita, and M. Nio, *Tenth-Order QED Contribution to the Electron g-2 and an Improved Value of the Fine Structure Constant*, Phys.Rev.Lett. **109** (2012) 111807, `arXiv:1205.5368 [hep-ph]`.

[6] K. Garrett and G. Duda, *Dark Matter: A Primer*, Adv.Astron. **2011** (2011) 968283, `arXiv:1006.2483 [hep-ph]`.

[7] Particle Data Group Collaboration, J. Beringer et al. Phys. Rev. **D86** (2012) .

[8] M. Kobayashi and T. Maskawa, *CP-Violation in the Renormalizable Theory of Weak Interaction*, Progress of Theoretical Physics **49** (1973) no. 2, 652–657.

[9] D. Griffiths, *Introduction to Elementary Particles.* Wiley-VCH Verlag GmbH, 2008. `http://dx.doi.org/10.1002/9783527618460.ch7`.

[10] Particle Data Group Collaboration, K. Nakamura et al. JPG 37, 075021 (2010) . `http://pdg.lbl.gov`.

[11] ATLAS Collaboration Collaboration, G. Aad et al., *Observation of a new particle in the search for the Standard Model Higgs boson with the ATLAS detector at the LHC*, Phys.Lett. **B716** (2012) 1–29, `arXiv:1207.7214 [hep-ex]`.

[12] CMS Collaboration Collaboration, S. Chatrchyan et al., *Observation of a new boson at a mass of 125 GeV with the CMS experiment at the LHC*, Phys.Lett. **B716** (2012) 30–61, `arXiv:1207.7235 [hep-ex]`.

[13] ATLAS Collaboration Collaboration, G. Aad et al., *Evidence for the spin-0 nature of the Higgs boson using ATLAS data*, `arXiv:1307.1432 [hep-ex]`.

[14] ATLAS Collaboration Collaboration, G. Aad et al., *Measurements of Higgs boson production and couplings in diboson final states with the ATLAS detector at the LHC*, `arXiv:1307.1427 [hep-ex]`.

[15] I. J. R. Aitchison and A. J. Hey, *Gauge theories in particle physics*, .

[16] F. Halzen and A. Martin, *QUARK & LEPTONS: AN INTRODUCTORY COURSE IN MODERN PARTICLE PHYSICS.* Wiley India Pvt. Limited, 2008. `http://books.google.co.uk/books?id=ITQy9G62H0gC`.

[17] *Partial-symmetries of weak interactions*, Nuclear Physics **22** (1961) no. 4, 579 – 588.

[18] S. Weinberg, *A Model of Leptons*, Phys. Rev. Lett. **19** (Nov, 1967) 1264–1266.

[19] A. Salam,
Gauge unification of fundamental forces, Rev. Mod. Phys. **52** (Jul, 1980) 525–538.

[20] S. P. Martin, *A Supersymmetry Primer*, 1997. `arXiv:hep-ph/9709356`.

[21] SNO Collaboration Collaboration, Q. Ahmad et al., *Direct evidence for neutrino flavor transformation from neutral current interactions in the Sudbury Neutrino Observatory*, Phys.Rev.Lett. **89** (2002) 011301, `arXiv:nucl-ex/0204008 [nucl-ex]`.

[22] S. Weinberg, *Implications of Dynamical Symmetry Breaking*,
Phys. Rev. **D13** (1976) 974–996.

[23] E. Gildener, *Gauge Symmetry Hierarchies*, Phys. Rev. **D14** (1976) 1667.

[24] S. Weinberg, *Implications of Dynamical Symmetry Breaking: An Addendum*,
Phys. Rev. **D19** (1979) 1277–1280.

[25] L. Susskind, *Dynamics of Spontaneous Symmetry Breaking in the Weinberg- Salam Theory*, Phys. Rev. **D20** (1979) 2619–2625.

[26] ALEPH Collaboration, CDF Collaboration, D0 Collaboration, DELPHI Collaboration, L3 Collaboration, OPAL Collaboration, SLD Collaboration, LEP Electroweak Working Group, Tevatron Electroweak Working Group, SLD Electroweak and Heavy Flavour Groups Collaboration, *Precision Electroweak Measurements and Constraints on the Standard Model*, `arXiv:1012.2367 [hep-ex]`.

[27] B. W. Lee, C. Quigg, and H. Thacker, *The Strength of Weak Interactions at Very High-Energies and the Higgs Boson Mass*, Phys.Rev.Lett. **38** (1977) 883–885.

[28] B. W. Lee, C. Quigg, and H. Thacker, *Weak Interactions at Very High-Energies: The Role of the Higgs Boson Mass*, Phys.Rev. **D16** (1977) 1519.

[29] *The hierarchy problem and new dimensions at a millimeter*, Physics Letters B **429** (1998) no. 34, 263 – 272.

[30] O. Klein, *Quantentheorie und fnfdimensionale Relativittstheorie*, Zeitschrift fr Physik **37** (1926) no. 12, 895–906. `http://dx.doi.org/10.1007/BF01397481`.

[31] H. Miyazawa, *Baryon Number Changing Currents*, Prog. Theor. Phys. **36 (6)** (1966) 1266–1276.

[32] R. Ramond, *Dual Theory for Free Fermions*, Phys. Rev. **D3** (1971) 2415–2418.

[33] Yu.A. Golfand and E.P. Likhtman, JETP Lett. **13** (1971) 323; A. Neveu and J.H. Schwartz, Nucl. Phys. **B31** (1971) 86; A. Neveu and J.H. Schwartz, Phys. Rev. **D4** (1971) 1109; P. Ramond, Phys. Rev. **D3** (1971) 2415; D.V. Volkov and V.P. Akulov, Phys. Lett. **B46** (1973) 109; J. Wess and B. Zumino, Phys. Lett. **B49** (1974) 52; J. Wess and B. Zumino, Nucl. Phys. **B70** (1974) 39.

[34] A. Neveu and J. Schwarz, *Factorizable dual model of pions*, Nucl. Phys. **B31** (1971) 86–112.

[35] A. Neveu and J. Schwarz, *Quark Model of Dual Pions*, Phys. Rev. **D4** (1971) 1109–1111.

[36] J. Gervais and B. Sakita, *Field theory interpretation of supergauges in dual models*, Nucl. Phys. **B34** (1971) 632–639.

[37] D. Volkov and V. Akulov, *Is the Neutrino a Goldstone Particle?*, Phys. Lett. **B46** (1973) 109–110.

[38] J. Wess and B. Zumino, *A Lagrangian Model Invariant Under Supergauge Transformations*, Phys. Lett. **B49** (1974) 52.

[39] J. Wess and B. Zumino, *Supergauge Transformations in Four-Dimensions*, Nucl. Phys. **B70** (1974) 39–50.

[40] P. Fayet, *Supersymmetry and Weak, Electromagnetic and Strong Interactions*, Phys. Lett. **B64** (1976) 159.

[41] P. Fayet, *Spontaneously Broken Supersymmetric Theories of Weak, Electromagnetic and Strong Interactions*, Phys. Lett. **B69** (1977) 489.

[42] G. R. Farrar and P. Fayet, *Phenomenology of the Production, Decay, and Detection of New Hadronic States Associated with Supersymmetry*, Phys. Lett. **B76** (1978) 575–579.

[43] P. Fayet, *Relations Between the Masses of the Superpartners of Leptons and Quarks, the Goldstino Couplings and the Neutral Currents*, Phys. Lett. **B84** (1979) 416.

[44] S. Dimopoulos and H. Georgi, *Softly Broken Supersymmetry and SU(5)*, Nucl. Phys. **B193** (1981) 150.

[45] *Comparison of grand unified theories with electroweak and strong coupling constants measured at {LEP}*, Physics Letters B **260** (1991) no. 34, 447 – 455.

[46] *Proton stability in grand unified theories, in strings and in branes*, Physics Reports **441** (2007) no. 56, 191 – 317.

[47] A. H. Chamseddine, R. Arnowitt, and P. Nath, *Locally Supersymmetric Grand Unification*, Phys. Rev. Lett. **49** (1982) 970.

[48] R. Barbieri, S. Ferrara, and C. A. Savoy, *Gauge Models with Spontaneously Broken Local Supersymmetry*, Phys. Lett. **B119** (1982) 343.

[49] L. E. Ibanez, *Locally Supersymmetric SU(5) Grand Unification*, Phys. Lett. **B118** (1982) 73.

[50] L. J. Hall, J. D. Lykken, and S. Weinberg, *Supergravity as the Messenger of Supersymmetry Breaking*, Phys. Rev. **D27** (1983) 2359–2378.

[51] N. Ohta, *Grand Unified Theories Based on Local Supersymmetry*, Prog. Theor. Phys. **70** (1983) 542.

[52] G. L. Kane, C. F. Kolda, L. Roszkowski, and J. D. Wells, *Study of constrained minimal supersymmetry*, Phys. Rev. **D49** (1994) 6173–6210.

[53] LHCb Collaboration Collaboration, R. Aaij et al., *Implications of LHCb measurements and future prospects*, Eur.Phys.J. **C73** (2013) 2373, `arXiv:1208.3355 [hep-ex]`.

[54] F. Mahmoudi, *Direct and indirect searches for New Physics*, `arXiv:1205.3099 [hep-ph]`.

[55] Muon G-2 Collaboration Collaboration, G. Bennett et al., *Final Report of the Muon E821 Anomalous Magnetic Moment Measurement at BNL*, Phys.Rev. **D73** (2006) 072003, `arXiv:hep-ex/0602035 [hep-ex]`.

[56] P. Bechtle, T. Bringmann, K. Desch, H. Dreiner, M. Hamer, et al., *Constrained Supersymmetry after two years of LHC data: a global view with Fittino*, JHEP **1206** (2012) 098, `arXiv:1204.4199 [hep-ph]`.

[57] O. Buchmueller, R. Cavanaugh, A. De Roeck, M. Dolan, J. Ellis, et al., *Higgs and Supersymmetry*, Eur.Phys.J. **C72** (2012) 2020, `arXiv:1112.3564 [hep-ph]`.

[58] K. A. Olive, *Searching for supersymmetric dark matter*, `arXiv:hep-ph/0208092 [hep-ph]`.

[59] WMAP Collaboration Collaboration, E. Komatsu et al., *Seven-Year Wilkinson Microwave Anisotropy Probe (WMAP) Observations: Cosmological Interpretation*, Astrophys.J.Suppl. **192** (2011) 18, `arXiv:1001.4538 [astro-ph.CO]`.

[60] CDF Collaboration, *Inclusive Search for Squark and Gluino Production in $p\bar{p}$ Collisions at $\sqrt{s}$ = 1.96-TeV*, Phys. Rev. Lett. **102** (2009) 121801, `arXiv:0811.2512 [hep-ex]`.

[61] D0 Collaboration, *Search for squarks and gluinos in events with jets and missing transverse energy using 2.1 fb^{-1} of $p\bar{p}$ collision data at $\sqrt{s}$ = 1.96- TeV*, Phys. Lett. **B660** (2008) 449–457, `arXiv:0712.3805 [hep-ex]`.

[62] *Searches for supersymmetric particles in e + e- collisions up to 208 GeV and interpretation of the results within the MSSM*, The European Physical Journal C - Particles and Fields **31** (2003) no. 4, 421–479. `http://dx.doi.org/10.1140/epjc/s2003-01355-5`.

[63] ALEPH Collaboration Collaboration, A. Heister et al., *Absolute lower limits on the masses of selectrons and sneutrinos in the MSSM*, Phys.Lett. **B544** (2002) 73–88, `arXiv:hep-ex/0207056 [hep-ex]`.

[64] H. Baer, V. Barger, and A. Mustafayev, *Implications of a 125 GeV Higgs scalar for LHC SUSY and neutralino dark matter searches*, Phys.Rev. **D85** (2012) 075010, `arXiv:1112.3017 [hep-ph]`.

[65] L. J. Hall, D. Pinner, and J. T. Ruderman, *A Natural SUSY Higgs Near 126 GeV*, JHEP **1204** (2012) 131, `arXiv:1112.2703 [hep-ph]`.

[66] P. Draper, P. Meade, M. Reece, and D. Shih, *Implications of a 125 GeV Higgs for the MSSM and Low-Scale SUSY Breaking*, Phys.Rev. **D85** (2012) 095007, `arXiv:1112.3068 [hep-ph]`.

[67] A. Djouadi, J.-L. Kneur, and G. Moultaka, *SuSpect: A Fortran code for the supersymmetric and Higgs particle spectrum in the MSSM*, Comput.Phys.Commun. **176** (2007) 426–455, `arXiv:hep-ph/0211331 [hep-ph]`.

[68] M. Frank, T. Hahn, S. Heinemeyer, W. Hollik, H. Rzehak, et al., *The Higgs Boson Masses and Mixings of the Complex MSSM in the Feynman-Diagrammatic Approach*, JHEP **0702** (2007) 047, `arXiv:hep-ph/0611326 [hep-ph]`.

[69] G. Degrassi, S. Heinemeyer, W. Hollik, P. Slavich, and G. Weiglein, *Towards high precision predictions for the MSSM Higgs sector*, Eur.Phys.J. **C28** (2003) 133–143, `arXiv:hep-ph/0212020 [hep-ph]`.

[70] S. Heinemeyer, W. Hollik, and G. Weiglein, *The Masses of the neutral CP - even Higgs bosons in the MSSM: Accurate analysis at the two loop level*, Eur.Phys.J. **C9** (1999) 343–366, `arXiv:hep-ph/9812472 [hep-ph]`.

[71] S. Heinemeyer, W. Hollik, and G. Weiglein, *FeynHiggs: A Program for the calculation of the masses of the neutral CP even Higgs bosons in the MSSM*, Comput.Phys.Commun. **124** (2000) 76–89, `arXiv:hep-ph/9812320 [hep-ph]`.

[72] ATLAS Collaboration, *Search for squarks and gluinos with the ATLAS detector in final states with jets and missing transverse momentum using 4.7 fb^{-1} of $\sqrt{s} = 7$ TeV proton-proton collision data*, Phys. Rev. D **87** (2013) 012008, `arXiv:1208.0949 [hep-ex]`.

[73] CMS Collaboration Collaboration, S. Chatrchyan et al., *Inclusive search for supersymmetry using the razor variables in pp collisions at $\sqrt{s} = 7$ TeV*, `arXiv:1212.6961 [hep-ex]`.

[74] CMS Collaboration Collaboration, S. Chatrchyan et al., *Search for supersymmetry in hadronic final states using MT2 in pp collisions at $\sqrt{s} = 7$ TeV*, JHEP **1210** (2012) 018, `arXiv:1207.1798 [hep-ex]`.

[75] CMS Collaboration Collaboration, S. Chatrchyan et al., *Search for Supersymmetry at the LHC in Events with Jets and Missing Transverse Energy*, Phys.Rev.Lett. **107** (2011) 221804, `arXiv:1109.2352 [hep-ex]`.

[76] `https://twiki.cern.ch/twiki/bin/view/CMSPublic/SUSYSMSSummaryPlots7TeV`.

[77] `https://twiki.cern.ch/twiki/bin/view/AtlasPublic/SupersymmetryPublicResults`.

[78] *Search for squarks and gluinos with the ATLAS detector in final states with jets and missing transverse momentum and 20.3 fb*$^{-1}$ *of* $\sqrt{s} = 8$ *TeV proton-proton collision data*, Tech. Rep. ATLAS-CONF-2013-047, CERN, Geneva, May, 2013.

[79] M. Perelstein, *Introduction to Collider Physics*, `arXiv:1002.0274 [hep-ph]`.

[80] R. K. Ellis, W. J. Stirling, and B. R. Webber, *QCD and Collider Physics*. Cambridge monographs on particle physics, nuclear physics, and cosmology. Cambridge Univ. Press, Cambridge, 2003. Photography by S. Vascotto.

[81] R. Feynman, *Photon-hadron interactions*, .

[82] R. Wallny, *A Measurement of the Gluon Distribution in the Proton and of the Strong Coupling Constant*, .

[83] A. D. Martin et al., *Parton distributions for the LHC*, Eur. Phys. J. **C63** (2009) 189–285, `arXiv:0901.0002 [hep-ph]`.

[84] Brüning, Oliver Sim and Collier, Paul and Lebrun, P and Myers, Stephen and Ostojic, Ranko and Poole, John and Proudlock, Paul, *LHC Design Report*. CERN, Geneva, 2004. `https://cds.cern.ch/record/782076`.

[85] T. Gleisberg et al., *Event generation with SHERPA 1.1*, JHEP **02** (2009) 007, `arXiv:0811.4622`.

[86] C. Lefevre, *The CERN accelerator complex. Complexe des acclrateurs du CERN*, Dec, 2008. `https://cds.cern.ch/record/1260465`.

[87] `https://cds.cern.ch/record/40525`.

[88] *Proceedings of the 3rd Evian Workshop on LHC beam operation*. CERN, Geneva, 2011. `https://cdsweb.cern.ch/record/1451243/`.

[89] ATLAS Collaboration, *The ATLAS Experiment at the CERN Large Hadron Collider*, JINST **3** (2008) S08003.

[90] J. Goodson. `http://www.jetgoodson.com/images/thesisImages/magnetSystems.png`.

[91] ATLAS Collaboration, *ATLAS inner detector: Technical design report. Vol. 2*, . CERN-LHCC-97-17.

[92] D. Robinson, *Silicon Central Tracker Commissioning in ATLAS. Commissioning of the ATLAS Silicon Tracker*, PoS **Vertex 2007** (2007) 001.

[93] B. Demirkoz, *Construction and Performance of the ATLAS SCT Barrels and Cosmic Tests*, .

[94] *ATLAS: Detector and physics performance technical design report. Volume 1*, . CERN-LHCC-99-14.

[95] C. Fabjan and F. Gianotti, *Calorimetry for particle physics*, Rev.Mod.Phys. **75** (2003) 1243–1286.

[96] `https://twiki.cern.ch/twiki/bin/view/AtlasPublic/LuminosityPublicResults`.

[97] `http://cms.web.cern.ch/news/jets-cms-and-determination-their-energy-scale`.

[98] G. P. Salam, *Towards Jetography*, Eur.Phys.J. **C67** (2010) 637–686, `arXiv:0906.1833 [hep-ph]`.

[99] G. Sieber, G. Quast, and K. Rabbertz, *Determination of the proton structure and the strong coupling from inclusive jet cross sections at the LHC*. PhD thesis, Karlsruhe, Inst. Technol., Mar, 2013. Presented 15 Mar 2013.

[100] G. S. M. Cacciari and G. Soyez, *The anti-k_t jet clustering algorithm*, JHEP **04** (2008) 063, `arXiv:0802.1189 [hep-ph]`.

[101] ATLAS Collaboration, *Jet energy measurement with the ATLAS detector in proton-proton collisions at $\sqrt{s} = 7$ TeV*, submitted to Eur. Phys. J. (2011) , `arXiv:1112.6426 [hep-ex]`.

[102] ATLAS Collaboration, *Expected Performance of the ATLAS Experiment - Detector, Trigger and Physics*, 2009. `arXiv:0901.0512 [hep-ex]`.

[103] ATLAS Collaboration, *Performance of the ATLAS Secondary Vertex b-tagging Algorithm in 7 TeV Collision Data*, Atlas-conf-2010-042, 2010.

[104] ATLAS Collaboration, *Expected Performance of the ATLAS Experiment - Detector, Trigger and Physics*, CERN-OPEN-2008-020 , `arXiv:0901.0512 [hep-ex]`.

[105] *Calibrating the b-Tag and Mistag Efficiencies of the SV0 b-Tagging Algorithm in 3 pb^{-1} of Data with the ATLAS Detector*, Tech. Rep. ATLAS-CONF-2010-099, CERN, Geneva, Dec, 2010.

[106] ATLAS Collaboration, *Commissioning of the ATLAS high-performance b-tagging algorithms in the 7 TeV collision data*, `https://cdsweb.cern.ch/record/1369219/`.

[107] ATLAS Collaboration, *Measurement of the b-tag efficiency in a sample of jets containing muons with 5* fb^{-1} *of data from the ATLAS detector*, ATLAS-CONF-2012-043 , `https://cdsweb.cern.ch/record/1435197/`.

[108] ATLAS Collaboration, *Measurement of the mistag rate with 5* fb^{-1} *of data collected by the ATLAS detector*, ATLAS-CONF-2012-040 , `https://cdsweb.cern.ch/record/1435194/`.

[109] M. Bosman, L. Fiorini, C. Helsens, A. Juste, L. Mir, J. Nadal, and V. Vorwerk, *Weighting method to propagate heavy-flavor tagging calibrations and related uncertainties*, Tech. Rep. ATL-COM-PHYS-2010-331, CERN, Geneva, Jun, 2010.

[110] ATLAS Collaboration, *Electron performance measurements with the ATLAS detector using the 2010 LHC proton-proton collision data*, Eur. Phys. J. **C72** (2012) 1909, `arXiv:1110.3174 [hep-ex]`.

[111] D. Orestano and W. Liebig, *Identification of muon candidates in pp collisions at sqrt(s)=900 GeV with the ATLAS detector*, Tech. Rep. ATLAS-COM-CONF-2010-015, CERN, Geneva, Feb, 2010. Re-submission of already aproved plots to become CONF note.

[112] ATLAS Collaboration, *Muon reconstruction efficiency in reprocessed 2010 LHC proton-proton collision data recorded with the ATLAS detector*, ATLAS-CONF-2011-063 , `https://cdsweb.cern.ch/record/1345743/`.

[113] ATLAS Collaboration, *Performance of missing transverse momentum reconstruction in proton-proton collisions at 7 TeV with ATLAS*, Eur. Phys. J. **C72** (2012) 1844, `arXiv:1108.5602 [hep-ex]`.

[114] ATLAS Collaboration, *Jet energy resolution and selection efficiency relative to track jets from in-situ techniques with the ATLAS detector using proton-proton collisions at a center of mass energy* $\sqrt{s} = 7$ *TeV*, ATLAS-CONF-2010-054 , `https://cdsweb.cern.ch/record/1281311/`.

[115] J. Beringer et al., *Review of Particle Physics*, .

[116] M. L. Mangano, M. Moretti, F. Piccinini, R. Pittau, and A. i. D. Polosa, *ALPGEN, a generator for hard multiparton processes in hadronic collisions*, JHEP **0307** (2003) 001, `arXiv:hep-ph/0206293 [hep-ph]`.

[117] J. Alwall et al., *MadGraph 5 : Going Beyond*, JHEP **1106** (2011) 128, `arXiv:1106.0522 [hep-ph]`.

[118] T. Sjöstrand, S. Mrenna, and P. Z. Skands, *PYTHIA 6.4 Physics and Manual*, JHEP **0605** (2006) 026, `arXiv:hep-ph/0603175 [hep-ph]`.

[119] T. Sjöstrand, S. Mrenna, and P. Skands, *A brief introduction to Pythia 8.1*, Comput. Phys. Commun. **178** (2008) 852–867, `arXiv:0710.3820 [hep-ph]`.

[120] G. Corcella et al., *HERWIG 6: An Event generator for hadron emission reactions with interfering gluons (including supersymmetric processes)*, JHEP **0101** (2001) 010, `arXiv:hep-ph/0011363 [hep-ph]`.

[121] M. Bahr et al., *Herwig++ Physics and Manual*, Eur. Phys. J. **C58** (2008) 639–707, `arXiv:0803.0883 [hep-ph]`.

[122] S. Frixione and B. Webber, *Matching NLO QCD computations and parton shower simulations*, JHEP **06** (2002) 029, `arXiv:hep-ph/0204244`.

[123] P. Nason, *A new method for combining NLO QCD with shower Monte Carlo algorithms*, JHEP **11** (2004) 040, `arXiv:hep-ph/0409146`.

[124] S. Alioli, P. Nason, C. Oleari, and E. Re, *A general framework for implementing NLO calculations in shower Monte Carlo programs: the POWHEG BOX*, JHEP **1006** (2010) 043, `arXiv:1002.2581 [hep-ph]`.

[125] G. P. Salam, *Elements of QCD for hadron colliders*, . Comments: 56 pages, 40 figures. Lectures given at the 2009 European School of High-Energy Physics, Bautzen, Germany, 14-27 June 2009.

[126] S. Catani, F. Krauss, R. Kuhn, and B. Webber, *QCD matrix elements + parton showers*, JHEP **0111** (2001) 063, `arXiv:hep-ph/0109231 [hep-ph]`.

[127] L. Lonnblad, *Correcting the color dipole cascade model with fixed order matrix elements*, JHEP **0205** (2002) 046, `arXiv:hep-ph/0112284 [hep-ph]`.

[128] N. Lavesson and L. Lonnblad, *W+jets matrix elements and the dipole cascade*, JHEP **0507** (2005) 054, `arXiv:hep-ph/0503293 [hep-ph]`.

[129] S. Mrenna and P. Richardson, *Matching matrix elements and parton showers with HERWIG and PYTHIA*, JHEP **0405** (2004) 040, `arXiv:hep-ph/0312274 [hep-ph]`.

[130] M. L. Mangano, M. Moretti, F. Piccinini, and M. Treccani, *Matching matrix elements and shower evolution for top-quark production in hadronic collisions*, JHEP **0701** (2007) 013, `arXiv:hep-ph/0611129 [hep-ph]`.

[131] G. Aad et al., *The ATLAS Simulation Infrastructure*, The European Physical Journal C **70** (2010) no. 3, 823–874. `http://dx.doi.org/10.1140/epjc/s10052-010-1429-9`.

[132] GEANT4 Collaboration, S. Agostinelli et al., *GEANT4: A simulation toolkit*, Nucl. Instrum. Meth. **A506** (2003) 250–303.

[133] ATLAS Collaboration, *The simulation principle and performance of the ATLAS fast calorimeter simulation FastCaloSim*, ATL-PHYS-PUB-2010-013 (2010) . http://cds.cern.ch/record/1300517.

[134] *ATLAS level-1 trigger: Technical Design Report.* Technical Design Report ATLAS. CERN, Geneva, 1998.

[135] P. Jenni, M. Nessi, M. Nordberg, and K. Smith, *ATLAS high-level trigger, data-acquisition and controls: Technical Design Report.* Technical Design Report ATLAS. CERN, Geneva, 2003.

[136] `https://twiki.cern.ch/twiki/bin/view/AtlasPublic/TriggerOperationPublicResults`.

[137] D. Tovey, *On measuring the masses of pair-produced semi-invisibly decaying particles at hadron colliders*, JHEP **04** (2008) 034, `arXiv:0802.2879 [hep-ph]`.

[138] G. Polesello and D. Tovey, *Supersymmetric particle mass measurement with the boost-corrected contransverse mass*, JHEP **03** (2010) 030, `arXiv:0910.0174 [hep-ph]`.

[139] C. Lester and D. Summers, *Measuring masses of semiinvisibly decaying particles pair produced at hadron colliders*, Phys. Lett. **B463** (1999) 99–103, `arXiv:hep-ph/9906349`.

[140] A. Barr, C. Lester, and P. Stephens, *m(T2) : The Truth behind the glamour*, J. Phys. **G29** (2003) 2343–2363, `arXiv:hep-ph/0304226`.

[141] D. Chakraborty, J. Konigsberg, and D. L. Rainwater, *Review of top quark physics*, Ann.Rev.Nucl.Part.Sci. **53** (2003) 301–351, `arXiv:hep-ph/0303092 [hep-ph]`.

[142] T. Han, *The 'Top Priority' at the LHC*, Int.J.Mod.Phys. **A23** (2008) 4107–4124, `arXiv:0804.3178 [hep-ph]`.

[143] S. Willenbrock, *The Standard model and the top quark*, `arXiv:hep-ph/0211067 [hep-ph]`.

[144] R. S. Chivukula, S. B. Selipsky, and E. H. Simmons, *Nonoblique effects in the $Zb\bar{b}$ vertex from ETC dynamics*, Phys. Rev. Lett. **69** (1992) 575–577, `arXiv:hep-ph/9204214 [hep-ph]`.

[145] C. Berger, M. Perelstein, and F. Petriello, *Top quark properties in little Higgs models*, in Proceedings of the 2005 International Linear Collider Physics and Detector Workshop and 2nd ILC Accelerator Workshop (Snowmass 2005) , `arXiv:hep-ph/0512053 [hep-ph]`.

[146] CDF Collaboration, T. Aaltonen et al., *First Observation of Electroweak Single Top Quark Production*, Phys. Rev. Lett. **103** (2009) 092002, `arXiv:0903.0885 [hep-ex]`.

[147] D0 Collaboration, V. M. Abazov et al., *Measurements of single top quark production cross sections and $|V_{tb}|$ in $p\bar{p}$ collisions at $\sqrt{s} = 1.96$ TeV*, Phys. Rev. **D84** (2011) 112001, `arXiv:1108.3091 [hep-ex]`.

[148] CMS Collaboration, *Measurement of the t-channel single top quark production cross section in pp collisions at $\sqrt{s} = 7$ TeV*, Phys. Rev. Lett. **107** (2011) 091802, `arXiv:1106.3052 [hep-ex]`.

[149] ATLAS Collaboration, *Measurement of the t-channel single top-quark production cross section in pp collisions at $\sqrt{s} = 7$ TeV with the ATLAS detector*, `arXiv:1205.3130 [hep-ex]`.

[150] CDF Collaboration, T. Aaltonen et al., *Searching the inclusive lepton + photon + missing E(T) + b-quark signature for radiative top quark decay and non-standard-model processes*, Phys. Rev. **D80** (2009) 011102, `arXiv:0906.0518 [hep-ex]`.

[151] CDF Collaboration, T. Aaltonen et al., *Evidence for $t\bar{t}\gamma$ Production and Measurement of $\sigma_{t\bar{t}\gamma}/\sigma_{t\bar{t}}$*, Phys. Rev. **D84** (2011) 031104, `arXiv:1106.3970 [hep-ex]`.

[152] ATLAS Collaboration, *Measurement of the inclusive $t\bar{t}\gamma$ cross section with the ATLAS detector*, ATLAS-CONF-2011-153 , `https://cdsweb.cern.ch/record/1398197/`.

[153] F. Larios, M. Perez, and C. Yuan, *Analysis of tbW and ttZ couplings from CLEO and LEP / SLC data*, Phys. Lett. **B457** (1999) 334–340, `arXiv:hep-ph/9903394 [hep-ph]`.

[154] U. Baur, A. Juste, L. Orr, and D. Rainwater, *Probing electroweak top quark couplings at hadron colliders*, Phys. Rev. **D71** (2005) 054013, `arXiv:hep-ph/0412021 [hep-ph]`.

[155] LEP Collaboration, ALEPH Collaboration, DELPHI Collaboration, L3 Collaboration, OPAL Collaboration, LEP Electroweak Working Group, SLD Electroweak Group, SLD Heavy Flavor Group Collaboration, *A Combination of preliminary electroweak*

measurements and constraints on the standard model, 2003. `arXiv:hep-ex/0312023 [hep-ex]`.

[156] U. Baur, A. Juste, D. Rainwater, and L. Orr, *Improved measurement of ttZ couplings at the CERN LHC*, Phys. Rev. **D73** (2006) 034016, `arXiv:hep-ph/0512262 [hep-ph]`.

[157] U. Baur, A. Juste, L. Orr, and D. Rainwater, *Probing electroweak top quark couplings at hadron and lepton colliders*, Nucl. Phys. Proc. Suppl. **160** (2006) 17–21, `arXiv:hep-ph/0606264 [hep-ph]`.

[158] A. Kardos, Z. Trócsányi, and C. Papadopoulos, *Top quark pair production in association with a Z-boson at NLO accuracy*, Phys. Rev. **D85** (2012) 054015, `arXiv:1111.0610 [hep-ph]`.

[159] M. Garzelli, A. Kardos, C. Papadopoulos, and Z. Trocsanyi, *Z^0 - boson production in association with a top anti-top pair at NLO accuracy with parton shower effects*, Phys. Rev. **D85** (2012) 074022, `arXiv:1111.1444 [hep-ph]`.

[160] A. Lazopoulos, T. McElmurry, K. Melnikov, and F. Petriello, *Next-to-leading order QCD corrections to $t\bar{t}Z$ production at the LHC*, Phys. Lett. **B666** (2008) 62–65, `arXiv:0804.2220 [hep-ph]`.

[161] CMS Collaboration, *Measurement of the Associated Production of Vector Bosons with Top-Antitop Pairs at 7 TeV*, CMS-PAS-TOP-12-014 , `https://cdsweb.cern.ch/record/1460101`.

[162] ATLAS Collaboration, *Measurement of the top quark-pair production cross section with ATLAS in pp collisions at $\sqrt{s} = 7$ TeV*, Eur. Phys. J. **C71** (2011) 1577, `arXiv:1012.1792 [hep-ex]`.

[163] ATLAS Collaboration, *Measurement of $t\bar{t}$ production with a veto on additional central jet activity in pp collisions at sqrt(s) = 7 TeV using the ATLAS detector*, Eur. Phys. J. **C72** (2012) 2043, `arXiv:1203.5015 [hep-ex]`.

[164] F. A. Berends, H. Kuijf, B. Tausk, and W. T. Giele, *On the production of a W and jets at hadron colliders*, Nuclear Physics **B357** (1991) 32 – 64.

[165] J. Alwall, S. Hoche, F. Krauss, N. Lavesson, L. Lonnblad, et al., *Comparative study of various algorithms for the merging of parton showers and matrix elements in hadronic collisions*, Eur. Phys. J. **C53** (2008) 473–500, `arXiv:0706.2569 [hep-ph]`.

[166] A. Caldwell, D. Kollar, and K. Kröninger, *BAT: The Bayesian analysis toolkit*, Computer Physics Communications **180** (2009) 2197 – 2209.

[167] P. H. Chankowski, J. R. Ellis, and S. Pokorski, *The Fine tuning price of LEP*, Phys.Lett. **B423** (1998) 327–336, `arXiv:hep-ph/9712234 [hep-ph]`.

[168] *Upper bounds on supersymmetric particle masses*, Nuclear Physics B **306** (1988) no. 1, 63 – 76.

[169] A. Strumia, *The Fine-tuning price of the early LHC*, JHEP **1104** (2011) 073, `arXiv:1101.2195 [hep-ph]`.

[170] W. Beenakker, R. Hopker, M. Spira, and P. Zerwas, *Squark and gluino production at hadron colliders*, Nucl.Phys. **B492** (1997) 51–103, `arXiv:hep-ph/9610490 [hep-ph]`.

[171] J. Alwall, P. Schuster, and N. Toro, *Simplified Models for a First Characterization of New Physics at the LHC*, Phys.Rev. **D79** (2009) 075020, `arXiv:0810.3921 [hep-ph]`.

[172] LHC New Physics Working Group Collaboration, D. Alves et al., *Simplified Models for LHC New Physics Searches*, J.Phys. **G39** (2012) 105005, `arXiv:1105.2838 [hep-ph]`.

[173] G. Aad et al., *Search for top and bottom squarks from gluino pair production in final states with missing transverse energy and at least three b-jets with the ATLAS detector*, The European Physical Journal C **72** (2012) no. 10, 1–19. `http://dx.doi.org/10.1140/epjc/s10052-012-2174-z`.

[174] *Search for strong production of supersymmetric particles in final states with missing transverse momentum and at least three b-jets using 20.1 fb1 of pp collisions at sqrt(s) = 8 TeV with the ATLAS Detector.*, Tech. Rep. ATLAS-CONF-2013-061, CERN, Geneva, Jun, 2013.

[175] S. Owen, *Data-driven estimation of the QCD multijet background to SUSY searches with jets and missing transverse momentum at ATLAS using jet smearing*, Tech. Rep. ATL-COM-PHYS-2011-1066, CERN, Geneva, Aug, 2011.

[176] `https://twiki.cern.ch/twiki/bin/viewauth/AtlasProtected/SusyFitter`.

[177]

[178] CDF Collaboration, T. Aaltonen et al., *Search for the Production of Scalar Bottom Quarks in $p\overline{p}$ Collisions at* $\sqrt{s}$ = 1.96 TeV, .

[179] *Search for scalar bottom quarks and third-generation leptoquarks in collisions at*, Physics Letters B **693** (2010) no. 2, 95 – 101.

[180] LEP SUSY Working Group (ALEPH, DELPHI, L3, OPAL), Notes LEPSUSYWG/01-03.1 and 04-01.1, http://lepsusy.web.cern.ch/lepsusy/Welcome.html.

[181] ATLAS Collaboration, *Charged particle multiplicities in pp interactions at* $\sqrt{s} = 900$ *GeV and 7 TeV in a diffractive limited phase-space measured with the ATLAS detector at the LHC and new PYTHIA6 tune.*, ATLAS-CONF-2010-031, 2010.

[182] A. Shertstnev and R. Thorne Eur. Phys. J. **C55** (2008) 553–575.

[183] J. Butterworth, J. R. Forshaw, and M. Seymour, *Multiparton interactions in photoproduction at HERA*, Z.Phys. **C72** (1996) 637–646, `arXiv:hep-ph/9601371 [hep-ph]`.

[184] F. P. K. Melnikov, *Electroweak gauge boson production at hadron colliders through O(alpha(s)**2)*, Phys. Rev. **D74** (2006) 114017, `arXiv:hep-ph/0609070`.

[185] R. Gavin et al., *FEWZ 2.0: A code for hadronic Z production at next-to-next-to- leading order*, **D74** .

[186] S. Moch and P. Uwer Nucl. Phys. Proc. Suppl. **183** (2008) 75–80.

[187] A. Sherstnev and R. Thorne, *Parton Distributions for LO Generators*, Eur. Phys. J. **C55** (2008) 553–575, `arXiv:0711.2473 [hep-ph]`.

[188] W. Beenakker, R. Hopker, and M. Spira, *PROSPINO: A Program for the production of supersymmetric particles in next-to-leading order QCD*, 1996. `arXiv:hep-ph/9611232 [hep-ph]`.

[189] http://web.physik.rwth-aachen.de/service/wiki/bin/view/Main/SquarksandGluinos.

[190] M. Aliev et al., *HATHOR: HAdronic Top and Heavy quarks crOss section calculatoR*, Comput. Phys. Commun. **182** (2011) 1034, `arXiv:1007.1327 [hep-ph]`.

[191] B. P. Kersevan and E. Richter-Was, *The Monte Carlo event generator AcerMC version 2.0 with interfaces to PYTHIA 6.2 and HERWIG 6.5, hep-ph/0405247*, 2004. `arXiv:hep-ph/0405247`.

[192] S. Catani et al., *Vector boson production at hadron colliders: A Fully exclusive QCD calculation at NNLO*, Phys.Rev.Lett. **103** (2009) 082001, `arXiv:0903.2120 [hep-ph]`.

[193] J. M. Campbell and R. K. Ellis, $t\bar{t}W^{+-}$ *production and decay at NLO*, JHEP **1207** (2012) 052, `arXiv:1204.5678 [hep-ph]`.

[194] J. M. Campbell, R. K. Ellis, and C. Williams, *Vector boson pair production at the LHC*, JHEP **1107** (2011) 018, `arXiv:1105.0020 [hep-ph]`.